Solving the Ubiquitous Problem of Stellar Radii

Samuel Arthur Frank Morrell

Submitted by Samuel Arthur Frank Morrell to the University of Exeter as a thesis for the degree of Doctor of Philosophy in Physics, September, 2019.

I certify that all material in this thesis which is not my own work has been identified and that no material has previously been submitted and approved for the award of a degree by this or any other University.

Signed: .....

Samuel A. F. Morrell

Date: .....

Abstract

1st Supervisor: Professor Tim Naylor 2nd Supervisor: Professor David Sing

This thesis will address the problem of measuring stellar radii, which is ubiquitous across many fields of modern astrophysics. A technique is introduced which integrates the area beneath the stellar spectral energy distribution (SED) of a star to measure its luminosity, and the shape of the SED to measure its temperature - from which follows its radius. This method addresses many of the problems facing of existing methods, which are reviewed, as it provides accurate measurements of stellar radius using only multiband photometry and precision parallaxes.

It is well known that the radii and temperatures of M-dwarf prescribed by models are in disagreement with observations, both on the pre-main-sequence (pre-MS) and the main-sequence (MS). This methodology is applied to pre-MS M-dwarfs in the Pleiades and Praesepe clusters to perform a direct comparison to the radii predicted by stellar interiors. Assessment of the physicality and accuracy of the stellar atmosphere models is also performed by comparing synthetic spectra generated from them to flux–calibrated spectroscopic observations. The parameters for the synthetic spectra are provided by the SED fitting, allowing verification of the methodology itself to be performed.

The advent of Gaia DR2 means that reliable distances are now available for field M-dwarfs, permitting the extension of this investigation to MS stars. Through this investigation, the nature of radius inflation in MS M-dwarfs is studied as a function of mass. This crucially allows insight into the physics behind the observed radius inflation, allowing current theories underpinning radius inflation to be critically assessed. The conclusion of this investigation is that magnetic models are currently unable to explain radius inflation in M-dwarfs.

Given the successful application of the SED fitting methodology in measuring the stellar radii of miscellaneous field stars, this work is built upon to address the problem of

determining the stellar parameters of exoplanet host radii. In doing so, it is demonstrated that the SED fitting technique extends well to the mass range of stars currently being scrutinised to discover and characterise exoplanets. Given its wide applicability for exoplanet host characterisation, the potential systematic errors that may prove problematic are reviewed and methods for their mitigation are suggested.

Contents

List of Figures

List of Tables

Declaration

The work presented in Chapter 4 was taken from a paper published in Monthly Notices of the Royal Astronomical Society by Sam Morrell and Tim Naylor entitled Exploring the M-dwarf Luminosity - Temperature - Radius Relationships using Gaia DR2 (MNRAS, 489, 2615). The work presented in Chapter 3 and Chapter 5 is due to be published in the near future, and presents a development upon the published work. The photometric and spectroscopic observations from the William Herschel Telescope were obtained by Tim Naylor, Bill Barnes and myself. The calculation of the system responses for the *Isaac Newton* Telescope Wide Field Camera photometric system were performed by Tim Naylor. The William Herschel Telescope is operated on the island of La Palma by the Isaac Newton Group of Telescopes in the Spanish Observatorio del Roque de los Muchachos of the Instituto de Astrofísica de Canarias. The rest of the work contained in this thesis is my own.

Acknowledgements

I would first like to extend sincerest thanks to my supervisor, Tim Naylor, for giving me the opportunity to pursue a lifelong passion and fulfil my dream of completing a PhD. Tim's infectious enthusiasm for science continues to inspire me, and his continued support, understanding, and insight into any problem I happen to darken his (metaphorical) doorstep with has made completing this thesis possible. I would like to thank Matthew Browning and Lewis Ireland for doing a critical reading of the work presented Chapter 4 and to Victor See and Sean Matt for useful conversations regarding stellar rotation. I would also like to gratefully acknowledge the feedback from the anonymous referee for the publication from which Chapter 4 was adapted for providing useful insight many facets of the work, including metallicity, activity and discrepancies in the parameters of eclipsing binaries. I would also like to thank Stuart Littlefair who prompted me to investigate correlations with activity in Chapter 4. I would like to acknowledge help from enthusiastic guest astronomer Bill Barnes, who helped with both planning and observations during the observing run the William Herschel Telescope for Chapter 3. I would also like to thank Aaron Labdon for useful conversations regarding interferometry. I would like to extend my thanks to all of the staff and students, past and present, in the astrophysics group who have made working on my PhD project an absolute pleasure throughout the past 4 years - especially my comrades in arms Alison Young, Ed Hone, Jayesh Goyal and Jess Spake, with whom I have shared this wild ride, and have provided encouragement and sympathetic commiserations along the way. Particular thanks go out to Felix Sainsbury-Martinez, Lewis Ireland, Chris Mowat, Angela Breimann and Jon Rees for providing oft needed distractions, complaining sessions and entertainment. I would also like to acknowledge my friends and PhD buddies Sam Cooper and Peter Inzani for keeping me sane throughout my PhD. An additional thanks goes out to Felix

Sainsbury-Martinez, Lewis Ireland and Sam Cooper who kindly took time out from their busy schedules (and holidays) to review this thesis as it was nearing completion - your expertise and feedback was invaluable.

On a personal note, I would like to express a heartfelt thank you to my parents, Bungy and Hazel, for their unwavering support and understanding throughout my seemingly eternal studenthood. I will always be thankful to them for indulging my interests and fascinations from a young age, and encouraging me not to merely accept things I was told, but to question them - which I am certain has contributed towards my passion for science today. I would also like to thank them for introducing me to and sharing with me a love for Star Trek and Queen, which has certainly served as inspiration along the way. An additional thanks goes to Sandy who has provided much needed dog-based de-stressing throughout my PhD. It is also my wish that my grandfather, Harold, could have seen the completion of this PhD - as he always served as a source of boundless optimism, enthusiasm and curiosity about my work.

Finally, I would like to thank my partner Laura for her continued love and support over the last seven years. Without her encouragement I would likely not have had the courage to apply for a PhD in the first place, so I am eternally grateful for that. Her continued bravery and tenacity in the face of lifes challenges continues to inspire me to this day. Also, her miraculous proof reading skills have been incredibly useful when completing the publications and thesis for this PhD - surely guaranteeing her the title of my proof reader extraordinaire.

I would like to acknowledge the UK Science and Technology Facilities Council (STFC) for financial support throughout this PhD.

This thesis made use of the William Herschel Telescope, which is operated on the island of La Palma by the Isaac Newton Group of Telescopes in the Spanish Observatorio del Roque de los Muchachos of the Instituto de Astrofísica de Canarias.

This thesis made use of photometric data from UK Infrared Deep Sky Survey (UKIDSS). The UKIDSS project is defined in Lawrence et al. (2007). UKIDSS uses the UKIRT Wide Field Camera (WFCAM; Casali et al. (2007)). The photometric system is

described in Hewett et al. (2006), and the calibration is described in Hodgkin et al. (2009). The pipeline processing and science archive are described in Irwin et al (2009, in prep) and Hambly et al. (2008).

This thesis has made use of data from the European Space Agency (ESA) mission *Gaia* (https://www.cosmos.esa.int/gaia), processed by the *Gaia* Data Processing and Analysis Consortium (DPAC, https://www.cosmos.esa.int/web/gaia/dpac/consortium). Funding for the DPAC has been provided by national institutions, in particular the institutions participating in the *Gaia* Multilateral Agreement.

This thesis makes use of data products from the Two Micron All Sky Survey, which is a joint project of the University of Massachusetts and the Infrared Processing and Analysis Center / California Institute of Technology, funded by the National Aeronautics and Space Administration and the National Science Foundation.

This thesis makes use of data products from the Wide-field Infrared Survey Explorer, which is a joint project of the University of California, Los Angeles, and the Jet Propulsion Laboratory/California Institute of Technology, funded by the National Aeronautics and Space Administration.

This thesis makes use of data obtained as part of the INT Photometric Hα Survey of the Northern Galactic Plane (IPHAS, www.iphas.org) carried out at the Isaac Newton Telescope (INT). The INT is operated on the island of La Palma by the Isaac Newton Group in the Spanish Observatorio del Roque de los Muchachos of the Instituto de Astrofisica de Canarias. All IPHAS data are processed by the Cambridge Astronomical Survey Unit, at the Institute of Astronomy in Cambridge. The bandmerged DR2 catalogue was assembled at the Centre for Astrophysics Research, University of Hertfordshire, supported by STFC grant ST/J001333/1.

Based on data products from observations made with ESO Telescopes at the La Silla Paranal Observatory under programme ID 177.D-3023, as part of the VST Photometric Hα Survey of the Southern Galactic Plane and Bulge (VPHAS+, www.vphas.eu).

This thesis has made use of data obtained from the 3XMM XMM-Newton serendip-

itous source catalogue compiled by the 10 institutes of the XMM-Newton Survey Science Centre selected by ESA.

This work is based in part on observations made with the Spitzer Space Telescope, which is operated by the Jet Propulsion Laboratory, California Institute of Technology under a contract with NASA.

Based on observations made with the NASA Galaxy Evolution Explorer. GALEX is operated for NASA by the California Institute of Technology under NASA contract NAS5-98034.

This thesis has made use of the VizieR catalogue access tool, CDS, Strasbourg, France. I gratefully acknowledge the software that made this work possible, including: STILTS and TOPCAT (Taylor 2006b), Scipy (Jones et al. 2001), Numpy (Oliphant 2015), Matplotlib (Hunter 2007) and Astropy (Astropy Collaboration et al. 2013).

Samuel Morrell

Exeter, U.K.

September 2019

Chapter 1

Introduction

"We're made of star stuff. We are a way for the cosmos to know itself."

— Carl Sagan

1.1 The Ubiquitous Problem of Stellar Parameters

After formation, the evolution of any given star is dictated by the ongoing conflict between two key processes: gravitation which acts to reduce potential energy within the system by contracting it inwards, and nuclear reactions within the core of the star which provide a counteracting pressure outwards. Once evolved onto the main sequence (MS) the star halts quasi-static contraction and begins a fine balancing act between gravity and nuclear burning which keeps it stable for Myr to many Gyr until core hydrogen is exhausted. What still remains somewhat unclear are all of the physical processes that act within stars throughout their evolution and their contribution towards expansion or contraction. Our understanding of stellar evolution comes from observing, and attempting to reproduce, the subtle interplay between these processes. This is done for billions of observable stars in our Milky Way galaxy, and other nearby galaxies, such as the notable examples of the Small and Large Magellanic Clouds. This necessitates a thorough understanding of the fundamental stellar parameters, which both mediate and are influenced by the physics within the star.

The most fundamental of these parameters are mass M and metallicity, i.e. the

chemical composition of the star. Metallicity is generally represented observationally as $\log_{10}$ of the ratio of iron abundance to hydrogen abundance [Fe/H] and theoretically as the ratio of the abundance of all metals to hydrogen abundance [M/H]; both of which are relative to the solar value, hence $[\mathrm{Fe/H}]_\odot = [\mathrm{M/H}]_\odot = 0$. In principle, without considering the effect of rotation, this combination dictates the entire evolution of a single star from the moment of its birth. However, determining both of these parameters has proven somewhat problematic. In particular, a reliable technique for determining precise stellar masses of single field stars in isolation would be the "holy grail" for practitioners of stellar evolution.

Owing to the balance between gravitation and nuclear reactions, in theory even a young, non-rotating star undergoing quasi-static contraction will approach hydrostatic equilibrium. Under this condition it will exhibit a spherical gravitational isosurface at the outer boundary of radius R, of surface area $4\pi R^2$. This defines two more parameters: stellar radius R and gravitational acceleration towards the star at the stellar surface g, defined as

$$g = \frac{GM}{R^2} = \frac{4\pi}{3} G\rho R, \tag{1.1}$$

where G is the Newtonian constant of gravitation and ρ is the mean mass density of the star. Although in reality, due to rotation, stars are oblate spheroids, most of their flattening ratios are sufficiently small that a sphere serves as a good approximation. Less inscrutable than mass, the stellar radius can be directly measured or inferred using a large variety of techniques, which are reviewed in Section 1.7. Surface gravity, which is measured in cm s^{-2} and expressed as $\log_{10}(g)$, serves as the proxy for the bulk mass of the star in observations. Because gravity influences the strength of spectral lines and opacity of the photosphere, it can be constrained using spectra. Spectra also encode a wealth of other information about the stellar photosphere. However, by ignoring absorption and emission due to molecular and atomic species, stellar spectral energy distributions (SEDs) can be approximated well by a blackbody of effective temperature T_{eff}. By definition this emits a flux of $\sigma T_{\mathrm{eff}}^4$ over the entire stellar surface, leading to the well-known relation

$$L = 4\pi R^2 \sigma T_{\mathrm{eff}}^4, \tag{1.2}$$

where σ is the Stefan–Boltzmann constant. This relation serves as a powerful tool that couples bulk stellar properties to those of the photosphere through R and our final two parameters: effective temperature $T_{\rm eff}$ and bolometric luminosity L. From Equation 1.2 any of L, R or $T_{\rm eff}$ can be found with knowledge of the other two, with all three defining a star.

The effective temperature $T_{\rm eff}$ characterises the temperature of the photosphere by its blackbody emission; negating spectral features. Conversely, temperature-sensitive spectral features can be employed to measure a spectroscopic temperature $T_{\rm sp}$. Despite multi-object spectrographs, such as WEAVE (Dalton et al. 2012), coming online, spectroscopic observations remain expensive and time consuming compared to photometric measurements. Eclipsing binary measurements also employ the brightness temperature $T_{\rm br}$, which determines temperatures of DEB components via Wien's law. In this thesis, I introduce a further measure of temperature which uses photometric data to sample the true shape of the stellar spectral energy distribution (SED) — the so called SED temperature $T_{\rm SED}$. Measurements of $T_{\rm SED}$ implicitly sample both continuum emission from the photosphere and strong spectral features which fall within the photometric system responses of bands used for the measurement.

The constraints on the parameters presented throughout this section have fundamental importance in providing key insights into many facets of modern astronomy. This thesis serves as an exploration of the ubiquitous problem of determining stellar parameters, in particular stellar radii, and how the lack of robust constraints on them is responsible for some of the most pressing open questions in low-mass stellar evolution (see Chapter 3 and Chapter 4) and exoplanet characterisation (see Chapter 5). In this chapter I will introduce the problems caused by poor constraints in radius for pre-MS M-dwarfs, MS M-dwarfs and exoplanet host stars, and perform a critical review on the techniques currently being employed by the astrophysical community to make radius measurements.

1.2 Forming Young Stellar Clusters

Any framework which hopes to understand stars, and by extension the planetary systems which orbit them, must necessarily account for the environment from which they originate. Stars form from a mixture of dust and gas, processed and enriched by previous stellar populations, which constitutes the interstellar medium (ISM). Most of the ISM is relatively diffuse, making the Jeans Mass parcel of material required to achieve instability and gravitationally collapse relatively scarce. Consequently, it is thought that most star formation is confined to cold, dense molecular gas clouds, which naturally form and dissipate through gravitation and turbulence in the ISM (e.g. Dobbs et al. 2006; Dobbs & Bonnell 2007), and survive on the order of 10^7 years (Blitz & Shu 1980). Simulations of Bonnell et al. (2011) show that indeed star formation efficiency in large stellar clusters is around 40%, as opposed to $< 1\%$ in regions of distributed star formation.

Understanding of the environments, masses and dissipation timescales of these regions is the foundation upon which modern star formation theory is built. Fortunately, our Solar system is in the midst of a flurry of both ongoing star formation and the resulting young stellar clusters. We have a front row seat to view the massive giant molecular clouds (GMCs), star formation regions (SFRs) and young stellar clusters which constitute Gould's Belt; named for the American astronomer who performed the first detailed study of the complex, Benjamin Gould (Gould 1879). This region remains somewhat puzzling due to its apparent ring-like morphology. One theory for its formation suggests a collision between a GMC of around 10^7 $M_\odot$ and a dark matter clump of around 10^6 $M_\odot$ at an oblique angle of between 16° and 22° inclined from the galactic plane. Simulations of Comeron & Torra (1994) and Bekki (2009) support this scenario. The ensuing shock wave is thought to have lead to the abundance of active and efficient star formation which we observe today. Importantly, the rich history of star formation in this region pre-dates this occurrence, with many young stellar clusters, such as the well studied Pleiades open cluster, being the result. Due to this there are comprehensive long-running surveys being carried out using SCUBA-2 on the James Clark Maxwell Telescope (Ward-Thompson et al. 2007).

The most scrutinised region of Gould's Belt is probably the Orion molecular cloud complex. Situated about 400 pc from Earth (Menten et al. 2007), this 90 pc long filamentary

structure (Großschedl et al. 2018) harbours at its centre the Trapezium cluster. At an estimated 2 to 6 Myr in age (Mayne & Naylor 2008; Bell et al. 2012), the majority of the stars in the cluster are pre–main sequence, and possess dusty circumstellar discs, within which planets are likely to form (Lada et al. 2000; Haisch et al. 2001).

1.2.1 Forming Clusters from Clouds

In considering the evolution of young stars, and the open clusters which they comprise, we must first consider the physical processes which drive their formation mechanisms. There are many intricacies involved in the process of star formation, including thorough treatments of hydrodynamic turbulence, magnetism and stellar feedback, which are beyond the scope of this thesis. However, it is advantageous to be aware of the broad picture of the formation of stellar clusters, as the context in which to view the remainder of stellar evolution.

To consider how open clusters form from GMCs, let us follow a spherical cloud of nearly uniform gas, with radius $R_{\rm cloud}$ and mass $M_{\rm cloud}$ within a GMC; such as the Orion Nebula. Whether the system us in equilibrium is established using the Virial theorem, expressed as

$$E_g + 2E_k = 0, \tag{1.3}$$

where E_g and E_k are the gravitational potential energy and the internal kinetic energy of the cloud. For the cloud the internal energy is given by

$$E_k = \frac{3}{2} N k_B T, \tag{1.4}$$

and gravitational potential energy is given by

$$E_g = -\frac{3}{5} \frac{G M_{\rm cloud}^2}{R_{\rm cloud}}, \tag{1.5}$$

where k_B is the Boltzmann constant, T is the thermodynamic temperature of the cloud, which contains N particles. The cloud will remain stable against collapse as long as the internal pressure of the gas exceeds the combination of the pressure from the surrounding gas combined with self gravitation ($2E_k \geq E_g$). In the situation where gravitation

overcomes internal energy ($2E_k < E_g$), the cloud will undergo collapse, and lead to the formation of a stellar cluster.

The cloud is forced out of equilibrium by small perturbations moving through the bulk cloud, amplified by a process known as gravitational instability. In his seminal work in Jeans (1902), James Jeans considered how perturbations moved through an infinite, uniform medium to estimate the minimum mass for a parcel to become unstable and collapse. The so called Jeans Mass M_J is given by the expression

$$M_J = \rho\lambda_J^3 = \sqrt{\left(\frac{5k_BT}{Gm}\right)^3\left(\frac{3}{4\pi\rho}\right)}, \tag{1.6}$$

where ρ is the uniform density of the medium, $c_s = \sqrt{kT/m}$ is the isothermal speed of sound in the medium, with m being the average particle mass. The characteristic scale length introduced in this equation λ_J is the Jeans Length, and describes the minimum length scale at which perturbations propagate. Below this limit perturbations grow exponentially due to being gravity dominated, leading to the gravitational collapse of the parcel. Although widely used in literature, it is noted that Jeans' analysis neglects the distant background density, making the analysis numerically inconsistent (Binney & Tremaine 1987). Several authors have attempted to show a mathematically clean derivation for Jeans' work (e.g. Falco et al. 2013; Kiessling 2003), however there have also been several reinterpretations of the problem. For example, by considering a self-gravitating, isothermal layer of fixed sound speed c_s, the critical wavelength of the turbulence is

$$\lambda_{\text{crit}} = 2\pi H = \frac{2c_s^2}{G\mu}, \tag{1.7}$$

where μ is the surface density of the layer and $H = \sqrt{c_s^2/\pi G\mu}$ is the scale height (Spitzer 1942). If perturbations are assumed to by cylindrical, then Larson (1985) shows that the minimum unstable mass within the contracting region becomes

$$M_{\text{crit}} = 4.67\frac{c_s^4}{G^2\mu}. \tag{1.8}$$

When the perturbations in the cloud compact the cloud sufficiently $M_J > M_{\text{cloud}}$,

such that the gravitational attraction can overwhelm the dispersive effects of the internal pressure, the cloud becomes gravitationally bound and begins to collapse. In the absence of any other effects which may invoke a pressure gradient, which is in reality rather unphysical, the collapse of this uniform sphere of material occurs over a free-fall time

$$t_{\rm ff} = \sqrt{\frac{3}{M}} 4\pi R^3, \tag{1.9}$$

defined by Spitzer (1978) as the time required to collapse to infinite density from a state of rest.

An interesting and important result of Equation 1.6 and Equation 1.7 is that the mass required for some section of the bulk cloud to collapse is inversely proportional to ρ; resulting in M_J decreasing during contraction. Although until now we have assumed the cloud to be isotropic, it is intuitive to see that there will be regions of differing density throughout the medium. When higher density regions reach M_J they begin to contract under their own self gravitation, somewhat decoupled from the bulk of the cloud; a process known as fragmentation. It is thought this process through which large GMCs collapse and fragment into young stellar clusters, and how these clusters fragment and collapse further into many stellar mass protostars (Prialnik 2009). The smallest scale of fragmentation is determined by the first 'hydrostatic' core. Further fragmentation is prevented when hydrogen within the protostar is ionised, stifling the transport of radiation through the collapsing envelope.

Throughout the remainder of pre–main sequence (pre-MS) evolution, the star follows a well-defined mass-dependent path through effective temperature–luminosity space. Stars with $M \leq 0.5\ M_\odot$ will follow the Hayashi track (Hayashi & Hoshi 1961; Hayashi 1961) until core hydrogen burning initiates, and the star enters the zero-age main sequence (ZAMS). Henyey et al. (1955) showed that stars with $2\ M_\odot \geq M \geq 0.5\ M_\odot$ can remain in radiative equilibrium while contracting onto the ZAMS. So intermediate mass stars will follow the Hayashi track until a radiative zone develops, at which point they will slowly contract onto the ZAMS in near hydrostatic equilibrium via the Henyey track. Figure 1.1 shows the evolution for the masses of star covered in this thesis, as prescribed

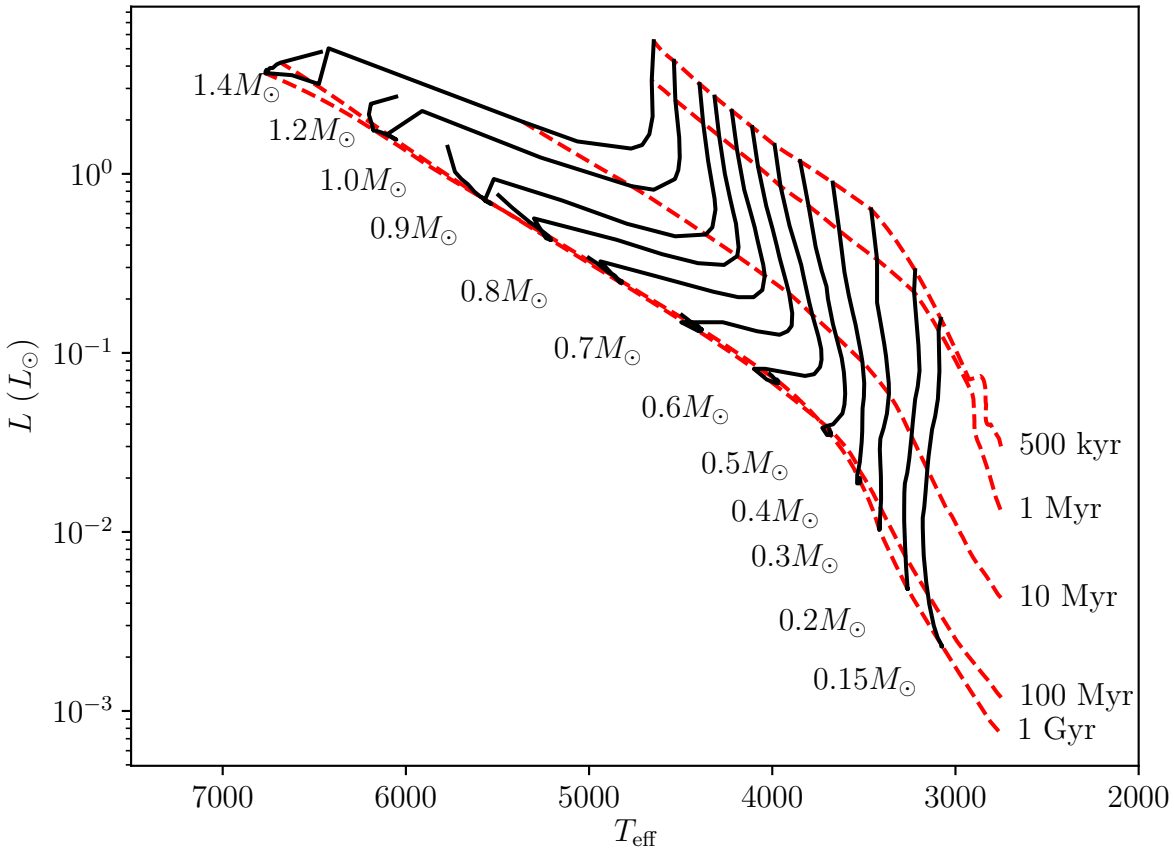

Figure 1.1: The pre-MS evolution for stars of $1.4M_\odot \geq M \geq 0.15\ M_\odot$ as given by the Baraffe et al. (2015) evolution models. The isochrones shown in the plot are quadratically interpolated in mass (see Section 3.5.3). The black lines trace lines of constant mass evolving through the red dashed lines of constant age (isochrones), from the Class I YSO phase onto the MS at 10^8 to 10^9 yr, depending on mass. For $M < 0.5\ M_\odot$ the collapse is exclusively via the Hayashi track (vertically downward onto the ZAMS in this space). However, for $M \geq 0.5\ M_\odot$ the collapse onto the ZAMS is performed via the Henyey track (which manifests as a collapse toward increasing $T_{\rm eff}$) when a radiative zone forms.

by the Baraffe et al. (2015) interiors.

Stars enter the main sequence when conditions are suitable for the onset of thermonuclear burning of hydrogen within the core. The radiation pressure resulting from core hydrogen burning stabilises the star against gravitational contraction, bringing it into equilibrium for the main sequence phase of its evolution.

1.3 The Stellar and Substellar Initial Mass Function

Hints of the complex multi-scale physics that govern pre-MS evolution are encoded into the distribution of stellar mass as stars reach the ZAMS. This is represented by an empirical function which essentially serves as a probability density function (PDF) for

the initial stellar mass. This can then usefully be sampled, for example with Monte Carlo methods, to produce synthetic stellar populations that are consistent with observations. As the evolution of a star is largely determined by its mass, it has long been known that constraining the initial mass function (IMF) is an important step in understanding stellar physics.

The process of constraining an empirical IMF, as described in Offner et al. (2014), can broadly be broken into 3 stages. Observations of a complete population of stars that lie within a given volume, such as our local volume, allow observers to measure a stellar luminosity function. A present day mass function is then produced from the luminosity function using a mass–luminosity relationship. Finally, the present day mass function is corrected for star-formation history, stellar evolution, galactic structure, cluster dynamical evolution and multiplicity to obtain an IMF—a complex and involved process, during which many biases and systematic uncertainties can be introduced. The first attempt to quantify the IMF was performed by Salpeter (1955), who was able to show that the occurrence rate of stars of each mass falls off rapidly with increasing mass. Using observations, Salpeter (1955) showed that stars with masses greater than a few solar masses adopt a power law distribution of the form $dN \propto M^{-\alpha} dM$, with $\alpha = 2.35$. This remains the standard IMF for stars with $M > \mathrm{M}_{\odot}$ (Offner et al. 2014), however this distribution diverges as $M \to 0$. It was noted in Miller & Scalo (1979) that the IMF was approximated by a log-normal distribution for $0.1\ \mathrm{M}_{\odot} < M \lesssim 30\ \mathrm{M}_{\odot}$. A more modern approach was adopted by Kroupa (2001) and Kroupa (2002) who presented an IMF which retained the Salpeter (1955) IMF for $M > M_{\odot}$, but introduced further power law segments of decreasing exponent for decreasing masses. The work of Chabrier (2003) and Chabrier (2005) once again adopted a power law tail above $1\ \mathrm{M}_{\odot}$, but represented the low mass population with a lognormal distribution. All three IMFs are shown for comparison in Figure 1.2. Regardless of the formulation, all three commonly utilised forms of the IMF concur on the fact that M-dwarfs are the most abundant stars in the galaxy; making up over 70% of the stars in the Milky Way (Bochanski et al. 2010).

Despite this, the exact form of the IMF at very low masses remains uncertain and relatively unconstrained. Thies & Kroupa (2007) show a discontinuity in the multiplicity-

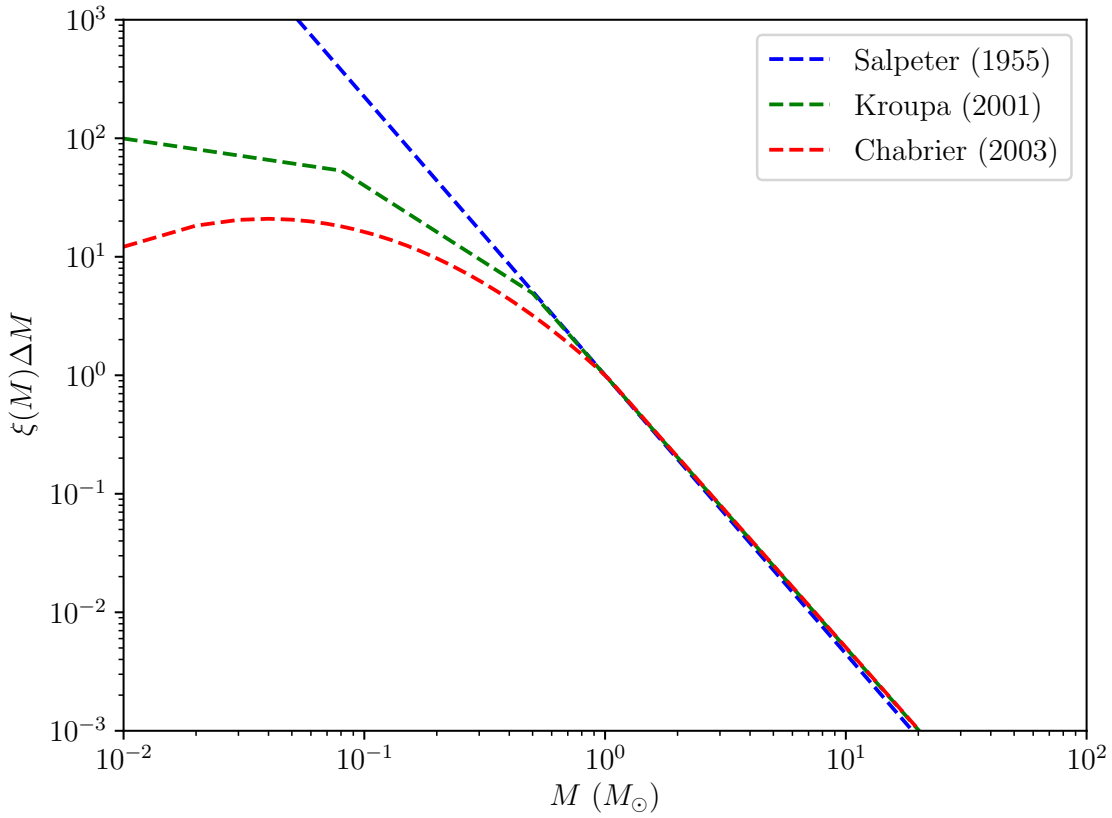

Figure 1.2: A comparison of the stellar initial mass functions discussed in this thesis. The Salpeter (1955) power-law IMF is shown in blue, the Kroupa (2001) segmented IMF is shown in green and the Chabrier (2003) log-normal IMF is shown in red. Importantly, despite their clear differences, they all concur that M-dwarfs are the most abundant stars in the galaxy by up to several orders of magnitude. Adapted from a figure by Johannes Buchner.

corrected mass function in the very low mass star and brown dwarf ($M < 0.07$ M$_\odot$) regime, which served as the impetus for an independent brown dwarf / very–low-mass star IMF in Kroupa et al. (2013). Another ongoing debate is with regard to the universality of the IMF, however studies of this are still hamstrung by robust constraints on stellar populations, and uncertainties in the mass–luminosity relation at very low masses and young ages (Offner et al. 2014). This serves as a strong motivation for better understanding the physics that drives these stars, and serves as the impetus for much that is to follow in this thesis.

1.4 The Characteristics of M-dwarfs

M-dwarfs are a very diverse demographic of stars, spanning 3 orders of magnitude in bolometric luminosity (Baraffe & Chabrier 1996). They also span a large range of masses,

from the M–K transition at 0.6 $M_\odot$ down to the hydrogen burning minimum mass at 0.07 $M_\odot$, below which is the domain of the sub-stellar population. The evolution of the stars differ considerably across the mass range, with calculations of Chabrier et al. (1996) finding that the age of the ZAMS varies from $\sim 10^8$ yr for 0.6 $M_\odot$ to $\sim 5 \times 10^9$ yr.

1.4.1 Stellar Structure

The internal structure of M-dwarfs was first modelled in Osterbrock (1953), who claimed that the observed properties of several early M-dwarfs could be understood in terms of an outer convective zone extended inwards to about 30% of the stellar radius. Indeed, like all main sequence stars, M-dwarfs contain regions of convective flows within their interior. The structure of the star, determined by the method by which energy is transported throughout its interior, is inextricably linked to its entropy structure (Stahler 1988). Much of the material in this section is adapted from Lamers & Levesque (2017), which provides a thorough review of stellar physics. Radiative zones are layers of the stellar interior where radiative diffusion and thermal conduction are dominant means of energy transport. Radiative energy transport through an optically thick medium is described by Eddington's equation of radiative equilibrium

$$\frac{dT}{dr} = -\frac{3}{4}\frac{1}{ac}\frac{\kappa\rho}{T^3}\frac{L_r}{4\pi r^2} \tag{1.10}$$

where $ac = 4\sigma$ is the radiation constant, κ is the opacity and other symbols have their usual thermodynamical meanings (e.g. Lamers & Levesque 2017). This describes the temperature gradient throughout the star, so long as radiative equilibrium is maintained, i.e. the total radiative flux in to a thin layer of the star of height dr is the same as the radiative flux out of the layer. Thus intuitively radiative transfer is the main means of energy transfer unless the temperature gradient is steep, in the case where large amount of energy transport are required, or in the presence of high opacity, such as in the atmospheres of M-dwarfs.

In regions of the stellar interior where radiative diffusion is not efficient enough, energy is also transported by the bulk convective motion of the gas in the star. In convective energy transport, parcels of hot material rise through buoyancy to deposit heat to cooler

layers, before descending again as much cooler parcels. This process was first formalised in Schwarzschild (1906) who considered a parcel of material which rises from an initial position at height r to the destination at $r + \Delta r$. Initially, the temperature T, pressure P and density ρ in the parcel match the conditions of the ambient background. After rising a distance of Δr the ambient conditions become $T + \Delta T$, $P + \Delta P$ and $\rho + \Delta\rho$. We recall from the ideal gas law that

$$\rho \propto \frac{P}{T}, \tag{1.11}$$

and

$$\frac{\Delta\rho}{\rho} = \frac{\Delta P}{P} - \frac{\Delta T}{T}. \tag{1.12}$$

Due to the high opacity within the rising parcel, we can assume that as it rises it adiabatically expands to $T + \delta T$, $P + \delta P$ and $\rho + \delta\rho$; note that the conditions within the parcel and in the ambient background now differ. Given that this process is adiabatic, i.e. the energy exchanged between the parcel and the ambient background $\delta Q = 0$, the pressure for an adiabatically expanding ideal gas is governed by

$$P \propto \rho^{\gamma_{\text{ad}}}, \tag{1.13}$$

where $\gamma_{\text{ad}} = C_P/C_V$ is the adiabatic index, and C_P and C_V are the heat capacity at constant pressure and volume respectively. By differentiating Equation 1.13 we find that

$$\frac{\delta\rho}{\rho} = \frac{1}{\gamma_{\text{ad}}}\frac{\delta P}{P}. \tag{1.14}$$

Given that we know that this is a buoyant process, convection persists as long as $\delta\rho < \Delta\rho$. Thus, by substituting Equation 1.12 and Equation 1.14 into this expression, we find the inequality

$$\frac{1}{\gamma_{\text{ad}}}\frac{\delta P}{P} < \frac{\Delta P}{P} - \frac{\Delta T}{T}. \tag{1.15}$$

We recall that during adiabatic expansion, the pressure of the parcel remains consistent with the ambient background, therefore $\delta P = \Delta P$, meaning that from Equation 1.15

$$\frac{\Delta T}{T} < \frac{(\gamma_{\text{ad}} - 1)}{\gamma_{\text{ad}}}\frac{\Delta P}{P}. \tag{1.16}$$

Thus it follows that the critical temperature gradient for convection is therefore

$$\frac{dT}{dr} < \frac{(\gamma_{\rm ad} - 1)}{\gamma_{\rm ad}} \frac{T}{P} \frac{dP}{dr}. \tag{1.17}$$

This is a condition for stability; as long as this inequality holds the parcel remains stable against convection. If this condition is exceeded, one would expect convection to occur. The parcel will remain convective as long as this inequality is not satisfied and the conditions within the parcel do not match its surroundings. However, convection will act to flatten the temperature gradient, bringing both sides of Equation 1.17 close to equality. Hence, we expect stars whose structure is controlled by this equation to exhibit a temperature gradient close to adiabatic, including the surrounding material.

A full treatment of convection requires a non-linear theory. Unfortunately, no such theory currently exists. However, convection can be crudely considered in 1D stellar models using mixing length theory (MLT) as prescribed in Böhm-Vitense (1958). MLT is a simple ballistic theory which considers the characteristic scale length a hot parcel rises or a cool parcel descends before it dissolves into and becomes indistinguishable from its surroundings. The mixing length $l_{\rm MLT}$ is defined as

$$l_{\rm MLT} = \alpha_{\rm MLT} H_p, \tag{1.18}$$

where $\alpha_{\rm MLT}$ is a dimensionless mixing length parameter (of roughly unity) and H_p is the pressure scale height, the height within the stellar interior in which P decreases as a factor of e; defined as

$$H_p = \frac{RT}{\mu} \frac{r^2}{GM_r} = \frac{RT}{\mu g}. \tag{1.19}$$

Mixing length theories suffer some well-known limitations. A major limitation of MLT is that the mixing length parameter $\alpha_{\rm MLT}$ is prescription dependent, and is not internally consistently provided by the theory itself (Canuto 1990). Thus, the mixing length used must be calibrated from other 2D/3D hydrodynamical simulations (see e.g. Abbett et al. 1997; Trampedach et al. 2014), or measured empirically using observations (see e.g. Ferraro et al. 2006; Bonaca et al. 2012). A further complication comes from the fact

that traditional mixing length theories consider only a global value of $\alpha_{\rm MLT}$, rather than a variable local value, which is physically counter intuitive. As noted in Renzini (1987), this alone can cause considerable problems for convective overshooting, where a convective flow overshoots the boundary with a region of stability. Furthermore, MLT makes the tacit assumption of isotropy, i.e. all scale lengths entering the problem are equal to $l_{\rm MLT}$ (Canuto 1990). A more physically motivated treatment would recognise that large-scale eddies that carry most of the flux are generally anisotropic; that their characteristic width and height are not equal. Finally, typical prescriptions of MLT do not consider rotation or magnetic fields, though work on prescriptions including these effects is ongoing (see e.g. Chabrier et al. 2007; Feiden & Chaboyer 2014; MacDonald & Mullan 2014; Ireland & Browning 2018). However, despite the many criticisms that can be levelled against MLT, it remains in commonplace use within 1D stellar models to this day.

Near to the surface of a star, the temperature gradient becomes superadiabatic, i.e. $(dT/dr) < (dT/dr)_{\rm ad}$, due to the decreasing density and hence temperature of the plasma. At around a radius of $r = 0.995R$, convective heat transport gives way to radiative dissipation due to the decreasing opacity in the photosphere. It is within this outer region that the radius of the star is largely determined (Stahler 1988, with more recent work by Ireland & Browning 2018).

M-dwarfs are notable in that they straddle the mass threshold for a fully convective interior at $M > 0.35$ M$_\odot$; first hypothesised by Limber (1958). Importantly, for stars close to isentropy, such as fully convective M-dwarfs, knowledge of their specific entropy $s_{\rm ad}$ is sufficient to define the adiabat upon which the star sits, and hence its entire structure. The nature of the adiabatic gas law can be shown by considering the first law of thermodynamics, which states that $du + PdV = dQ$, where u is the specific internal energy, V, defined as $1/\rho$, is the specific volume of the gas and Q is the specific heat content. As I stated previously convection within the stellar interior is an adiabatic process, thus $dQ = 0$ resulting in $du = -PdV$. For an ideal gas $u = (3/2)Nk_BT$ where N is the number of particles per unit mass, we find the ubiquitous $PV = nk_BT$ where n is the number of particles per unit volume, thus $u = (3/2)PV$. So, for an adiabatic process performed on a

rising or falling convective parcel, given that $du = -PdV$,

$$\frac{3}{2}PdV + \frac{3}{2}VdP = -PdV, \tag{1.20}$$

which can be rearranged and simplified to

$$\frac{dP}{P} = -\frac{5}{3}\frac{dV}{V}. \tag{1.21}$$

Hence $P \propto \rho^{5/3}$ is the equation of state for both the ambient background and parcels in convective regions, indicating $\gamma_{\rm ad} = 5/3$ for those regions (e.g. Lamers & Levesque 2017). This is a polytropic equation of state, where the relationship between pressure and density is given by

$$P = K\rho^{(n+1)/n} = K\rho^{\gamma}, \tag{1.22}$$

where K is a constant of proportionality, n is the polytropic index. This demonstrates that the convective zones within stellar interiors can be approximated well by an $n = 1.5$ polytrope—a simple stellar model that serves as a solution to the Lane–Emden equation.

As a result of the structure of M-dwarfs, many open questions remain about the morphologies and strengths of the global magnetic fields within M-dwarfs. The standard model of the stellar dynamo mechanism suggest that magnetic fields are generated at the interface between the inner radiative zone and outer convective zone (Parker 1955, 1979). At this interface is a shear layer known as the tachocline. However, this mechanism is unable to explain how fully convective stars, which by definition do not possess a tachocline, generate and sustain strong magnetic fields. There is an alternative suggestion of a stellar dynamo driven by rotation and turbulent convection (Durney et al. 1993; Dobler et al. 2006; Chabrier & Küker 2006). Further discussion of magnetism is presented in Section 1.8.1.

1.4.2 Observational Characteristics

Unlike intermediate mass stars, such as our Sun whose SED peaks at optical wavelengths, the SEDs of M-dwarfs peak in the near-IR, due to their having much cooler effective temperatures of between 1800 − 4000 K. Consequently, M-dwarfs can be found at the

faint, red end of the MS in colour-magnitude diagrams (CMDs). Their cool photosphere leads to one of their most notable spectral characteristics - the formation of diatomic and triatomic molecules; such as SiH, CaH, TiO, VO, CrH, MgH, OH, CO, CaOH, H_2O and FeH (e.g. Rajpurohit et al. 2018; Rajpurohit et al. 2019). Hot dust grains have also been observed in M-dwarf spectra by Tsuji et al. (1996), who identified that the condensation temperatures of said grains occur in line-forming layers of their photospheres. It was also noted in Rajpurohit et al. (2018) that the outer layers of M-dwarfs with spectral types M5 or later are sufficiently cool to form dust and clouds. All of the molecular species incident in the photospheres of M-dwarfs have the effect of adding opacity and forming large absorption bands, which are ubiquitous in very low mass stars.

By virtue of their convective outer envelopes, it is probable that all M-dwarfs possess cool starspots on their surfaces (Strassmeier 2009). Starspots are observational manifestations of magnetic flux tubes—generated by the interior dynamo—intersecting the photosphere and inhibiting convective heat transfer, resulting in areas of the stellar surface with a lower temperature and brightness than that of the stellar photosphere. Hence, not only do these dark spots attenuate the flux from the star, but they also contribute towards a second, cooler blackbody component seen in the SED (Berdyugina 2005; Oshagh et al. 2014). This spotted photosphere has a temperature contrast with the immaculate photosphere $T_{\rm eff,imac} - T_{\rm eff,spot}$ and occupies some fraction of the surface area of the star, its filling factor γ. The degeneracies inherent in stellar activity make it problematic both to measure the intrinsic properties of active stars, and to infer the characteristics of the starspots themselves. However, much work has been done to develop techniques for characterising starspots. Since the first unexpected observations of dark spots in Kron (1947)—who found anomalous photometric variability while studying the eclipsing binary, AR Lacertae—applying inversion models to observed light curves has proven a fruitful method for spot characterisation. The rotation period $P_{\rm rot}$ of the star then follows from the inverted model; under the assumption that the starspots survive on timescales longer than the rotation period of the star. Furthermore, careful analysis of the light curve yields the spatial distribution of spots. However, as the time series data is 1-dimensional, under most circumstances only the longitudinal spot distribution can be reliably constrained—the latitudinal distribution remains highly uncertain (Berdyugina

2005). A novel method for avoiding this problem was presented in Morris et al. (2017), who used the well known orientation and highly misaligned orbit of HAT-P-11 b to unambiguously resolve spot latitudes on its K4 dwarf host from time-series data. Due to the increasing ubiquity of short-cadence, all-sky surveys searching for stellar oscillations and exoplanet transits, it is becoming possible for many active stars to be probed using this family of techniques.

Spectra of active stars also encode much information about starspots. Given an adequately hot photosphere molecular species cannot form—that of around mid–K or earlier—meaning that detections of molecular bands result only from the much cooler spotted regions. Since the first detection of TiO and VO on a K2 dwarf in Vogt (1979), molecular band modelling (MBM) has proven effective for determining the temperatures of starspots. As suggested in Huenemoerder & Ramsey (1987) and developed in Neff et al. (1995) and O'Neal et al. (1996), MBM allows the determination of spot filling factors and temperatures from molecular features. Furthermore, first conceived in Deutsch (1958), and developed into an inversion technique in Goncharskii et al. (1977), the Doppler imaging technique aims to determine the the starspot distribution on the stellar surface using information contained in the time varying line profiles of rotating stars (Berdyugina 2005). Hence through all three methods, measurements of the spot filling factors and temperature contrast can be made. Berdyugina (2005) compiled many of these measurements from the literature to show the overall correlation between immaculate photosphere temperature $T_{\mathrm{eff,imac}}$ and temperature contrast for a variety of stellar demographics; shown in Figure 1.3.

Additional markers of magnetic activity come in the form of plage and faculae, which are signatures of particularly dense collections of small flux tubes (Solanki 1999). Although only directly observed on the Sun, intuition and indirect evidence from photometric variations (e.g. Wilson 1978; Lockwood et al. 2007) would suggest these are also present on other active stars with convective envelopes. Solar faculae are bright, extended structures in the Sun's photosphere that are seen in visible light around sunspots (Berger et al. 2007). Interestingly, they appear brighter, and contrast with the background granulation, more at the limb than they do at the disc centre. This lead Spruit (1976) to

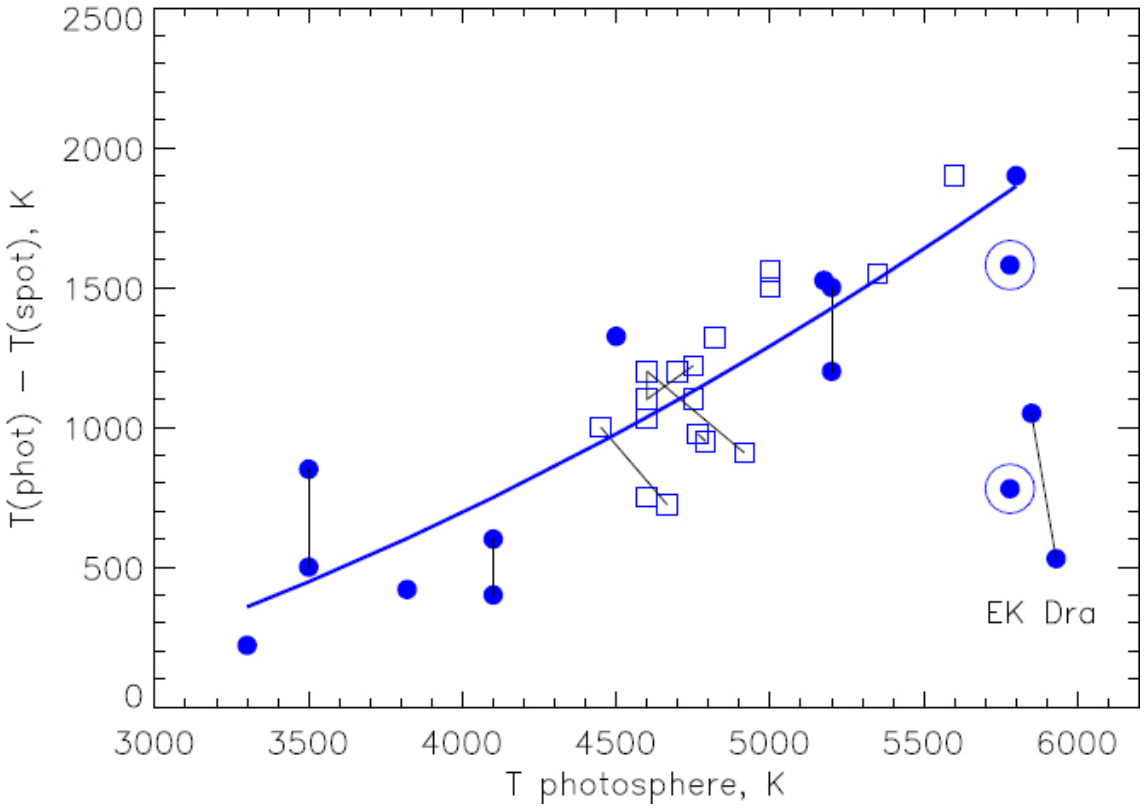

Figure 1.3: The temperature contrast of starspots as a function of the temperature of the immaculate photosphere for active giants (squares) and dwarfs (circles). Lines connect measurements of the same star. The curve is a second-order polynomial fit to this data, excluding EK Dra. The circled points represent measurements of the solar umbra (ΔT = 1700K) and penumbra (ΔT = 750K). **Source:** Berdyugina (2005)

construct the so called 'hot wall' model, which posits that thin tubes of magnetic flux cause depressions in the photosphere. When observed from oblique angles, such as at the limb, the decreased density of material, and hence longer optical depth, allow lines-of-sight to intersect the deeper, hotter layers of the photosphere which form the walls of these depressions. Faculae typically form hours before an active region, and can persist weeks after the spot has disappeared. Conversely, although plage is also the result of magnetic flux tubes, it does not result from depressions in the photosphere, and is instead a chromospheric effect. In this region of stellar atmosphere, H_α and Ca II K & H are the dominant sources of strong emission, making these high-contrast features ideal for studying plage (Walter 1996). Plage appears hotter than the immaculate photosphere, with a temperature contrast of $300 - 500$ K (Topka et al. 1997). Hence, as with spots, a two-temperature photosphere can be used to model its effect on observations (e.g. Oshagh et al. 2014).

It is by adopting the two temperature model that I will proceed with modelling the effect stellar activity on SEDs throughout this remainder of this thesis. I detail the model that I adopt for studying starspots in M-dwarfs in Section 4.3.2.3, and develop it further to encompass plage in Section 5.4.1.3.

1.5 Open Clusters - Benchmarks for Stellar Evolution

The evolution of planets and their stellar hosts are inexorably linked, from their formation to their inevitable demise. Determining the circumstellar environments within which planets may be forming, and the characteristic timescales upon which these processes are occurring, necessarily requires robust constraints on evolutionary stage, hence stellar age, of the subject. Measuring the ages of miscellaneous, isolated field stars has proved intractable, as no methods exist which are reliably capable of doing so. Because of this, open galactic clusters, such as the Pleiades and Praesepe, have historically served as crucial laboratories with which stellar evolution can be scrutinised. There are several important, and well founded, assumptions that go into these studies. Open clusters and the stars they contain form via fragmentation from the same common progenitor cloud. The intuitive supposition is that the population of the cluster is spatially proximate, allowing both

the extinction and distance to the cluster as a whole to be determined during the fitting process. That all members have identical metallicities is another assumption that naturally follows, permitting constraints on the tracks that the clusters will follow throughout their evolution. The final expectation is that the entire sample is coeval, meaning that the entire population can be fit with a single isochrone, or line of constant age. By improving the constraints on these parameters with the whole ensemble of stars whose cluster membership is confirmed, other important parameters can be determined.

As age and metallicity can be assumed to be homogeneous across the cluster, a large number of members can be simultaneously fitted with isochrones to infer properties of the population as a whole. The ability to constrain cluster parameters in this way, such as distance and extinction, is one of the key advantage to working with them. Importantly, one of the most crucial tasks for young stellar clusters is to test the veracity of stellar evolution models, by providing a snapshot of stellar evolution for a homogeneous sample of stars. The models that can be fitted to clusters include those by D'Antona & Mazzitelli (1997), Baraffe et al. (1998), Siess et al. (2000), Yi et al. (2003), Demarque et al. (2004), Dotter et al. (2008), and Tognelli et al. (2011). The models provide R, $T_{\rm eff}$ and L for a given mass at a given age, providing a single star sequence which can be fit trivially in the theoretical $T_{\rm eff} - L$ plane of the Hertzprung–Russell (H–R) diagram. However, this poses problems when fitting to observations, as the parameters required for such diagrams are troublesome to infer from brightnesses and colours available from photometry. An alternative is to transform models into the observational plane by generating bolometric corrections from model stellar atmospheres. Bolometric corrections are calculated for a given star observed through the photometric system response S_λ for a specific band, and denote the correction required to convert the absolute magnitude in that band M_i to the bolometric magnitude $M_{\rm bol}$ of the star. This can be represented easily as

$$BC_i = M_i - M_{\rm bol}, \tag{1.23}$$

with the useful property that observed colours can be derived from them using

$$m_i - m_j = BC_j - BC_i, \tag{1.24}$$

however not without the unfortunate consequence of an inconvenient minus sign. These provide the absolute magnitudes and colours required for fitting the single star sequence of clusters in CMDs.

1.6 Radius Inflation in pre-MS M-dwarfs

Naylor (2009) used isochrone fitting to determine the pre-MS for a number of associations and young clusters, finding that the ages were a factor of 1.5 - 2.0 longer than the commonly accepted ages for the studied regions. Stauffer et al. (2007) also noted that there was a problem with the theoretical pre-MS isochrones. Expanding on this, Bell et al. (2012) firmly established that the discrepancy was not due to calibration issues and that models were in fact unable to reproduce the observed single star sequence for $T_{\rm eff} < 4000$ K for even the most well understood open clusters in the sky. Developing on this work Bell et al. (2012) found that the isochrones generated by the interior models of Baraffe et al. (1998), D'Antona & Mazzitelli (1997), Siess et al. (2000), and Dotter et al. (2008) all fail to reproduce the Pleiades single star sequence for $T_{\rm eff} \leq 4000$ K at optical wavelengths. It was shown that the flux is overestimated by a factor of 2 at 0.5 μm, decreasing with increasing wavelength and becoming imperceptible in the K_s-band at 2.2 μm. Problematically, Bell et al. (2012) showed that this discrepancy could lead to underestimating the age of pre-MS stars $\tau < 10$Myr by a factor of $2-3$. From this it appears clear that some physics is missing from stellar evolution models that attempt to adequately describe M-dwarfs up to 100 Myr.

A complication with methods such as this is that, although they are able to fit the single star sequence to infer much about the cluster, the colours and magnitudes used in the fitting are far removed from the outputs of the models. This makes it difficult to backtrack the root cause of the discrepancies in said models. The purpose of Chapter 3 of this thesis is to present investigations designed to ascertain the key physics that is missing from the models. Both the Pleiades and Praesepe clusters were chosen due to their robust characterisation (e.g. in Bell et al. 2014), and for reasons detailed in Section 3.1.1 and Section 3.1.2.

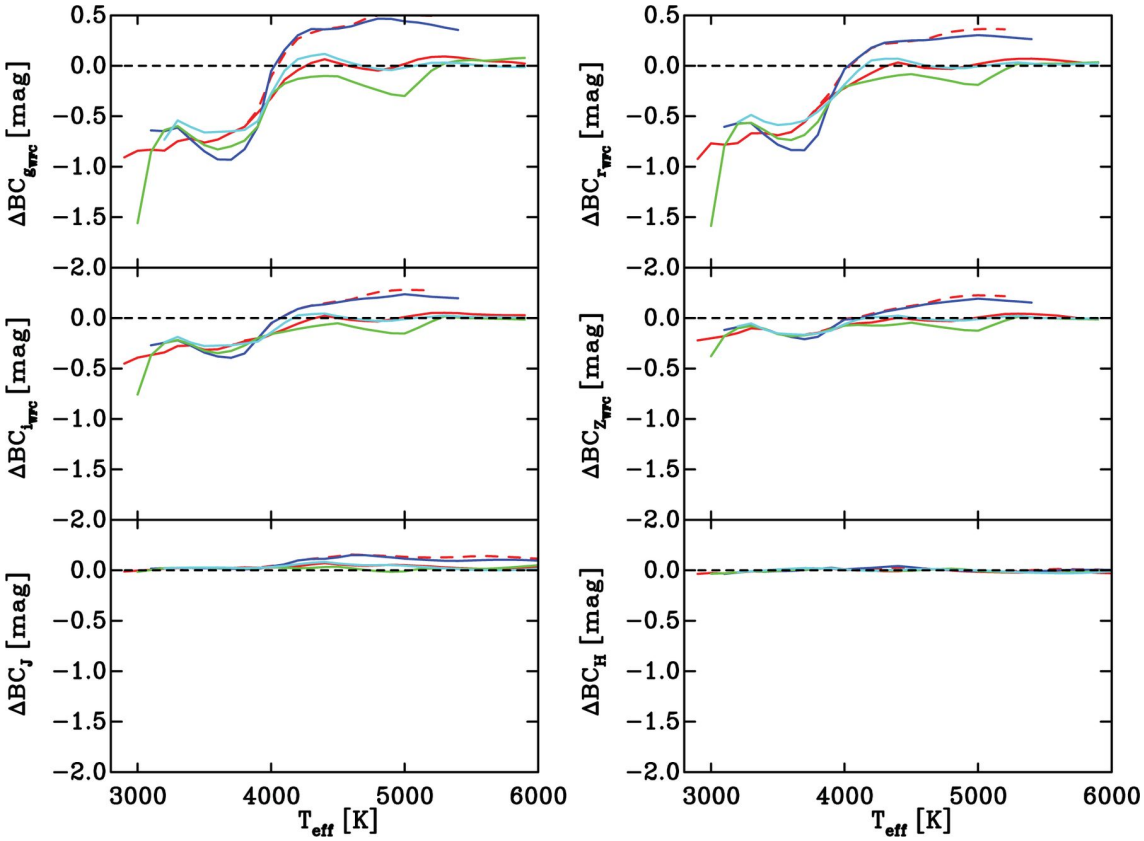

Figure 1.4: This figure shows the model-dependent corrections to bolometric correction ΔBC as a function of $T_{\rm eff}$ for the optical $(griz)_{\rm WFC}$ and NIR JH bands. These were calculated in Bell et al. (2012) by finding the difference between the model colours and observed Pleiades colours as a function of $T_{\rm eff}$. The lines represent the models of Baraffe et al. (1998) (red, continuous), Baraffe et al. (2015) (red, dashed), Siess et al. (2000) (blue), D'Antona & Mazzitelli (1997) (green) and Dotter et al. (2008) (cyan). This shows that for $T_{\rm eff} < 4000$ K all models fail to match the observations at optical wavelengths, with the discrepancy reducing towards the H-band. **Source:** Bell et al. (2012).

1.6.1 The Cause of the Discrepancy

The discrepancy is demonstrated for the Pleiades in Figure 1.4, which plots the corrections required for a variety of stellar interiors to bring their colours in line with those observed for stars of an equivalent $T_{\rm eff}$ in the Pleiades. The question remains: what key physics that is absent from the models causes this discrepancy? The discrepant model isochrones are the result of coupling two models—the stellar atmosphere that models the photosphere of the star, and the interiors that describe the internal structure of the star. From the manifestation demonstrated in Figure 1.4 the culprit could be either of them, or even a combination of both. In solving this we need to disentangle both models and examine them in isolation. In Chapter 3 I will show how new techniques described in Chapter 2 were applied to readily available public astrometric and multi-waveband photometric data from a variety of all-sky surveys to perform SED fitting of members of Pleiades and

Praesepe. By removing the constraint that the model needs to lie on the isochrone, more accurate radii for each source can be determined. The stellar parameters determined by this fitting are used as inputs to generate synthetic spectra of those stars. I will then compare robustly flux calibrated spectra with these synthetic spectra to perform a differential study of the effect that opacities have on the stellar atmospheres.

Although some problems have been resolved, there still remains one burning question; is this discrepancy a result of poorly constrained stellar evolution, and hence disappears in stars on the MS at sufficiently old ages, or does this discrepancy persist far onto the MS?

1.7 Radius Inflation in Main-Sequence M-dwarfs

I have already established that pre-MS M-dwarf stars disagree with models. Now we must address whether this disagreement persists onto the MS, and crucially determine the missing physics that is the culprit. All of the open astrophysical problems that are addressed throughout this thesis are unified by one commonality: greater insight into them is gleaned by more robust measurements of fundamental stellar parameters. Fortunately, there has been much work over the last century to develop methods to provide observational constraints to the rapidly developing field of stellar evolution. In this section I will review the current gold standard of techniques for measuring stellar parameters. I will discuss their advantages, and some of their inherent deficiencies to converge on a schematic for improving measurements of stellar parameters, and attempting to settle the open questions we have discussed. In doing so, I will show that the radii predicted by the models and those measured for MS M-dwarfs are also in disagreement.

1.7.1 Detached Eclipsing Binaries

Observations of binary stars date back to the discovery that β Persei (Algol) was variable by Goodricke (1783), with Herschel (1802) terming them 'binary stars'. Since the first observations of the mass of the components of β Aurigae in Stebbins (1911), eclipsing binaries have been the most time honoured and tested means of determining fundamental stellar parameters, and hold the distinction of being the only truly fundamental measure-

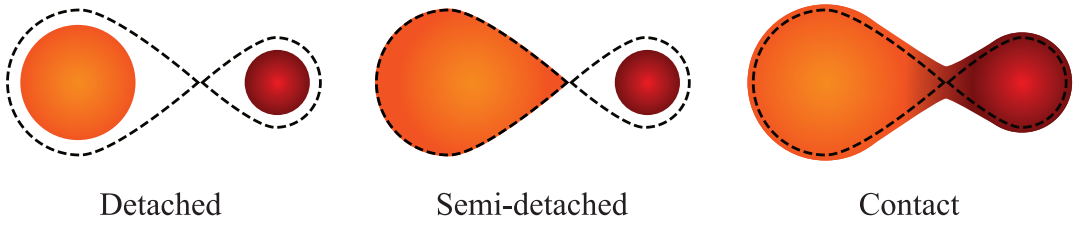

Figure 1.5: A schematic representation of the morphological classifications of binary stars. The dotted line indicates the Roche lobe—the gravitational equipotential around the star within which material is bound to the star. When a star overflows its Roche lobe, as is the case with semi-detached binaries, the material becomes unbound and can fall onto the other star via the L_1 Lagrange point of the system; known as the gravitational capture equilibrium point. A contact binary is the case when both stars overflow their respective Roche lobes and touch, and may in fact share a common gaseous envelope. The detached case is of most interest to practitioners of stellar evolution. In the detached state, neither star overflows their respective Roche lobes, and they in fact evolve effectively independent, in the same way that single field stars do.

ment of stellar masses. Systems with two or more stellar components are thought to make up around a third of the stellar systems in the galaxy, with the remaining being single stars (Lada 2006). As such, these stars make up a considerable component of the galactic population, and serve as an important tool for studying stellar evolution. Some binaries are orientated such that their orbital plane is close to our line of sight, meaning that they occult one another when observed from the Earth. Careful analysis of the light curves resulting from occultations can provide a wealth of information about the stellar system. Figure 1.5 shows a schematic view of different kinds of binary stars. In particular, for the purposes of stellar evolution, it is important to distinguish between detached eclipsing binaries (DEBs) and the other classifications. DEBs do not fill or overflow their Roche lobe, meaning there is no mass transfer between the components, hence their evolution is asserted to remain decoupled. Star formation also stipulates that both components formed at the same time and are thus coeval. Although this is generally a safe assumption, I note in passing that observations of G11.92-0.61 MM 1 published in Ilee et al. (2018) appear to show a stellar companion forming via circumstellar disc fragmentation; potentially challenging this supposition. Given how diverse DEB components are, this has the powerful result that a differential study between types can be performed at the same age within each binary.

As both components occult one another, the resulting light curve can be used to infer radii and inclination. The light curve resulting from occultations, supplemented with spectroscopic (radial velocity) measurements, permit the inference of a large array

of fundamental stellar parameters for both components. Modelling the light curves is an involved process, and as a result has many different approaches. Initial attempts to determine stellar properties from EB light curves were set out in Russell (1912a). Importantly, this method was updated by Russell (1912b) to include eccentric orbits, and again in Russell & Shapley (1912a) and Russell & Shapley (1912b) to introduce limb darkening. Increasing computational power over the past century has permitted increasingly complicated models that can correctly deal with the full intricacies of fitting EB light curves. Analysis of light curves provides measures of the radius ratios of each of the stellar components R_1/a and R_2/a, as well as the inclination i and eccentricity e, which is usually expressed as $e \sin \omega$ or $e \cos \omega$ as they can be better determined for eccentric orbits. Spectroscopic observations are responsible for measurements of radial velocity, which themselves yield measurements of $M_1 \sin^3 i$ and $M_2 \sin^3 i$ and $e \sin \omega$. Crucially, radial velocities make accessible measurement of the semi-major axis $a \sin i$ of the system. By modelling these observations, the radii, masses, and $\log(g)$ of individual components can be determined. Thus DEBs provide most fundamental test of stellar models, as they yield radii at a given mass.

Although binaries are relatively common, the sample size is limited by the probability of finding them in a configuration where they will eclipse one another. There are at this point tens of thousands of known eclipsing binaries, with many more being discovered as a result of Gaia, however their study still poses an ongoing challenge. Light curves require fine enough sampling that both occultations are visible and the limb darkening can be determined, with adequately long time baselines that the occultations can be sampled. Consequently, characterising DEBs can take much time and many observations, hence only 239 well-studied examples are included in DEBCat at the time of writing (Southworth 2015). To further complicate matters, there can be considerable disagreements between the measured parameters for the same binary (see Han et al. 2017; Kraus et al. 2017; Gillen et al. 2017).

A review of literature shows that it has long been known that M-dwarf DEB components appear to be inflated for their mass (see Figure 2 of Chen et al. 2014; Kraus et al. 2011a; Chaturvedi et al. 2018; Parsons et al. 2018; Mann et al. 2019), however it

was pointed out by Torres (2013) that the effect was a subtle one. Parsons et al. (2018) measured the radii of 23 M-dwarfs in eclipsing binaries with white dwarfs and found that radii were inflated by an average of 6.2 ± 4.8% from theoretical models. However, additional controversy stems from the concern that their binarity may affect their structure; in particular that if they are tidally locked their high rotation rate may inflate them. This eventuality would undermine the veracity of DEBs for stellar evolution studies, rendering moot the most powerful tool for determining the elusive stellar mass–radius relationship. However, as I shall show in Section 4.3.1, this does not appear to be the case, and the DEB observations are in fact in the best agreement with our radius measurements of single stars.

1.7.2 Interferometry

Adequately bright, nearby M-dwarfs can additionally have their radii probed by interferometric observations. The first interferometric measurements of stellar parameters date back to Michelson & Pease (1921), who used an interferometer with the 100-inch Hooker telescope to measure the diameter of α Orionis. Since then interferometry has become an indispensable tool for high angular resolution astronomy, being used to probe stellar parameters and discs around young stars. In discussing this method, I consulted the review of optical interferometry of Monnier (2003).

Interferometric observations find their origins in the classic *Young's double slit experiment*, in which monochromatic light from a distant point source impinges upon two slits separated by a distance b. Due to the wave-like nature of light, the wavefronts propagating from both slits take different path lengths to a plane, hence causing alternating fringes of constructive and destructive interference. With this setup the fringe spacing $\Delta\theta$ is

$$\Delta\theta = \frac{\lambda}{b}. \tag{1.25}$$

Stellar interferometry works on the same premise, but substitutes the idealised slits for telescopes separated by a baseline B. We recall the **Rayleigh criterion** which states that

the resolution of a telescope $\Delta\theta_{\text{telescope}}$ is proportional to the diameter of its aperture D,

$$\Delta\theta_{\text{telescope}} = 1.22\frac{\lambda}{D}, \tag{1.26}$$

where λ is the wavelength of the light being observed. This places a fundamental constraint on the resolution limit of a given telescope, meaning that high angular resolution studies (on sub-mas scales) are impossible with anything short of intractably large apertures. However, if we wish to observe two features in an interferometer, they can be thought of as resolved if one feature is centred in the first null of the diffraction pattern of the other. Thus it follows that the resolution of the interferometer $\Delta\theta_{\text{interferometer}}$ is

$$\Delta\theta_{\text{interferometer}} = \frac{\lambda}{2B}. \tag{1.27}$$

This equation concisely states that the resolution of the interferometer array is equal to the longest baseline, effectively performing as a telescope of aperture B, although the array does not form an image in the same way as a single telescope. The measurements recorded on an array are considered by the Van-Cittert - Zernicke theorem, which states that the contrast of the fringes are related to a unique Fourier component of the observed brightness distribution. Thus from this theorem, the interferometer response—the amplitude and phase of the interference fringes—manifests as the frequency-dependent complex visibility $\widetilde{\mathcal{V}}$. This is defined as the Fourier Transform of the brightness distribution $I_\nu(\vec{r_\Omega})$ using

$$\left|\widetilde{\mathcal{V}}\right| e^{-i\phi_{V_\nu}} = \frac{\int_{d\Omega} dx_\Omega dy_\Omega I_\nu(\vec{r_\Omega}) e^{-2\pi i\left((\vec{D}/\lambda).\vec{r_\Omega}\right)}}{\int_{d\Omega} dx_\Omega dy_\Omega I_\nu(\vec{r_\Omega})}. \tag{1.28}$$

This equation makes the tacit assumption that the target only emits light over a small enough portion of the sky that the spherical coordinates can be considered Cartesian coordinates (x_Ω and y_Ω) around the centre of the source at (θ_0, ϕ_0). The notation that follows is that $\vec{r_\Omega} = (x_\Omega, y_\Omega)$, and that $\vec{D}/\lambda$ is the baseline vector $\vec{D}$ projected onto the plane of the sky in units of wavelength λ. The conventional (u, v) notation for baseline vectors on the sky then follows from this.

From the complex visibility amplitude and phase, the geometry of objects on the

sky can be inferred by comparing to an intensity model. Interference in astronomical interferometers manifests itself as intensity oscillations, called fringes. $\mathcal{V}$ is known as the fringe visibility, and is given by the contrast between the minimum I_{min} and maximum I_{max} intensity of these fringes using

$$\mathcal{V} = \frac{I_{\text{max}} - I_{\text{min}}}{I_{\text{max}} + I_{\text{min}}}. \tag{1.29}$$

Equation 1.28 is the way of mapping from the intensity distribution, given by a model, to the visibility V, and can be simplified to

$$\mathcal{V}(u, v) = \mathcal{F}(I(x_\Omega, y_\Omega)), \tag{1.30}$$

where $\mathcal{F}$ is a Fourier transform. By finding the intensity of the model that best reproduces the contrast of the first lobe of the visibility, the angular diameter of the target can be determined. However, model assumptions are necessary in order to do so. Seminal attempts, such as that of Michelson & Pease (1921), assumed a disc of uniform brightness as a model for the intensity distribution of the star, yielding an angular diameter θ_{UD}. Of course, when measuring diameters of stars to precision, a uniform disc is an inadequate assumption. Thus, contemporary treatments adopt a limb darkened model with which to fit the visibility, yielding θ_{LD}. Hanbury Brown et al. (1974) showed that assuming a uniform disc model instead of a limb darkened one can cause overestimates in the angular diameter of over 10%. Given well constrained parallaxes which yield a distance d, such as those provided by Hipparcos (van Leeuwen 2007), measurements of the limb darkened angular diameter θ_{LD} can be converted into stellar radii R using

$$\theta_{\text{LD}} = \frac{2R}{d}. \tag{1.31}$$

Applications of this technique to the study of M-dwarfs includes the crucial work of Ségransan et al. (2003), Demory et al. (2009), Boyajian et al. (2012), and von Braun et al. (2014). This technique has yielded some of the most precise measurements of stellar radii, however it does not come without its downsides. Problematically, the stars that can be studied with interferometric methods are limited by the complex optics required to

perform interferometric observations, whose visible light transmission is only $1-10\%$. This is due to the degradation of the coatings of mirrors over time, the requirement of dichroics and filters with high losses, and diffractive losses during beam transport (Monnier 2003). As a result of this, parallel study with multi waveband observations from all-sky surveys proves problematic, as most targets accessible via interferometry are bright, and will saturate or damage the detectors utilised by such surveys. An additional result of the low transmission, and the requirements to fill the $u-v$ plane with multiple baselines, makes interferometric studies of stars a lengthy and expensive process; making assembling a statistically significant sample of stars an intractable proposition. As a result there are fewer than 20 M-dwarfs that have been studied interferometrically, with only two of those being later then M3.5 (Kesseli et al. 2018). Finally, one issue that is particularly pertinent to observations of low-mass stars are the hurdles presented by starspots. The stellar diameters that are measured at visible wavelengths can often differ from those measured in the infrared; an effect to which starspots may contribute for adequately close stars. For example, by examining the uniform disc diameters from the JMMC Stellar Diameters Catalogue of Bourgés et al. (2014), I found that the V-band angular diameter is $2-5\%$ larger than that measured in the K-band, with the redder objects tending to exhibit a larger difference. Boyajian et al. (2012) derived interferometric radii and luminosities, through fitting broadband photometry, for low-mass stars. They concluded that MS M-dwarf stars are inflated by 5% compared to models.

1.7.3 Infrared Flux Method (IRFM)

Fundamentally, the infrared flux method (IRFM) exploits the fact that infrared flux is relatively insensitive to $T_{\rm eff}$ in stars whose $T_{\rm eff} \gtrsim 4000$K. This is the case for the test cases of the Sun and Arcturus in Blackwell & Shallis (1977); where the method was introduced. Elaborating in Blackwell et al. (1979), they describe that the first stage of the method involves calculating the flux of the source using model atmosphere $f_{\rm syn,IR}$ and comparing it to the observed flux at the Earth $f_{\rm obs,IR}$ to give the angular diameter θ of the star using

$$\theta = 2\sqrt{\frac{f_{\rm obs,IR}}{f_{\rm syn,IR}}}. \tag{1.32}$$

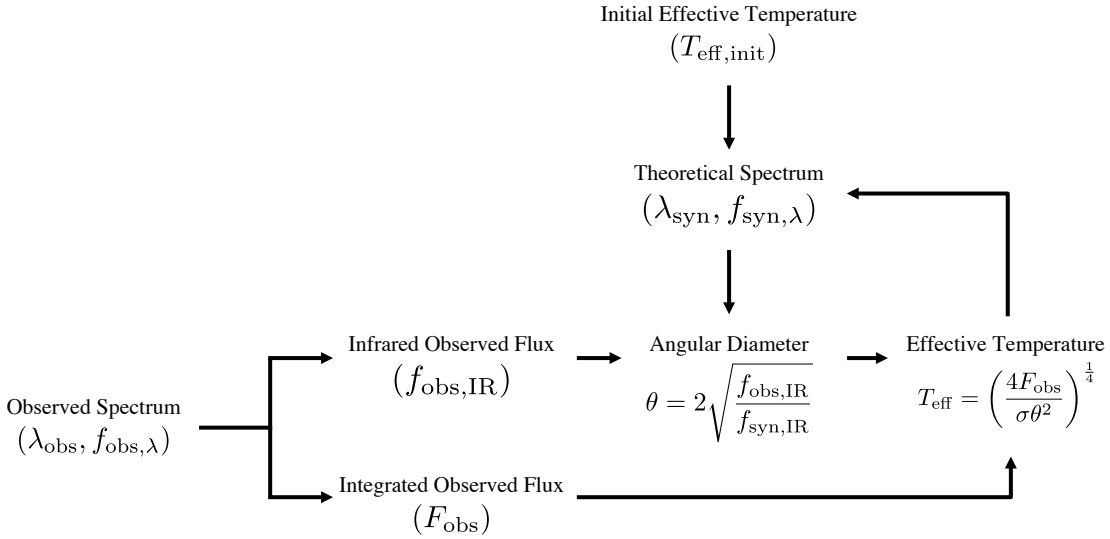

Figure 1.6: A schematic view of the infrared flux method (IRFM). Adapted from a figure in Dubaj & Monier (2005).

Importantly, this leads to the formal definitions of the equations driving the method, which relate the observed integrated flux $F_{\rm obs}$ and IR monochromatic flux $f_{\rm obs,IR}$, both measured at Earth, in terms of the $T_{\rm eff}$ and θ

$$F_{\rm obs} = \int_0^\infty f_{{\rm obs},\lambda} d\lambda = \frac{\theta^2}{4}\sigma T_{\rm eff}^4, \tag{1.33}$$

$$f_{\rm obs,IR} = \frac{\theta^2}{4} f_{\rm syn,IR} = \frac{\theta^2}{4}\phi(T_{\rm eff}, \log(g), \lambda_0), \tag{1.34}$$

where $\phi(T_{\rm eff}, \log(g), \lambda_0)$ corresponds to the flux provided by the model atmosphere at the given IR wavelength λ_0. From this point on, the task of the method is to determine a combination of $(\theta, T_{\rm eff})$ which simultaneously satisfies Equation 1.33 and Equation 1.34. This process is represented schematically in Figure 1.6.

Although Blackwell & Shallis (1977) and Blackwell et al. (1979) employ the IRFM for characterising M-dwarfs, Figure 1.7 demonstrates that for M-dwarf stars ($T_{\rm eff} \lesssim 4000$ K) the condition that IR flux remain insensitive to $T_{\rm eff}$ does not hold, meaning it may prove unreliable for very low mass stars.

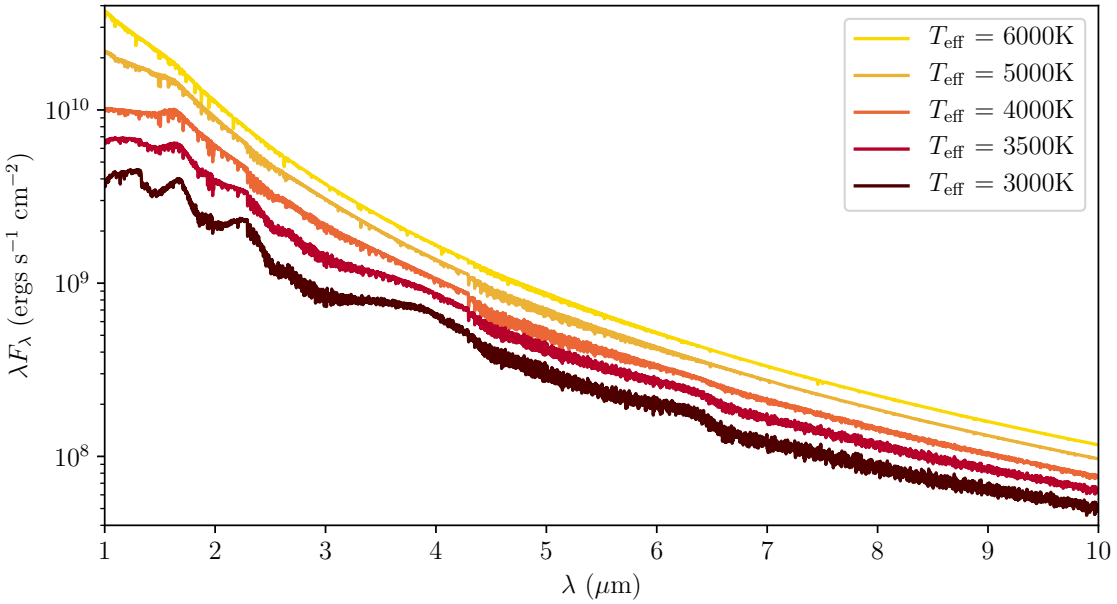

Figure 1.7: The synthetic IR spectra for $T_{\rm eff}$ = 6000 K, 5000 K, 4000 K, 3500 K and 3000 K plotted in yellow, mustard, orange, red and maroon respectively. This demonstrates that for M-dwarf stars ($T_{\rm eff} \lesssim 4000$ K) molecular features begin to dominate the NIR spectrum, making the IRFM difficult to apply in the presence of molecules with poorly understood opacities.

1.7.4 $R \sin i$ Technique

One method that has shown some favour in recent years is the measurement of $v \sin i$. Some prominent uses of this technique include Rhode et al. (2001) who studied pre-MS stars in the Orion Nebula Cluster (ONC), Lanzafame et al. (2017) and Jackson et al. (2018) who applied it to the Pleiades, and Kesseli et al. (2018) who applied it to field M-dwarfs. The crux of the method involves measuring the rotation period $P_{\rm rot}$ and rotational velocity v modulated by the inclination $\sin i$. Making the reasonable assumption that the star is spherical, one can effectively integrate the angular velocity around the equator of the star to yield its equatorial radius

$$R \sin i = \frac{1 \text{ day}}{R_\odot \times 2\pi} P_{\rm rot} v \sin i = 0.0198 P_{\rm rot} v \sin i. \tag{1.35}$$

One of the main disadvantages of this method is that it requires observations of both $v \sin i$ and $P_{\rm rot}$. $P_{\rm rot}$ can be obtained by photometric monitoring of the stars within a stellar sample. However, measurements of $v \sin i$ are inferred spectroscopically by measuring the rotational broadening of spectral features; generally by fitting a Gaussian to the cross-correlation function resulting from a correlation between the spectra from

the target and a standard star, and finding its width. Kesseli et al. (2018) obtain $v \sin i$ measurements through the rotational broadening of the CO bandhead at $\simeq 2.3$ μm, which remains relatively unaffected by magnetic fields and pressure broadening. Due to the $\sin i$ dependence, only the minimum radii of individual stars can be determined, so this technique is only applicable for measuring statistical radii of homogeneous samples, and under the assumption that spin axes are randomly spatially oriented (Jackson et al. 2018). In addition, as Kesseli et al. (2018) state, adequately slow rotators $P_{\rm rot} > 50$ days show no appreciable broadening, meaning their radii are not measurable through this method. Jackson et al. (2018) applied this technique to pre-MS M-dwarfs in the Pleiades and found that they were inflated by an average of $14 \pm 2\%$ above the theoretical stellar models.

1.8 Why a New Technique?

The methods presented in Section 1.7 have traditionally been the means by which the radii of MS M-dwarfs have been measured. However, as I have noted in their respective sections, they all suffer deficiencies. Historically interferometry and DEBs have been the most accurate methods, however they suffer from small-number statistics. The work of Mann et al. (2013) and Mann et al. (2015) overcomes the small–number-statistics problem. They measure L through broadband photometry and the temperature using spectroscopy by matching spectral features in model atmospheres, hence I term this a spectroscopic temperature $T_{\rm sp}$. Unlike $T_{\rm eff}$ which describes the temperature by invoking the blackbody component of the stellar SED, $T_{\rm sp}$ describes the temperature through correlations with the depths of carefully chosen spectral features. In contrast to the effective temperature, measurements of spectroscopic temperature are typically performed on normalised spectra, meaning that they discard the overall shape of the blackbody; thus $T_{\rm eff}$ and $T_{\rm sp}$ probe different observables. In addition, such measurements can be highly sensitive to the wavelength range and species used in measurements which, given the molecular species in their photospheres (see Section 1.4.2), can be especially problematic for M-dwarfs. For example, temperatures determined from optical (Mann et al. 2015; Cortés-Contreras et al. 2017) and near infrared (Newton et al. 2014) can differ by up to 1.5 spectral sub-types; around $5-10\%$ in $T_{\rm sp}$. However, by invoking the tacit assumption that $T_{\rm sp} \equiv T_{\rm eff}$, one can

determine a radius from T_{sp} and L using Equation 1.2. The work of Mann et al. (2015) suggests that M-dwarfs are inflated by 4.4% from the theoretical models. Based on their measurements of T_{sp} they also suggest that models systematically overestimate T_{eff} by 2.2%.

Unlike DEBs, none of the other methods yield a mass. This presents the additional complication that to compare radii to the models another parameter is required, so one must adopt one of T_{eff} or L to hold constant. T_{eff} is dictated by the outer layers of the star, down to optical depth $\tau = 1$, giving it a strong dependence on R; making it undesirable for this purpose. An additional complication is that all methods implicitly rely on some measurement of the temperature of the photosphere, however there are many different measures of the photosphere temperature. DEBs predominantly utilise surface brightness temperature T_{br}, interferometric measurements infer T_{eff} and all methods can utilise spectroscopic temperatures T_{sp}. In doing so, all methods make the assumption that $T_{eff} \equiv T_{sp} \equiv T_{br}$. Its strong correlation with radius and inconsistent measurement techniques make temperature an undesirable abscissa with which to perform a comparison. However, despite being loosely coupled to R, L is largely dictated by the energy budget provided by thermodynamic properties of the core and energy transport in the envelope; meaning it has a strong dependence on mass.

I have established that many methods appear to show some level of inflation in M-dwarfs, however we have yet to settle on a satisfactory method with which to study the nature of this effect in detail. It is clear that the approach of using broadband photometry to determine fundamental stellar parameters is sound in principle, however the inherent uncertainties and relative time expense of measuring T_{sp} still proves a limitation. In Section 1.10 I will introduce a method which overcomes the deficiencies of the previously reviewed methods, and introduce a new measure of temperature which is measured using the entire SED. The SED temperature accounts for both the overall shape of the blackbody and strong spectroscopic features that fall within the bands used for the fitting, and is so called T_{SED}.

While my methodology was in development, there were other recent attempts at applying SED fitting to stellar characterisation which have seen some success; all of which

have been enabled or improved by the Gaia mission. With the publication of Gaia DR1 came Stassun et al. (2017), who attempted an SED fitting technique by adopting extinction A_V as the free parameter in their fitting; neglecting T_{SED} in favour of their measured T_{sp}. Due to the initial precision of parallaxes in Gaia DR1, the uncertainties in radius of this sample were also comparatively large; even compared to the literature values. More recently, studies such as Nielsen et al. (2019), Rodriguez et al. (2018), and Rodriguez et al. (2019) have harnessed the Gaia DR2 parallax measurements to perform SED fitting through the newly updated `EXOFAST v2` code (Eastman et al. 2013; Eastman et al. 2019). SED fitting is one of the methods that can drive its global characterisation routines; however it still optionally draws upon stellar interior models to guide parts of its joint modelling. Another example of recent work that employs SED fitting for exoplanet host characterisation is the "Zodiacal Exoplanets in Time" series of papers, of which Rizzuto et al. (2018) is the most recent, who use the method of Mann et al. (2015) to characterise the host. This involves determining the bolometric flux from an SED fitting method, but determining R using the empirical $M_{K_s} - R$ relation of Mann et al. (2015), which I show in Chapter 4 is inconsistent with other methods. Most recently Ligi et al. (2019) performed SED fitting on optical and near-IR photometry to determine the bolometric flux of the source, however they use knowledge of an interferometrically measured angular diameter θ_{LD} to drive the characterisation process. Historically, one of the tools that has proven useful for SED fitting is the Virtual Observatory SED Analyser (VOSA, Bayo et al. 2008), which was recently upgraded to support parallaxes from Gaia (Rodrigo et al. 2019). Of all of the techniques presented, this method is the most reminiscent of mine.

The methodology presented in Chapter 2 is novel in that it offers a unique combination, which none of the aforementioned have yet achieved. First, at no point in the characterisation process are stellar interior models used, meaning that the technique I am using is semi-fundamental. None of the other methods, aside from VOSA, use the overall shape of the SED to measure the temperature of the photosphere; instead usually favouring spectroscopic temperatures. In my framework, both the R and T_{SED} are simultaneously determined, meaning that the technique is implicitly flux conserving, and all measures are self consistent. Thanks to its being implemented using a simple grid search paradigm, it is also much simpler than other methods, making it easier to interpret the

output and track down issues. The simplicity of this technique, paired with high quality input data, mean that unprecedented precision can be achieved for measurements of stellar temperature and radius. Unlike other methods, the best-fitting R is analytically determined for each grid cell, meaning that the technique is applicable to large catalogues of stars in a reasonable time frame; something more problematic for other methods which probe large, multivariate parameter spaces. Despite this, a rigorous treatment of radius uncertainties is still easily forthcoming by searching the χ^2 space around the analytically determined R.

1.8.1 The Causes of Radius Inflation

Given that convective flows are the dominant means of energy transport out of the star, many have made the reasonable assertion that inhibiting convection would cause an increase in the stellar radius, and hence explain the inflation of M-dwarfs. This inhibition could be accomplished by strong magnetic fields (Mullan & MacDonald 2001; MacDonald & Mullan 2017) that are thought to be the fundamental drivers of both magneto-convection and the delay of convective onset (e.g. MacDonald & Mullan 2014). Hence there has been much theoretical work over the last decade to develop consistent stellar evolution models that correctly account for dynamo effects and stellar magnetism, including the resulting starspots (Mullan & MacDonald 2001; Feiden & Chaboyer 2013; Somers & Pinsonneault 2016; MacDonald & Mullan 2017). Recently these effects have been modelled in 1D stellar structure models by Ireland & Browning (2018), who adopt a depth dependent mixing length theory parameter $\alpha_{\rm MLT}$; emulating the effect of convective inhibition. In their work they observe radii inflated by 10 to 15% when compared to models that do not treat convection in this way, though they caution that such treatments of magnetic inhibition are highly uncertain and may be difficult to calibrate.

Despite this success, the hypothesis that magnetic fields cause inflation has been brought into question by Kesseli et al. (2018), who used a $v\sin(i)$ technique to show that the radii of samples of rapidly-rotating stars are consistent (to within 5%) with those of slowly-rotating stars, and the inflation in eclipsing binaries consistent with single stars. In addition Kochukhov & Shulyak (2019) conclude that magnetic inflation models do not

support their observations of the DEB YY Gem.

Theories which invoke magnetism to explain the radius inflation of M-dwarfs make two predictions which will be tested in this thesis. The first is that unless M-dwarfs all have very similar fields, at a given mass (or luminosity) they should have radii which range between the predictions of the non-magnetic models and some maximum inflation. The sample presented in Chapter 4 is sufficiently large to show that any spread in M-dwarf radii is much less than $1-2\%$ (Section 4.3.2), apparently ruling out the magnetic inflation models. The second prediction is that the degree of radius inflation should correlate with magnetic activity indicators (López-Morales 2007). Again I find no such relationships (Section 4.3.2.4), but for indicators such as X-ray activity this could be explained if the surface field is unrelated to the magnetic field in the bulk of the star (see Brun & Browning 2017, for a discussion of how under-developed models of M-stars are). However this criticism cannot be levelled at the absence of a correlation between rotation period (or Rossby number) and inflation I find, which again suggests magnetic fields may not be responsible for radius inflation. But to draw any solid conclusions, radius inflation needs to be studied as a function of mass, which I will do in Chapter 4.

1.8.2 Revising Exoplanet Radii using Gaia DR2

It is becoming increasingly apparent that the formation of planets during star formation is commonplace, with the probability of detecting hosted planets approaching unity for well-studied stars (Winn & Fabrycky 2015). Since the first confirmed discovery of 51 Pegasi b, a hot-Jupiter exoplanet oribiting a Solar-like star, in Mayor & Queloz (1995), the drive of the exoplanet community has been twofold. The number of known exoplanets has traditionally been small, prohibiting statistical studies of exoplanet populations. This has been the drive behind the Kepler mission, which has bolstered the number of known exoplanets to over 4100 at the time of writing. This has also served as the impetus for the next generation of exoplanet discovery missions, such as TESS (Ricker et al. 2014), which is expected to yield thousands of planets smaller than Neptune, with tens of planets comparable in size to Earth. As shown in Figure 1.8, current methods of exoplanet discovery have inherent biases, which favour massive planets whose orbits are close to their stellar

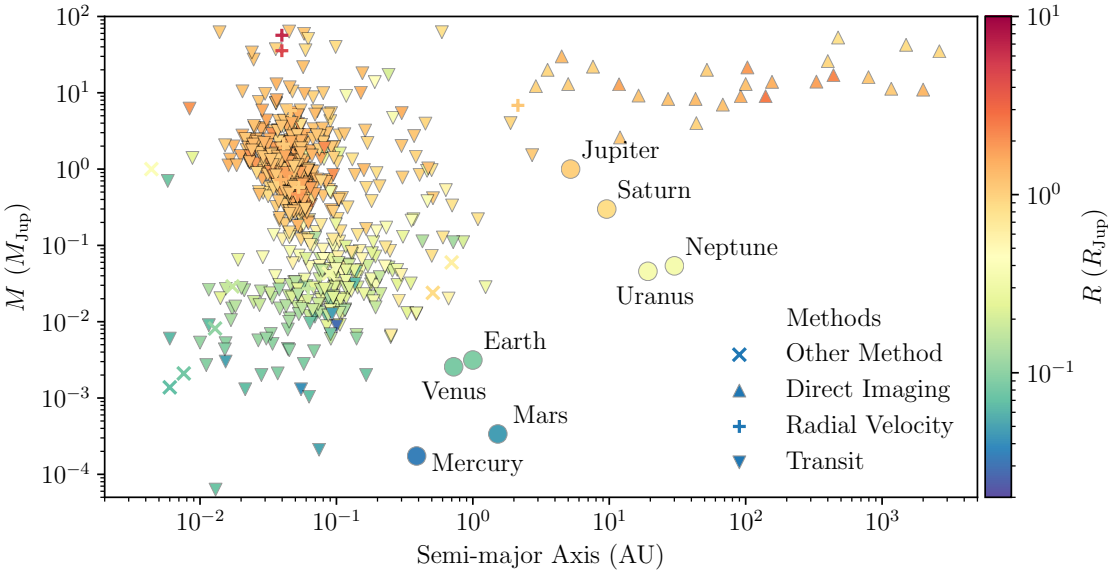

Figure 1.8: The > 4000 confirmed exoplanets plotted in the Semi-major axis – radius plane. The measured radius is indicated by the colour of each point. The detection method is also indicated by the marker, with transits, radial velocity, direct imaging and all other methods being indicated by a triangle, plus sign, inverted triagnel and cross respectively.

host. Thanks to the continued successes in building an increasingly statistically significant sample, recent efforts within the community have been applied to characterising this cornucopia of far away worlds. I will now briefly review the progress that is being made in this endeavour, and the techniques which are being employed to do so.

1.8.3 Exoplanet Characterisation Techniques

Accurate stellar host parameters should serve as the solid foundation upon which any attempts to characterise extrasolar planets are built. Inaccuracies in stellar properties can quickly ripple on to larger inaccuracies in exoplanet host properties. For example, a 10% discrepancy in $R_\star$ becomes a 30% discrepancy in mean planet density ρ_p. This is to say that the quality of measurements of exoplanet properties are inextricably linked to those of the host, and care should be taken in their measurement.

This is of particular concern in the regime of low-mass stars, where I have already established that there are disagreements between models and observations. Historical discoveries have yielded larger planets around intermediate-mass stars, as the ubiquitous transit method favours high signal to noise. However, at least 63% of the stars in the Solar neighbourhood are classified as M-dwarf stars (Dieterich et al. 2012), a sample

which until recently has been largely unprobed by large exoplanet discovery campaigns. With improving technology, the exoplanet community has been driving further down the stellar sequence towards the low-mass regime. As well as drastically increasing the potential sample, the improved signal-to-noise increases the likelihood of discovering super-Earths—terrestrial like planets on the order of several Earth-masses. There are many ongoing surveys, such as MEarth (Nutzman & Charbonneau 2008), CARMENES (Quirrenbach et al. 2014) and TESS (Ricker et al. 2014), and upcoming instruments, such as JWST (Gardner et al. 2006), ESPRESSO (Pepe et al. 2010) and CHEOPS (Broeg et al. 2013), making extensive observations of this population. This is to say that techniques used for measuring the properties of exoplanet hosts should be applicable to a wide stellar demographic.

1.9 Methods for Exoplanet Characterisation

The typical workflow for characterising transiting exoplanets can be regarded as two tasks: measurement of observables to infer properties of the stellar host–exoplanet system as a whole, and characterisation of the stellar host to disentangle the properties of the two. The measurements involved in performing characterisations come predominantly from two methods. Since the initial work of Mayor & Queloz (1995), stellar radial velocity measurements—the Doppler shift induced as the star orbits the barycentre of its planetary system—have been a steadfast method for measuring exoplanet masses. However, a thorough characterisation cannot be accomplished without the ubiquitous transit method, with which the ratio of the planet radius to the star radius can be measured. Problematically, measurements alone have not been able to fix the gauges of many of the ratios; especially with regard to stellar properties. Hence, it has remained necessary for exoplanet characterisation pipelines to also draw estimations of certain absolute properties from model stellar interiors. To gain insight into this process, I will briefly review the exoplanet characterisation methods employed within the sample used in Chapter 5. The material in this section draws from the chapters by Winn (2010) and Murray & Correia (2010).

Since the first observation of a transiting exoplanet, that of HD 209458 b in Char-

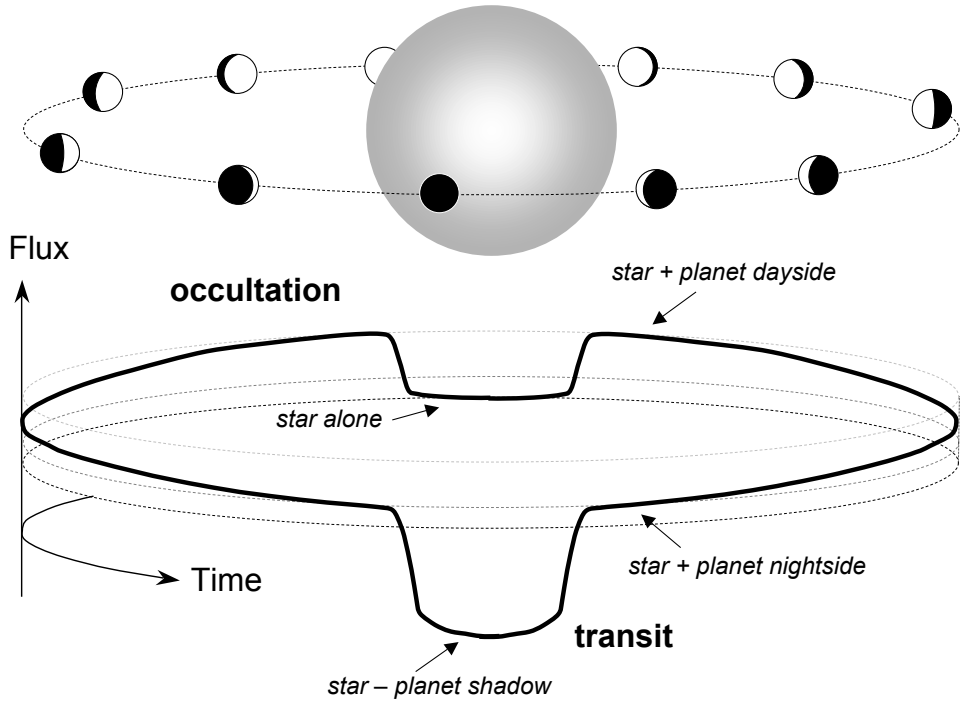

Figure 1.9: An illustration of the orbit of an exoplanet around the star, and the accompanying change in combined flux of the system. The flux from the system is dominated by that of the star, plus a small contribution from the day side of the exoplanet. During transit, when the night side of the planet is in the line of sight, the exoplanet blocks some portion of the flux from the star. As the day side of the planet comes into view, the stellar flux is supplemented by exoplanetary emission. As the star occults the planet, a secondary, smaller dip is evident when this exoplanetary emission is blocked. **Source: Winn (2010).**

bonneau et al. (2000), the transit method has formed an integral part of both speculative exoplanet hunting campaigns, and in-depth characterisation studies. Due to their relatively inexpensive nature, transit observations have become the de facto method by which exoplanets are now discovered; as evidenced by the imbalance of methods in Figure 1.8.

To understand the detailed workings of the transit method, it is useful to refer to a schematic of the orbit of an exoplanet around its host, shown in Figure 1.9, along with an intuitive illustration of the transit method in action. Furthermore, the observables that can be measured from a transit are illustrated in Figure 1.10. By considering host star as a disc of uniform brightness, and by assuming the transit is non-grazing, i.e. the transit reaches fullness, the maximum loss of light in a transit is given by

$$\delta \approx k^2 \left[1 - \frac{I_p(\text{tra})}{I_\star}\right], \tag{1.36}$$

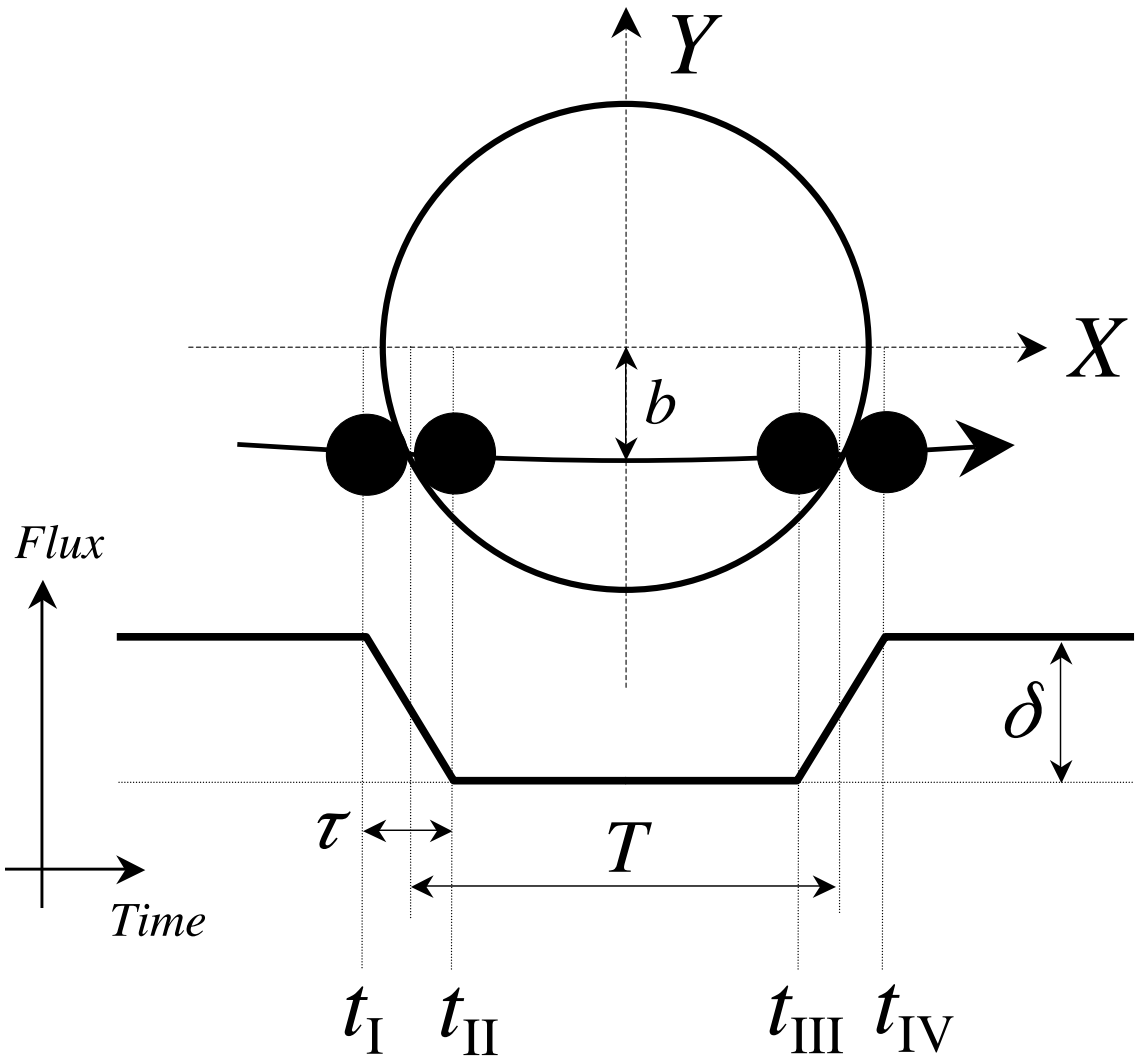

Figure 1.10: An illustration of a transit. Indicated are the parameters that influence and can be measured directly from the transit. **Source: Winn (2010).**

where $I_p(\text{tra})$ and $I_\star$ are the intensity of the planet during transit and the host star respectively. By assuming the flux contribution from the planet nightside is negligible, one can determine the ratio of the planet radius R_p to the stellar host radius $R_\star$, $\sqrt{\delta} \approx k \approx R_p/R_\star$; so symbolised in deference to the literature on eclipsing binaries. By measuring the duration between the successive brightness minima, the times of mid-transit can be determined, whose difference directly gives the orbital period of the exoplanet P. Scrutinising the slope of the ingress and egress of the transit provides the total duration T_{tot} and full duration T_{full} of the transit which, assuming a circular exoplanet orbit, are given by

$$T_{\text{tot}} \equiv t_{\text{IV}} - t_{\text{I}} = \frac{P}{\pi} \sin^{-1}\left[\frac{R_\star}{a}\frac{\sqrt{(1+k)^2 - b^2}}{\sin i}\right], \tag{1.37}$$

$$T_{\text{full}} \equiv t_{\text{III}} - t_{\text{II}} = \frac{P}{\pi} \sin^{-1}\left[\frac{R_\star}{a}\frac{\sqrt{(1-k)^2 - b^2}}{\sin i}\right], \tag{1.38}$$

where i is the inclination between the orbital plane and the line of sight, a is the semi-major axis of the orbit and b is the sky-projected distance between the planet and star centres at conjunction; termed the impact parameter of the transit. Although both Equation 1.37 and Equation 1.38 assume circular orbits, they can be augmented with a factor of $\sqrt{1-e^2}/(1 \pm e\sin\omega)$ to serve as good approximations for eccentric orbits; where the '+' solution refers to transits and the '-' solution refers to occultations. In the limit where $R_p \ll R_\star \ll a$, a rearrangement of Equation 1.37 and Equation 1.38 yields the impact parameter b and the scaled stellar radius $R_\star/a$ through the approximate equations

$$b^2 \approx \frac{(1-\sqrt{\delta})^2 - (T_{\text{full}}/T_{\text{tot}})^2(1+\sqrt{\delta})^2}{1-(T_{\text{full}}/T_{\text{tot}})^2}, \tag{1.39}$$

$$\frac{R_\star}{a} \approx \frac{\pi}{2\delta^{1/4}}\frac{\sqrt{T_{\text{tot}}^2 - T_{\text{full}}^2}}{P}\left(\frac{1+e\sin\omega}{\sqrt{1-e^2}}\right), \tag{1.40}$$

where e is the eccentricity of the orbit and ω is the argument of periapsis.

Unlike the simplistic model I have adopted thus far, in reality the geometry and opacity of the stellar photosphere lead to a radial brightness profile; an effect known as limb darkening. Limb darkening is represented in models as a function of $\mu = \cos\gamma$, where γ is the angle between the line normal to the stellar surface and the line-of-sight to

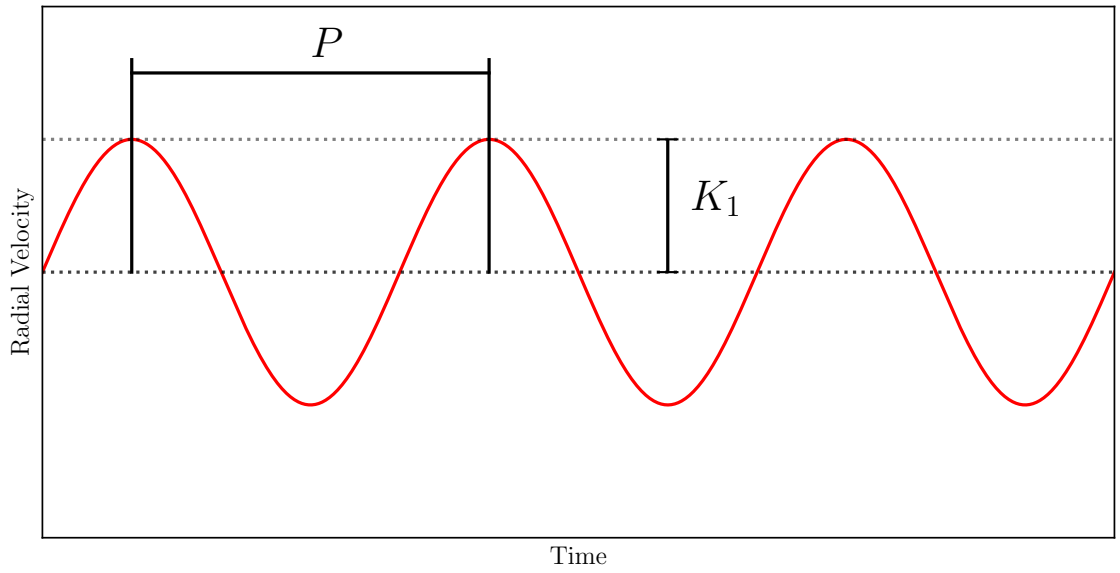

Figure 1.11: An illustration of a periodic radial velocity curve of a planetary orbit with P and K_1 annotated. **Adapted from Figure 1.1 in Pudritz et al. (2007).**

the observer. There are a variety of prescriptions which quantify this, however the most successful of these has been found in the four-parameter law, introduced in Claret (2000) and expanded in Claret (2004), which is represented as

$$\frac{I_\mu}{I_0} = 1 - c_1(1 - \mu^{\frac{1}{2}}) - c_2(1 - \mu) - c_3(1 - \mu^{\frac{3}{2}}) - c_4(1 - \mu^2), \tag{1.41}$$

where I_0 is the specific intensity at the centre of the disc, I_μ the limb darkened specific intensity and c_1, c_2, c_3 and c_4 are the limb darkening coefficients. These coefficients are derived numerically from stellar model atmospheres, and are provided in a tabulated form as a function of T_{eff}, [Fe/H] and $\log(g)$.

The parameter conspicuously missing from those that can be determined from transits is the mass of the planet, which requires a radial velocity measurement of the combined star–exoplanet system. As both components orbit their barycentre, the star undergoes reflex motion with a radius $a_\star$, given by

$$a_\star = a\left(\frac{M_p}{M_\star}\right), \tag{1.42}$$

where M_p and $M_\star$ are the masses of the exoplanet and star respectively. As the star orbits the barycentre of the system, its line-of-sight velocity is regularly Doppler shifted. By

carefully measuring the Doppler shift of the stellar spectral lines over time, an illustration of which is shown in Figure 1.11, a measurement of the semi-amplitude of the radial velocity of the star K_1 and validation of P can be achieved. By balancing the gravitational force between the star ($GM_\star M_p/[a_\star + a]^2$) and the planet with the centripetal force on the planet ($M_\star K_1^2/a_\star$), and using Equation 1.42, we find that K_1 is related to M_p and $M_\star$ by

$$K_1 = \left(\frac{2\pi G}{P}\right)^{\frac{1}{3}} \frac{M_p \sin i}{(M_\star + M_p)^{\frac{2}{3}}} \frac{1}{\sqrt{1-e^2}}, \tag{1.43}$$

where e is the eccentricity of the orbit, and $a_\star$ is the semi-major axis of the star's orbit around the systems combined barycentre. By balancing Newton's law of gravitation with centripetal force, we can state Kepler's third law for an elliptical orbit as

$$\frac{a^3}{P^2} = \frac{G(M_\star + M_p)}{4\pi^2}. \tag{1.44}$$

Using Equation 1.44, Equation 1.43 can be rearranged to find the mass of the planet

$$M_p = \frac{2\pi a^2}{PG} \frac{K_1\sqrt{1-e^2}}{\sin i}. \tag{1.45}$$

The radial velocity method has been instrumental in the discovery of exoplanets—it is in fact the second most productive discovery method (see Figure 1.8). Despite this, it does have some clear limitations. Measuring Doppler shifts requires spectroscopic data, making observations inefficient when compared to the photometric measurements required for the transit method. Furthermore, current observing technologies impose a strong bias towards detections of massive exoplanets in orbital configurations which result in a large radial velocity signal; further contributing to the already endemic selection bias in known exoplanet populations. However, combining radial velocity measurements with transit light curve analysis has proven a powerful pairing; as, with accurate measurements of both, one can infer much about both components of the system.

Thorough characterisation of the system via transits and radial velocities is a complex multivariate problem which, in practice, necessitates a model inversion technique. This is accomplished by fitting appropriate models to time series spectroscopic and pho-

tometric data, overwhelmingly through the use of Markov-Chain Monte Carlo (MCMC) methods; which are used to sample the high dimensional parameter spaces inherent in the problem. Most literature sources utilise the eclipse model of Mandel & Agol (2002), and incorporate the limb darkening law of Claret (2000, 2004). The fitting process involves exploring the parameter space by drawing samples from their multivariate posterior probability distribution. The parameters that comprise the space which is explored, the so called jump parameters, serve as proxies for the underlying physical properties of the system, with the exploration of the space yielding the distributions of said properties. The first link in the chain is formed by guessing values for each of the jump parameters. The chain is then evolved using the an algorithm, such as the Metropolis–Hastings algorithm, where a new trial state is generated, and randomly transitioned to in favour of the current state. After a sufficient number of links, the chain can be sampled to find an approximation of the distributions of the jump parameters—the longer the chain, the better the approximation of the underlying distribution.

Until now, I have mainly described parameters relative to the stellar host. Hence, stellar host characterisation is an important part of the process of determining absolute measurements of hosted exoplanets, in particular its radius which sets the gauge of many other measurements, and is largely performed using a combination of spectroscopy and stellar models. The determination of $R_\star$ from the model prescription is a function of measures of luminosity, effective temperature and stellar composition (Pál 2009). The easier to obtain of these are spectroscopic temperature $T_{\rm sp}$, and composition—given by metallicity [Fe/H]—which can be determined from an intermediate resolution spectrum using a spectral analysis package. Literature values in this sample typically use Spectroscopy Made Easy (SME) (Valenti & Piskunov 1996) operating with the spectral line profiles of Valenti & Fischer (2005). More problematic is the observational determination of luminosity, from which the stellar mass $M_\star$ can be determined using an empirical relation. Seminal attempts at exoplanet characterisation employed the spectroscopic determination of $\log(g)$ as a luminosity indicator. However, it was shown in Sozzetti et al. (2007) that $\log(g)$ has only a subtle effect on the shapes of spectral lines, thus for transits $R_\star/a$ and $\rho_\star$ are now widely used to impose a stronger constraint on interrogations of stellar models. An empirical constraint on $R_\star$ can also be achieved through the previously described

infrared flux method (IRFM, see Section 1.7.3), which yields the angular diameter of the star on the sky θ, and a distance measurement. From the sample of stars studied in this thesis, both WASP-80 b (Triaud et al. 2013) and WASP-6 b (Gillon et al. 2009) have additional IRFM measurements, with which observational constraints can be placed on their radii.

An interface to the stellar interior models comes in the form the stellar density $\rho_\star$, which Seager & Mallén-Ornelas (2003) showed can be directly determined from the transit using

$$\rho_\star = \frac{M_\star}{R_\star^3} = \left(\frac{4\pi}{P^2 G}\right)\left\{\frac{(1+\sqrt{\delta})^2 - b^2(1-\sin^2(T_{\rm tot}\pi/P))}{\sin^2(T_{\rm tot}/P)}\right\}. \tag{1.46}$$

The measurements for the star can then be placed in the $T_{\rm eff} - \rho_\star$ plane and mapped onto stellar interior models to determine a theoretical $M_\star$ and age for the host (e.g. Gillon et al. 2009). The Yonsei-Yale (Y^2) (Yi et al. 2001; Demarque et al. 2004) and Baraffe et al. (1998) isochrones are routinely applied to this task for intermediate and low-mass stars respectively. Determinations of $M_\star$ can be combined with radial velocity measurements through Equation 1.45 to infer the mass of the hosted exoplanet. Empirical constraints can also be placed upon stellar mass using an empirical mass–radius relationship. The seminal works of Hertzsprung (1923), Russell et al. (1923) and Eddington (1926) showed that there were empirical relationships between a star's mass and its observables. These observables can be measured, and then mapped onto a given mass. In this dataset, for example, the properties of WASP-52 b (Hébrard et al. 2013) were determined from the empirical mass–radius relationships of Torres et al. (2010) and Enoch et al. (2010); some of the most widely used for exoplanet characterisation.

Despite its successes, as I will show in Chapter 5, there are some serious deficiencies with existing exoplanet characterisation methodology, which mean that the determinations of luminosity are inconsistent with that observed in Gaia DR2. In said chapter, I will draw upon the SED fitting methodology to provide a self-consistent revision to the radii of exoplanet host stars to ensure that they are in-line with those suggested by Gaia DR2. In doing so, I will show that the method presented in this thesis shows the potential

for considerable improvement in both the accuracy and precision of exoplanet parameter measurements compared to those presented in the literature.

1.9.1 The Effect of Stellar Host Parameters on Exoplanet Atmospheres

My suggested revisions to established stellar host parameters will have a ripple-on effect to the observed exoplanet parameters, notably the inferred characteristics of their climates. With the current focus on characterising the atmospheres and climates of distant worlds, considering how revised stellar radii will affect them is advantageous. The transit method makes the reasonable assumption that exoplanets are implicitly solid spheres; either by summing up the flux across the transmission spectrum of the star and measuring the white light-curve, or by ignoring wavelength dependence altogether and measuring the transit in a single band. However, in reality the observed radius of the planet is a combination of the bulk radius of the exoplanet $R_{p,\mathrm{bulk}}$ in addition to a wavelength dependent contribution from the atmosphere $z(\lambda)$

$$R_p(\lambda) = z(\lambda) + R_{p,\mathrm{bulk}}, \tag{1.47}$$

where $z(\lambda)$ depends on the properties and chemistry of the atmosphere (e.g. Goyal et al. 2019). By making geometric arguments, an order of magnitude for the observed transit signal from the atmosphere is provided by Winn (2010). Thus, the observable transit signal for one scale-height H_P of the atmosphere (OTS), measured in parts per million (ppm), is given by

$$\mathrm{OTS} = \frac{2R_p(\lambda)H_P}{R_\star^2}10^6, \tag{1.48}$$

where $R_\star$ is the radius of the host star and H_P is the pressure scale height of the atmosphere

$$H_P = \frac{k_B T}{\mu_m g}. \tag{1.49}$$

H_P is itself a strong function of g, which is determined by the bulk density of the planet. Thus, by revising the stellar host to larger or smaller radii, the density of the planet inferred from the transits will decrease and increase proportionally. As well as potentially drastically changing the inferred interior structure of the planet, the retrieved $P-T$ profile of the atmosphere can also see drastic changes.

It is by measuring this variation in transit depth as a function of wavelength that transmission spectroscopy can be fitted to models of the atmospheric transmission, such as those of Goyal et al. (2018) and Goyal et al. (2019), to infer the $P-T$ profile of the atmosphere and atmospheric chemistry. Given the cross-section $\sigma_{\rm abs}$ and abundance of $\xi_{\rm abs}$ of the most dominant species causing absorption in a planetary atmosphere, Lecavelier Des Etangs et al. (2008) provided an approximate analytical solution $z(\lambda)$, given by

$$z(\lambda) = H_P \ln\left(\frac{\xi_{\rm abs} P_{z=0}\sigma_{\rm abs}(\lambda)}{\tau_{\rm eq}}\sqrt{\frac{2\pi R_{p,\rm bulk}}{k_B T \mu_m g}}\right) = H_P \ln\alpha, \tag{1.50}$$

where $P_{z=0}$ is the pressure at the base of the atmosphere and $\tau_{\rm eq}$ is the optical depth in the atmosphere.

The effect of the host star is also seen in the energy budget available to a given exoplanetary climate. This can be naively estimated by considering the equilibrium temperature $T_{\rm eq}$ of the atmosphere, which is given by

$$T_{\rm eq} = T_{\rm eff}(1-\alpha)^{1/4}\sqrt{\frac{R_\star}{2a}}, \tag{1.51}$$

where α is the planetary albedo; the fraction of the incident radiation from the host star that is reflected back into space. Although $T_{\rm eq}$ is not itself dependent on the exoplanetary radius, it is dependent on the luminosity of the stellar host. Hence, incorrect determinations of either $T_{\rm eff}$ or $R_\star$ will result in an errant estimation of exoplanet energy budget. In this approximation, the planet is considered as a pure blackbody that is being heated by its host star with all atmospheric effects, including the inherent greenhouse effect, neglected. Thorough treatments of exoplanet climatology are currently at the cutting edge of the field. Of note is the work of Boutle et al. (2017) who applied the Met Office global circulation model, the Unified Model, to studying the climate of Proxima Centauri b. With the complexity of such studies continuing to increase, improved constraints on exoplanet host properties are becoming imperative.

In Chapter 5 I will apply the SED fitting technique detailed in Section 2.1, to measuring accurately the temperature $T_{\rm SED}$ and radius $R_\star$ of exoplanet hosts, including

M-dwarfs. I will present revised stellar properties for a sample of exoplanet hosts from the PanCET input catalogue (Sing 2016) in Section 5.3. I will also assess the veracity of the method by performing a critical assessment of potential systematic uncertainties, and suggest methods of mitigation in Section 4.3.

1.10 Spectral Energy Distribution Fitting

The stellar SED encodes important information about the stellar photosphere, including its total flux, dictated by the total luminosity of the photosphere, and the effective temperature of the star, which dictates the overall shape of the SED. Spectral energy distribution fitting entails sampling the entire SED of the star to infer these properties. Unlike other observational methods which can be stymied by wavelength dependent effects, such as starspots and plage / faculae, given adequate wavelength coverage, SED fitting can account for and probe for these photospheric effects. In M-dwarfs in particular, the deep TiO and VO absorption bands which fall within the sampled regions of the SED wield some influence over the final solution for the temperature, making the method useful for fitting the SEDs of low-mass stars. Importantly, given an accurate distance measurement to the target the luminosity can be determined. This has proven problematic until very recently, however the advent of Gaia DR2 brings with it a radical increase in the accuracy, precision and abundance of astrometric solutions to nearby stars (see Section 1.10.1.2). The input data for SED fitting is comprised of multi-waveband photometry, which can be readily obtained from archival data of all-sky surveys; making this method readily applicable across the entire sky. It is due to these considerations that I have adopted an SED fitting method for determining the radii of stars in this thesis. The full method used for this fitting is detailed in Section 2.1.

However, there are some caveats to using this method. Fitting is performed between observed photometry and synthetic photometry generated from stellar model atmospheres, meaning that the quality of the fit is largely determined by how well the synthetic photometry can reproduce observed magnitudes. Thus missing physics, and in particular poorly characterised spectral features, in the model atmospheres will cause inconsistencies to the fit; as evidenced in Figure 4.4. However, I will show in Section 3.5.1

that current stellar atmosphere models are suitable for this task. Poorly characterised system responses will also cause the fit to be incorrect. The model considerations are further complicated by the requirement that observational data needs to be high quality, and the inherent characteristics and systematics of the survey need to be well understood. However, the abundance of multi waveband archival data mean that even with selective constraints imposed on the input sample, a statistically significant sample of stars can still easily be drawn. The primary consideration that has prevented widespread use of this method for the determination of stellar radii is that this requires prior knowledge of the distance to the target. However, I will show throughout this thesis that, thanks to the advent of Gaia Data Release 2 (DR2), this is no longer the case.

1.10.1 Gaia: The Vanguard of an Astronomical Revolution

The ability to easily determine distances, and hence set the gauge on many other related parameters, to clusters have made them the workhorses of studying stellar evolution until at least the end of the 20$^{\text{th}}$-century. However, the advent of the Hipparcos spacecraft which spawned the Hipparcos (Perryman et al. 1997), Tycho-2 (Høg et al. 2000) catalogues, as well as the 2007 re-reduction presented in van Leeuwen (2007), provided positions, parallaxes and annual proper motions for around 118 000 stars to an unprecedented accuracy of 0.7 – 0.9 mas for stars brighter than 9$^{\text{th}}$ magnitude. This is a precision about a factor of 50 over previous ground-based attempts (Perryman et al. 1997). Hipparcos provided an unprecedented view into the H–R diagram and stellar evolution. It cannot be denied the impact that the mission had on modern astrophysics, some of the key outcomes of which were reviewed in Perryman (2009). The successes that were achieved with Hipparcos led to a whole slew of ambitious space-based astrometric missions being proposed, with the only one that was approved being the Gaia mission. The Gaia mission was originally proposed as an optical interferometer with a baseline of a few metres, operated in a continuous scanning mode, however the optical design was later revised to resemble an enhanced version of Hipparcos (Vallenari 2018). One of the main improvements over Hipparcos was the addition of the Radial Velocity Spectrometer (RVS), which provides radial velocity measurements in the 8470 – 8740 Å band, and inclusion of continuous spectral integration in the 3200 – 10 000 Å band. In particular the lack of radial velocity

capabilities on Hipparcos was noted, e.g. by Blaauw in Torra et al. (1988), which provided the motivation for inclusion on Gaia (Cropper et al. 2018).

1.10.1.1 Improved Constraints on Stellar Parameters

As well as providing crucial coverage of the time dimension in astronomy, the unprecedented accuracy of Gaia astrometry is also expediting studies of stellar evolution. There exist a variety of methods for determining the fundamental properties of stars (see Section 1.7 for a review of them), however they all have trade offs and caveats which make them unsuitable for large, statistical samples of stellar populations. The $\sim 10^9$ stars observed by Gaia serve as a strong tonic against the small number statistics problems of other methods, as even a sample subject to very rigorous constraints yields $10^4 - 10^5$ stars. With trigonometric distances being readily available for such a large sample, techniques used to study young stellar clusters can be used to study widely distributed populations of field stars. For example, as we did with the colour magnitude diagram in Section 1.5, Gaia data can be used to construct a CMD / H–R diagram of over four million field stars, shown in Figure 1.12. This contains a factor of 10 more stars than was accessible from the previous Hipparcos data, while also being much more accurate ($30 - 50$ μas; Luri & Gaia DPAC 2019). Given the number of different methods for inferring stellar parameters, which were reviewed in Section 1.7, there is a clear demand for inferences of robust stellar parameters from this newly available dataset. Andrae et al. (2018) applied the extremely randomised trees machine learning technique of Geurts et al. (2006) to attempt to infer these parameters using only Gaia data products. The veracity of this regression is yet to be determined, especially when applied to red stars such as M-dwarfs. However, given adequate sampling of the stellar SED with multi-waveband photometric data, the parallaxes from Gaia DR2 can be used to derive stellar parameters for large populations of stars using simple statistical inference. The method for this is presented in Chapter 2. I will then show how this method can be used to answer key questions about the long standing problem of radius inflation in M-dwarfs in Chapter 4 and to improve constraints on host parameters used in exoplanet characterisations in Chapter 5.

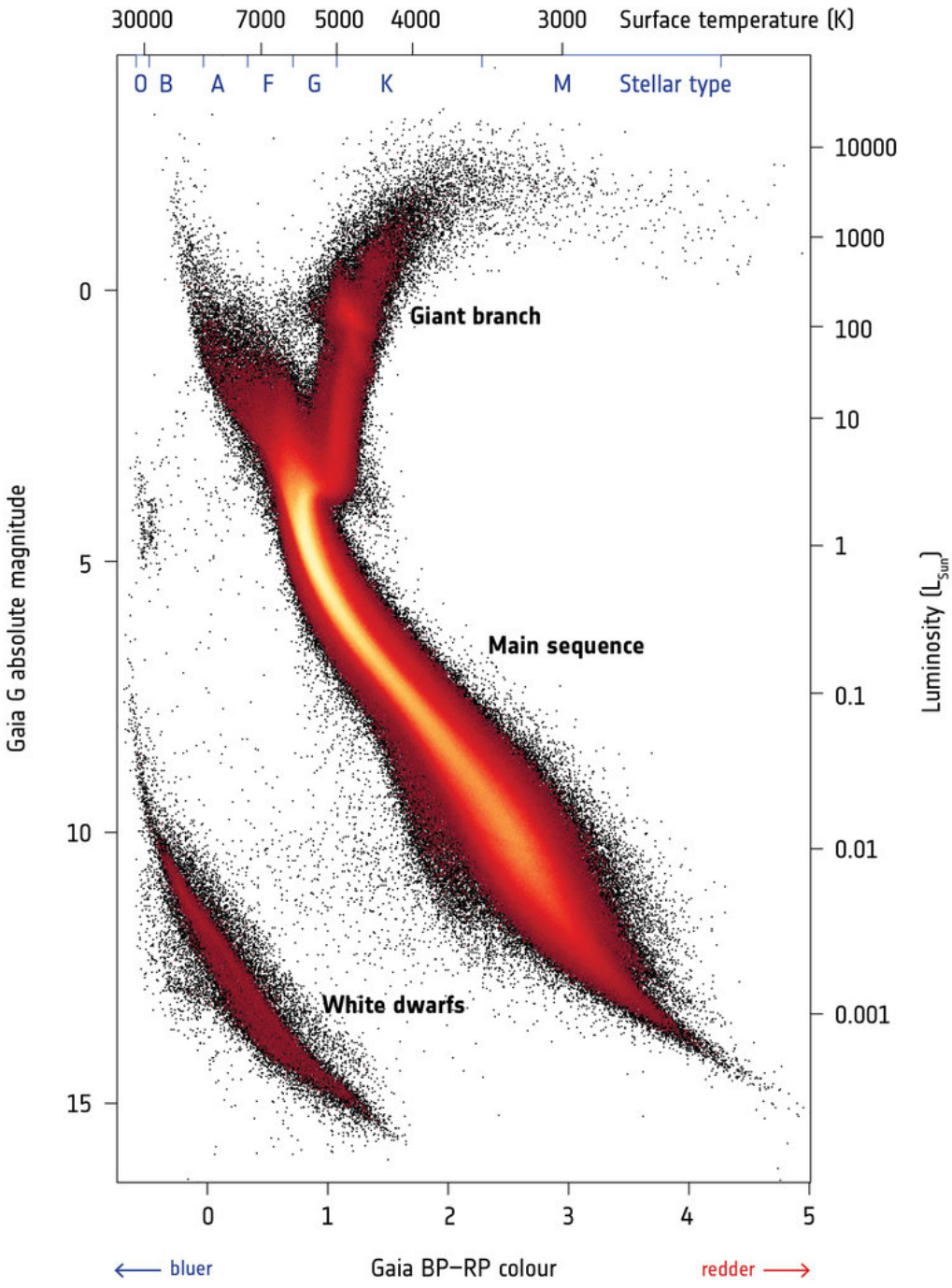

Figure 1.12: The H-R diagram of over four million stars within 1.5kpc of the Sun produced from the second data release from the Gaia satellite. Unlike other H-R diagrams which are usually sampling single populations, such as SFRs or open clusters, this one takes in isolated field stars. It also contains over a factor of 10 more stars than previous attempts to make such a diagram with data from the Hipparcos mission.
Acknowledgement: Gaia Data Processing and Analysis Consortium (DPAC); Carine Babusiaux, IPAG – Université Grenoble Alpes, GEPI – Observatoire de Paris, France.
Available from: http://sci.esa.int/gaia/60198-gaia-hertzsprung-russell-diagram/

1.10.1.2 Deriving Distances from Gaia Parallaxes

Much of the work in this thesis relies heavily upon the distance measurements afforded by Gaia DR2, which are presented as trigonometric parallaxes. The naive way of calculating a distance r, measured in pc, from a given parallax ϖ, measured in mas, is through a simple inversion using

$$r = \tan\left(\frac{1000 \text{ mas}}{\varpi}\right) \approx \frac{1000 \text{ mas}}{\varpi}. \tag{1.52}$$

However, for the majority of stars in Gaia Data Release 2, the origin of the parallaxes used in Chapter 4 and Chapter 5, a simple parallax inversion is not sufficient to produce reliable distances. The main issues include the non-linearity of the transform, the constraint that the derived distance must be positive, and very low signal-to-noise ratios on some measurements (Bailer-Jones et al. 2018). Measurements are also susceptible to the Lutz & Kelker (1973) bias where, due to the fact that the number density of stars increases towards smaller parallaxes, more stars will be scattered into a parallax bin from larger distances than will be scattered out; causing a systematic bias in distance measurements. The final of these issues means that properly treated distance uncertainties are of vital importance. So, Bailer-Jones et al. (2018) asserts that the only consistent and physically meaningful way of deriving distances and accompanying uncertainties from parallaxes is through Bayesian inference. Bayesian inference computes a posterior probability distribution $p(r \mid \varpi)$ given an expected distance r and measured parallax ϖ using Bayes' theorem

$$p(r \mid \varpi) = \frac{p(\varpi \mid r)\, p(r)}{p(\varpi)}. \tag{1.53}$$

$p(r)$ serves as the prior in this inference—the initial degree of belief a distance distribution r with no knowledge of the measured parallax ϖ. $p(\varpi \mid r)$ is the probability distribution of observing the measured ϖ at a distance r, and is known as the likelihood. Finally $p(\varpi)$ is known as the marginal likelihood distribution, which serves as model evidence and is independent of r. This inference process requires the specification of both a likelihood and prior.

Each star in Gaia DR2 lies at a true distance r from the observer, however the measured parallax ϖ is a noisy measurement of this quantity. Hence, the likelihood, as

specified in Bailer-Jones (2015), assumes the measurements are normally distributed with standard deviation σ_ϖ, giving

$$p(\varpi \mid r, \sigma_\varpi) = \frac{1}{\sqrt{2\pi}\sigma_\varpi} \exp\left[-\frac{1}{2\sigma_\varpi^2}\left(\varpi - \frac{1}{r}\right)^2\right]. \tag{1.54}$$

Lindegren et al. (2018) confirms empirically that adopting the Gaussian form for the measurement model of Gaia DR2 parallaxes is a good approximation. Then the purpose of the prior is to encode relevant aspects of the distance distribution that are not included in the likelihood; such as the requirement of the resulting $r > 0$, properties of the source survey and pertinent knowledge about the structure of the galaxy. Bailer-Jones (2015) and Astraatmadja & Bailer-Jones (2016) explore the consequences of utilising different priors before adopting the exponentially decreasing space density (EDSD) prior for inferring distances for 1.33 billion stars in Gaia DR2 in Bailer-Jones et al. (2018). The EDSD prior takes the form

$$p(r \mid L) = \begin{cases} \frac{1}{2L^3} r^2 e^{-r/L} & \text{if } r > 0 \\ 0 & \text{otherwise.} \end{cases} \tag{1.55}$$

The prior also ensures unbiased distances by adopting $L > 0$ as a length scale. For Gaia DR2 this length scale is provided by fitting the EDSD prior to the median stellar distances in each HEALpix cell of a catalogue of mock Gaia observations. The catalogue uses a chemo-dynamical model of the galaxy, which includes extinction, samples all stars with an apparent magnitude of $G \leq 20.7$ mag and is presented in Rybizki et al. (2018). To avoid inherent discontinuities across HEALpix grid boundaries the length scales in the resulting map are fitted with spherical harmonics, yielding $L_{\text{sph}}(l, b)$. The final map from which values of $L_{\text{sph}}(l, b)$ are drawn is shown in Figure 1.13. As a result of this methodology, although distances are determined independently of one another, the EDSD prior is correlated on small spatial scales. However, because the samples used in this thesis are either all sky, or widely spatially distributed, this does not pose a problem during my investigations.

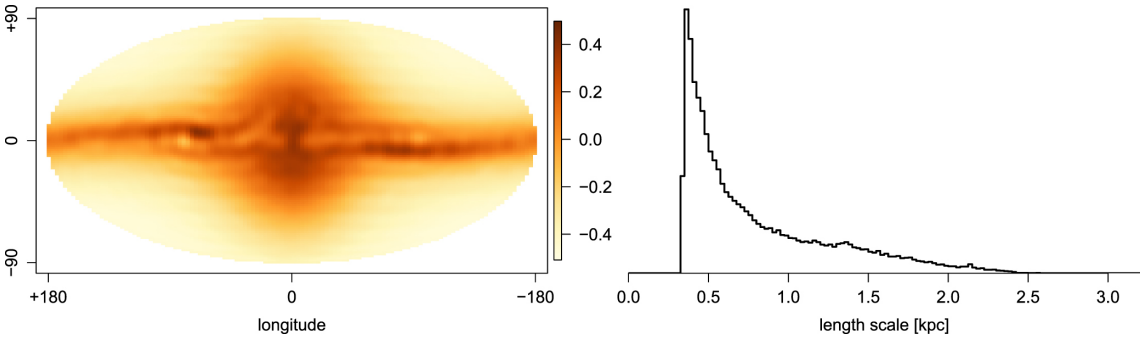

Figure 1.13: The values of $L_{\text{sph}}(l, b)$ used for inference of distances from parallaxes in Gaia DR2. The left pane shows the map in l and b, presented in Mollweide (equal area) projection, from which $L_{\text{sph}}(l, b)$ is drawn. The histogram on the right shows a the distribution of length scales (over equal-area cells).
Source: Bailer-Jones et al. (2018).

The unnormalised posterior of the distance to a given source is then

$$p^*(r \mid \varpi, \sigma_\varpi, L_{\text{sph}}(l, b)) = \begin{cases} r^2 \exp\left[-\frac{r}{L_{\text{sph}}(l,b)} - \frac{1}{2\sigma_\varpi^2}\left(\varpi - \varpi_{\text{zp}} - \frac{1}{r}\right)^2\right] & \text{if } r > 0, \\ 0 & \text{otherwise,} \end{cases} \tag{1.56}$$

where $\varpi_{\text{zp}} = -0.029$ mas is the global parallax zeropoint for Gaia, measured using observations of quasars (Lindegren et al. 2018). The final estimation of distance r_{est} is performed by taking the mode of the posterior, which can be done by solving

$$\frac{r^3}{L_{\text{sph}}(l, b)} - 2r^2 + \frac{\varpi}{\sigma_\varpi^2} r - \frac{1}{\sigma_\varpi^2} = 0, \tag{1.57}$$

for r. By slightly rearranging Equation 1.57, one can intuit the purpose of each term

$$\underbrace{\frac{r^3 \sigma_\varpi^2}{L_{\text{sph}}(l, b)}}_{\text{Lutz - Kelker Bias}} - \underbrace{2r^2\sigma_\varpi^2}_{\text{Asymmetry}} + \underbrace{\varpi r - 1}_{\text{Transform}} = 0. \tag{1.58}$$

The final two terms are responsible for performing the transformation between parallax and distance. The first and second terms provide corrections to the parallax inversion to account for Lutz & Kelker (1973) bias and the asymmetry of the transform respectively. To assess the effect of these terms, I rearranged Equation 1.58 to find

$$\frac{r}{L_{\text{sph}}(l, b)} - 2 + \frac{\varpi}{\sigma_\varpi^2 r} - \frac{1}{r^2\sigma_\varpi^2} = 0, \tag{1.59}$$

For the samples presented in this thesis r remains comparable to the most common scale lengths shown in Figure 1.13, indicating that accounting for the Lutz & Kelker (1973) bias is important for this work. In the regime where $r \ll L_{\rm sph}(l, b)$, and the first term can be neglected, Equation 1.58 can be further re-arranged to find the distance r using

$$r = \frac{1 + 2\sigma_{\varpi}^2 r^2}{\varpi}. \tag{1.60}$$

This shows that regardless of the uncertainty in the measured parallax, there is always some correction required to account for the asymmetry of the transformation between parallax and distance. Upon examining the sample used in Chapter 4, I found that the correction due to both the Lutz & Kelker (1973) bias and asymmetry contributions peaked at around 0.25%. So for this work, the correction provided by the Bayesian approach of Bailer-Jones et al. (2018) is required; else the measured luminosity would be subject to a systematic error of up to 0.5%.

The uncertainty in the inferred distance is measured from the highest density interval (HDI) with probability p, bounded by values $r_{\rm hi}$ and $r_{\rm lo}$. Bailer-Jones et al. (2018) adopts $p = 0.6827$, corresponding to $\pm 1\sigma$ for a Gaussian distribution. The HDI has no analytical solution, so is computed by taking small steps away from $r_{\rm est}$ in both directions, compute the area contained under the normalised posterior in this step, and iterate this procedure until the desired p is achieved. It is worth noting that due to the $r_{\rm hi}$ and $r_{\rm lo}$ being iterated independently, the resulting bounds need not be symmetrical. In a small part of the parameter space, the posterior is bimodal. In these cases $r_{\rm est}$ is estimated using the median of the distribution. $r_{\rm hi}$ and $r_{\rm lo}$ are estimated using the $16^{\rm th}$ and $84^{\rm th}$ percentiles of the equal tailed interval, which has as much probability below the span as above, with p in between (Bailer-Jones 2015).

Chapter 2

Methods

"You know the greatest danger facing us is ourselves, and irrational fear of the unknown. There is no such thing as the unknown. Only things temporarily hidden, temporarily not understood."

— James T. Kirk

2.1 Spectral Energy Distribution Fitting

In determining the fundamental properties of stars, the choice of technique is of critical importance. Traditionally, when determining the properties of large numbers of stars, particularly in young open clusters, photometric observations are fitted to isochrones generated from a combination of stellar atmospheres and stellar interior models. The combination whose synthetic photometry most closely resembles the observations supplies the fundamental properties, such as mass, radius, luminosity and temperature. However, as it was noted in Chapter 1, the accuracy of this approach is compromised due to models being unable to describe the low-mass end of the stellar sequence. This served as our motivation to devise an alternative technique, which can infer stellar properties while being decoupled from the model interiors. Additionally, accurate determinations of temperature are made by measuring the spectral indices of certain lines in the spectra of the target stars. However, this has the reliance on spectroscopic data, which is relatively difficult to obtain and comparatively expensive compared to the abundance of pre-existing multicolour broadband photometry available from publicly accessible survey

archives.

Until recently it has remained problematic to reliably constrain distances to field stars. This is one of the main reasons that galactic open clusters have been crucial benchmarks employed in studying stellar astrophysics - a homogeneous sample of stars at constant distance allows fitting of CMDs to stellar models, hence determination of distances are possible. However, the advent of Gaia DR2 allows us to extend this same level of rigour to field stars, and allows us to improve the precision of constraints on open clusters. The newly acquired wealth of both photometry and parallaxes for over 1.3 billion stars makes the exploitation of them to determine stellar radii a tantalising possibility.

Photometry samples the stellar spectral energy distribution (SED), which itself encodes some of the fundamental parameters of the stars. Given an accurate distance, one can integrate beneath the SED to determine the stellar luminosity, while the shape of the SED is a function of the temperature of the photosphere. Given the measurements of these parameters, the radius of the star is then forthcoming. Importantly, both the luminosity and effective temperature of the star are determined only by the stellar photosphere. This allows determination of radius to be uncoupled from the stellar interior models, which have been shown to be discrepant with observations.

The method I developed uses stellar SEDs, sampled by multicolour broadband photometry, to determine these parameters using a grid search. The technique itself is related to the infrared flux method (IRFM) (Blackwell & Shallis 1977; Blackwell et al. 1979), reviewed in Casagrande (2008), in principle, however it differs in a number of key ways. Unlike the IRFM, which relies on the smooth correlation between temperature and flux in the Rayleigh–Jeans tail, the SED fitting methodology presented in this thesis generalises to the entire SED of the star. Hence, a more robust measurement of luminosity is made, from which the radius of the object can be derived. The IRFM implicitly assumes that the SED of the star can be represented well by a pure blackbody. As Figure 1.7 demonstrates, stars later than mid-K exhibit strong molecular opacities, making this a faulty assumption for low-mass targets. However, the stellar atmosphere models used as inputs to synthetic photometry provide good estimates of these large molecular features. Hence, the temperatures from my methodology are measured from the overall shape of

the SED, which includes the bloackbody shape and opacity contributions from strong spectral features, making this methodology broadly applicable to a wide range of spectral types; including M-dwarfs.

2.1.1 Stellar Atmospheres

The synthetic photometry used in grids is computed by folding theoretical stellar atmosphere models through the system response of the appropriate photometric band. The work in this thesis concentrates in particular on stars inhabiting the very–low-mass regime, which in turn exhibit cool effective temperatures $T_{\rm eff} > 4000$ K. At temperatures cooler than ~ 4500 K molecular species such as metal hydrides, TiO, CO and water vapour have been observed to form in stellar atmospheres (Allard et al. 2012b). As most of the work herein addresses M-dwarf stars, a competent treatment of molecular opacities is a key consideration in the choice of atmosphere library. Additionally, this method should be able to cover a large enough area of the $T_{\rm eff} - \log(g)$ parameter space that measurements of Solar-like exoplanet host stars can also be made. Hence I used the BT-Settl CIFIST stellar model atmosphere grid of Allard et al. (2012b), Allard et al. (2012a), and Rajpurohit et al. (2013) to produce synthetic photometry.

The BT-Settl CIFIST atmosphere grid employs the 3D non local thermodynamic equilibrium (non-LTE) radiative transfer code, `PHOENIX` (Hauschildt 1992, 1993), in tandem with a radiative-magneto-hydrodynamical code, such as `CO$^5$BOLD` (Freytag et al. 2012). The latter first performs a hydrodynamical simulation of the stellar atmosphere, using a radiative transfer scheme is focused on accurately estimating the energy budget of the atmosphere. In these simulations, a full treatment of the radiation in the model, in particular atomic and molecular species, would be computationally prohibitive. The `PHOENIX` code is then provided a pre-computed output from am MHD simulation to generate synthetic observables using a full non-LTE treatment of radiative transfer. The `PHOENIX` code performs a line-by-line opacity sampling in spherical symmetry, as opposed to the plane parallel approach employed previously, computes stellar atmospheres using full spherical radiative transfer and includes a sophisticated dust model that describes condensation and sedimentation of grains below about 2600 K (Allard et al. 2003; Allard et

al. 2012a); an important consideration for late M-dwarfs and brown dwarfs. Unlike older codes, which largely use pre-computed opacity tables, `PHOENIX` uses a direct opacity sampling method to dynamically calculate the opacity within an arbitrary wavelength window by dynamically selecting and summing LTE background lines. This approach is vital for non-LTE calculations upon a wavelength grid which is irregular and variable between iterations (Hauschildt et al. 1999). The current version of the BT-Settl models include updated line lists for water (Barber et al. 2006), metal hydrides such as CaH, FeH, CrH and TiH (Bernath 2006), VO, CO_2 (Tashkun et al. 2004) and TiO (Plez 1998); all of which are important when considering low-mass stars. The solar abundances for the CIFIST grid are provided by Asplund et al. (2009) with revisions of elemental abundances for C, N, O, Ne, P, S, K, Fe, Eu, Hf, Os and Th by Caffau et al. (2011), which results in an increased total heavy element fraction. Convection within the models is treated using the mixing length theory of Kippenhahn & Weigert (1990), which adopts an $\alpha_{\rm MLT}$ dependent on pressure scale height H_P. Mixing length parameter $\alpha_{\rm MLT}$ also scales with spectral type, with $\alpha_{\rm MLT} \approx 1.6 H_P$ for the Sun, and increasing to $\alpha_{\rm MLT} \gtrsim 2.0 H_P$ for the coolest and densest models. However, this MLT prescription makes the assumption that the atmosphere is non-rotating, and that magnetic fields are not present. In reality, both of these physical effects are present in some way in all stars, and will act to reduce the convective efficiency; making the photosphere appear cooler than models for active stars. The CIFIST atmosphere grid provides the outer boundary conditions for calculations of the Baraffe et al. (2015) interiors, providing another good reason to adopt them for this project.

The BT-Settl CIFIST atmospheres are provided for solar metallicity. For situations where grids were required to deviate away from solar metallicity, I instead adopted the BT-Settl AGSS2009 models, which cover non-solar values of [M/H] by scaling the abundances from solar. These models purely use Asplund et al. (2009) solar abundances, ignoring the CIFIST revisions from Caffau et al. (2011).

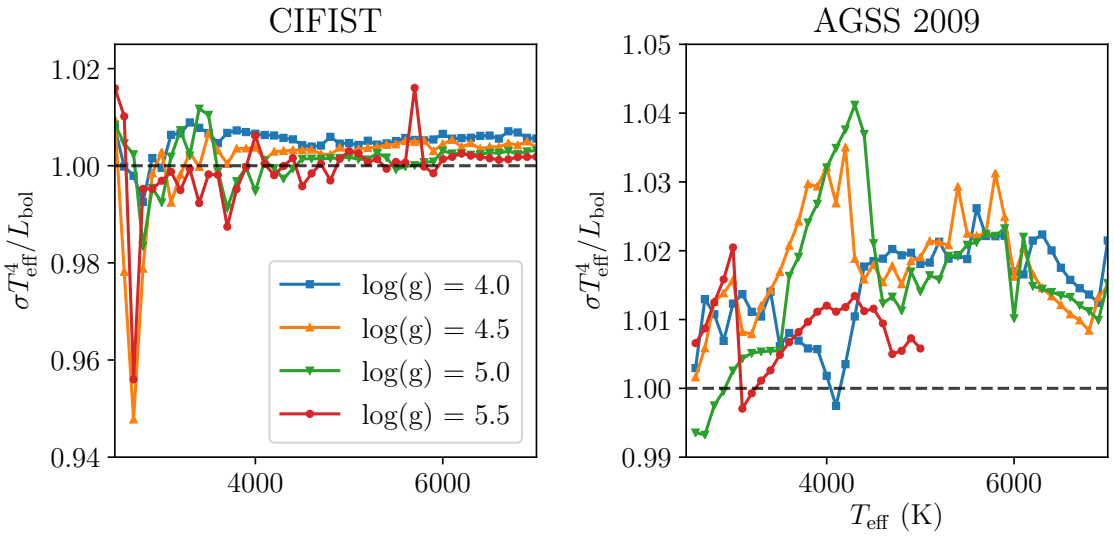

Figure 2.1: The correction factor δ_L for the CIFIST (left) and the AGSS 2009 (right) stellar atmospheres as a function of $T_{\rm eff}$. The different lines denote $\log(g)$ of 4.0 (blue square), 4.5 (amber triangle), 5.0 (green down-pointing triangle) and 5.5 (red circle). For convergent solutions δ_L should remain near unity, however I found that that atmospheres can differ from their defined luminosity by up to 4% throughout the range of $\log(g)$.

2.1.2 Correcting Luminosity Discrepancies in Model Stellar Atmospheres

As the methodology presented in this chapter effectively integrates the luminosity beneath the SED to infer the radius, it was advantageous to perform simple validation upon the provided model fluxes. From the definition of effective temperature, the total radiant flux from a stellar atmospheres must satisfy

$$\frac{\sigma T_{\rm eff}^4}{\int_\lambda I_\lambda d\lambda} = \delta_L, \tag{2.1}$$

where I_λ is the specific intensity of a unit surface area of the synthetic atmosphere and $\delta_L \simeq 1$ for a given solution. By numerically integrating the across all the flux bins of the model atmospheres, and placing the result into Equation 2.1, I was able to show that the atmosphere models do not satisfy this constraint, and as such do not properly conserve energy. This discrepancy is demonstrated for both atmosphere grids used in this thesis as a function of both $T_{\rm eff}$ and $\log(g)$ in Figure 2.1. The discrepancy is much lower, and systematic, in the CIFIST model grid than in the AGSS grids, with an RMS of 0.7% versus 1.7% respectively within the parameter space used for this thesis. To remedy this issue, I multiplied each flux bin in the model atmospheres by δ_L before further use. Although potentially unphysical, simply scaling the flux of the atmosphere in this way ensures that

total luminosity of the model is corrected, while leaving structure of the spectral features unaffected.

2.1.3 Interpolation of Model Stellar Atmospheres

The density of stellar atmosphere models in $T_{\rm eff} - \log(g)$ space is sparse in comparison to the density required for the fitting, so a bilinear interpolation is performed to sample between the available models. The four bounding models are found for the required $T_{\rm eff}$ and $\log(g)$ by first finding the closest $T_{\rm eff}$ in the nearest column of $\log(g)$. The neighbouring model which properly bounds $\log(g)$ is then found. The grid is then searched until the corresponding model is found at each $\log(g)$ which correctly bounds $T_{\rm eff}$. In the unlikely circumstances that the parameters cannot be bounded, such as at a grid boundary, the offending iteration is reset to the starting model and a flag is raised for that interpolation.

A bilinear interpolation produces the final I_λ from the four bounding models. This interpolation process must satisfy two constraints - it must accurately interpolate flux while maintaining the integrity of temperature-dependent spectral features. Thus intensity is logged throughout this process to make the steep changes in flux between models easier to interpolate. Each interpolation has the possibility of introducing small numerical errors in spectral features, so I first chose to perform the dual interpolation in $\log(g)$, where the differences between spectral features is small. The $T_{\rm eff}$ interpolation is then performed between these two spectra. Given the steep, linear or higher, dependence of stellar flux, the interpolation is performed in the $\log_{10}(T_{\rm eff})$ space; to make this interpolation linear and further reduce discrepancies.

2.1.4 Model Grid

The grid of synthetic photometry used in the fitting is produced by folding stellar atmospheres through photometric system responses. The choice of atmosphere grid is determined by the physics of the grid, such the abundance and metallicity required for the effect being investigated, as well as the spread of $T_{\rm eff}$ that is covered. The stellar atmosphere grids used in this thesis are summarised in Section 2.1.1. All atmospheres

that are utilised are provided in units of mean disk intensity at the stellar surface I_λ, meaning that the atmospheres are sampled in spherical mode at a variety of sightlines to produce model spectra. This means that the synthetic photometry correctly accounts for limb darkening—given the precision of the fits, ignoring this effect is noticeable.

Before producing synthetic photometry for the grid, the input stellar atmospheres are pre-processed. The grid of model stellar atmospheres is interpolated, as described in Section 2.1.3, to produce a theoretical prediction of I_λ for a star at the required $T_{\rm eff}$ and $\log(g)$. To improve performance, the interpolated synthetic spectra are binned into a coarser resolution using a flux conserving algorithm such that there are a minimum of $N = 50$ bins spanning the narrowest system response of the bands being used in the grid. From this the flux at the surface of the Earth can be determined using

$$F_\lambda = I_\lambda \frac{R^2}{d^2} 10^{-0.4 A_\lambda}, \tag{2.2}$$

where R is the stellar radius, d is its distance from the Earth and A_λ is the interstellar extinction along the sightline (e.g. Girardi et al. 2002). In the case where extinction is negligible, which is the case in nearby stars, this equation can be simplified to

$$F_\lambda = I_\lambda \frac{R^2}{d^2}. \tag{2.3}$$

To generate the synthetic photometry for each band, I folded the interpolated I_λ through the system responses to yield the mean apparent synthetic magnitude of a unit surface area of the model atmosphere at its surface within the $i^{\rm th}$ band Z_i with

$$\begin{aligned} m_{i,\rm syn} &= -2.5 \log_{10} \left[\frac{\int_\lambda F_\lambda S_{\lambda,i} d\lambda}{\int_\lambda f^\circ_{\lambda,i} S_{\lambda,i} d\lambda} \right] + m^\circ_i \\ &= -2.5 \log_{10} \left[\frac{\int_\lambda I_\lambda S_{\lambda,i} d\lambda}{\int_\lambda f^\circ_{\lambda,i} S_{\lambda,i} d\lambda} \right] - 5 \log_{10} \left[\frac{R}{d} \right] + m^\circ_i \\ &= Z_i - 5 \log_{10} \left[\frac{R}{d} \right], \end{aligned} \tag{2.4}$$

where $S_{\lambda,i}$, $f^\circ_{\lambda,i}$ and m°_i are the system response, zero point flux and zero point of the $i^{\rm th}$ band.

2.1.5 Free–Temperature Radius Fitting

For the fitting, I adapted the spectral energy distribution fit (SEDF) method (e.g. Pecaut & Mamajek 2013; Masana et al. 2006) with an addition to remove the dependence on *a priori* knowledge of the angular radius of the star θ (see Section 2.1.6). Essentially it uses the shape of the SED to measure the temperature.

The synthetic photometry $m_{i,\mathrm{syn}}$ is compared to the photometric data m_i using

$$\chi^2 = \sum_i^N \left(\frac{m_i - m_{i,\mathrm{syn}}}{\sigma_i} \right)^2 = \sum_i^N \left(\frac{m_i - Z_i + 5\log_{10}(R/d)}{\sigma_i} \right)^2, \tag{2.5}$$

where σ_i is the statistical uncertainty in the ith photometric band and i corresponds to one of the bands employed in the fitting process. The measured σ_i in a given band can be smaller than the systematic uncertainties inherent in the data; which can stem from uncertainties in the system responses and data analysis. Hence, throughout this thesis I have adopted a minimum floor value for σ_i that was used for fitting to remain clear of these systematics. The free parameters for the fit are R/d, T_{eff} and $\log(g)$, which was explored using a simple grid search to generate a 3D cube of χ^2. The minimum value of χ^2 within the grid determines the best fitting solution. I constrained the $\log(g)$ axis by applying a tophat prior of ± 0.5 dex around the prescribed model $\log(g)$, which was found by matching M_G of each star with the Baraffe et al. (2015) 4 Gyr isochrone.

The grids were first transformed into probability space, using $P(T_{\mathrm{SED}}, \log(g), R/d) = \exp(-\chi^2/2)$, and normalised. The 2D χ^2 space necessary for producing confidence contours was then calculated by marginalising the 3D cube over $\log(g)$. R/d is next converted to R using the geometric distances of Bailer-Jones et al. (2018), and uncertainty in distance is allowed for by convolving each row of constant T_{eff} in the 2D χ^2 space with a Gaussian whose standard deviation is the mean uncertainty from the lower and upper distance bounds; as these are nearly symmetrical. The confidence contours can be determined from the resulting 2D PDF by identifying the set of highest probability pixels whose integral is 0.68 and drawing a contour around them. Uncertainties in T_{SED} and R can be obtained from a 1D distribution of probability by marginalising along the remaining axis. To illustrate the correlation between R and T_{eff}, I include an example plot of the χ^2 space

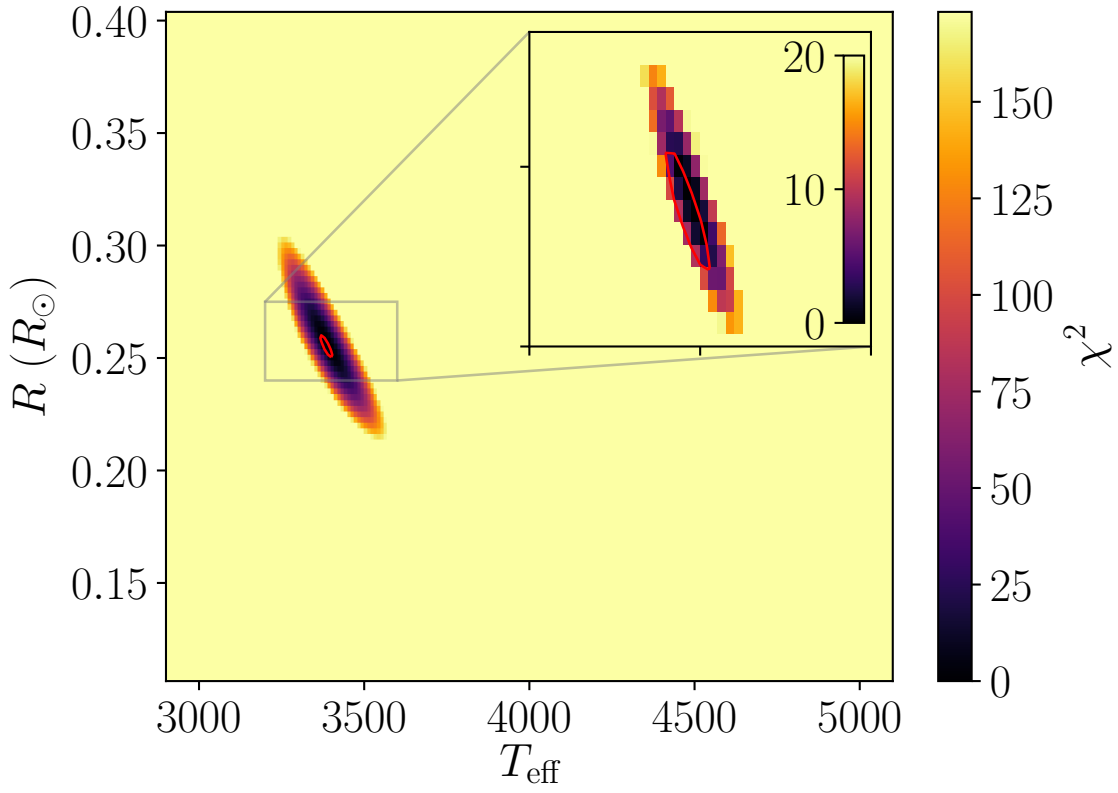

Figure 2.2: The search space for one of the targets from Chapter 4 whose χ^2 lies at the median value of the randomly selected uncertainty sample. The red ellipsoid indicates the 68% confidence contour resulting from the process. The inset at the upper right shows the zoomed-in detail around this contour.

resulting from a fit to one of the targets from Chapter 4 in Figure 2.2.

2.1.6 Analytical Determination of Stellar Radii

Performing a full 3D grid search on our entire input catalogue is intractable due to computational time constraints. So for a particular $T_{\rm eff}$ and $\log(g)$ the best fitting R is determined by analytically minimising χ^2, effectively making the search space 2D. I accomplished this by differentiating Equation 2.5 with respect to the $5\log_{10}(R/d)$ term and finding the stationary point of the derivative to analytically minimise χ^2, yielding

$$\log_{10}\left(\frac{R^2}{d^2}\right) = \log_{10}\left(\theta^2\right) = -0.4\left(\sum_i^N \frac{Z_i - m_i}{\sigma_i^2}\right) \Big/ \left(\sum_i^N \frac{1}{\sigma_i^2}\right). \tag{2.6}$$

This provides the dilution factor R^2/d^2 and hence, by applying the distances from Bailer-Jones et al. (2018), the stellar radius R. For each $\log(g)$ and $T_{\rm eff}$ I analytically minimised χ^2 to find the radius in this way. This results in a 2D $\log(g) - T_{\rm eff}$ space. An example of

the resulting χ^2 space is shown in Figure 2.2, and example fits shown in Figure 2.3.

2.1.7 Including Extinction

In cases where extinction cannot be neglected, such as for exoplanet host determinations in Chapter 5, the magnitude of a unit surface area at the stellar surface Z_i can be substituted with

$$Z_i = -2.5 \log_{10} \left[\frac{\int_\lambda I_\lambda S_{\lambda,i} 10^{-0.4 A_\lambda} d\lambda}{\int_\lambda f^\circ_\lambda S_{\lambda,i} d\lambda} \right] + m^\circ_i, \tag{2.7}$$

which is generalised to include extinction A_λ. A_λ is provided by an extinction law, which prescribes the extinction that should be applied to the model atmosphere at a given λ. For this thesis I adopt the extinction law of Fitzpatrick (1999), which provides an estimate of the shape of the UV-through-IR extinction law for a value of $R = A(V)/E(B-V) = 3.1$; the mean value of R for the Milky Way. This extinction law provides $A_\lambda/E(B-V)$, thus the output must be multiplied by a value of $E(B-V)$ before being applied to the stellar models. Due to the weight of flux across the system responses, the measured $E(B-V)$ varies with the colour of the star. Hence, nominal $E(B-V)$ is adopted to represent just the intervening material between the observer and the star (Bell et al. 2013). In this thesis, $E(B-V)$ refers to nominal $E(B-V)$.

2.1.8 Constraining to an Isochrone

To perform comparisons to isochrones, I constrained some of the fitting that was performed to a given isochrone. As the underlying interiors dictate the radius, this need not be determined by the fitting routine. In addition, as the distance to the cluster is known *a priori*, $m_{\mathrm{i,syn}}$ can be computed analytically during the creation of the grid using

$$m_{i,\mathrm{syn}} = -2.5 \log_{10} \left[\frac{\int_\lambda I_\lambda S_{\lambda,i} 10^{-0.4 A_\lambda} d\lambda}{\int_\lambda f^\circ_{\lambda,i} S_{\lambda,i} d\lambda} \frac{L_{\mathrm{bol,iso}}}{4\pi d^2 \sigma T^4_{\mathrm{eff,iso}}} \right] + m^\circ_i, \tag{2.8}$$

where $L_{\mathrm{bol,iso}}$ and $T_{\mathrm{eff,iso}}$ are the stellar luminosity and effective temperature prescribed by a given isochrone point. Thus, to constrain the fitting to the grid, I followed the same methodology as in Section 2.1, with several important distinctions. Instead of iterating over a 2D $T_{\mathrm{eff}} - \log(g)$ search space, I simply iterate over the parameters prescribed by the isochrone, reducing the fitting to a 1D problem. As opposed to determining an analytical

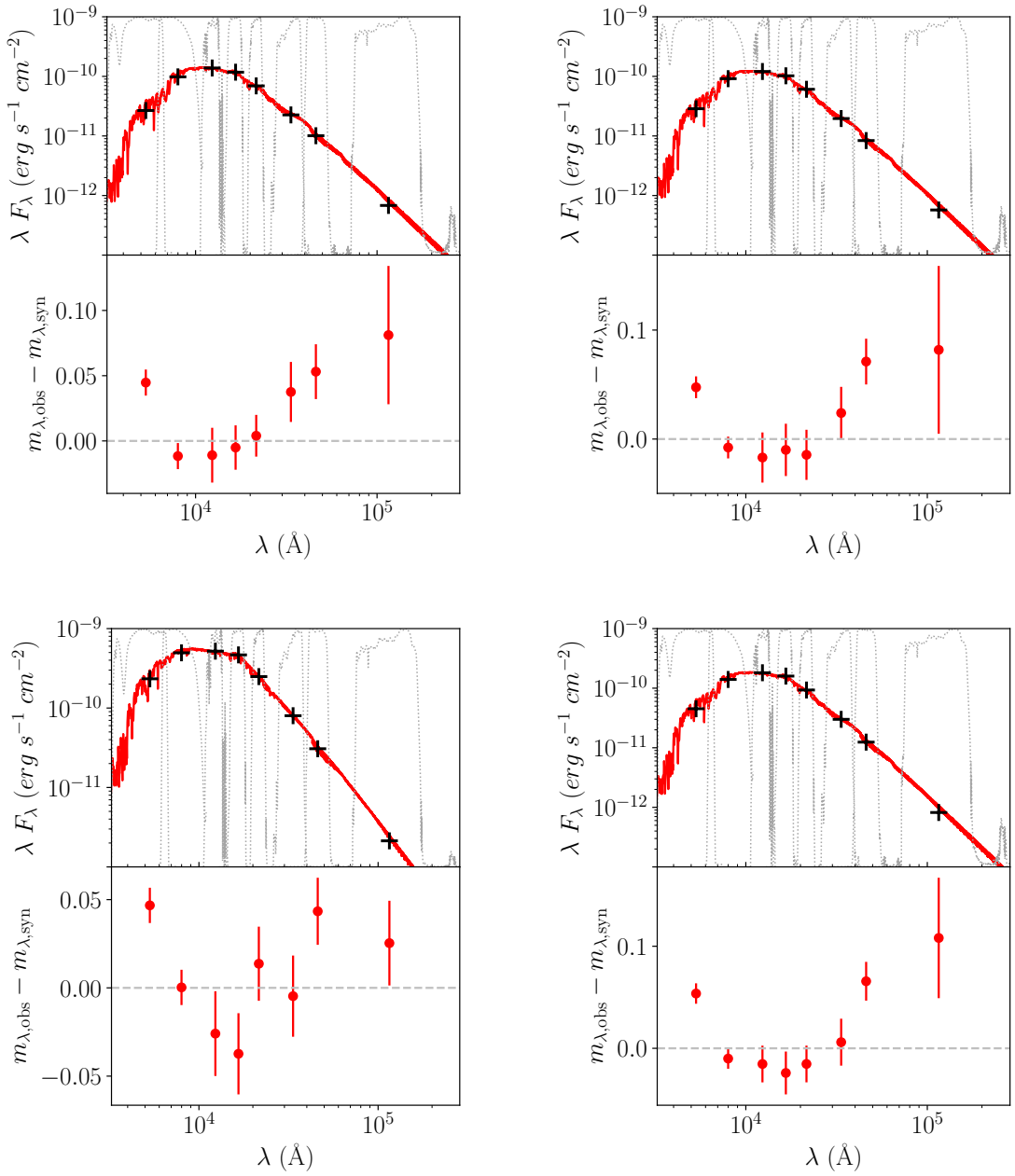

Figure 2.3: Fits from Chapter 4 resulting from the use of the method presented in Section 2.1.5 and Section 2.1.6. The best fitting model spectrum for each target is shown in the top panel (red) with the observed photometry from which it was derived overlaid (black). The appropriate bandpasses are plotted in light grey for reference. In the bottom panel are the residuals and uncertainties in magnitudes for each photometric band. The top panels correspond to the median χ^2 (left) and just above the median (right) of our randomly selected uncertainty sample, while the bottom left and right panels show the stars at the lower and upper 68% density bounds respectively.

minimisation, or via a 3D grid search, the stellar radius can be trivially computed from the parameters provided by the isochrone using

$$R = \sqrt{\frac{L_{\mathrm{bol,iso}}}{4\pi\sigma T_{\mathrm{eff,iso}}^4}}. \tag{2.9}$$

Chapter 3

Characterising Discrepancies in Models of Pre-Main Sequence M-dwarfs

"The most elementary and valuable statement in science, the beginning of wisdom is: I do not know."

— Data

3.1 Motivation

Young open clusters and eclipsing binaries have thus far provided our greatest insights into stellar evolution. In particular, clusters provide an unparalleled opportunity to simultaneously study a complete population of hundreds to thousands of coeval single stars in the wild. However, as discussed in Section 1.5, this powerful tool comes with caveats. The age of any given cluster can be determined by fitting the stellar sequence to an isochrone — a line of constant stellar age that spans the mass range of members. To perform this fitting, one has to address the philosophical question of whether to work in the theoretical $T_{\rm eff} - -L$ plane, or the observational colour-magnitude plane. Both methods bring along with them inherent trade offs.

Pre-MS stars are axiomatically still quasi–statically contracting, thus their measure-

ments of $\log(g)$ will be inherently lower than their MS counterparts for a given mass. The stellar flux can also suffer considerable contamination across the SED, including UV emission from accretion shocks in the photosphere, signs of youth in X-ray, and circumstellar discs throughout the near and mid IR. These caveats make transforming observations into the theoretical plane undesirable at best, and untenable at worst.

Alternatively, theoretical stellar evolution models can be transformed into the observational colour–magnitude plane through the use of bolometric corrections. This method is preferable because fewer assumptions are required about the nature of the stellar sample. However, this does come with its own slew of complications. Bolometric corrections, and the resulting colours, are far removed from the model parameters from which they are derived, making it difficult to pinpoint problems with said models.

As noted in Bell et al. (2012), the observed colours and magnitudes of the low-mass population of the Pleiades are inconsistent with those provided by theoretical isochrones. To remedy these inconsistencies, Bell et al. (2012, 2013) and Bell et al. (2014) assembled a selection of well understood fiducial clusters to act as benchmarks in the production of a consistent set of semi-empirical isochrones with which to perform fitting. Examples of these semi-empirical isochrones for the Pleiades and Praesepe clusters are plotted with observed members in Figure 3.5. You will note that the semi-empirical isochrone (Bell et al. 2012) traces the sequence laid out by the observations of cluster members, whereas the purely theoretical isochrone diverges from this sequence for a large portion of the lower-MS and pre-MS.

Although this methodology does provide a panacea to the issues facing theoretical isochrones, it is a somewhat inelegant solution which does not address the missing physics underpinning models of pre-MS M-dwarfs. A spline fit to an observed sequence in colour–magnitude space does not glean any physical insight into the clusters themselves. Instead of simply iterating on this semi-empirical method, this chapter proposes understanding the physical implications behind the discrepancy; and consequentially why cutting edge stellar evolution models are unable to correctly reproduce the isochrones of well understood populations.

In this chapter, I will explore the fundamental parameters of the Pleiades and Praesepe open clusters through photometric observations from surveys. I will apply the method for SED fitting, introduced and detailed in Section 1.10 and Chapter 2, to multi-waveband photometry, which spans the entire SED of each cluster member. From this fitting the $T_{\rm SED}$, L, and R can be inferred—allowing the measured stellar parameters to be uncoupled from the problematic model interiors. These parameters will then be compared to isochrones to determine the degree of radius inflation, and to permit insight into missing physics.

Although this method does not rely on stellar interiors, it does utilise synthetic photometry from stellar atmospheres. To assess their veracity, I will compare to observed low-dispersion spectra for a number of carefully selected stars within each cluster to synthetic spectra generated from the properties determined by the SED fitting. By imposing a flux calibration upon these spectra, they serve a two-fold purpose in this investigation. The direct comparison between observations and models derived from orthogonal methods serves as a powerful consistency check for both. Agreement between them would provide a strong indication that the SED fitting methodology is reliable, the input physics to stellar models is accurate, and the flux calibration is robust. Once the reliability of the observed spectra is established, their spectral features can be carefully compared to those of the synthetic spectra to assess the physical accuracy of stellar atmospheres. First, I will perform a review of the clusters upon which the work in this chapter is being performed.

3.1.1 The Pleiades

The Pleiades is one of the key clusters utilised in critical analyses of stellar evolution models and adopted as a fiducial cluster for benchmarking in Bell et al. (2012, 2013) and Bell et al. (2014). This is owing to several very important properties. The Pleiades has an age of 135^{+20}_{-11} Myr (Bell et al. 2014), meaning that the low-mass members are still undergoing Pre-MS evolution, while there is still a well populated main-sequence, by virtue of the intermediate mass members (Soderblom et al. 2014). This is crucial as it means that the members in the upper-MS can be fitted with the model isochrones to determine the age of and distance to the cluster. Once cluster properties are well

constrained, the lower-MS and pre-MS members of the cluster can be plied to critically examining discrepant models. The age was well determined in Barrado y Navascués et al. (2004) to be 130 ± 20 Myr, using the semi-fundamental lithium depletion boundary method. It is subject to a modest extinction of $E(B-V) = 0.04$, based on an $A_V = 0.12$ from Stauffer et al. (1998), and is solar metallicity; a requirement imposed by the stellar interior models which are largely supplied with solar metallicity ([Fe/H] = 0). Until recently the distance of the Pleiades has remained controversial, as distances determined using the Hipparcos catalogue (Perryman et al. 1997; van Leeuwen 2007) remain inconsistent with methods determined by any other method. This is demonstrated in Figure 3.1, which shows how the distances determined using a variety of different methods is markedly different from that provided by Hipparcos. However, Gaia DR2 has now more or less confirmed that the Hipparcos measure is an underestimate, likely due to systematics (Gaia Collaboration et al. 2018a). Bell et al. (2014), which pre-dates this measurement, as well as the VLBI measurement of Melis et al. (2014), adopts the Soderblom et al. (2005) trigonometric parallax measurement of 132 ± 2 pc. I also adopt this distance to the Pleiades to retain agreement with stellar models, while remaining consistent with the distance estimate from Gaia DR2 (136 ± 4 pc, Gaia Collaboration et al. 2018a; Abramson 2018). Finally, robust memberships were derived in Stauffer et al. (2007) and Lodieu et al. (2012), eliminating potential contamination due to field stars erroneously being included in the fitting.

3.1.2 Praesepe

Praesepe is the second cluster that was chosen as a fiducial cluster for benchmarking in Bell et al. (2012, 2013) and Bell et al. (2014), as well as an additional cluster adopted for this investigation. This cluster is as well characterised as the Pleiades, with robust ages, metallicity and memberships (Kraus & Hillenbrand 2007) being readily available. Praesepe was measured to be at a distance of 184 ± 2 pc by Bell et al. (2014), a measurement which I adopt to remain consistent with them and the 186 ± 1 pc measured by Gaia DR2 (Gaia Collaboration et al. 2018a). Despite being a longer distance away from Earth than the Pleiades, observations still suffer smaller amounts of extinction. Taylor (2006a) found $E(B-V) = 0.027$ for Praesepe using a combination of polarisation measurements,

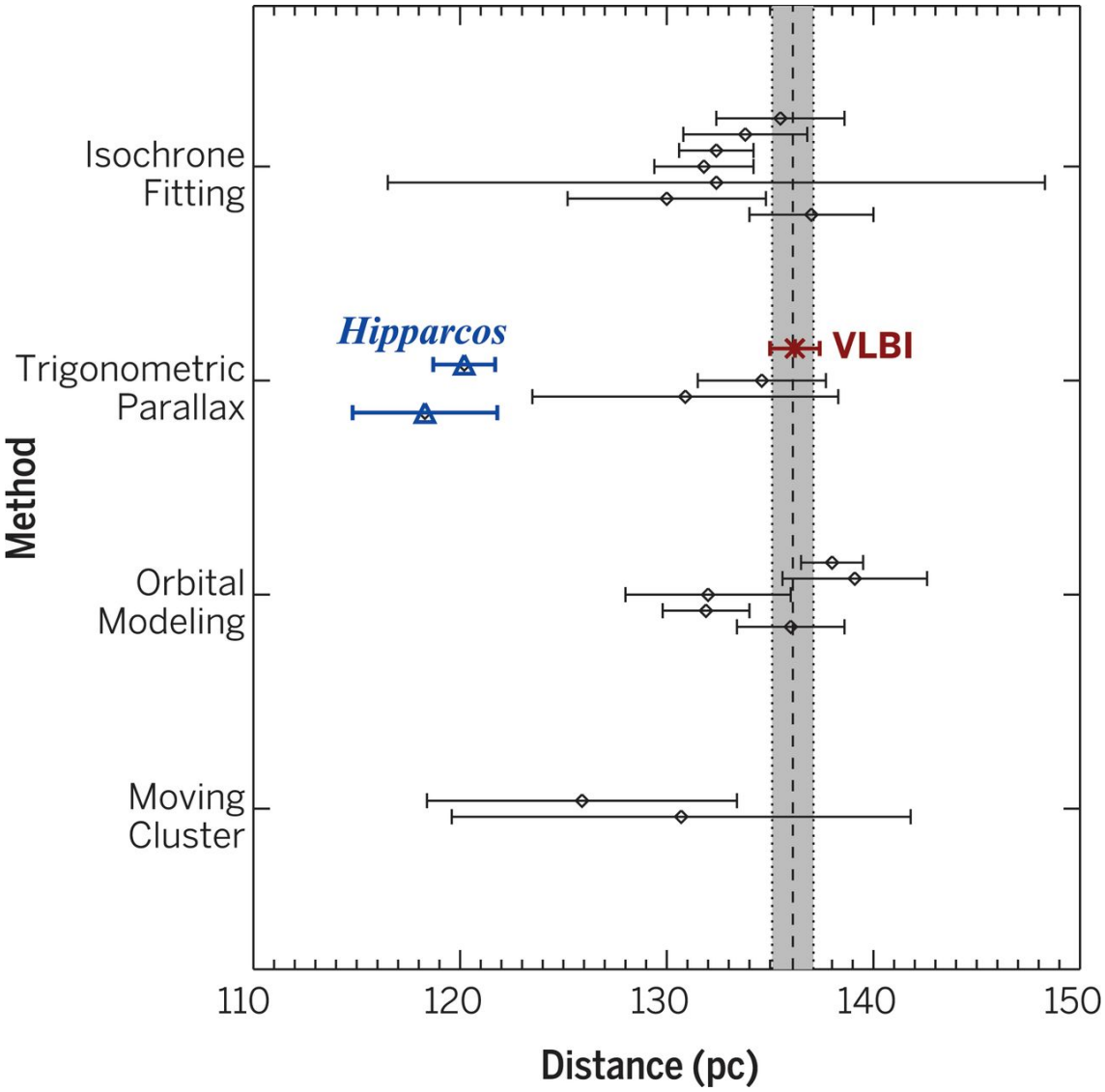

Figure 3.1: A summary of some of the distance measurements obtained through a variety of methods. Of particular note is the Hipparcos distances of 120.2 pc; markedly lower than the 132 ± 2 pc presented in Soderblom et al. (2005), and adopted in Bell et al. (2014). The distances determined using isochrone fitting (An et al. 2007; Percival et al. 2005; Stello & Nissen 2001; Pinsonneault et al. 1998; Giannuzzi 1995; van Leeuwen 1983; Nicolet 1981), non-Hipparcos or VLBI trigonometric parallax (Soderblom et al. 2005; Gatewood et al. 2000), modelling the orbits of eclipsing binaries (Groenewegen et al. 2007; Southworth et al. 2005; Zwahlen et al. 2004; Munari et al. 2004; Pan et al. 2004) and based purely on radial velocities and proper motions (Röser & Schilbach 2013; Narayanan & Gould 1999). The distance presented in the source paper, shown in red, is determined using trigonometric parallax using radio interferometry, is consistent with the other measurements; alleviating the concern over the inconsistent Hipparcos distance.
Source: Melis et al. (2014)

comparison of Strömgren β and $R - I_C$ for F stars, and Strömgren β analysis of A stars. However, unlike the Pleiades which is to within uncertainties solar metallicity, the literature values measure [Fe/H] = 0.07–0.09 for Praesepe; from An et al. (2007) and Boesgaard et al. (2013) respectively. This led Bell et al. (2014) to adopt the mean value of [Fe/H] = 0.08 for Praesepe; making the metallicity of the cluster supersolar. Crucially, the age of $\tau = 665^{+14}_{-7}$ Myr for Praesepe determined by Bell et al. (2014) is considerably older than that of the Pleiades. The overall consistency between both target clusters lends itself to a differential study of the two. The span between cluster age and metallicity permits us to ascertain how the discrepancy varies with composition, and more importantly if it varies as a function of evolution.

3.2 Photometric Fitting

The SED fitting I performed in this chapter was the first application of the SED fitting method detailed in Section 2.1. Thus, as stated in Section 3.1, the fitting process herein is acting as a validation for the method itself, as well as providing measurements of stellar parameters. Due to the relatively crowded fields presented by open clusters, the bands and selection criteria, presented in Table 3.1, were carefully chosen to provide accurate probes of the SED. The floor value of σ_i was also motivated by this consideration; chosen to be 0.05 for this fitting. This was also motivated by the caution inherent in the application of an untested methodology.

3.2.1 Free Temperature Radius Fitting

One of the problems facing our understanding of the discrepancy in M-dwarf stars is the coupling between the stellar interiors and the photospheres. Allowing the temperature and radius to run free for the fitting, instead of being constrained to the isochrone, permits a comparative study between observed and synthetic spectra in isolation. The angular diameter for each case was analytically determined for every star using the method detailed in Section 2.1.6. The determined distance to each cluster was used to determine the radius. The stellar parameters determined from this fitting process were then used as inputs to produce the synthetic spectra to compare to observations in Figure 3.17 and

Figure 3.18.

3.2.2 Isochronal Model Fitting

A further fitting of each of the stars in the sample was performed by substituting the 2D grid evenly spaced in $T_{\rm eff}$ and $\log(g)$ with a grid generated from an isochrone; described in Section 2.1.8. This effectively limits the allowable SEDs to those dictated by the stellar interior models at the age of the cluster. By comparing the best fits and residuals of the fits from both the free temperature radius fit case, and the isochrone constrained case, we can glean powerful insight into the source of the discrepancy. Hence, the synthetic spectra that best match the parameters determined from the isochrone fitting are compared to observations in Figure 3.19 and Figure 3.20.

Band	λ_{iso} (Å)	System	Selection Criteria	Source
g_{WFC}	4878	INT-WFC	g / r / i_FLAG = "OO"	Rees (2017)
r_{WFC}	6222		g / r / i_UNCERT < 0.1	
i_{WFC}	7675			
Z_{UKIDSS}	8817	UKIDSS	pstar > 0.99	Lawrence et al. (2007)
Y_{UKIDSS}	10305		j/h/k_1/x/ypperrbits < 256	
J_{UKIDSS}	12483			
H_{UKIDSS}	16313			
$K_{s,UKIDSS}$	22010			
J_{2MASS}	12410	2MASS	cc_flags = "000"	Skrutskie et al. (2006)
H_{2MASS}	16513		ph_qual = A or B	
$K_{s,2MASS}$	21656			
I_1	35573	Spitzer IRAC	i1/i2/i3/i4_fluxflag = 0	Spitzer Enhanced Imaging Products (SEIP)$^{\alpha}$
I_2	45049		i1/i2/i3/i4_softsatflag = 0	
I_3	57386		i1/i2/i3/i4_seflags = 0	
I_4	79274			
W_1	33792	WISE	ext_flg = 0	Wright et al. (2010)
W_2	46293		cc_flags = "000"	
W_3	123338		ph_qual = A or B	

Table 3.1: The sources of the photometric data used for the SED fitting. To aid in comparison to plots, each filter is listed with its isophotal effective wavelength λ_{iso}, criteria used to select the photometry and original source. The bands are grouped into photometric systems and in order of ascending λ_{iso}. The λ_{iso} is determined by integrating $f_\lambda = 1$ across the filter, unless directly quoted in the source paper. W_4 is missing from this table, as none of the W_4 photometry was uncontaminated, thus we only select and match the other bands.
α: https://irsa.ipac.caltech.edu/data/SPITZER/Enhanced/SEIP/docs/seip_explanatory_supplement_v3.pdf

3.2.3 The Pleiades and Praesepe Temperature - Radius Relation

When producing theoretical isochrones, stellar interiors are tasked with providing the underlying luminosity–temperature–radius relationships used to sample bolometric corrections. The SED fitting code is able to directly measure these quantities, the results of which can be overlaid on the tracks of the interiors as a test of their accuracy. The inflation in radius from the Baraffe et al. (2015) isochrones of the stars run through the fitting process (see Section 3.2) are shown as a function of $T_{\rm SED}$ in Figure 3.2. This figure shows that the both the Pleiades and Praesepe single star sequences are inflated above those predicted by stellar interiors. I wished to assess the nature of this inflation, so I plotted the stars from each cluster in the $T_{\rm SED} - R$ plane alongside a series of isochrones decreasing in age from the current age of each cluster; shown in Figure 3.3. This figure implies that were I trying to determine the age of both clusters using low-mass members alone, I would likely place them to be $20 - 50$ Myr—considerably younger than both clusters. Furthermore, the age I would measure would be subject to extreme selection bias, as the cluster would appear older as I traverse further down the stellar sequence.

3.2.4 Comparison to $R \sin i$ Measurements

Lanzafame et al. (2017) used radius determinations of Pleiades members, measured using the $R \sin i$ technique, to show that low-mass members of the cluster were indeed inflated above the isochrone. This sample was split into fast rotators (with $P_{\rm rot} < 2$ d), slow rotators defined in Lanzafame & Spada (2015) and stars transitioning onto the slow rotator sequence, termed gap rotators. They showed that gap rotators with $0.8\,M_{\odot} \geq M \geq 0.6\,M_{\odot}$ were inflated above the Baraffe et al. (2015) isochrones, unlike the fast rotators which remained in good agreement with the theoretical models. Were this corroborated, it would provide a crucial insight into the physics underlying the discrepancy. So, I took the sample of stars presented in Lanzafame et al. (2018) and performed the same fitting process as detailed in Section 3.2.1. The results of this fitting are shown in the $T_{\rm SED} - R$ plane in Figure 3.4. Lanzafame et al. (2017) demonstrated that it was the stars who were converging onto the slow-rotator sequence that exhibited radius inflation. As shown in Figure 3.4, I found that the stellar sequences for all three samples remain remarkably consistent, with the fast rotator sample also appearing to be inflated. That the mean

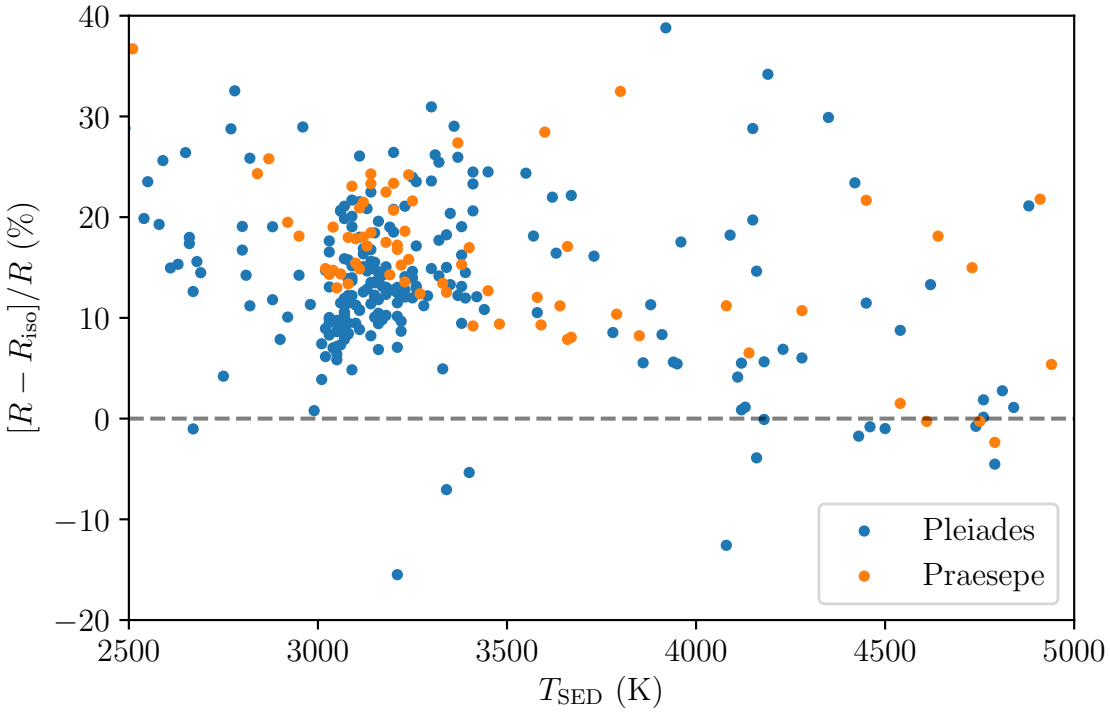

Figure 3.2: The inflation of Pleiades (blue) and Praesepe (orange) members from the isochrone appropriate for the age, metallicity, extinction and distance of the cluster, generated from the Baraffe et al. (2015) interiors. To aid legibility of the plot, a small number of stars have been omitted from the plot, most of which are on the high inflation wing, and thus are suspected binaries. This plot shows that the radius measured at a given luminosity for both clusters is incorrect by about 20% in the M-dwarf regime; with the older Praesepe exhibiting a few per cent more inflation than the Pleiades.

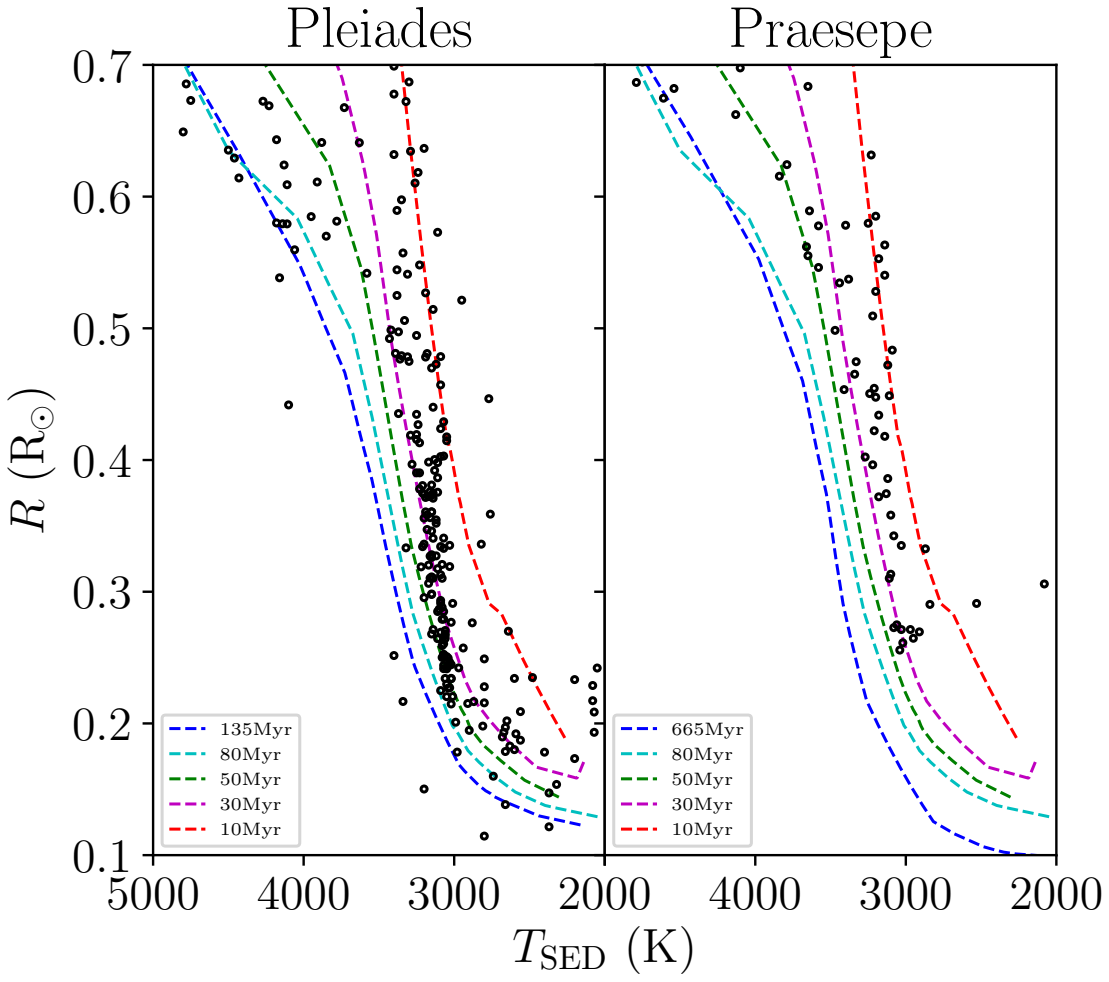

Figure 3.3: The relationship between R and $T_{\rm SED}$ resulting from the fitting in Section 3.2. Also plotted are the theoretical isochrones resulting from the interiors of Baraffe et al. (2015), with additional isochrones for previous ages of each cluster. The data not only prove a poor match for the canonical isochrone for the cluster, but none of the theoretical isochrones at any age are able to reproduce the observed sequence.

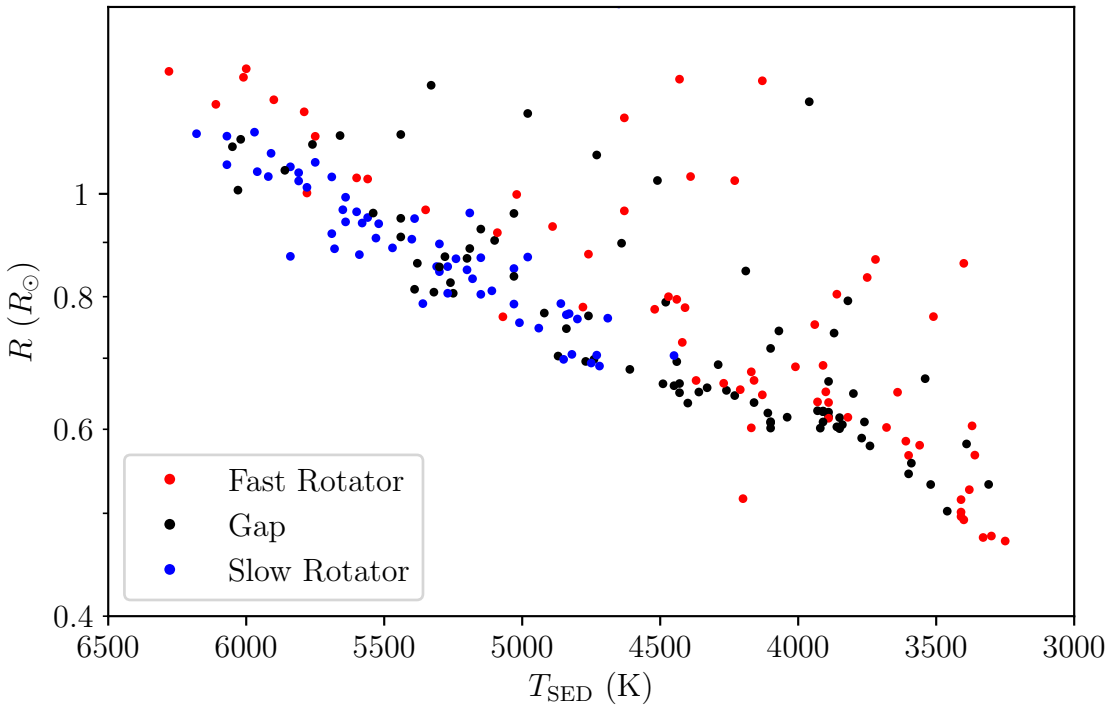

Figure 3.4: The measurements of R and $T_{\rm SED}$ resulting from SED fitting for the sample of Pleiades members in Lanzafame et al. (2017). The stars are colour-coded by the rotation rate samples which contain them. The blue and red points denote slow and fast rotators respectively, with the gap rotators being shown in black.

radius measurements from the $R \sin i$ technique does not also show this could indicate some systematic error in the technique at fast rotation rates. Moreover, the fast rotators appear to be slightly more inflated than those with longer rotation periods, indicating magnetism may be responsible for this inflation.

The implication of the fitting performed in this section is that the measured radius and temperature of cluster members is inconsistent with those predicted by theoretical isochrones. A crucial test of this hypothesis, and the SED fitting methodology itself, lies with spectroscopy. Along with the shape of the spectrum, spectroscopic data provides an abundance of temperature sensitive spectral features with which to thoroughly compare both the measured and theoretically predicted temperatures. To perform a direct comparison, spectroscopic observations of a number of pre-MS M-dwarfs were performed and subjected to the rigorous reduction process detailed in the Section 3.3.

3.3 Spectroscopic Data Reduction

3.3.1 Target Selection

I selected the observation targets by plotting the theoretical and semi-empirical isochrone amongst the members of each cluster in CMDs, shown in Figure 3.5. In the observational plane, the discrepant region in $T_{\rm eff}$ is evident as the theoretical isochrone for a given cluster diverges from the observed sequence. The observing target selection strategy I adopted for this work aims to sample stars which lie above the divergence, to be used as a control sample, stars straddling the transition, to probe changes in physics across the boundary between discrepant and non-discrepant $T_{\rm eff}$, and finally a sample in the discrepant region. The non-discrepant control sample serve double duty, in so much as they can provide corroboration to the flux calibration by providing a comparison to models resulting from the isochrone. The targets chosen for observation, along with the isochrones that were employed in their selection, are shown in Figure 3.5. The final spectroscopic targets from each cluster are tabulated in Table 3.2 and Table 3.3 with initial estimates of their stellar parameters.

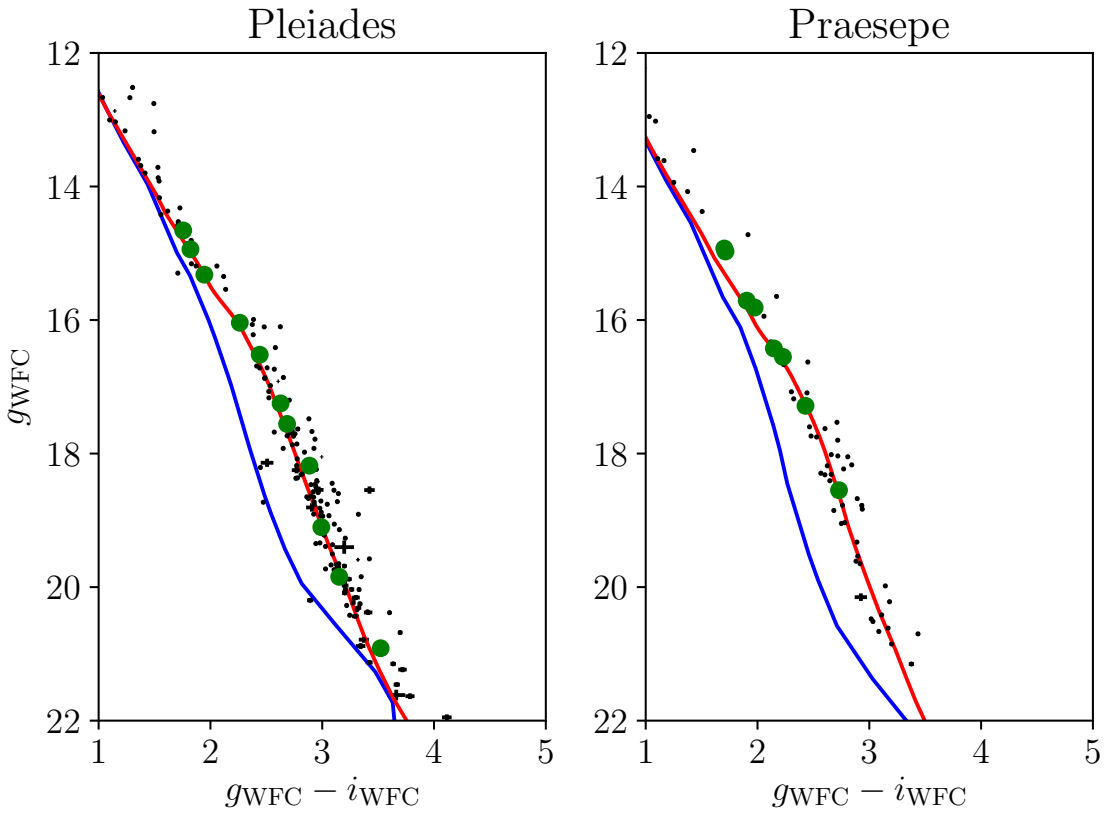

Figure 3.5: The target selection for both clusters in the colour-magnitude plane. The lines through the plot are the appropriate isochrone for each cluster, generated from the Baraffe et al. (2015) stellar interiors and the BT-Settl CIFIST stellar atmospheres. They have had the correct extinction and the distance modulus applied to them. The blue and red lines are the theoretical and semi-empirical isochrones respectively. The black points are photometry of known cluster members, from Rees (2017), including uncertainties. The green points denote a target upon which spectroscopy was undertaken for this work. Note that care has been taken to sample the affected parameter space as thoroughly as possible, given the constraints of the instruments.

Target Name	RA (J2000)	Dec (J2000)	$T_{\rm eff}$ (K)	Mass $(M_\odot)$	$\log(g)$	$\log\,(L_{\rm bol}/L_\odot)$	Source
Melotte 22 DH 293	03:43:48.61	+23:32:21.0	4165.63 ± 14.4	0.6403 ± 0.0038	4.7099 ± 0.0019	−1.0422 ± 0.0106	2MASS
Melotte 22 SK 378	03:48:10.99	+23:30:24.0	4084.8 ± 11.84	0.6184 ± 0.0033	4.7208 ± 0.0016	−1.1025 ± 0.009	2MASS
Melotte 22 SK 709	03:41:58.69	+23:42:26.0	3967.78 ± 0.48	0.5846 ± 0.0001	4.7385 ± 0.0001	−1.1955 ± 0.0004	UKIDSS
V392 Tau	03:52:20.65	+24:33:55.0	3817.49 ± 0.42	0.5355 ± 0.0001	4.7671 ± 0.0001	−1.3304 ± 0.0004	UKIDSS
LM Tau	03:42:10.93	+24:05:08.0	3820.03 ± 10.15	0.5364 ± 0.0036	4.7666 ± 0.0022	−1.328 ± 0.0098	2MASS
Melotte 22 DH 345	03:44:31.73	+23:35:25.0	3486.65 ± 0.2	0.3656 ± 0.0001	4.891 ± 0.0001	−1.774 ± 0.0004	UKIDSS
V442 Tau	03:45:12.15	+23:21:52.0	3461.27 ± 0.18	0.3458 ± 0.0001	4.9003 ± 0.0001	−1.8208 ± 0.0003	UKIDSS
V734 Tau	03:41:19.35	+23:51:41.0	3346.06 ± 0.42	0.2525 ± 0.0003	4.9345 ± 0.0001	−2.0537 ± 0.0008	UKIDSS
Melotte 22 STAR 42	03:44:59.48	+23:21:18.0	3211.54 ± 0.78	0.1765 ± 0.0003	4.9598 ± 0.0001	−2.3074 ± 0.0013	UKIDSS
Melotte 22 HHJ 16	03:47:29.92	+23:33:14.0	3090.86 ± 0.97	0.1353 ± 0.0003	4.9702 ± 0.0001	−2.5064 ± 0.0016	UKIDSS
Melotte 22 PPL 2	03:45:09.46	+23:58:44.0	2901.65 ± 2.05	0.0891 ± 0.0003	4.9695 ± 0.0001	−2.785 ± 0.0025	UKIDSS

Table 3.2: This table contains the Pleiades target list. Each target is listed along with its coordinate, as well as derived stellar properties. These properties were derived by performing a 1D match with absolute K_s band magnitude derived from the the UKIDSS GCS catalogue, or 2MASS where the photometry for the UKIDSS source was flagged as bad, against an appropriate isochrone with the corresponding K_s. The interpolated values of $T_{\rm eff}$, $\log(g)$ and M from which the matched isochrone locus was derived are then adopted as the properties of that target star.

Target Name	RA (J2000)	Dec (J2000)	$T_{\rm eff}$ (K)	Mass $(M_\odot)$	$\log(g)$	$\log(L_{\rm bol}/L_\odot)$	Source
NGC 2632 JC 180	08:40:00.67	+19:18:34.0	4420.65 ± 20.87	0.7078 ± 0.0046	4.6662 ± 0.0023	−0.8467 ± 0.013	2MASS
EO Cnc	08:39:03.17	+20:02:37.0	4321.4 ± 0.63	0.685 ± 0.0001	4.6775 ± 0.0001	−0.9119 ± 0.0004	UKIDSS
NGC 2632 JC 167	08:39:37.12	+19:48:57.0	4042.62 ± 0.61	0.6181 ± 0.0001	4.711 ± 0.0001	−1.1123 ± 0.0005	UKIDSS
NGC 2632 JC 165	08:39:36.41	+19:29:07.0	4031.69 ± 0.61	0.6154 ± 0.0001	4.7123 ± 0.0001	−1.1206 ± 0.0005	UKIDSS
2MASS J08391453+2001191	08:39:14.48	+20:01:19.0	3853.81 ± 0.45	0.5651 ± 0.0001	4.7469 ± 0.0001	−1.2711 ± 0.0004	UKIDSS
NGC 2632 JC 250	08:41:20.40	+19:37:22.0	3841.1 ± 0.45	0.561 ± 0.0001	4.7504 ± 0.0001	−1.2832 ± 0.0004	UKIDSS
2MASS J08402657+2015132	08:40:26.52	+20:15:13.0	3672.37 ± 8.7	0.4961 ± 0.004	4.8134 ± 0.0036	−1.4693 ± 0.0109	2MASS
NGC 2632 HSHJ 284	08:39:42.53	+19:18:28.0	3531.27 ± 4.88	0.4094 ± 0.0046	4.8896 ± 0.004	−1.6956 ± 0.0114	2MASS

Table 3.3: This table contains the Praesepe target list. Each target is listed along with its coordinate, as well as derived stellar properties. These properties were derived in same way as Table 3.2, by my matching absolute K_s against a stellar model with the same K_s.

I initially derived parameter estimates by naively matching the observed K_s band magnitude to the closest model on the appropriate isochrone. This method is effective due to the strong correlation between mass and K_s-band luminosity at low masses, as shown in Figure 3.6. However these parameters are far from a robust means of stellar characterisation; as the entire knowledge of the star is none-the-less being drawn from a single data point. Although, as demonstrated in Section 1.6.1, the differences between the model and observed colours are negligible in the K_s-band, we are also none-the-less drawing our estimations from interiors with known issues. In addition, as you will note from Table 3.2 and Table 3.3, drawing physically meaningful estimates of precision and uncertainty for derived parameters is somewhat problematic. The uncertainties presented in tables are driven solely by the K_s-band photometric uncertainty, and do not account for any systematic uncertainties inherent in the parameter estimation. It was the desire for reliable and well conditioned stellar parameter estimations that initially drove attention towards the spectral energy distribution fitting method used pervasively throughout the remainder of this thesis.

3.3.2 Observing Methodology and Spectroscopic Data Reduction

These sections are combined because the requirements of the subsequent data processing is stringent enough as to largely dictate observing methodology; thus it would be counter-productive to discuss each in isolation. The data for this investigation were collected at the William Herschel Telescope (WHT) on the nights of the 19th and 20th December 2015. The low-resolution, broad coverage spectroscopy and photometry were collected using the the Auxiliary Camera (ACAM; Benn et al. 2008) mounted at the folded Cassegrain focus of the WHT. The data reduction pipeline used for this spectroscopic data reduction consists of shell scripts, and Fortran and Python software written by me. The format for the data during this reduction is the native format of the ARK software package, also written in Fortran. Due to this compatibility, and its maturity, I adopted some of the ARK software and libraries where appropriate to reduce development time.

To effectively compare to the models, an observing methodology was devised to accurately reproduce the spectral flux density of the observed targets while maintaining

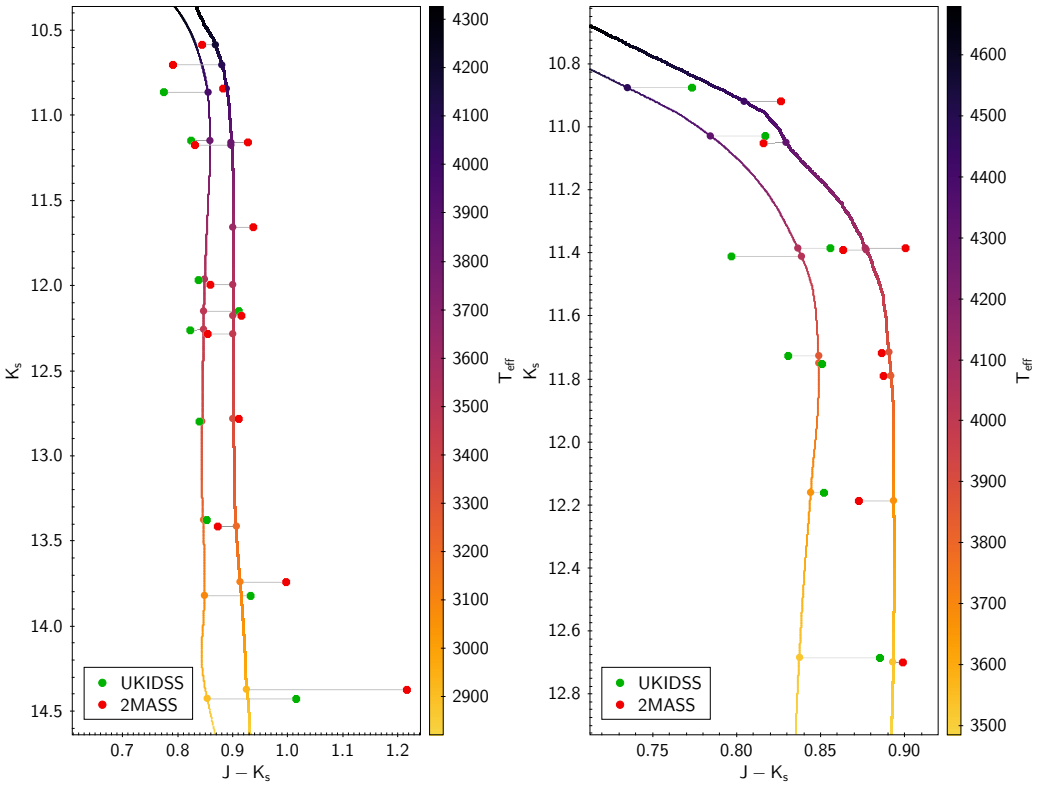

(a) Pleiades **(b)** Praesepe

Figure 3.6: The parameter matching performed on the J vs. J - K_s isochrones.

the integrity of spectral features. The entire reduction process that I devised to accomplish this is shown schematically in a reduction cascade in Figure 3.7. All of the spectroscopic observations were performed using both a 2 ″ and 10 ″ slit, which henceforth I will term narrow slit and wide slit respectively. Although the stars are point sources on the sky, both the atmospheric seeing, and the finite radius of telescope aperture cause the light to be spread in a circular distribution across the image plane. This is characterised by measuring the atmospheric seeing with differential image motion monitor (DIMM), and the intrinsic Airy disc of the telescope optics; the combination of which are represented in the observed point spread function (PSF). For some portion of both nights upon which these data were observed, the measured seeing alone exceeded 2.0 ″. Thus, the stars PSFs were much larger than the width of the narrow slit. In these conditions, observing through the narrow slit leads to considerable slit losses; resulting in an errant flux calibration. Thus, to encompass the entire PSF of the spectroscopic targets and compensate for slit losses, observations were also made through the wide slit. The 10 ″ slit was chosen to maximise slit transmission factor, and hence reproduce the actual flux from the star as accurately as

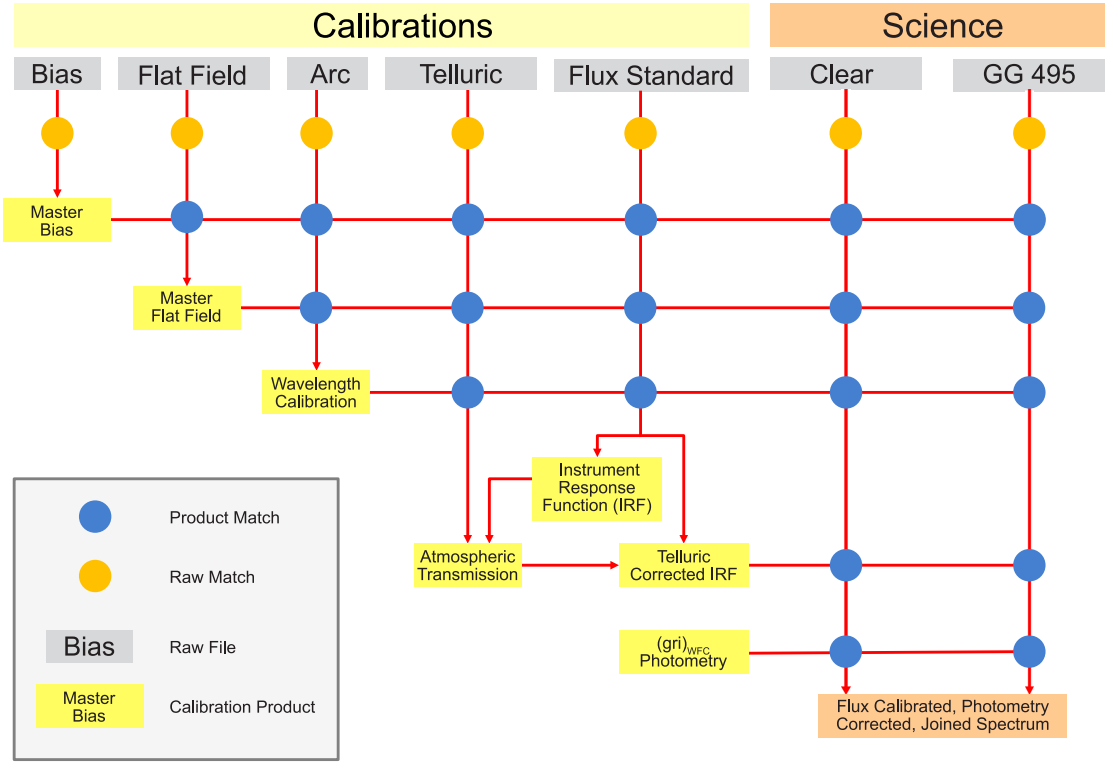

Figure 3.7: The reduction cascade for the data reduction presented in Section 3.3, shown as an association diagram. The raw data files are shown at the top and map down to the resulting calibration products, which match across to later stages of the reduction. The final result are the joined spectra shown in orange at the bottom right.

possible. However, as wider slits are deployed into the optical path the combined image of the slit and stellar PSF becomes larger than the intrinsic resolution of the spectrograph - leading to blending of spectral features. The solution to this trade-off was therefore to derive a flux calibration with the wide slit spectra, and then apply the resulting calibration to the narrow slit spectra; with a small addition correction to account for slit losses.

To make effective use of the entire 4000Å - 9000Å range of ACAM without any contamination from second order diffraction, the entire sample were observed both with and without the GG495 order sorting filter. This captures both the 4000 Åto 6500 Å and 4950 Å to 9000 Å ranges of the spectrum free of contamination from second order diffraction. Before each spectroscopic science observations, g, r and i-band photometric observations were performed with ACAM. These data are used to aid the flux calibration in Section 3.3.2.6.

3.3.2.1 De-biasing and Flat Fielding

The first step of data reduction involves de-biasing and flat fielding our spectroscopic observations. Electronics that readout CCDs induce a small bias current in the signal, causing a nearly constant offset from zero across the image. To account for bias in the observations, bias frames were observed at dawn and dusk and combined into a median stacked bias frame for each night's observing. I applied this by subtracting the pixel values of the bias frame from the value of the corresponding pixel in each raw image.

An ideal flat field image is intended to compensate for imperfections in the response of the CCD and telescope optics, and flatten the background of the image in both the spatial and dispersion direction. However, the pixel-to-pixel variations in the dispersion axis are negligible compared to the uncertainty in the spectra. Hence, I focussed on flat fielding the spatial direction. The convention for flat fielding in the ARK software involves multiplying each pixel in the source image by a coefficient, which is calculated and supplied in images of the same dimensionality as the source image, such that

$$F_{\mathrm{flat},i,j} = F_{\mathrm{raw},i,j} \times C_{\mathrm{flat},i,j}, \tag{3.1}$$

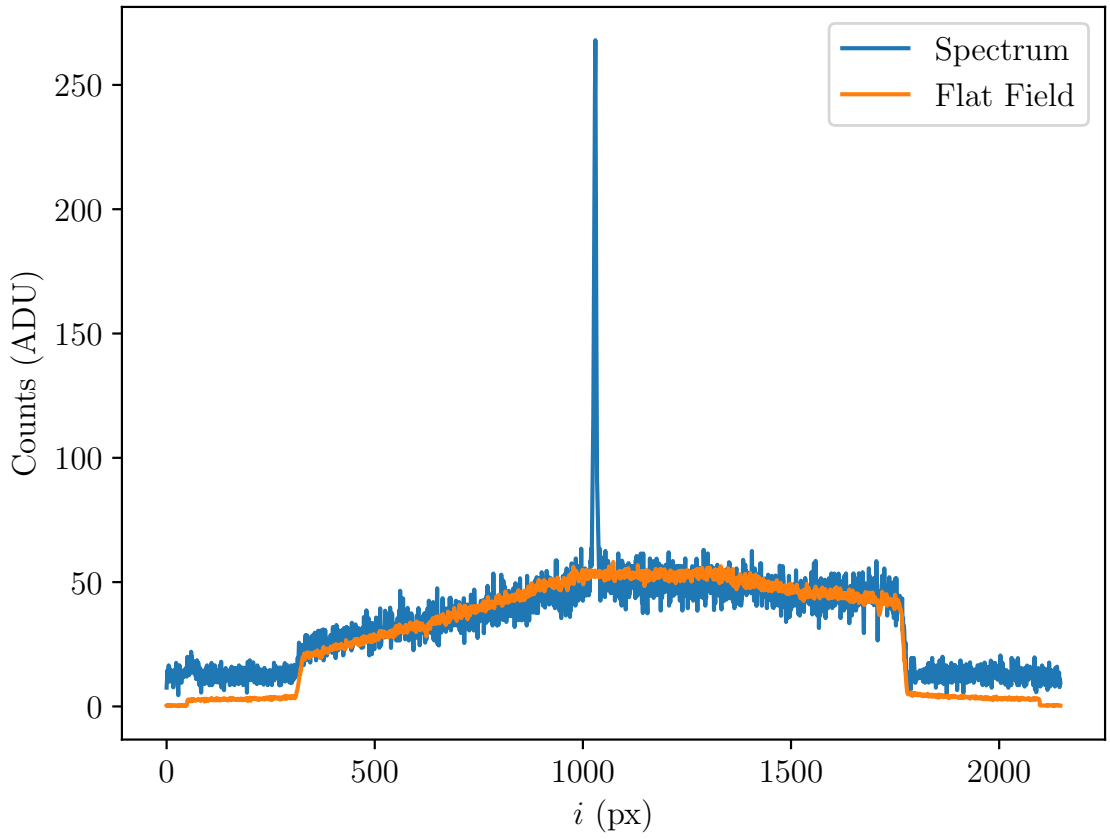

Figure 3.8: A cut across the spatial direction of one of my spectra images. The blue line shows the shows the spectral profile, around pixel 1000, complete with background. I have overlaid a scaled version of the same crosscut from the flat field image in orange. By dividing this image by a normalised flat field, a crude flat fielding can be performed.

where $F_{\text{flat},i,j}$ and $F_{\text{raw},i,j}$ are the values, in counts, contained in the pixel on the i^{th} column and j^{th} row in the de-biased and flat fielded images respectively, and $C_{\text{flat},i,j}$ is an arbitrary dimensionless coefficient which flat fields the corresponding pixel. For this section, the dispersion axis of the spectra is approximately aligned with the y-axis, such that lines of constant j intersect the spectral profile nearly orthogonally. The operation is chosen to be multiplicative as not only does this prevent divide-by-zero errors, which may result from bad pixels on the CCD, but it also allows me to set unwanted areas of the frame to zero. The challenging part of this process is deciding upon the process used to produce the coefficients; which I resolved by experimenting with different methods. I initially attempted generating coefficients by fitting a polynomial to the reciprocal of the flat field pixel values along the dispersion axis of the CCD. An adequately high order polynomial can capture the details of the background, an example of which is shown in Figure 3.8. However, I found that even high order polynomials were unable to reproduce this over the

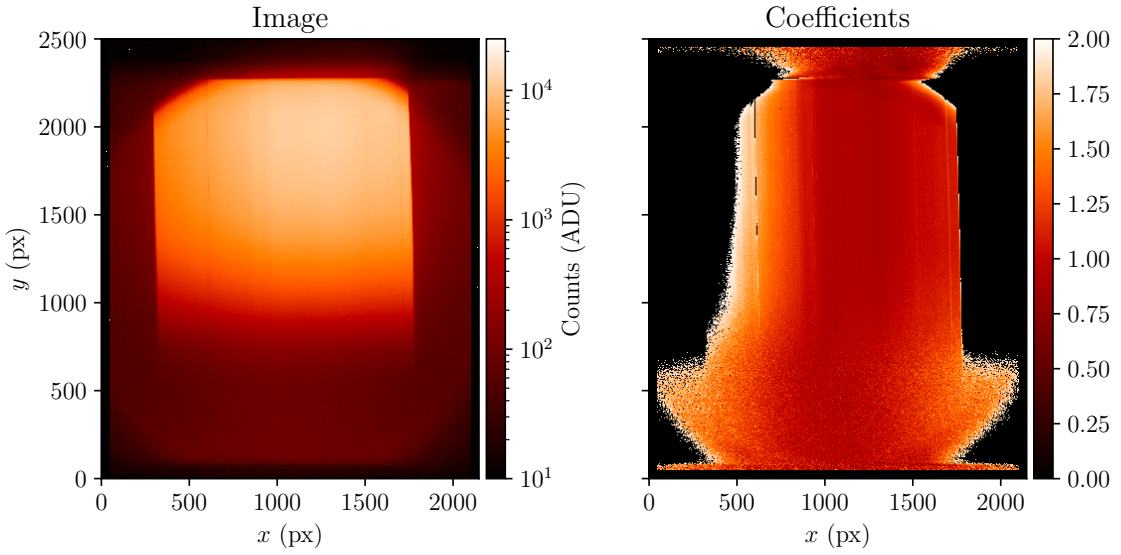

Figure 3.9: An example of a typical flat field image (left), along side the coefficients produced from it (right). Note how both the overscan region (black area around the border of the image) and bad pixels are zeroed in the coefficients to prevent errors later in the reduction process.

full range of λ, meaning that the flux at the blue end was lost. Thus I instead calculated the coefficients using the mean normalised value of pixels along each row of the spatial axis with

$$C_{\text{flat},i,j} = \frac{1}{F_{\text{ff},i,j}} \frac{1}{N_{\text{ff}}} \sum_i F_{\text{ff},i,j}, \tag{3.2}$$

where $F_{\text{ff},i,j}$ is the value in counts of the corresponding pixel in the flat field image. An example input flat field image and output coefficient image are shown in Figure 3.9. This method does result in a small variation of the flat field between rows, however it ensures that the integrity of blue flux is preserved. This method also does not remove the gradient across the background, however this is addressed by the sky subtraction performed during the extraction process. In addition, the coefficients outside of the active area of the CCD, which are used for neither spectra nor reduction purposes, were zeroed. This prevented edge effects of the detector and over-scan causing problems later in the reduction process. At this stage, bad pixels were also dealt with, as pixels that contained coefficients greater than the threshold value of 2.0 were zeroed and flagged in a bad pixel mask.

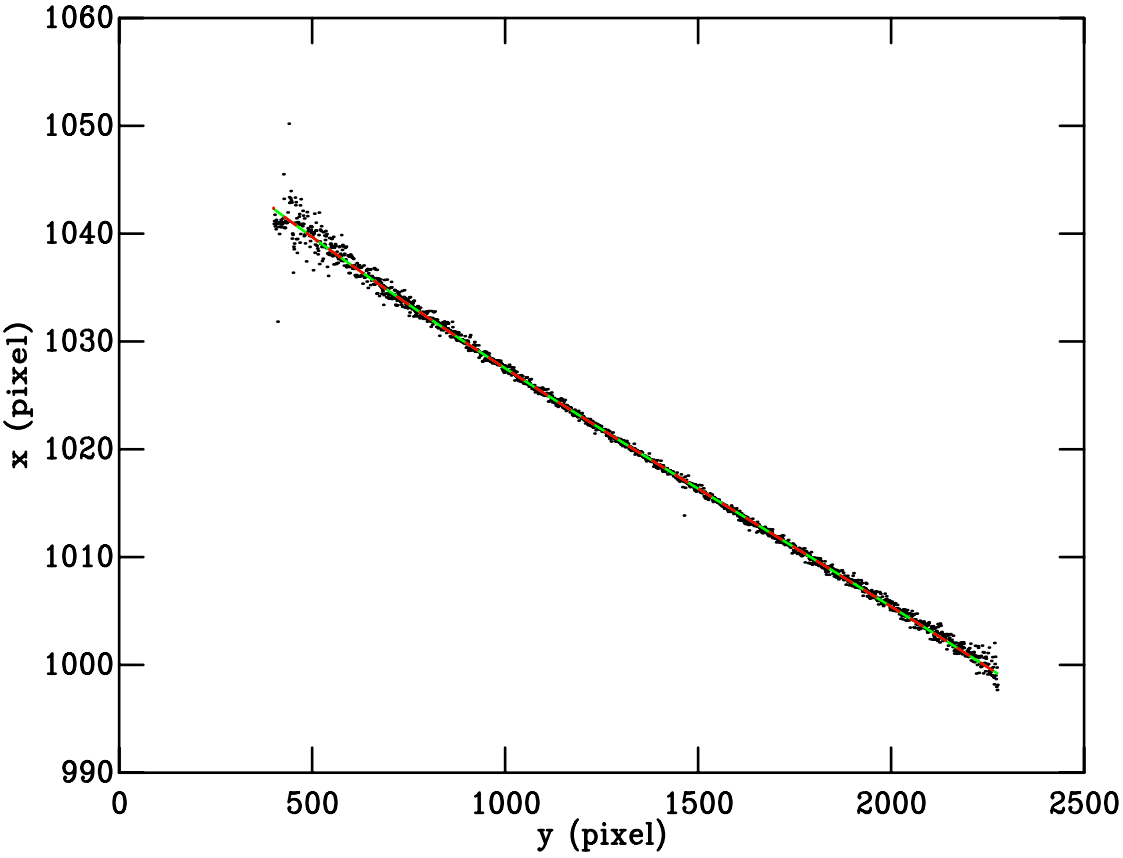

Figure 3.10: The track for flux standard star, GD 153, that served as the track for the extraction of spectra in this thesis. A first order and second order polynomial fit to the profile at shown as the red and green dotted lines respectively. The solution has converged well in both cases.

3.3.2.2 Extraction

The spectral flux is spread across a profile in the spatial dimension, which follows a line through the $x - y$ coordinates of the image plane. One may naively assume that this is a straight line along the dispersion axis, however in reality the spectra are skewed across the frame. Before extraction, I employed an algorithm which tracked the profile through the image; outputting the track in the form of a polynomial which gives y coordinate as a function of x. Initially, I wished to track the true curvature of the line across the CCD using a high-order polynomial fit. However, as Figure 3.10 demonstrates, the true track of the profile through the image plane can be well reproduced by low-order polynomials. Consequently, I adopted a linear function for the track and compensated for the small amount of curvature by using an adequately wide extraction window. As the tracking routine can meet with problems when performed on a spectrum with lower SNR, it is most effective when supervised and the outputs are manually checked. Thus the final track was

generated using an observation of GD 153, as it exhibited a well defined spectral profile across the entire dispersion axis. This single track was then used for all observations, through both the Clear and GG495 filters; as the choice of filter does not have a strong effect on the position of the profile.

When performing the extraction, the choice of algorithm is an important consideration. Long exposures are required to obtain spectra with adequately high SNR. Problematically, longer exposures inherently increase the likelihood of contamination from cosmic ray hits to the detector. To mitigate against cosmic rays, the spectra were extracted using the optimal extraction algorithm of Horne (1986). This algorithm masks out pixels containing suspected cosmic ray hits while conserving photometric accuracy when integrating over the spectral profile. The software for extraction and profile tracking was provided by the ARK package.

3.3.2.3 Wavelength Calibration

Once successfully extracted, the spectra are contained in the pixel number–count plane. To convert the counts into physically meaningful fluxes, one must first impose a wavelength scale. Both the slits and filters in ACAM are mounted in filter wheels, which have a small variance in their position when deployed into the optical path. This imposes the constraint that an independent wavelength solution is required for observations after every slit / filter deployment, even when returning to an identical configuration. A further issue facing the wavelength calibration of the ACAM spectra is flexure of the instrument at low elevation. For example, at an elevation of 15° the spectral lines can move on the ACAM CCD by up to ±5 px (±16 Å) in the dispersion direction due to flexure[1]. The observations performed for this thesis remained at an adequately high elevation such that they never exceed an airmass of 1.5 (42°), aside from a single science exposure at an airmass of 1.65 (37°); ensuring the effect of flexure remained small.

To compensate for both effects, the observing strategy that was adopted ensured that time on sky was maximised, while ensuring that arc lamp exposures were performed after each slew and change of slit or grism. The arc exposures were performed using both

1. http://www.ing.iac.es/Astronomy/instruments/acam/flexuretests.html

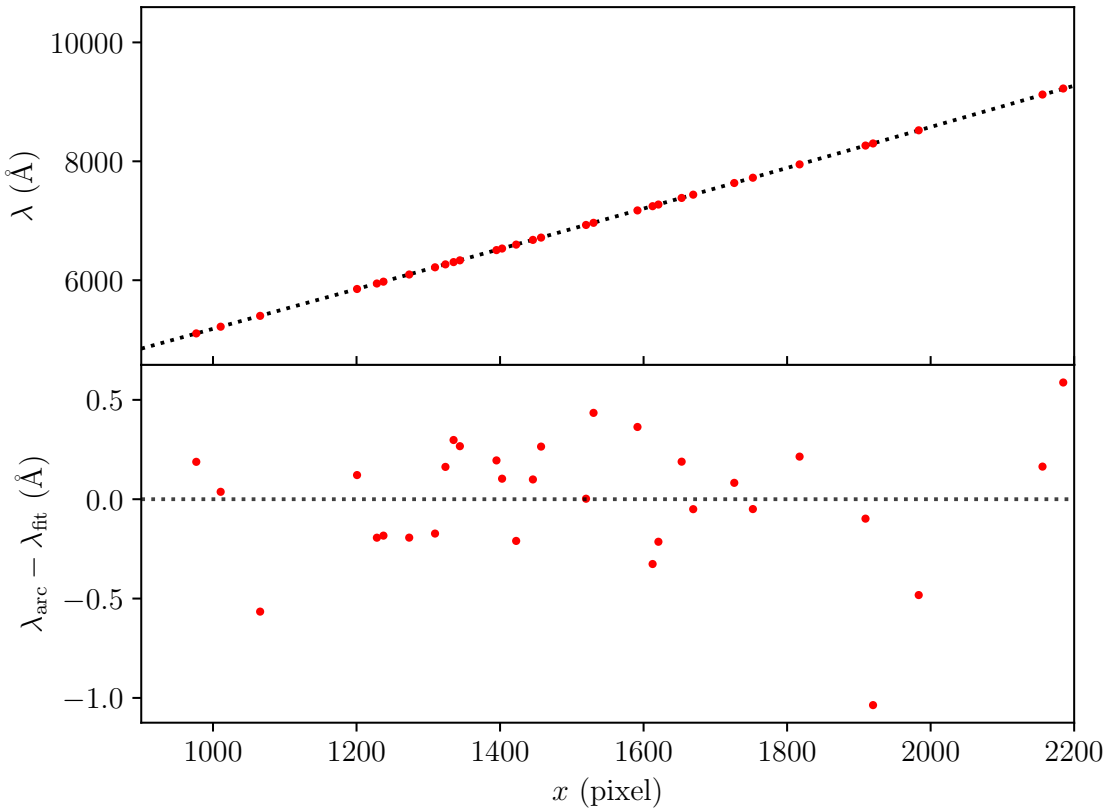

Figure 3.11: An example of the second-order polynomial solution that maps pixels position along the dispersion axis to physical wavelengths for this arc lamp exposure is shown in the top pane as a dotted line. The arc lines used to fit this solution are shown as red circles; with their residual from the fit being shown in the bottom pane.

CuAr and CuNe arc lamps, providing a wealth of spectral lines from which to draw a calibration. The extraction of each of the arc spectra was performed along the same track as those of the science observations in order to accurately reproduce the pixel scale. The lines chosen for the calibration were drawn from the arc lamp maps of Hardy et al. (2013). The positions of these well defined spectral lines were fit to provide a direct mapping from the pixel space of the detector to physical wavelength space. I eventually settled on a second order polynomial fit for the wavelength scale, as it was the least complex fit that exhibited no systematic and whose residual RMS remained below 1 Å. One of the final solutions, along with the arc lines used to determine it, is shown in Figure 3.11.

Although the PSF of the star is guaranteed to fall within the slit during wide slit observations, its position within the slit is not guaranteed to remain consistent between slews. Thus despite a converged wavelength solution, there was a fluctuation on the order of 20 Å in the wavelength scales of individual wide-slit spectra. This proved a

Target Name	RA (J2000.0)	Dec. (J2000.0)	Spectral Type	Source
BD +28 4211	21:51:11.1	+28:51:52	Op	Oke (1990)
GJ 894.3	23:19:58.4	-05:09:56	DOp	Oke (1990)
HZ 44	13:23:35.4	+36:08:00	sdO	Oke (1990)
GJ 398.2	10:39:36.7	+43:06:10	DO	Oke (1990)
GD 153	12:57:02.3	+22:01:53	DAw	Moehler et al. (2014)

Table 3.4: This table shows all of the flux standards that were used to derive the instrument response for reliable flux calibration of our observational data. Due to their being early-type, resulting in high SNR spectra with few intrinsic lines, they also served double service as telluric calibrators (see Section 3.3.2.5)

considerable problem during telluric correction and flux calibration. To circumvent this complication, the strong H_α line in the early-type flux standards and telluric calibrators was used to shift the wavelength scale such that the peak of feature corresponded to 6563 Å. Due to lack of strong H_α features which can be reliably fitted in late-type stars, this method of correction was not applicable to the M-dwarf spectra. However, due to being observed through a narrow slit, the final science observations remained unaffected. The final wavelength solution was fitted and applied to observed spectra using software from the ARK package.

3.3.2.4 Flux Calibration

The main concern of this project was the necessity of a robust fluxing solution for spectra. Observations were carefully planned to make it possible for the spectra to be flux calibrated to $\sim 1\%$. Images from ACAM are output in the native counts space of the detector. To draw valid comparisons between models and observations, these observational spectra had to undergo a transformation to the flux space. To this end, throughout the night wide slit observations were performed of spectrophotometric standards; stars whose flux as a function of wavelength is empirically well determined. The stars that were adopted as spectrophotometric standards are listed in Table 3.4, along with the source of the reference spectra.

Before performing the final flux calibration, I corrected for telluric absorption using the process described in Section 3.3.2.5. An instrument response function (IRF) was derived by first calculating F_ν/count within a number of wavelength bins. F_ν/count was calculated for each wavelength bin by dividing the integrated flux of the spectrophoto-

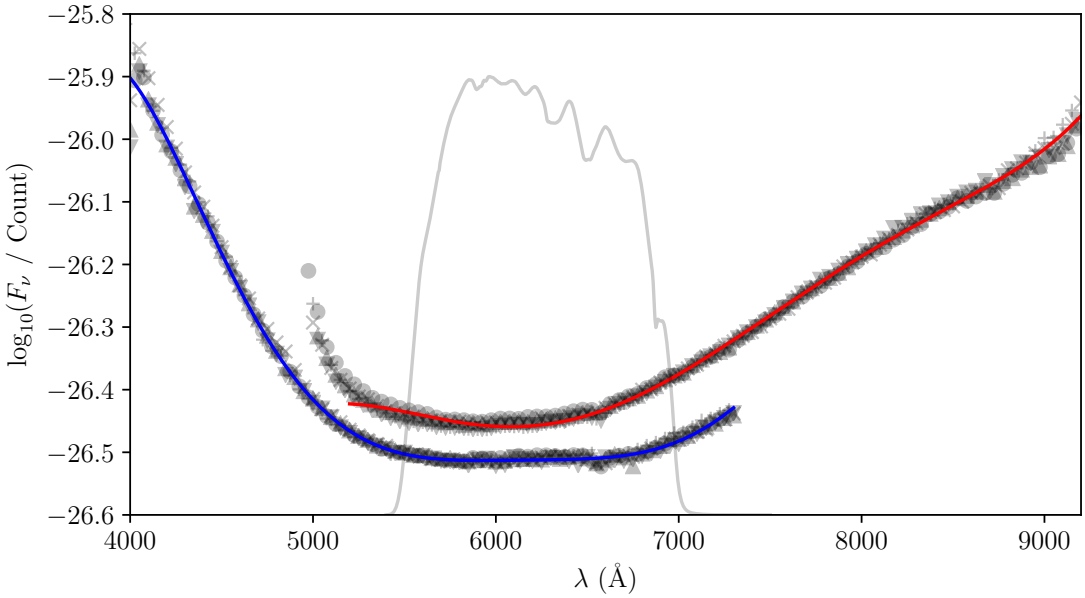

Figure 3.12: The measured ACAM instrument response functions for the clear (blue) and GG495 (red) filters. The observations are denoted by semi-transparent black points, with each star being represented by a different symbol. The observations have been offset to lie atop one another. The r_{WFC} system response has been overlaid to illustrate the transition region between the two when joined.

metric standard in each bin by the counts from the observed spectrum. The mapping between F_ν and counts for each spectrum as a function of wavelength was then derived by fitting a third order polynomial to the data in the resulting F_ν/count − λ plane. To achieve a robust fit of this function all spectrophotometric standards were fit simultaneously. Their baseline F_ν/count was subtly different, hence a small multiplicative offset was applied such that they lie atop the first reference spectrum. The resulting IRFs for the Clear and GG495 observations in ACAM are shown along with the observations used to derive them in Figure 3.12. Both the wide and narrow slit spectra were flux calibrated with the final IRF resulting from this process. To correct for slit losses in the narrow slit spectra, both spectra were binned into 100 bins and the wide slit flux in each bin was divided by the narrow slit flux in each bin. The ratio of fluxes was then fit with a low-order polynomial to yield a multiplicative slit correction as a function of wavelength. This slit correction function was finally applied to the narrow slit spectra, bringing its flux close to parity with the wide slit spectrum. The flux calibration was determined and applied to counts space spectra using software from the ARK package.

3.3.2.5 Telluric Correction

The spectroscopic observations are from a ground-based observatory, thus they are subject to considerable amounts of telluric absorption and emission. The telluric emission lines were removed during the extraction process, as the optimal extraction algorithm performs a sky subtraction (Horne 1986). However, extraction does not compensate for telluric absorption, which I instead compensated for using the `MOLECFIT` code of Smette et al. (2015) and Kausch et al. (2015).

The methodology employed by this code first involves determining abundances of the required atmospheric chemical species. For fitting of the atmospheric absorption, the telluric calibration stars 22 Tau and λ Cancri were chosen for Pleiades and Praesepe targets respectively. Early-type stars make ideal telluric calibrators, as their spectra are relatively free of intrinsic spectral features. Additionally, their high luminosity means that high SNR observations are achievable at much shorter exposure times than later-type stars at an equivalent distance. Observations of the appropriate telluric calibrator were made between science observations throughout the night, to ensure that the airmass and changing atmospheric conditions were well sampled.

The `MOLECFIT` code first fitted the continuum with a polynomial, so the spectra could be normalised. For the purposes of this experiment, I chose to use a third order polynomial. Once normalised, the abundances were determined by fitting synthetic transmission spectra to the normalised calibration spectrum. To achieve a convergent fitting of the line profiles, I limited the selection of species that were fit to O_2 and H_2O; the two main contributors to atmospheric extinction at optical wavelengths. I initially included O_3 in the molecules that were fit, however `MOLECFIT` found constraining the Chappuis bands that occur between 4000 and 6500 Å to be problematic, so it was neglected during the final fitting process. Because these broad absorption features occur in the flux standard observations, they are accounted for during the flux calibration process anyway. To include line profiles for O_2 and H_2O, as well as enough continuum to obtain a robust fit, I opted to use the region of spectrum ranging from 6700 to 8400 Å, as this allows constraints to be placed on all abundances without risking contamination from Hα absorption in the A0 and B9 telluric standards. The transmission of the atmosphere was then calculated by

performing a radiative transfer simulation of the atmosphere; which included absorption appropriate to the abundances that had been fitted, as well as the state of the atmosphere. The standard equatorial atmospheric profile derived by J. Remedios[2] was used for the radiative transfer calculations, with refinements provided by the on-site meteorological conditions during each exposure. The surface-level humidity, atmospheric pressure and ambient temperature for this process were supplied by the National Schools Observatory, who constantly monitor the conditions at the nearby Liverpool Telescope[3].

You may have noted the feedback loop between telluric calibration and flux calibration in Figure 3.7. This is because I wished to perform a telluric correction on flux standards in their native counts space, before deriving an IRF. However, to determine physically meaningful abundances from telluric calibrators, `MOLECFIT` fits spectral features in the flux space. Hence, to remove the telluric contamination before deriving the final IRF, I first fluxed the telluric calibration stars, then performed the `MOLECFIT` fitting on them to determine abundances. The calculated transmission was then used to correct the counts space spectra. Of course, the flux calibrators will have initially had telluric absorption evident in their spectra, so they were once again fitted, this time with the telluric absorption corrected, to determine the final IRF.

3.3.2.6 Ideal Fluxing

At this point, thanks to the initial flux calibration and wide slit correction, both ends of the narrow slit spectra were flux calibrated and free of slit losses. However, by comparing the folded photometry, produced from the flux corrected narrow slit spectra, with the observed photometry, I found that there was still a small residual of about 3%. Hence, to correct for this, I wrote software to perform an ideal fluxing on the narrow slit spectra before joining. The ideal fluxing is simply derived by folding the fluxed, narrow-slit spectrum through the system responses corresponding to the available photometry, in this case $(gr)_{\mathrm{WFC}}$ for the blue end and $(ri)_{\mathrm{WFC}}$ for the blue end, and comparing it to said photometry. This comparison allowed me to draw correction factors for the flux that fell within each filter. A linear fit was performed to these correction factors, meaning that

2. http://eodg.atm.ox.ac.uk/RFM/atm/
3. https://www.schoolsobservatory.org/obs/weather?tel=lt

a small correction for colour and flux could be applied individually across the entirety of both ends of each spectrum; effectively allowing the colour to slightly pivot around the r_{WFC}-band. This is termed the ideal flux calibration, as it acts to adjust the flux, and colour, of the spectrum to directly match that of the photometry. The ACAM photometry observed during the same run was calibrated from the INT-WFC photometry of Rees (2017). This was then used to verify that the target stars had not significantly varied in brightness between the epochs within which each catalogue was observed. As the INT-WFC system responses were used for the folding in this process, the ideal fluxing was performed relative to the WFC photometry; as opposed to that from ACAM. This method provided the sole flux calibration for Melotte 22 PPL 2, for which no wide slit spectrum was observed owing to time constraints. However, due to the poor quality of the spectrum, this target was omitted from the proceeding analysis. To verify the quality of the flux calibration, I performed the brutal test of folding the observed spectra through the g_{WFC} and i_{WFC} system responses and comparing them directly to the photometry. The residuals of this comparison are shown in Figure 3.13 as a function of $(g-i)_{\mathrm{WFC}}$ colour. This demonstrates that my flux calibration pipeline was able to reproduce both the overall colour and flux within the individual bands well, showing an RMS in residual of 1.4%, and a small systematic on the order of 1%

3.3.2.7 Joining Spectra

Throughout this process, there have been two pipelines working in parallel to treat the clear filter and GG495 observations separately (see Figure 3.7 for a schematic representation). To produce a complete visible spectrum, they require joining together. To join them, I initially attempted writing software to splice the spectra in an area of continuum at 6940 Å; however this resulted in an unphysical discontinuity if not performed carefully. Hence, my final solution was to transition between them smoothly across the r_{WFC} filter. This represented a well defined region of spectrum for which the flux was known via photometry, providing a means of flux normalisation. The fluxes from both input spectra were combined across the filter by performing a smooth linear transition between both spectra. The flux calibration was maintained while avoiding discontinuities by adjusting the normalisation of the both spectra such that their fluxes when folded through the

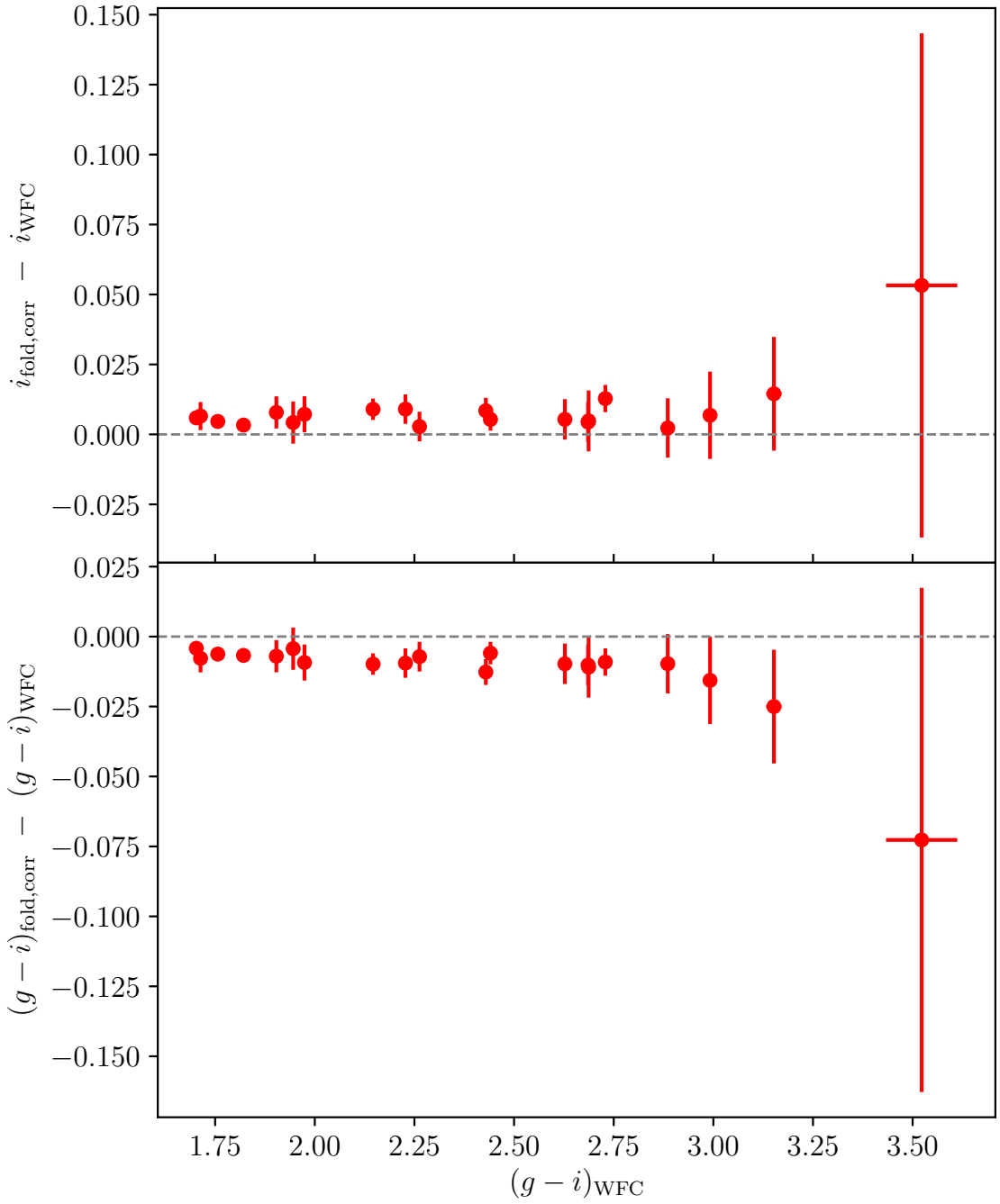

Figure 3.13: A comparison between the folded magnitudes derived from the flux calibrated spectra and the observed photometry. The top pane shows the difference between the i_{WFC}-band magnitudes and the bottom plane shows the difference between the $(g-i)_{\mathrm{WFC}}$ colours. The sample is shown with their accompanying uncertainties, determined during folding from the uncertainty in the spectral flux density. The colour is in good agreement with observations—a result of performing the ideal fluxing across $(gri)_{\mathrm{WFC}}$. The flux is also in good agreement with photometry, with the accuracy potentially suffering towards dimmer, redder stars. However, as the reddest star remains consistent within uncertainties, this could merely be the result of an increasingly large scatter, as opposed to a systematic effect.

system response matched that of the observed photometric magnitude in that band.

3.3.3 The Improved INT-WFC System Responses

An integral ingredient in reliable synthetic photometry is well characterised system response functions. The filters mounted in the ACAM filter wheel are very similar to those mounted in the Isaac Newton Telescope's (INT) Wide Field Camera (WFC), which themselves closely resemble those of SDSS. The SDSS system responses are well constrained, and presented in Doi et al. (2010). However, those available for the WFC only combine filter throughput and CCD quantum efficiency. This led Bell et al. (2012) to calculate their own INT-WFC system responses, which included the reflectivity of the telescope mirror, the transmission of the prime focus corrector optics, the quantum efficiency of the detector and the filter response. Atmospheric transmission was accounted for by incorporating a model of the La Palma atmosphere derived by King (1985). Unfortunately, the King (1985) model does not incorporate telluric absorption bands, so Bell et al. (2012) estimated atmospheric absorption using the spectrum of an F8 star.

During telluric correction, `MOLECFIT` performs a full radiative transfer calculation of the transmission of the atmosphere from the fitting performed on each calibrator. Consequently the atmospheric transmission as a function of wavelength, including the molecular bands whose abundances were fitted, are available as a by-product of this process. Hence, the aforementioned atmospheric transmission derived by Bell et al. (2012) was substituted for the theoretical transmission function derived from **22 Tau**, observed through a narrow slit. The airmass of this observation was 1.33; close to the mean airmass of our observations. The effect of this substitution can be seen in Figure 3.14. These are the responses that have been adopted for synthetic photometry performed throughout this chapter.

3.4 Generating Synthetic Spectra

To draw meaningful comparisons between models and observations, one must ensure that their characteristics match as closely as possible. My spectroscopic observations suffer the limitations of coarse spectral resolution, making it impossible to scale up to

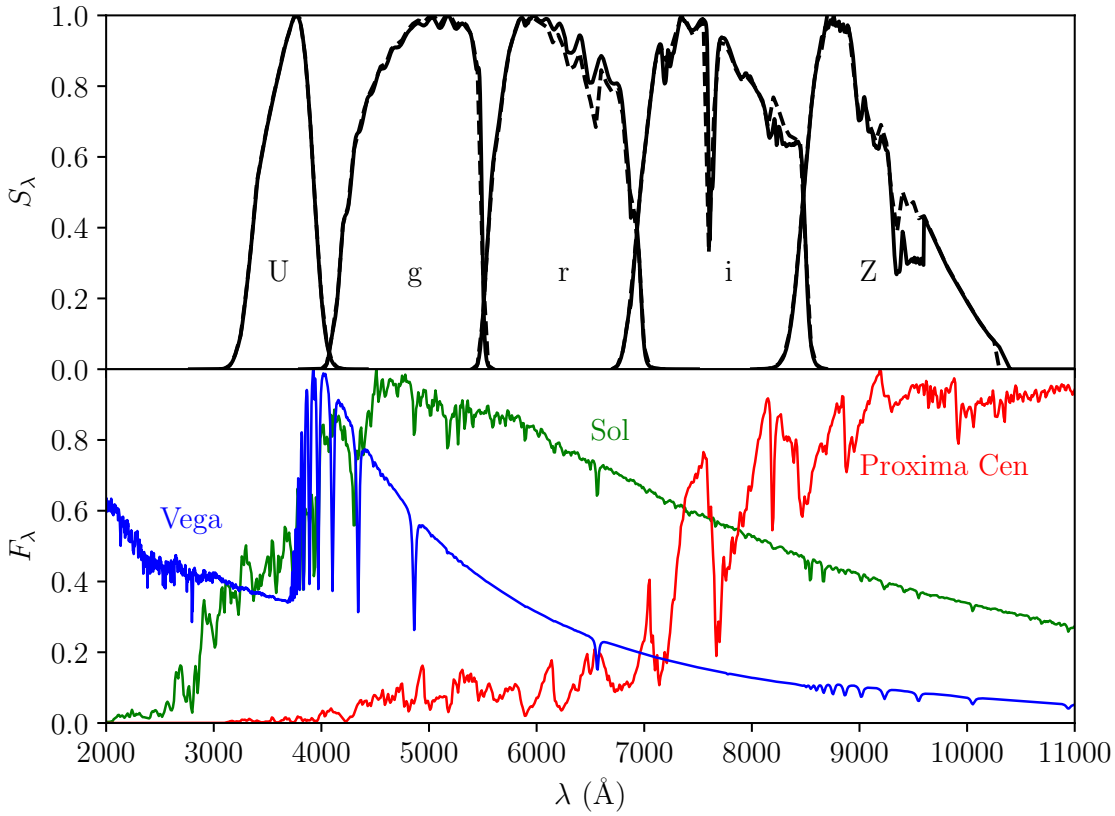

Figure 3.14: The improved INT-WFC responses (solid lines) are plotted over the INT-WFC responses from Bell et al. (2012). The crucial distinction between these two sets of responses is that the new ones use a fit of the observed atmospheric transmission at an airmass of 1.33, whereas the dashed responses use an atmospheric transmission model from King (1985) at an airmass of 1.4 combined with the atmospheric absorption bands from the spectrum of an F8 star.

compare with the models. Thus I wrote a piece of software which processed the synthetic model atmospheres in such a way that they correspond closely to what would be observed by ACAM. As with the grid from which synthetic photometry were produced in Section 2.1.4, I first interpolated the model grid to match the required $T_{\rm eff}$ and $\log(g)$ (see Section 2.1.3 for details). Preserving the flux in models is important when producing synthetic photometry, however particular care must be taken to preserve both flux and spectral features when producing synthetic spectra. Fortunately, the bilinear interpolation method devised in Section 2.1.4 was designed with this purpose in mind, and endeavours to preserve temperature sensitive features. Unlike the grids, which I simply downsample with a flux conserving algorithm, spectroscopic data require more attention to detail. The shape of spectral features in models is determined by the intrinsic shape of the lines, however for instruments such ACAM the line spread function of the optics causes considerable spread away from the intrinsic profile. To correctly account for the line spread function of ACAM and preserve the flux, I performed a Gaussian convolution across the entire synthetic spectrum to emulate this line spread function. Thus, the intensity for a given bin $I_{\lambda,j}$ in the spectrum with the appropriate line spread for ACAM is given by

$$I_{\lambda,j} = \sum_{i=j-k}^{j+k} I_{\lambda,i} \frac{1}{\sigma\sqrt{2\pi}} e^{-\frac{(\lambda_i-\lambda_0)^2}{2\sigma^2}} \Delta\lambda_i, \tag{3.3}$$

where λ_0 is the central wavelength of the $j^{\rm th}$ bin of the destination wavelength scale, λ_i is the central wavelength of the source model spectrum, k is the number of pixels in the source model scale that lie within 10σ of λ_0 and σ is defined as

$$\sigma = \frac{\text{FWHM} \times D}{2\sqrt{2\ln 2}}, \tag{3.4}$$

where FWHM is the measured full width at half maximum (FWHM) of the line-spread in the destination spectrum and D is the dispersion of the instrument. Intrinsically, the spectral lines in arc lamps are narrow, thus the majority of their spread is caused by the line spread function of the spectrograph. Thus, by measuring the width of spectral lines in the combined arc lamp spectrum, I was able to determine the line spread function for the instrument. I determined a FWHM = 2.0px to match well the spectroscopic observations

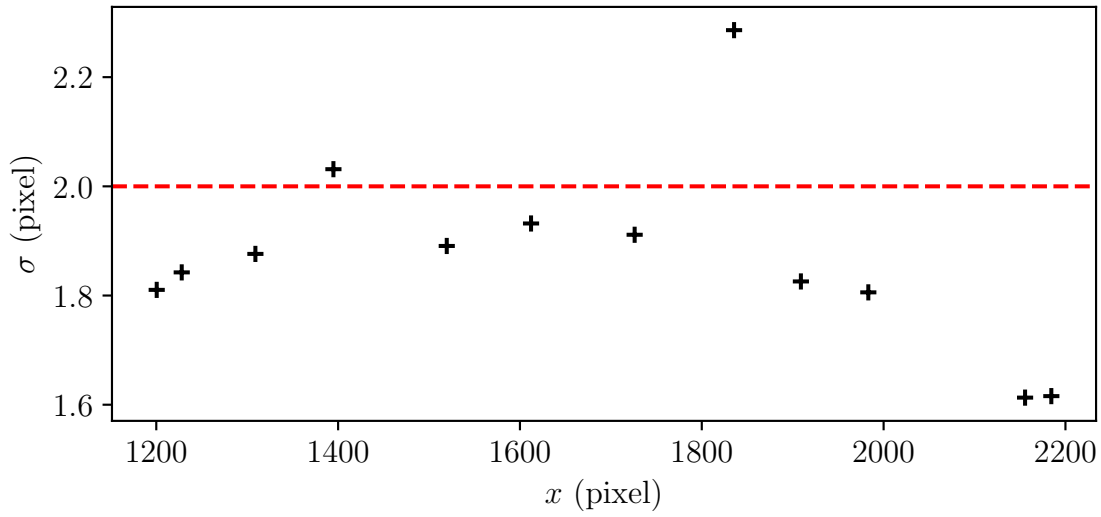

Figure 3.15: The measured FWHM of the line spread function of ACAM, as measured from lines in arc lamp exposures. I adopted the value of 2px, as this encompasses the mean line spread measured for the instrument.

from ACAM (see Figure 3.15) and $D = 3.3$ Å px^{-1}.

Finally, the synthetic spectra must be transformed from their native space of mean disc intensity at the stellar surface to the flux as observed from earth. Thus the flux density F_λ of the final synthetic spectrum is given by Equation 2.2. The angular radius of the source, which acts as the dilution factor, was set individually for each target using the fitting performed in Section 3.2.1 and Section 3.2.2, depending on the comparison being drawn. An extinction appropriate for the cluster which contains the target star was then also applied to the synthetic spectrum (see Section 2.1.7 for details of this process).

To verify the accuracy of this process, I used the parameters determined from fitting constrained to the isochrone (detailed in Section 3.2.2) to generate synthetic spectra for each of the targets. I then folded the resulting synthetic spectra through the appropriate bandpasses, using the same method as in Section 2.1.4 to produce synthetic photometry. This was then compared back to the magnitude and colour prescribed by the isochrone, which were shown to be in good agreement. It was by comparing this folded synthetic photometry to the colours and magnitudes predicted by the theoretical isochrone, which uses the same stellar atmosphere grid to generate bolometric corrections, that allowed me to discover the problems caused by the default sampling of the stellar interiors addressed in Section 3.5.3. Spectroscopic outputs of all synthetic spectra used in this experiment are

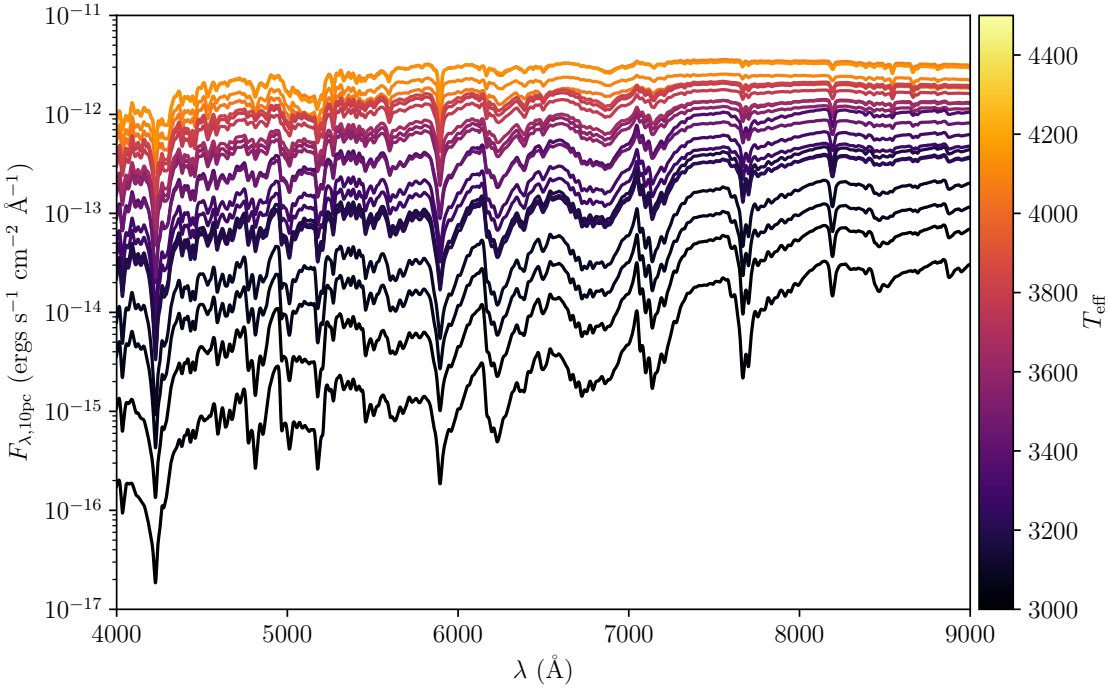

Figure 3.16: An example output of all the synthetic spectra required for the comparison. The spectra are coloured corresponding to T_{eff}, given the radius for the star and placed at 10 pc for comparison. This demonstrates that the interpolation and Gaussian convolution in tandem are able to emulate synthetic spectra from ACAM.

shown in Figure 3.16, demonstrating the accuracy of the ACAM line spread function.

3.5 Results and Discussion

The culmination of all of the work in this chapter is a powerful test of both the methods devised for this thesis and the physics of the input models for theoretical isochrones. The SED fitting process yielded reliable stellar parameters for cluster members in the Pleiades and Praesepe. This permitted me to perform an exploration of the luminosity–temperature–radius relationships for pre-MS stars, and directly compare them to those dictated by the theoretical stellar interiors. Meanwhile, these parameters were used as the inputs to synthetic spectra, which can be directly compared to robustly flux calibrated observed spectra. Thus, using the work laid out in this chapter, I have produced the theoretically consistent spectra via two orthogonal methods. While acting as a test of both the flux calibration and the parameter estimation, whose success is indicated by broad agreement between continuum flux and temperature sensitive spectral features, this comparison also serves as a diagnostic check for opacities of molecular species in

M-dwarf photospheres; as inconsistencies should be readily apparent when compared.

3.5.1 Comparison Between Observed and Synthetic Spectra

I have established that the interior models do indeed suffer missing physics for pre-MS stars, as exhibited by their inability to reproduce the stellar sequences of either of the studied clusters (see Section 3.2.3). However, this does not address potential problems with the stellar atmospheres. In performing the previous experiment, I have made a tacit assumption that the atmospheres are accurate enough to produce synthetic photometry to fit the SED. However, the SED probes the overall shape and continuum flux of the photosphere, which has not so far shown inconsistencies. Though this does not allow me to comment on the opacities of specific species within the atmospheres of low-mass stars.

Thus the aim for the flux calibrated spectra was twofold. First, it does indeed allow me to verify how well the optical component of the SED agrees with the synthetic models. The flux calibrated observations are entirely empirical, thus represent a completely orthogonal means of verification. Once the overall reliability of the atmosphere models has been assessed, I can then progress to scrutinising the accuracy of individual features to test the hypothesis that inconsistencies are due to incorrect opacities in molecular species.

The comparison of spectra can be performed trivially be simply overlaying them. Deficiencies in any part of the process will result in a difference between the two. This is precisely what I have done in Figure 3.17 and Figure 3.18.

By performing the same fitting with the constraint that the solution is bound to the isochrone, the resulting comparisons between the models and observations are shown in Figure 3.19 and Figure 3.20. From these comparisons we can spot the important differences between these two fits. Indeed, it does appear that the fluxes are incorrect for the isochronal fits, a result of the incorrect temperature and radius being prescribed by the interiors. As a result of this the isochronal temperature $T_{\rm eff,iso}$ does not reproduce the overall shape of the spectra. The free temperature radius fitting on the other hand provides models whose continuum is an excellent match to that of the observations. This is unsurprising, given that the grids used for fitting and model spectra originate from

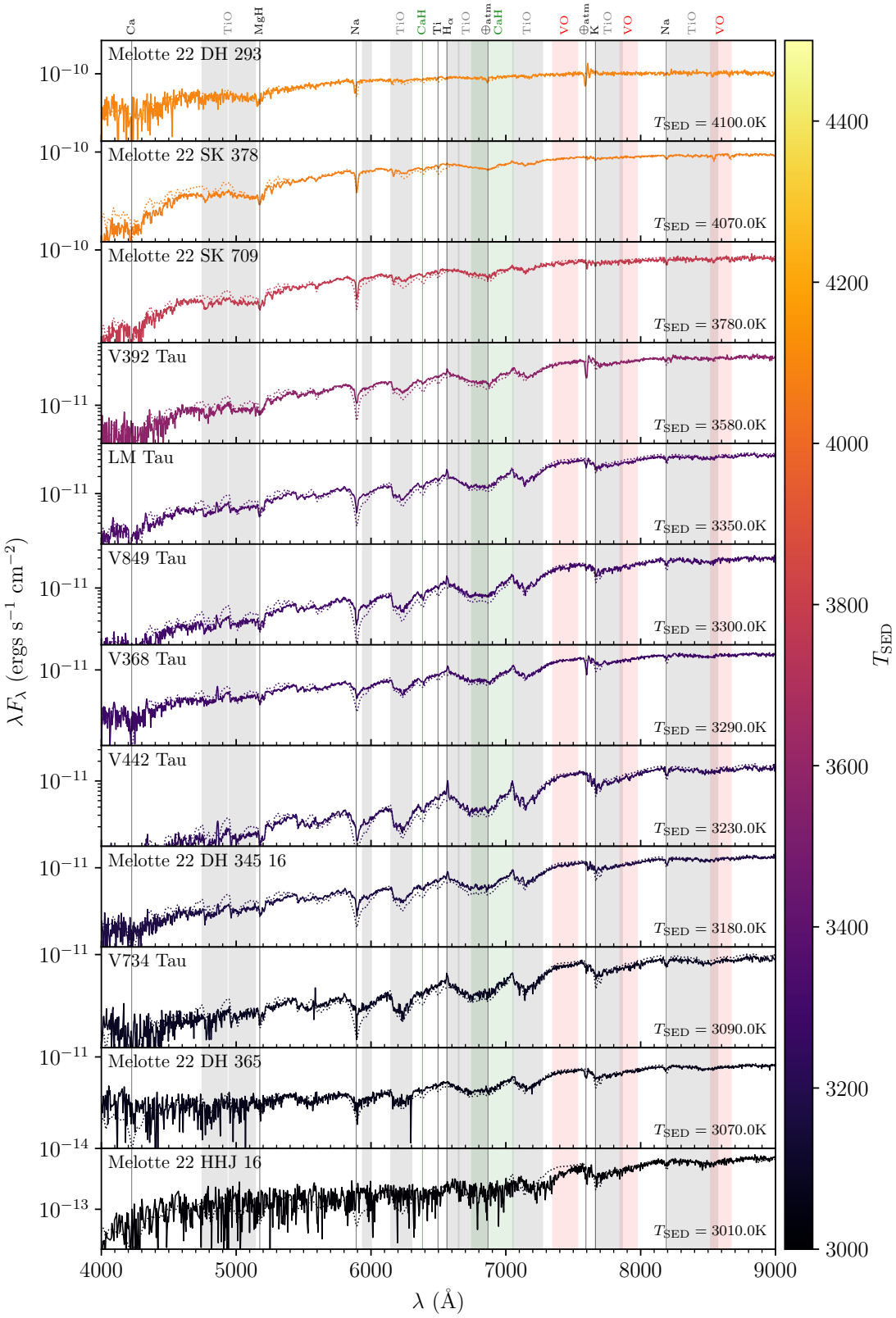

Figure 3.17: A comparison between the observed, flux calibrated spectra (solid lines) and the model spectra (dotted line) from parameters determined by free temperature–radius fitting for Pleiades targets. The colours of the lines denote the T_{SED} of the generated models, determined in the photometric fitting. The fluxes of observations are adaptively binned such that each bin has an uncertainty of 1%.

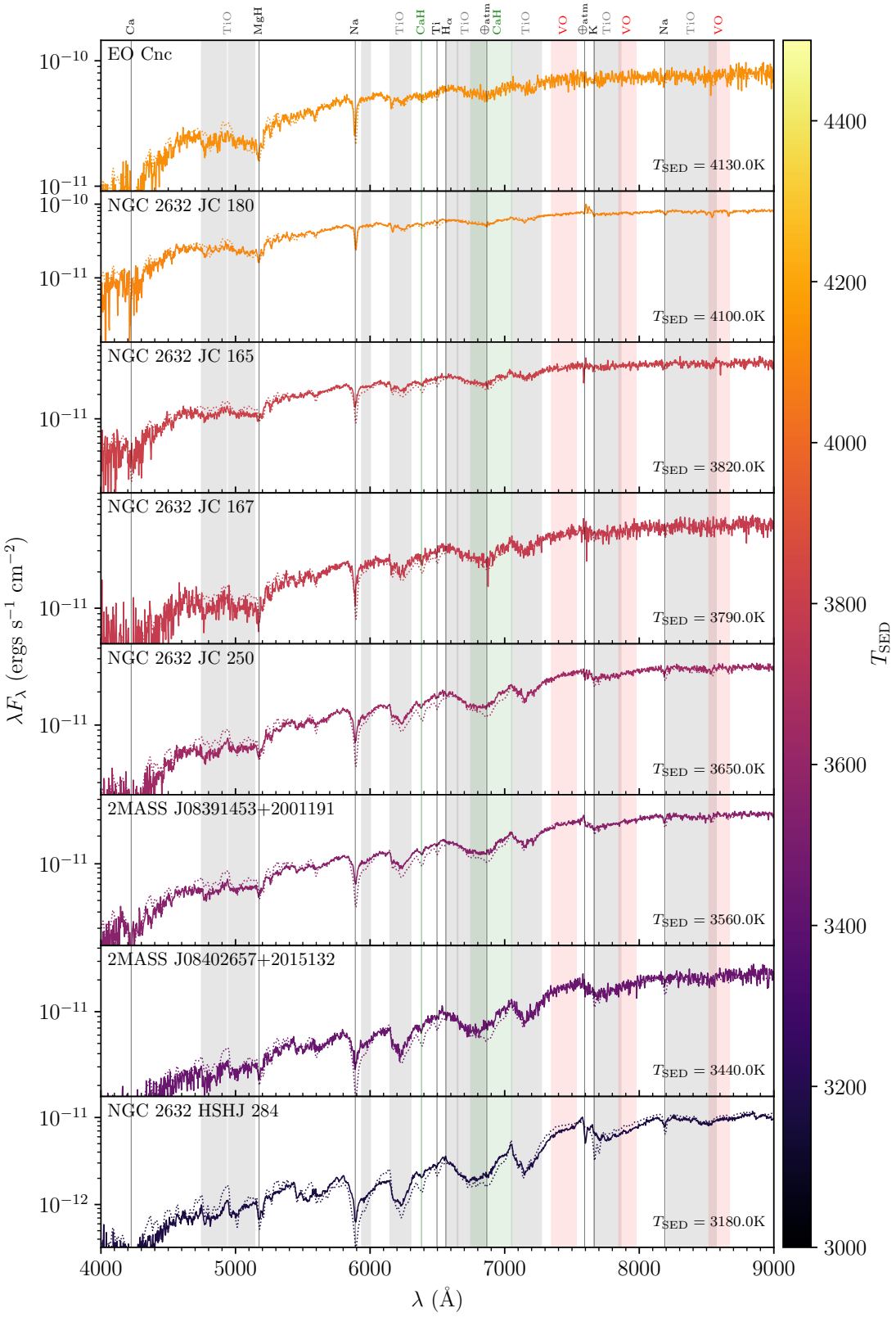

Figure 3.18: As Figure 3.17, except for the targets in Praesepe.

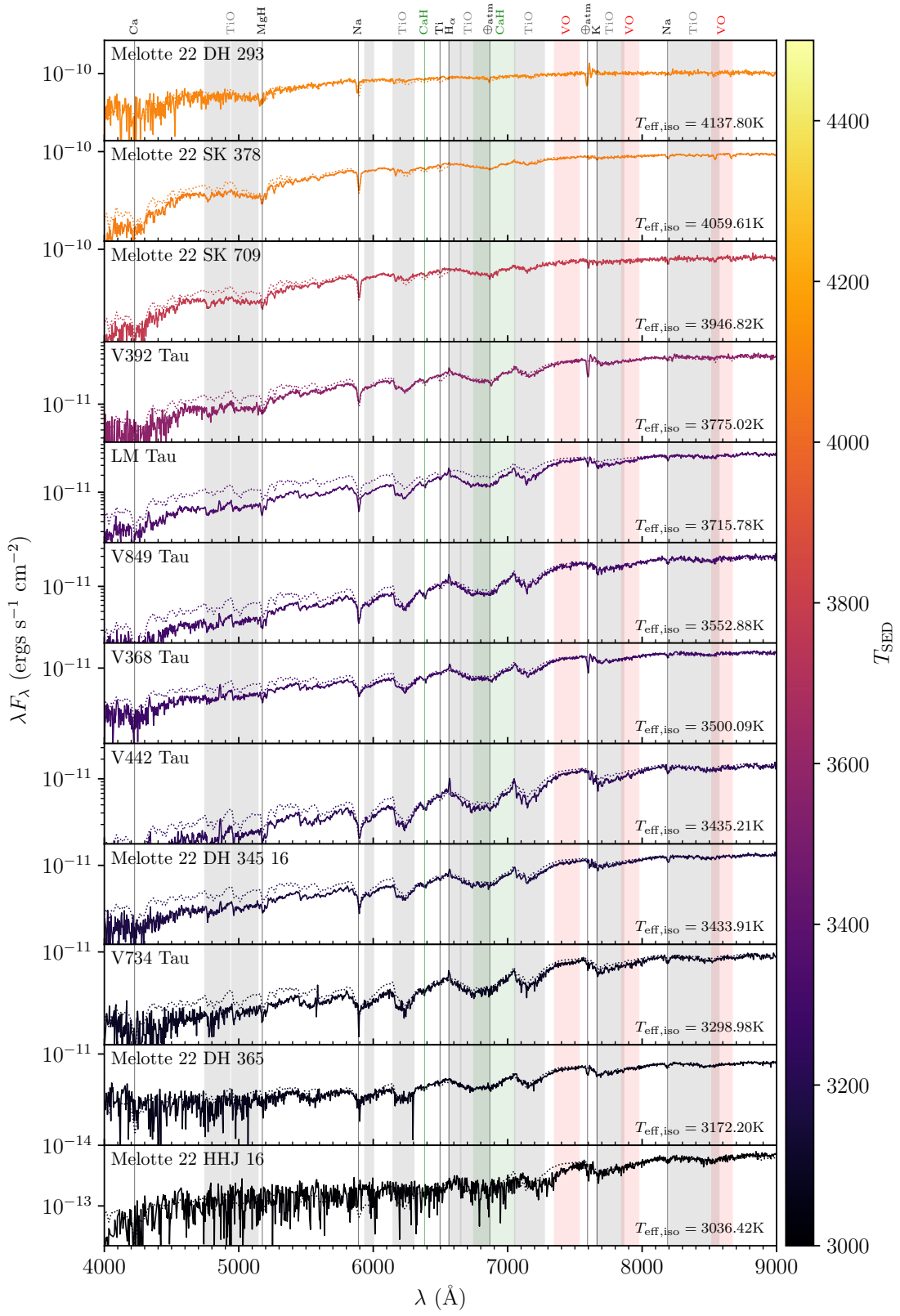

Figure 3.19: A comparison between the observed, flux calibrated spectra (solid lines) and the model spectra (dotted line) corresponding to the best fitting isochrone constrained fit for each of the Pleiades targets. The colours again denote the T_{SED} of the models. As previously, the fluxes of observations are adaptively binned such that each bin has an uncertainty of 1%.

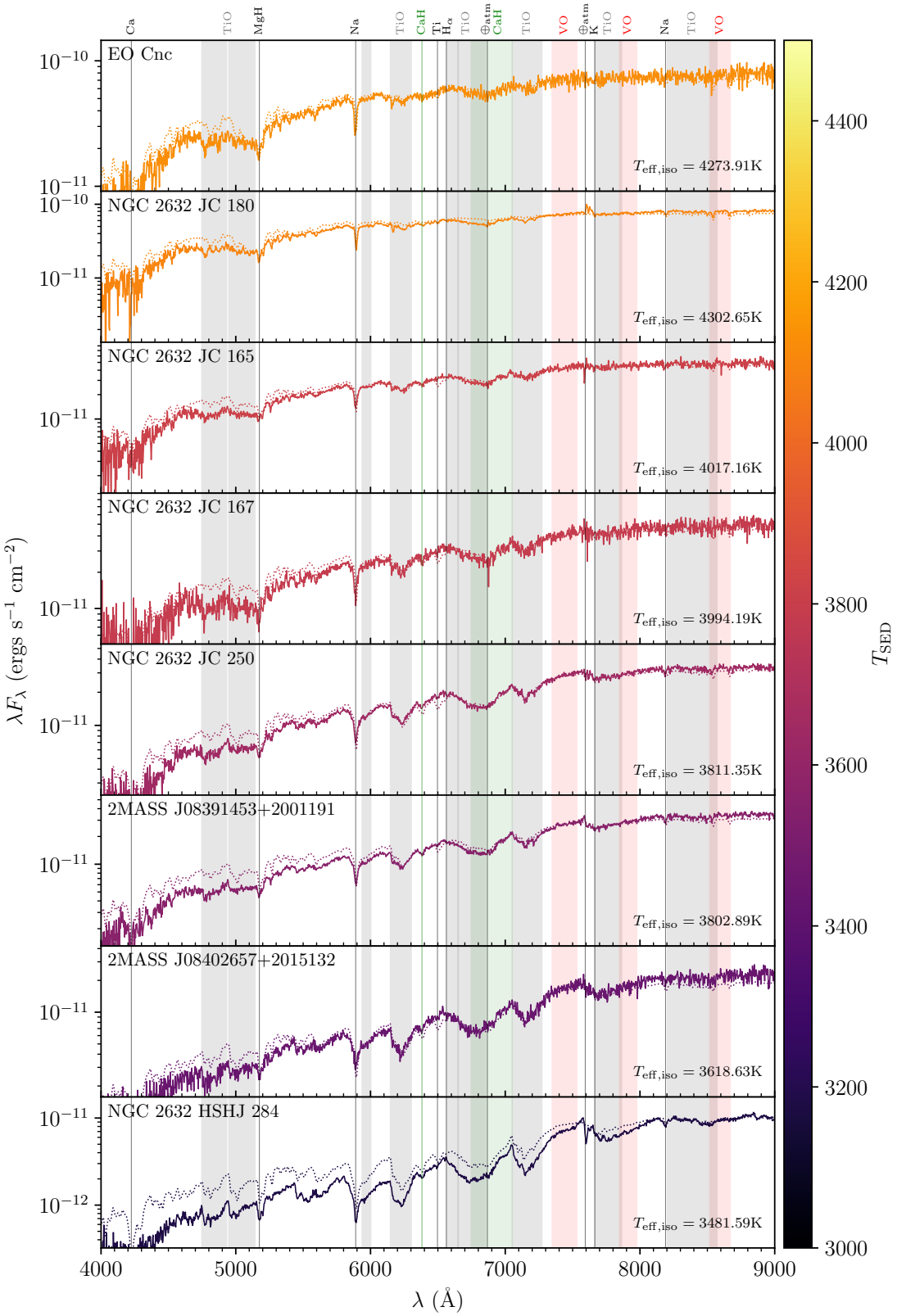

Figure 3.20: As Figure 3.19, except for the targets in Praesepe.

the same stellar atmosphere grid, and that their $T_{\rm eff}$ is imposed as my $T_{\rm SED}$, especially at wavelengths that fall within photometric bands. This also shows that indeed the bands for a number of molecular species, including TiO and CaH, are inconsistent with observations, indicating issues with their opacities. In addition, the width of the Na feature at 5890 Å is under-predicted by the models, and the K and Na features at 7665 Å and 8190 Å respectively appear at much lower $T_{\rm eff}$ than is suggested by observations. Of particular concern is the large disagreements between the observed and synthetic spectra shortward of about 5500 Å. Comparisons in this region indicate that more opacity is required in the models to allow them to match the flux of observations across a wide range in $T_{\rm eff}$; potentially implicating incomplete line lists.

3.5.2 Comparison between SED and Spectroscopic Temperatures

Along with a direct qualitative comparison of my observed spectra with the models, I also quantitatively measured their spectroscopic temperature $T_{\rm sp}$ using spectral index fitting. To do so, I implemented a Python code, based on the spectral index fitting methodology of Covey et al. (2007), to draw measurements of $T_{\rm sp}$ by measuring the mean fluxes of a selection of atomic and spectral features and fitting them to a grid of synthetic indices; generated from BT-Settl CIFIST atmosphere models. This method was chosen as it does not rely on normalised spectra, and instead measures the flux of spectral features relative to the mean fluxes of nearby regions of continuum. The spectral indices that were used for this work are the single numerator indices from Covey et al. (2007), and are listed in Table 3.5. As all of the spectroscopic targets are late-type stars, I excluded those tuned for early-type stars (Ca K, H_δ, Ca 4227 Å, Na D, H_γ, Fe I 4383 Å, Fe I 4405 Å, H_β, Ca I 6162 Å, H_α, Ca II 8662 Å, Fe I 8689 Å), as well as the blue colour index. I note in passing that I have also omitted the CaH III index at 6975Å due to the continuum region being too narrow for the resolution of my intermediate dispersion spectra. I also note that, although this method is spectroscopic based, the final estimate draws heavily upon the red and G-band colour indices; which mimic my SED fitting-based approach.

I performed spectral index fitting on all of the flux calibrated spectra, which are shown alongside the equivalent $T_{\rm SED}$ measurement in Table 3.6. The poorly localised

Name	N Start (Å)	N End (Å)	D Start (Å)	D End (Å)
G-band	4285.0	4315.0	4260.0	4285.0
Mg I 5172 Å	5152.7	5192.7	5100.0	5150.0
VO 7434 Å	7430.0	7470.0	7550.0	7570.0
VO 7912 Å	7900.0	7980.0	8100.0	8150.0
Na I 8189 Å	8177.0	8201.0	8151.0	8175.0
TiO B	8400.0	8415.0	8455.0	8470.0
TiO 8440 Å	8440.0	8470.0	8400.0	8420.0
CrH-a	8580.0	8600.0	8621.0	8641.0
Red Colour	8900.0	9100.0	7350.0	7550.0

Table 3.5: The spectral indices, from Covey et al. (2007), used to measure the the spectroscopic temperature from my intermediate dispersion spectra. For this fitting, the spectral indices tuned to early-type stars were omitted.

uncertainty bounds for the R and $T_{\rm SED}$ values is the result of both the large (0.05 mag) floor value imposed for the photometric uncertainty, and the poor constraint on $\log(g)$. These were solved in the proceeding chapters by reducing the floor value of photometric uncertainties and imposing a wide tophat prior on $\log(g)$ using stellar models. Covey et al. (2007) state that the combination of their algorithm and the indices derived from spectral template libraries yields spectral types to ±2 subtypes for late-type (K and M) stars. Taking the measured $T_{\rm SED}$ as the ground truth for the purposes of this comparison, this does indeed seem to be borne out. However, the formal uncertainty estimates of $T_{\rm sp}$ appear to be underestimated; presumably due to the spectral indices not being a smoothly varying function of $T_{\rm eff}$.

3.5.3 Sampling of the Stellar Interiors

The isochrones used in this work are produced by multivariate interpolations of the underlying stellar models. To provide the isochrone, the underlying stellar interiors are first interpolated in age to produce a single star sequence appropriate for the cluster. The spacing of points in the output isochrone is directly taken from the spacing of initial mass $M_{\rm ini}$ points in the input interiors. To complicate the process, the interiors need not be spaced regularly in $M_{\rm ini}$, and the resulting spacing in $T_{\rm eff}$ and $\log(g)$ will not necessarily correspond with the models in the atmosphere grid. Hence, the transformation to the observational plane is performed by interpolating the model bolometric corrections

Name	R ($R_\odot$)	$T_{\rm SED}$ (K)	$T_{\rm sp}$ (K)
Melotte 22 DH 293	$0.588^{+0.013}_{-0.033}$	4100^{+100}_{-40}	4290^{+20}_{-20}
Melotte 22 SK 378	$0.549^{+0.025}_{-0.020}$	4070^{+60}_{-80}	3760^{+0}_{-10}
Melotte 22 SK 709	$0.581^{-0.015}_{-0.065}$	3780^{+200}_{+60}	3600^{+0}_{-20}
V392 Tau	$0.542^{-0.015}_{-0.060}$	3580^{+200}_{+70}	3370^{+10}_{-10}
LM Tau	$0.598^{-0.012}_{-0.063}$	3350^{+180}_{+60}	3290^{+10}_{-10}
V849 Tau	$0.476^{-0.012}_{-0.055}$	3300^{+180}_{+70}	3170^{+10}_{-10}
V368 Tau	$0.419^{-0.008}_{-0.043}$	3290^{+170}_{+60}	3000^{+10}_{-10}
Melotte 22 DH 345 16	$0.398^{-0.007}_{-0.042}$	3180^{+160}_{+50}	3050^{+0}_{-10}
V442 Tau	$0.378^{-0.008}_{-0.040}$	3230^{+160}_{+50}	3080^{+0}_{-10}
V734 Tau	$0.314^{+0.003}_{-0.025}$	3090^{+100}_{+0}	3040^{+0}_{-10}
Melotte 22 DH 365	$0.241^{+0.003}_{-0.017}$	3070^{+80}_{+0}	2800^{+10}_{+0}
Melotte 22 HHJ 16	$0.195^{+0.020}_{+0.003}$	3010^{-30}_{-110}	2780^{+10}_{-10}
Melotte 22 PPL 2	$0.155^{+0.015}_{-0.003}$	2820^{-10}_{-90}	2710^{+30}_{-30}
NGC 2632 JC 180	$0.698^{+0.020}_{-0.037}$	4100^{+90}_{-50}	3800^{+0}_{-10}
EO Cnc	$0.662^{+0.005}_{-0.047}$	4130^{+140}_{-20}	3870^{+20}_{-30}
NGC 2632 JC 167	$0.624^{-0.012}_{-0.067}$	3790^{+210}_{+40}	3570^{+10}_{-20}
NGC 2632 JC 165	$0.627^{-0.030}_{-0.090}$	3820^{+270}_{+90}	4090^{+10}_{+0}
2MASS J08391453+2001191	$0.590^{-0.020}_{-0.070}$	3560^{+210}_{+80}	3480^{+10}_{-10}
NGC 2632 JC 250	$0.555^{-0.017}_{-0.062}$	3650^{+210}_{+80}	3550^{+10}_{-10}
2MASS J08402657+2015132	$0.500^{-0.025}_{-0.070}$	3440^{+210}_{+100}	3310^{+10}_{-10}
NGC 2632 HSHJ 284	$0.434^{-0.005}_{-0.045}$	3180^{+150}_{+40}	3200^{+0}_{-10}

Table 3.6: A comparison between the temperatures derived from both SED fitting, and spectral index fitting. I have also provided the radii corresponding to the $T_{\rm SED}$ measurement for reference. They are shown along with their uncertainties, which are generated using the upper and lower bound values found from their χ^2 grids (see Section 2.1.5 for details).

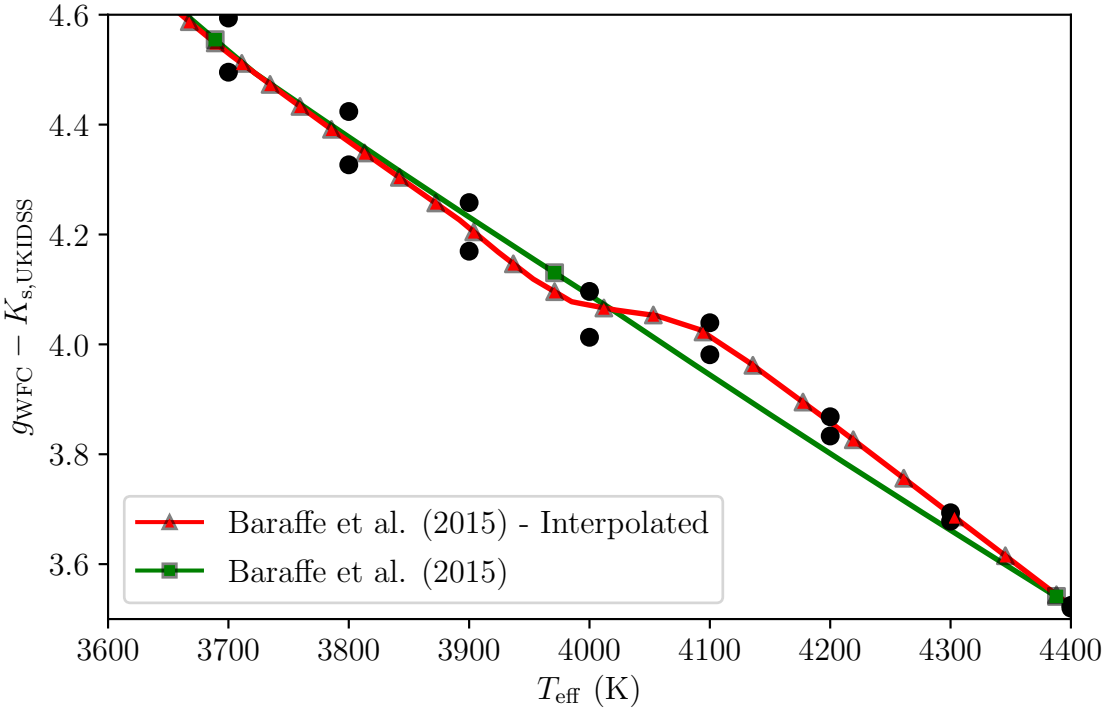

Figure 3.21: The Pleiades isochrone generated from the Baraffe et al. (2015) interiors at default sampling is shown in green, with the mass points of the underlying interiors indicated with square markers, in the $(g_{\rm WFC} - K_{\rm UKIDSS}) - T_{\rm eff}$ plane. The isochrone generated from the quadratically interpolated interiors is shown in red, with triangles indicating the interpolated mass points. The underlying bolometric corrections for $\log(g) = 4.5$ and $\log(g) = 5$ are interpolated in this $T_{\rm eff}$ range by the interiors, and are shown as black circles on the plot. At the original mass spacing the interiors are improperly sampling these bolometric corrections. The interpolated interiors are much better able to reproduce this sequence.

for each point on the interpolated single star sequence. This chain of interpolations is predicated on the understanding that the underlying stellar interiors provide adequate sampling in mass points to reflect changes in the photosphere encoded into bolometric corrections. Our exploration of the Pleiades single star sequence with the folded stellar atmospheres shows that the Baraffe et al. (2015) isochrones suffer from a paucity of $M_{\rm ini}$ samples. As shown in Figure 3.21, this can cause the interiors to poorly sample the bolometric corrections, leading to discrepancies in magnitudes and colours. Our solution to this was to quadratically interpolate the interiors to a factor of 10 more points in mass. Figure 3.21 shows how the models with finer sampling are better able to reproduce the colours of the bolometric corrections. Figure 3.22 shows the difference that increased sampling offers as a function of $T_{\rm eff}$. This suggests that we could expect discrepancies of up to $g_{\rm WFC} - K_{\rm s,UKIDSS} = 0.1 - 0.5$ in the colours of the model isochrones for the Pleiades.

What remains for debate is how physical rapid changes in colour actually are. As

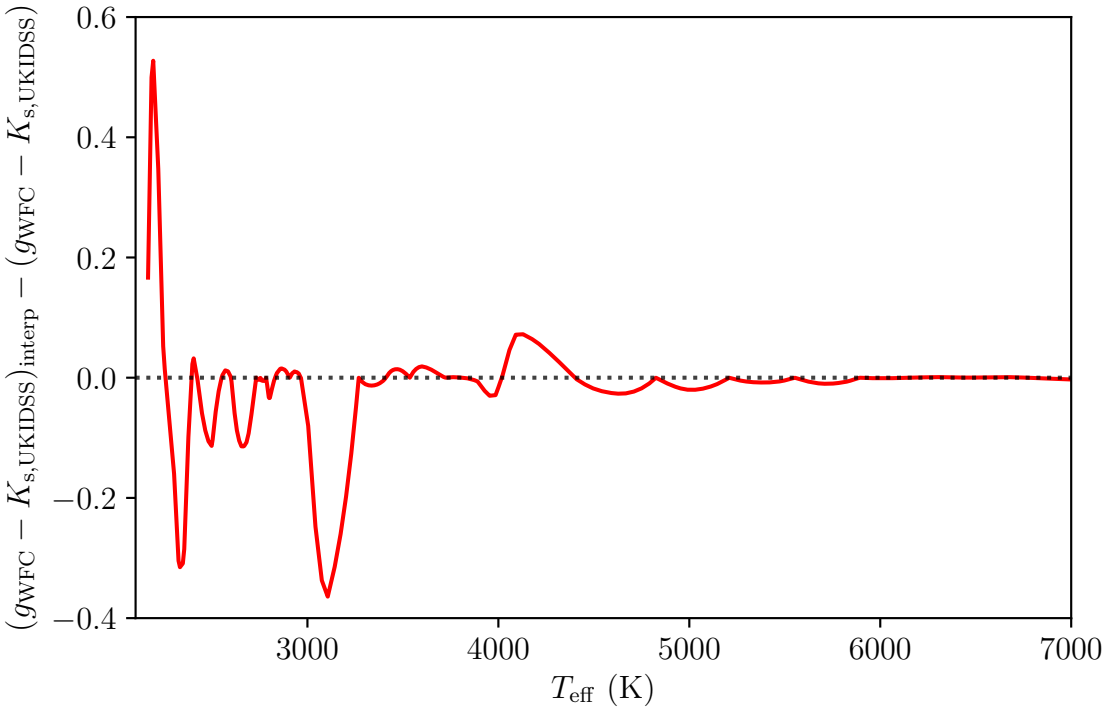

Figure 3.22: The discrepancy between the quadratically interpolated and non-interpolated Baraffe et al. (2015) Pleiades isochrone in the $(g_{\rm WFC} - -K_{\rm UKIDSS}) - -T_{\rm eff}$ plane. This suggests that colour discrepancies of up to $g_{\rm WFC} - K_{\rm s,UKIDSS} = 0.1 - 0.5$ can be expected, depending on temperature, at $T_{\rm eff} < 6000$ K. When the isochrone becomes more finely sampled at $T_{\rm eff} > 6000$ K the discrepancy largely disappears.

is demonstrated in Section 4.2, the CIFIST atmospheres, and therefore bolometric corrections, exhibit a discontinuity at 4000 K—indicating that the discrepancy is unphysical. Regardless, this demonstrates that one should carefully consider the sampling of interpolations when producing isochrones.

3.6 Chapter Summary

I have used photometric and robustly flux calibrated spectroscopic data to perform an exploration of the temperature–radius relations of the single star sequence in the Pleiades and Praesepe cluster. Colours and magnitudes in both clusters indicate inconsistencies between observations and theoretical models. Indeed, by measuring the radii and temperatures by employing my SED fitting technique to cluster members, this assertion is corroborated. This SED fitting methodology allows the decoupling of the stellar interiors from the atmospheres, permitting both to be studied in isolation. By using the temperature and radius measurements as inputs, I was able to produce a set of synthetic spectral

observations, which could be directly compared to spectroscopic observations. A direct comparison was drawn between them by plotting one atop the other. This study shows that the continuum fluxes of both are in excellent agreement, with many spectral features being replicated between the two. However, it was also clear that some opacities still need refining. The interiors were tested by plotting the isochrones alongside the $T_{\rm SED} - R$ measurements themselves. The SED fitting yields an empirical single star sequence for each cluster, which was found to be inflated by between $8 - 20\%$ for $T_{\rm eff} < 4000$ K. Thus I conclude that the stellar interiors are missing key physics that is required to properly describe the interiors of pre-MS stars. Furthermore, I have been able to confirm that isochrone fitting performed in the theoretical plane only on low-mass pre-MS cluster members will yield ages that are a factor of 2–3 too short for both studied clusters.

Chapter 4

Exploring the M-dwarf Luminosity–Temperature–Radius Relations using Gaia DR2

"There is a way out of every box, a solution to every puzzle; it's just a matter of finding it."

— Jean - Luc Picard

I established in Chapter 3 that pre-MS, low-mass stars are inflated above theoretical models. The work in this chapter demonstrates that their MS counterparts are also inflated. Importantly, I will assess how this inflation varies as a function of stellar mass and whether all stars at a given mass are equally inflated.

4.1 Method

Given a precise parallax one can integrate the area beneath the SED to find the luminosity of the star, while the shape of the SED is a function of temperature. With these, the radius of the star can be calculated. Importantly, both are a function of only the stellar photosphere; allowing the fitting process to be uncoupled from the model interiors. Hence using just synthetic photometry from model atmospheres I have developed a method that

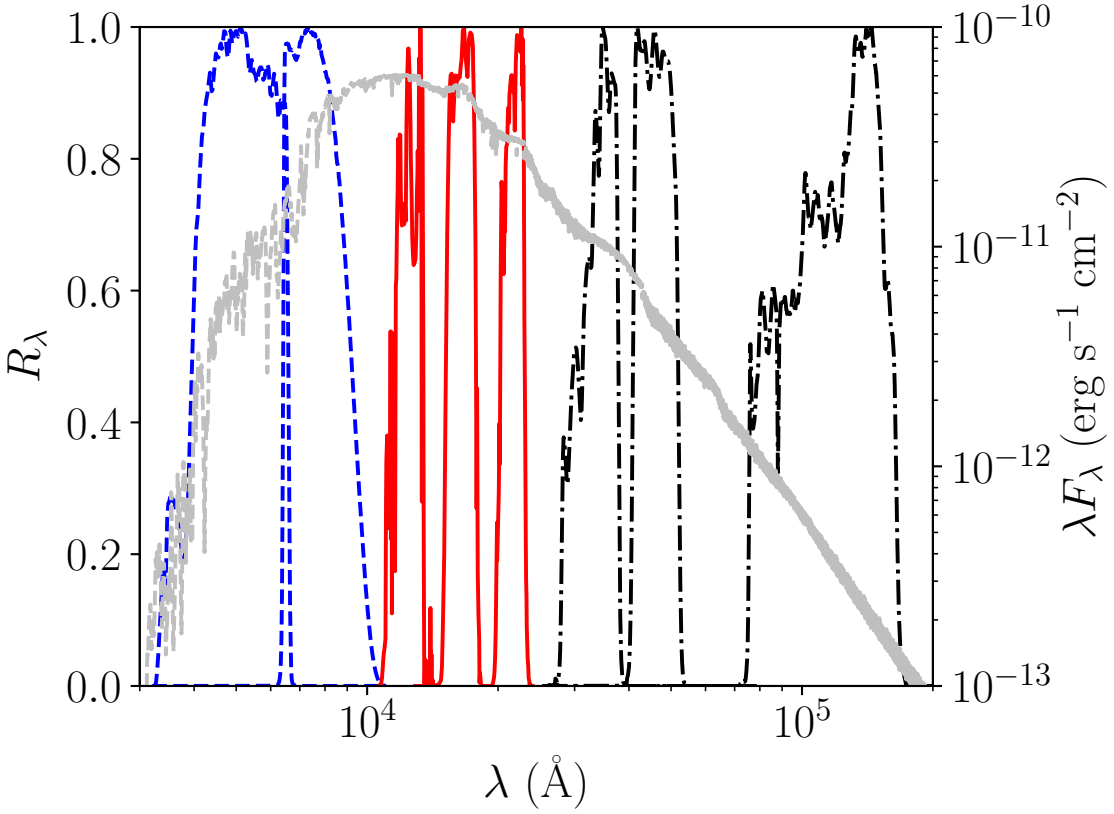

Figure 4.1: The system responses used to generate the synthetic photometry. The photometry is comprised of magnitudes from Gaia (blue dashed), the Two Micron All-Sky Survey (red solid) and WISE (black dot-dashed). For reference, the model spectrum for an M-dwarf star with an effective temperature $T_{\rm eff}$ = 3300 K is included (grey dashed)

.

uses broadband photometry, readily available from public surveys, to sample the SED and infer these properties.

The bands that were used, which comprised broadband photometry from optical, near-infrared and mid-infrared surveys, are detailed in Table 4.1. The system responses used to generate the synthetic photometry are plotted in Figure 4.1, along with a model spectrum of an M-dwarf star. This helps justify my motivation for the choice of data and photometric systems. First, all photometric systems correspond to all sky surveys whose system responses are well understood. This means that not only can I draw a sample of stars from the entire sky, but the characterisation of the system responses means that the folded photometry will closely replicate the original photometry. Using these surveys, I also have excellent coverage of the stellar SED, with the optical Gaia prism photometry (Gaia Collaboration et al. 2016; Gaia Collaboration et al. 2018b) sampling blue-ward of the

blackbody peak, 2MASS NIR photometry (Skrutskie et al. 2006) sampling the peak itself and AllWISE photometry (Wright et al. 2010) constraining the Rayleigh-Jeans tail down to fluxes 3 orders of magnitude lower than the peak. This combination means that I have the ability to accurately constrain the colour of the objects, and thus the $T_{\rm SED}$, and make a robust estimate of the luminosity of a star from its entire SED.

Band	λ_{iso} (Å)	System	Selection Criteria	No. Sources	Coverage	Source
–	–	–	$r_{est} \leq 100pc$ $(r_{hi} - r_{lo})/r_{est} < 0.01$	138 279	100.0%	Bailer-Jones et al. (2018)
G_{BP} G_{RP}	5320 7970	Gaia DR2	G_{BP} - $G_{RP} > 1.5$ $\pi > 9.0$ $\delta\pi/\pi < 0.02$	99 288	71.8%	Gaia Collaboration et al. (2016) Gaia Collaboration et al. (2018b) Passbands: Evans et al. (2018) [α,β]
J_{2MASS} H_{2MASS} $K_{s,2MASS}$	12410 16513 21656	2MASS	ph_qual = "AAA"	55 379	40.0%	Skrutskie et al. (2006)
W_1 W_2 W_3	33792 46293 123338	WISE	ext_flg = 0 cc_flags = "000" ph_qual = A or B $\delta W_3/W_3 < 0.05$	26 182	18.9%	Wright et al. (2010)
All				15 765	11.4%	

Table 4.1: The sources of the photometric data used for the SED fitting described in Section 2.1. To aid in comparison to plots, each filter is listed with its isophotal effective wavelength λ_{iso}, criteria used to select the photometry, and original source. The bands are grouped into photometric systems and in order of ascending λ_{iso}. The λ_{iso} is determined by integrating $f_\lambda = 1$ across the filter, unless directly quoted in the source paper. Due to the poor quality of the photometry, the W4 band has been omitted from the fitting.

[α] Passbands available from https://www.cosmos.esa.int/web/gaia/iow_20180316.

[β] As this paper was nearing completion Maız Apellániz & Weiler (2018) was published which presented further revisions to the Gaia system responses. After careful analysis we found that the differences between the fits resulting from grids consisting of both sets of response curves was contained within the majority of formal uncertainties of our resulting stellar properties.

4.1.1 Target Selection

Each catalogue used is shown in Table 4.1 along with the relevant publications. I began by selecting all stars from Gaia DR2 with $r_{\rm est} < 100$pc from Bailer-Jones et al. (2018). I chose this distance cut because the systematic uncertainties in the Gaia DR2 parallaxes generally remain below 0.1mas (Lindegren et al. 2018). This constraint guarantees that my distances are not affected by Gaia's astrometric systematics while remaining good to 2% uncertainty in luminosity. Interestingly, by considering Equation 1.58, one can see that at the short distances (< 0.1kpc) and small distance uncertainty (< 1%) used in this catalogue, the terms that provide the correction for both the Lutz & Kelker (1973) bias and the asymmetry in the transform between parallax and distance become negligible; meaning that there is only a small benefit in using the full Bayesian treatment over simply inverting the parallax for this input sample. This preliminary sample comprised 138 279 sources. Each photometric catalogue was then cross matched with this preliminary sample and the quality cuts shown in Table 4.1 applied. I omitted the W_4 band from the fitting process due to its poor signal-to-noise, and because W_3 does an adequate job of characterising the Rayleigh–Jeans tail of even the coolest stars in the sample. The final input catalogue was then constructed by combining the photometry for only the stars common to all source catalogues. The number of sources remaining in the final input catalogue is 15 765.

4.1.2 Flagging

In addition to the initial cuts that were performed on the source catalogues, which already produced a stringently constrained sample, I also performed additional post processing to produce flags to be included with the fitted parameters. As the $G_{\rm BP}$ and $G_{\rm RP}$ fluxes are integrated over a 3.5×2.5 arcsec^2 field they are susceptible to contamination from both bright, nearby sources and sky background. Following the method of Evans et al. (2018), I applied the **bad_phot** photometric contamination flag by σ-clipping sources in the flux excess ratio vs. colour plane. See Figure 4.2 for the resulting classification after 8 iterations.

The Gaia astrometric data can similarly suffer contamination from crowding and

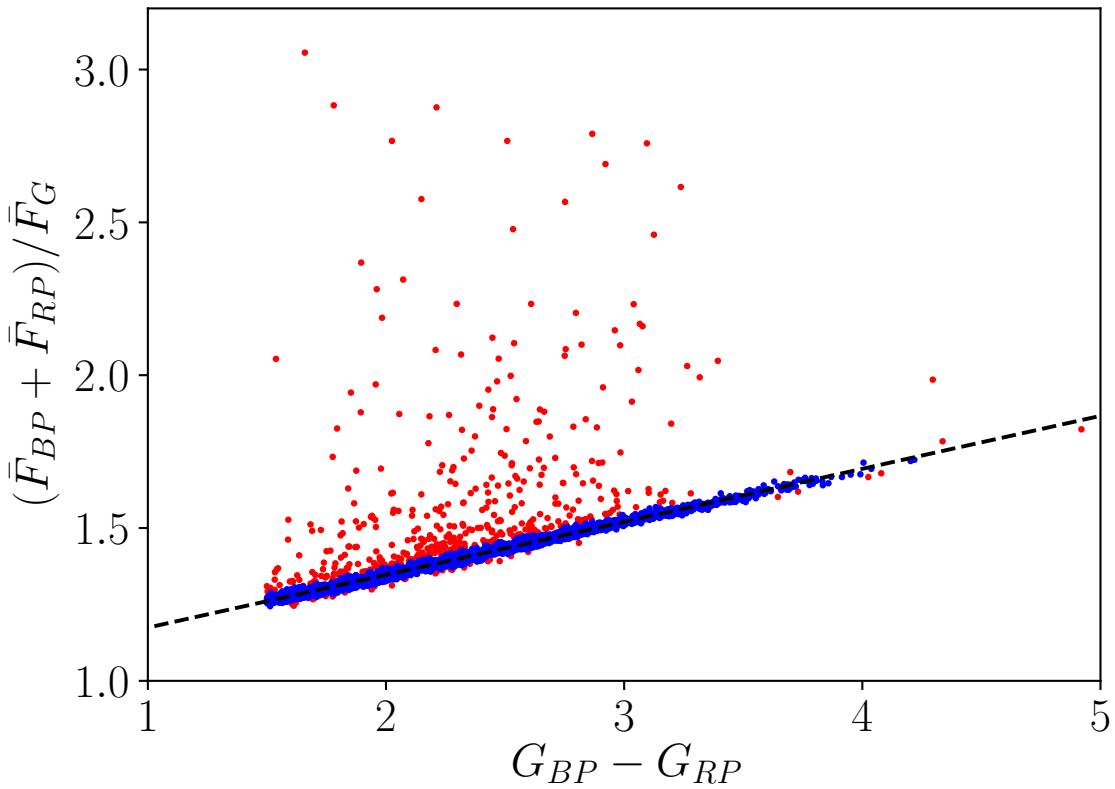

Figure 4.2: This figure illustrates the sigma clipping performed on the final catalogue. The black dashed line shows the final linear fit to the clipped sample after 8 iterations. The red points in this plot are those lying more than 5σ away from this line, and are thus flagged as **bad_phot**. Those points remaining in blue lie within 5σ of the fit, and are considered to have uncontaminated Gaia photometry.

binaries, causing both exaggerated and errant parallaxes (Lindegren et al. 2018). For a similar sample in Lindegren et al. (2018), the criterion

$$u < 1.2 \times \max\left(1,\ e^{-0.2(G_G - 19.5)}\right) \tag{4.1}$$

was used to clean the sample of poor astrometry. Thus, any source that does not satisfy this expression is flagged with the **bad_astr** flag in the final catalogue.

There are also those sources for which the fitting could not converge on a reasonable solution, probably because their true $T_{\rm SED}$ lies outside the bounds of my sample space. Thus sources lying on either $T_{\rm eff}$ bound are flagged as **bad_teff** in the final catalogue. Finally, those sources which remained unflagged were assigned the **good** flag, meaning their input data should be free of both photometric and astrometric contamination, and they should have a well constrained $T_{\rm SED}$.

4.1.3 Photometric Fitting

I performed the fitting on the input catalogue using the methodology described in Section 2.1. For σ_i I adopted a floor value of 0.01 mag, which corresponds to roughly 1%, for all photometric uncertainties in the entire sample. Due to computational time constraints, performing a full 3D grid search on the full sample was intractible. Thus, the stellar radii were determined using the analytical minimisation method detailed in Section 2.1.6. I randomly picked 158 stars from my input catalogue, 1% of the sample, upon which the full grid search was performed. I used this subset to determine uncertainties characteristic of the full sample. The 68% confidence contours from which those uncertainties are derived are shown in Figure 4.3.

4.2 Results

Of the 15 765 targets in the input catalogue, 15 279 of them are flagged as **good**. The sample have been plotted in $R - T_{\rm SED}$ space in Figure 4.5, along with a selection of solar metallicity isochrones at 1 Gyr and 4 Gyr. The 68% confidence contours in the $R - T_{\rm SED}$ space from the subset described in Section 2.1 are shown in Figure 4.3. These show that

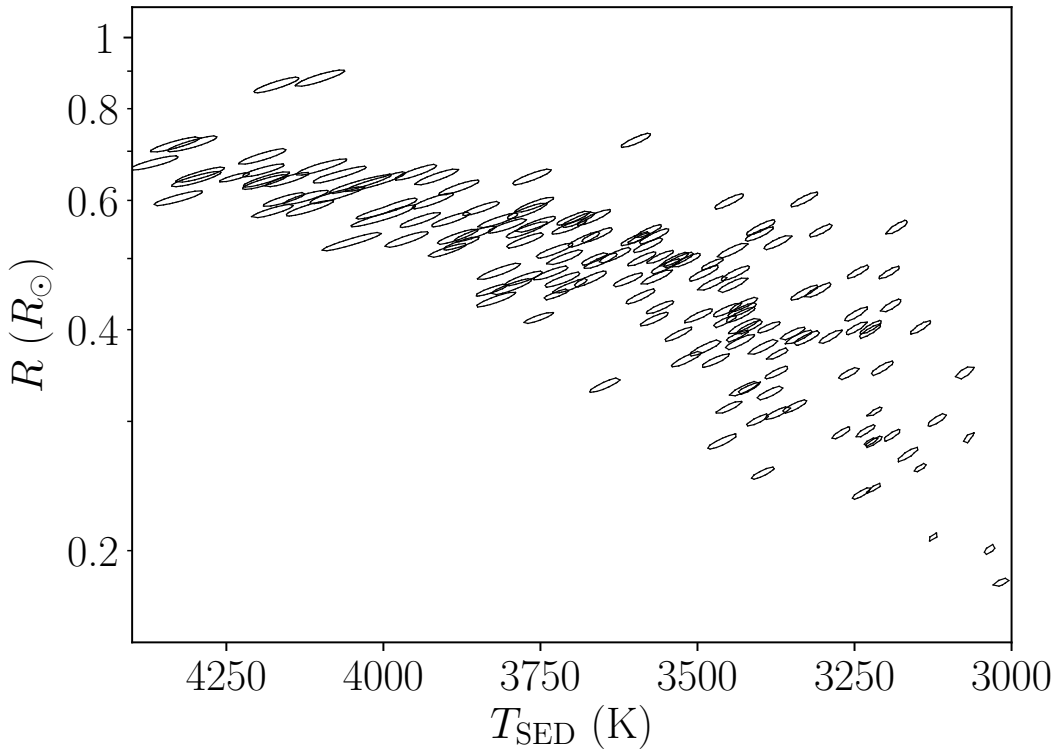

Figure 4.3: The 68% confidence contours resulting from the full 3D grid search I performed on 1% of my sample (158 stars) in Section 2.1.

I am able to determine the radius to a median statistical uncertainty of 0.009 $R_\odot$ (1.6%), ranging to a maximum uncertainty of 0.025 $R_\odot$ (2.6%). I found the mean uncertainty in temperature $T_{\rm SED}$ was 35 K (1.0%), ranging to a maximum of 100 K (2.7%).

The gap in the stellar sequence at 4000 K in Figure 4.5 is caused by a discontinuity in the CIFIST BT-Settl model grid where the monotonic relationship between bolometric correction, defined as $M_{\rm bol} - M_i$ where M_i is the absolute magnitude of the $i^{\rm th}$ photometric band, and $T_{\rm eff}$ breaks down (Figure 4.4). I found that comparisons between observations and the SED resulting from the atmosphere at 4000 K produce a higher χ^2 than those from the neighbouring atmospheres, causing my fitting to favour the SEDs produced from the atmospheres adjacent to that at 4000 K. That this is a property of the model, as opposed to the fitting process, is supported by the fact that when the fitting is performed with grids derived from different atmospheres, as with the sub and super-solar metallicity grids in Section 4.3.2.5, the discontinuity disappears.

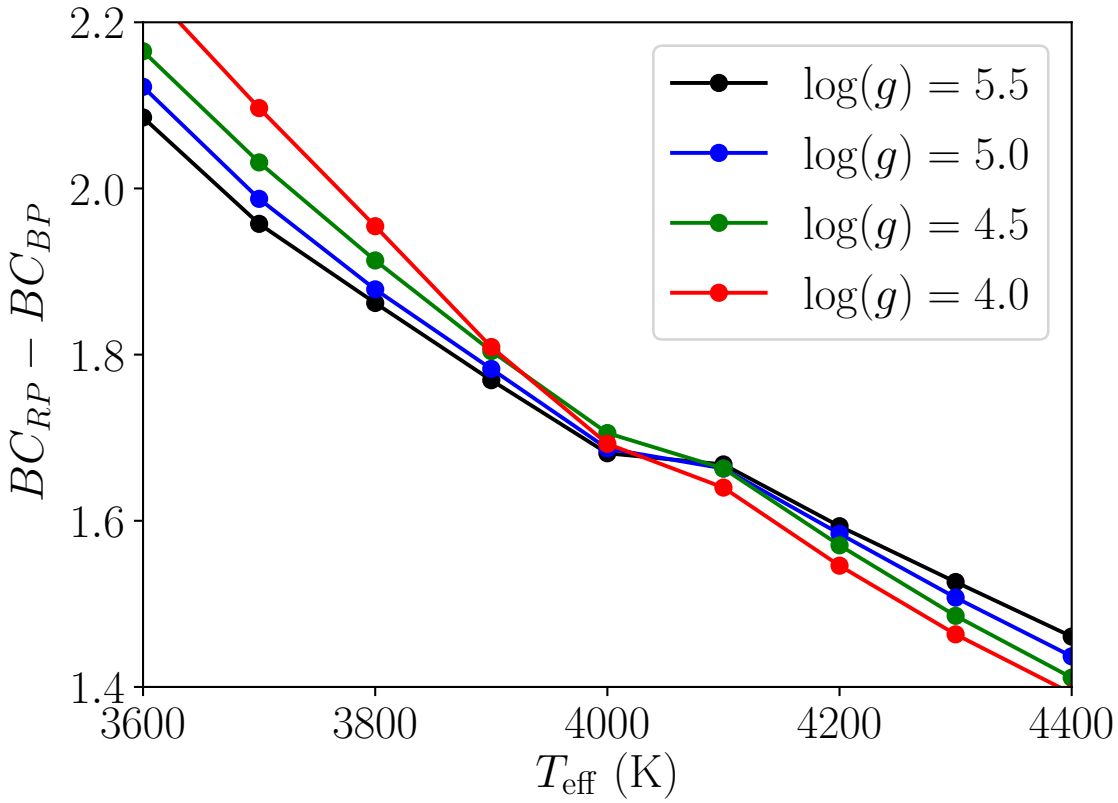

Figure 4.4: The gap in the stellar sequence at 4000 K evident in Figure 4.5 is due to a discontinuity in the CIFIST BT-Settl model grid. By plotting the bolometric corrections from the Gaia DR2 bands this effect is clearly seen. The plot shows $\log(g) = 4.0, 4.5, 5.0$ and 5.5 (black, blue, green and red respectively) to demonstrate that this discontinuity affects the entire span of $\log(g)$ sampled by my grid.

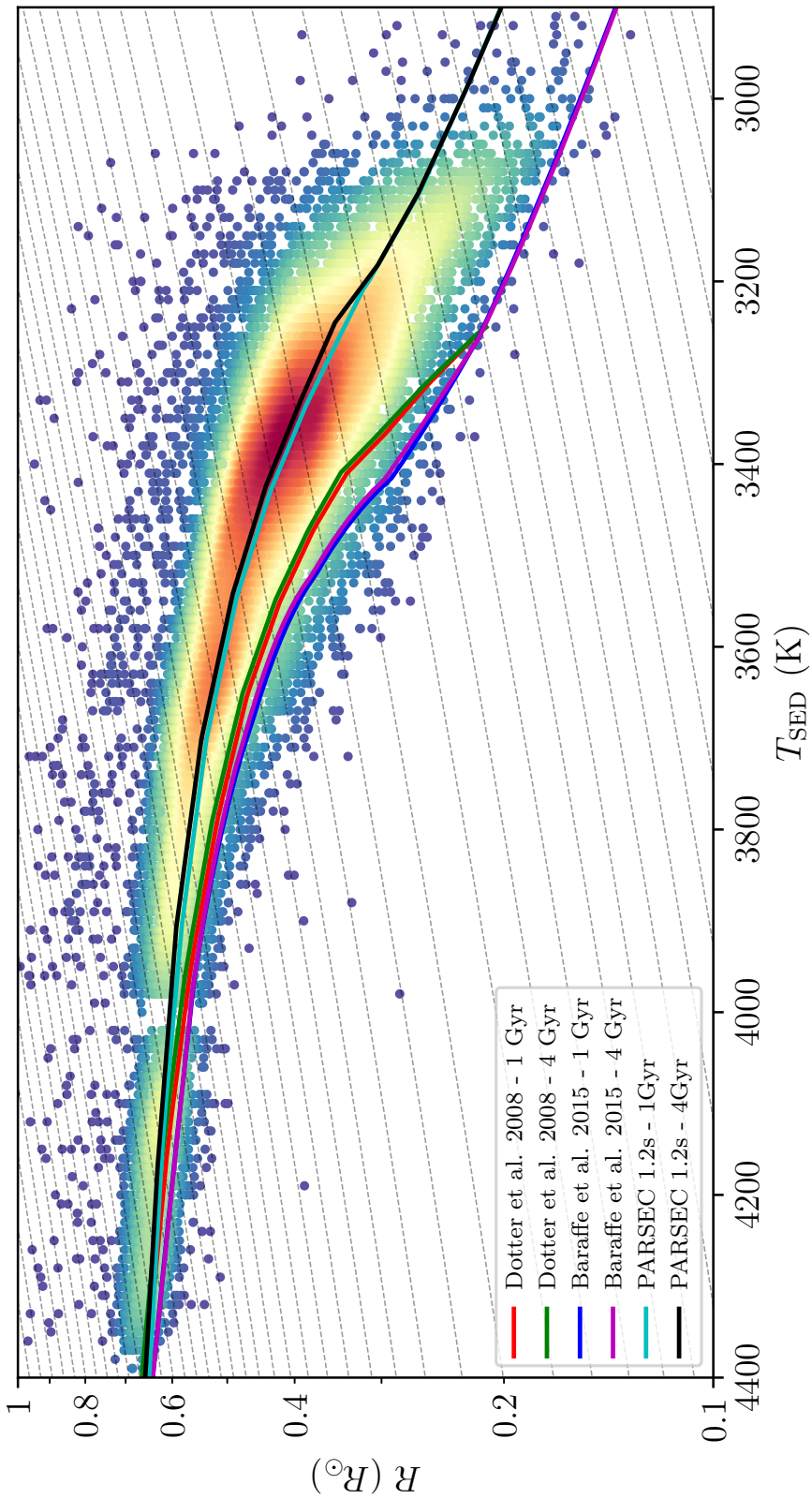

Figure 4.5: The distribution of points from the full sample of 15 279 sources in $T_{\rm SED} - R$ space. The colour map results from a kernel density estimation, which is intended to indicate the density of points within the plot. For comparison, I have included the Dotter et al. (2008) isochrones for z=0.018 at 1 and 4 Gyr, Baraffe et al. (2015) isochrones for 1 and 4 Gyr and PARSEC 1.2S (Chen et al. 2014; Marigo et al. 2017) isochrones for 1 and 4 Gyr in red, green, blue, purple, cyan and black lines respectively. Several points are clipped off the sides of the figure. The dashed lines trace constant luminosity, drawn every 100 K along the Baraffe et al. (2015) isochrone.

4.2.1 Radius Inflation

In Figure 4.5 the purely theoretical models undershoot the median of the radius distribution for all M-dwarf stars within my sample. However the PARSEC 1.2S model, which is calibrated by adopting an empirical $T - \tau$ relation derived from DEBs as the boundary condition for the stellar interiors, traces the median radius well for the whole sample. When inferring the radius inflation of a sample of stars, the choice of parameters is of vital importance. As Figure 4.3 shows, the uncertainties in $T_{\rm SED}$ and R are strongly correlated; one cannot simply trace upwards from the theoretical sequence to infer the inflation. As mass is most closely related to luminosity, the radius inflation should in fact be measured in the more fundamental $L_{\rm SED} - R$ plane, shown in Figure 4.6. I measured the radius inflation for each of the models used in this work by picking a point of identical luminosity from the models and finding the difference between the prescribed model radius and my inferred radius.

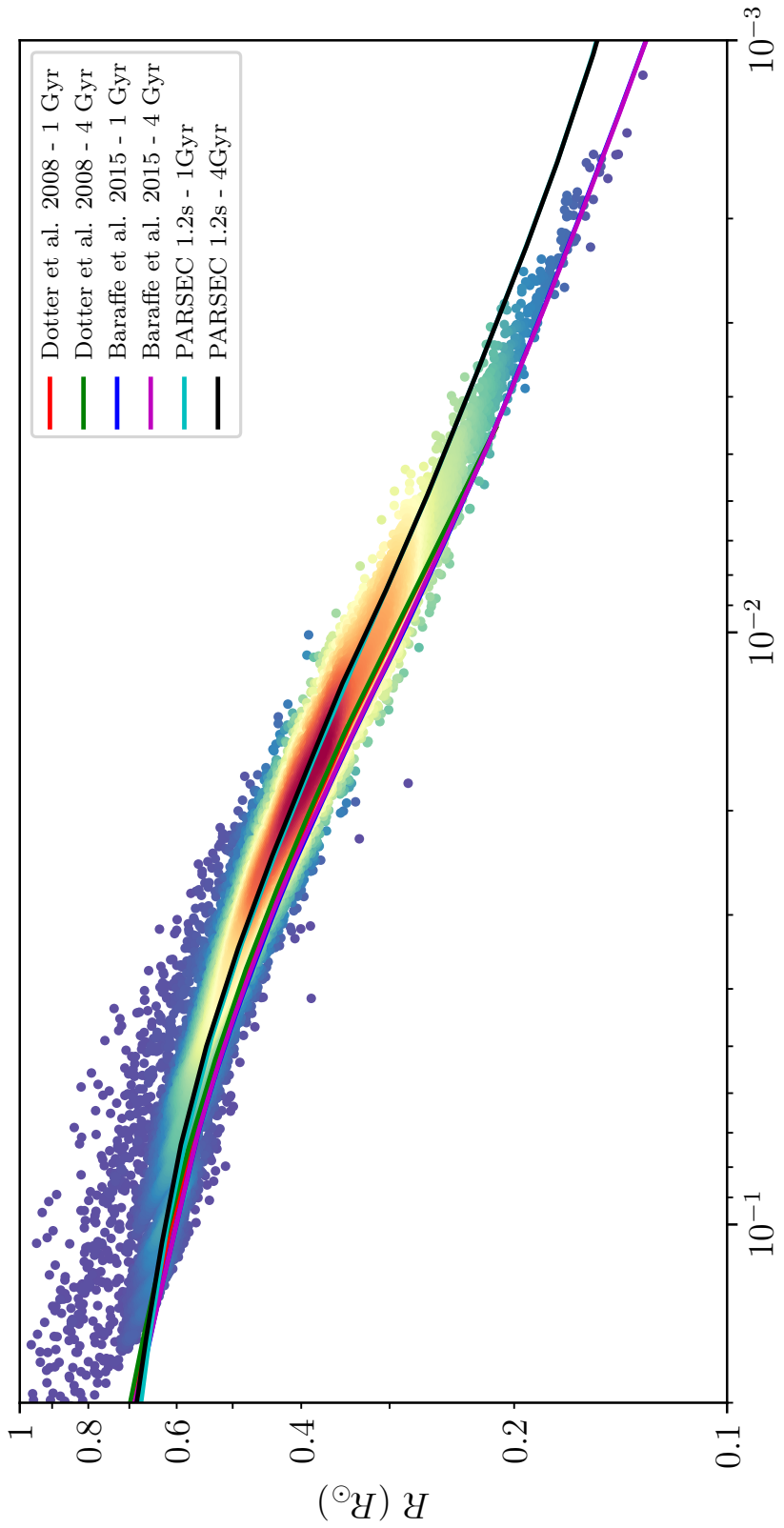

Figure 4.6: The **good** sample of the dataset in the $L_{\rm SED} - R$ plane. Due to the strong correlation between the axes in the $T_{\rm SED} - R$ plane, this plane is preferable for accurately measuring radius inflation in my sample. Accompanying the data are the same isochrones as in Figure 4.5. The Dotter et al. (2008) and Baraffe et al. (2015) isochrones trace a similar sequence in this space, resulting in the Dotter et al. (2008) isochrones being hidden behind the Baraffe et al. (2015) isochrones.

4.2.2 Temperature - Radius Relation

The fits can be used to derive a relation between temperature $T_{\rm SED}$ and radius R. I split the sample into 10 K bins and took the median value from each bin. I required a minimum of 11 sources per bin, otherwise the entire bin was ignored. I fitted the medians with a 2$^{\rm nd}$-order polynomial, which is shown in Figure 4.7 as the blue line, with the black points being the median values. The error bars are the standard deviation of the radius distribution within each bin. The relation that was fitted from this sample is

$$\begin{aligned} R_{\rm fit}(T_{\rm SED}) &= -3.842 + 2.046\times10^{-3}\,T_{\rm SED} - 2.328\times10^{-7}\,T_{\rm SED}^2, \\ & 3000\ {\rm K} \leq T_{\rm SED} \leq 4400\ {\rm K}. \end{aligned} \tag{4.2}$$

Using the same bins as before, I also drew the points that lie at the 16$^{\rm th}$ and 84$^{\rm th}$ percentiles to find the value of 1σ for each bin. These points were used to fit further 2$^{\rm nd}$-order polynomials to yield upper $R_{\rm high}$ and lower $R_{\rm low}$ confidence radii for each bin. The upper and lower bound radii are given by

$$\begin{aligned} R_{\rm high}\,(T_{\rm SED}) &= -3.336 + 1.835\times10^{-3}\,T_{\rm SED} - 2.090\times10^{-7}\,T_{\rm SED}^2, \\ & 3000\ {\rm K} \leq T_{\rm SED} \leq 4400\ {\rm K}, \end{aligned} \tag{4.3}$$

$$\begin{aligned} R_{\rm low}\,(T_{\rm SED}) &= -3.258 + 1.674\times10^{-3}\,T_{\rm SED} - 1.792\times10^{-7}\,T_{\rm SED}^2, \\ & 3000\ {\rm K} \leq T_{\rm SED} \leq 4400\ {\rm K}. \end{aligned} \tag{4.4}$$

These functions are also shown in Figure 4.7. These bounds are separated by 4% at 4400 K, increasing to 12% at 3500 K and reaching a maximum separation of 30% at the lower temperature limit of 3000 K. This scatter is further discussed in Section 4.3.

4.2.3 Luminosity–Radius Relation

Temperature–radius relations are useful for the purposes of exoplanet host characterisation, however the stellar modelling community relies on more fundamental parameters when testing models. I have therefore transformed the temperature–radius data into the arguably more fundamental luminosity–radius plane, and used it to fit a relationship using a similar methodology. However, deriving a relation between luminosity L and radius

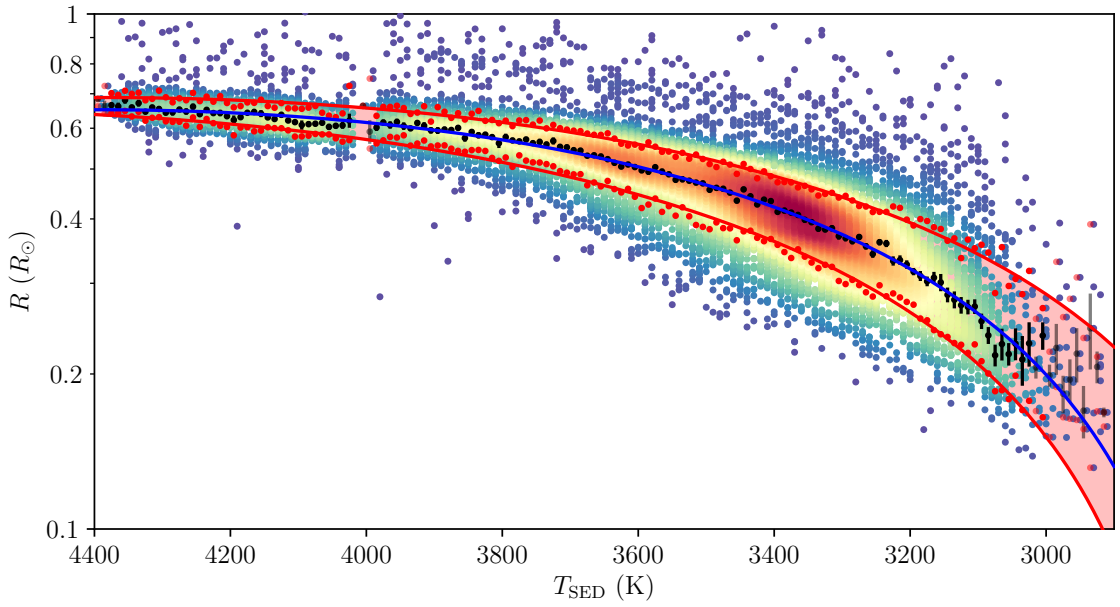

Figure 4.7: The $T_{\rm SED} - R$ relationship derived for the sample. The final relationship, given by Equation 4.2, is the solid blue line along with its 68% confidence intervals shown in red. The black dots show the stars used to perform the fit of the relationship. The red points bordering the upper and lower bound lines also show the stars used to fit them. The points in bins flagged as not good, and thus not used during fitting, are shown with semi-transparent markers.

R is more problematic, as high order polynomials are required to capture the detail in the relation. Despite falling below the majority of the radius distribution, the isochrones do a good job of predicting the shape of this dataset; suggesting the models capture the physical changes involved. Hence I created the $L_{\rm SED} - R$ relationship as corrections to the Dotter et al. (2008) 4Gyr solar metallicity isochrone. I subtracted the radius given by the isochrone from the median, upper and lower bound radius in each bin, leaving the difference between theoretical and observed radii. Then, to get the relation, I simply added the correction to the radius prescribed by the isochrone. This relation holds for values between $L_{\rm SED} = 0.003\ L_\odot$ and $L_{\rm SED} = 0.1\ L_\odot$. The correction to the Dotter et al. (2008) isochrone is given by

$$R_{\rm fit}(L_{\rm SED}) = R_{\rm D08}(L_{\rm SED}) + 0.0136 + 0.7087 L_{\rm SED} - 7.6924 L_{\rm SED}^2,$$
$$0.003\ L_\odot \leq L_{\rm SED} \leq 0.1\ L_\odot \tag{4.5}$$

where $L_{\rm SED}$ is the luminosity derived from my SED fitting and $R_{\rm D08}(L_{\rm SED})$ is the theoretical radius of the star predicted by the Dotter et al. (2008) isochrone at the given luminosity.

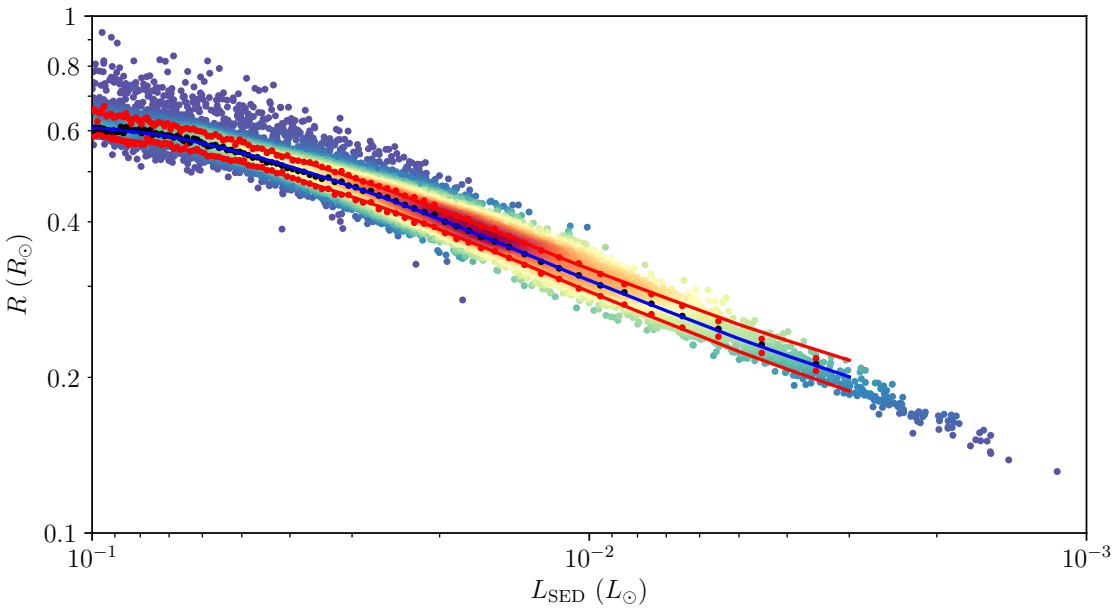

Figure 4.8: The luminosity - radius relationship plotted atop the stars from the sample. As with Figure 4.7, the relation (blue) and upper and lower bound lines (red) are shown, with the points from which each of the lines were fit in the corresponding colour.

The upper and lower bounds for the relation are given by

$$R_{\rm high}\ (L_{\rm SED}) = R_{\rm D08}(L_{\rm SED}) + 0.0288 + 0.7662 L_{\rm SED} - 5.4204 L_{\rm SED}^2,$$
$$0.003\ L_\odot \leq L_{\rm SED} \leq 0.1\ L_\odot \tag{4.6}$$
$$R_{\rm low}\ (L_{\rm SED}) = R_{\rm D08}(L_{\rm SED}) + 0.0026 + 0.2696 L_{\rm SED} - 4.2515 L_{\rm SED}^2,$$
$$0.003\ L_\odot \leq L_{\rm SED} \leq 0.1\ L_\odot. \tag{4.7}$$

The correction and final relation are shown atop the data in Figure 4.9 and Figure 4.8 respectively.

4.3 Discussion

4.3.1 Comparison with Literature Radii

To compare my measure of radius inflation with that from DEBs, interferometry and $L_{\rm SED} + T_{\rm sp}$ (Mann et al. 2015) I limited the data to the range 3400 K to 4400 K, where all methods are well sampled. The mode of all methods coincides at 3−7% inflated compared to the models. In Figure 4.10 I plotted the distribution of relative radius residual from

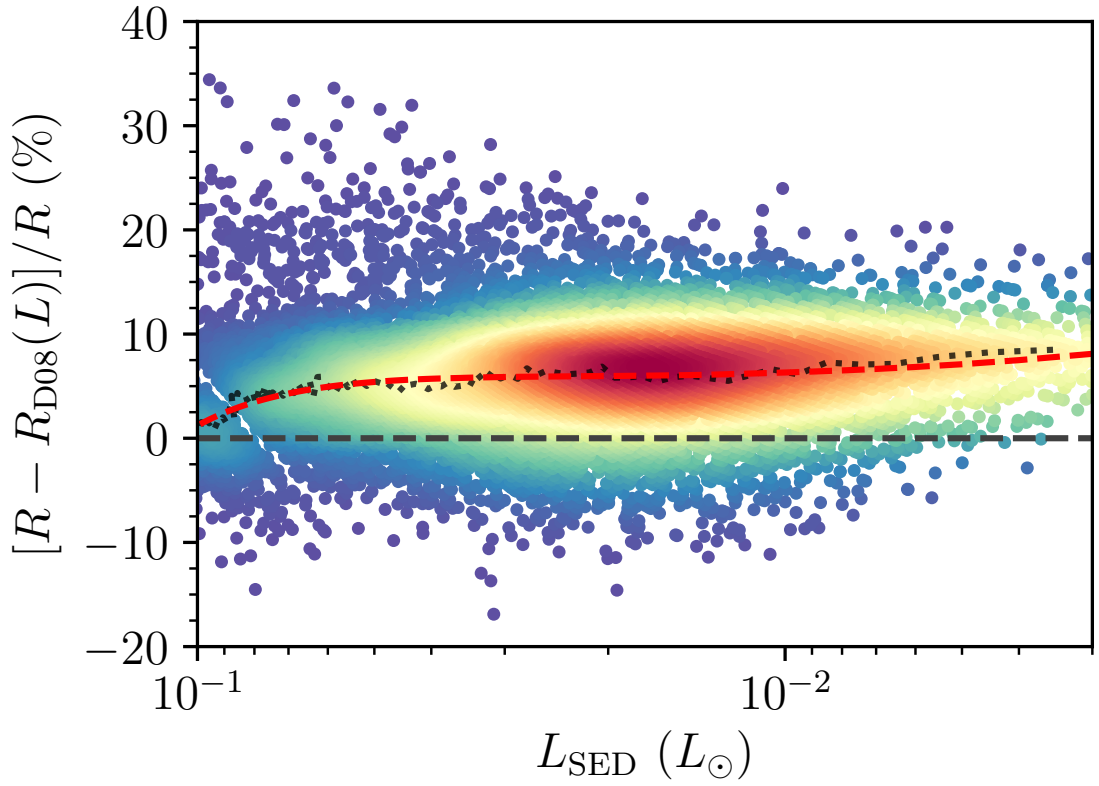

Figure 4.9: The radius inflation of my data from the 4 Gyr Dotter et al. (2008) solar metallicity isochrone $[R - R_{\rm D08}(L)]/R$. The median radius inflation within each luminosity bin is shown as a black point. The luminosity–radius correction to this same isochrone is overlaid as a dashed red line.

Equation 4.5 (see Section 4.2.3). The DEB and interferometric samples show medians at around 3% lower than mine. The $L_{\rm SED} + T_{\rm sp}$ median corresponds well with mine, however it does exhibit a second peak at 7% under inflation, though it is difficult to be sure whether this is a genuine feature of the population. There is also a long tail of outliers on the high inflation wing of my distribution; I suggest that these are a small number of binaries that have leaked into the sample.

In Figure 4.11 I compare the interferometric, eclipsing binary and $L_{\rm SED} - T_{\rm sp}$ datasets with mine as a function of luminosity, as I require that the datasets have another physical quantity in common in addition to the radius. For the reasons outlined in Section 4.3.2 luminosity is the best abscissa to use. Although the eclipsing binaries are normally viewed as a mass-radius dataset, the eclipsing binaries to which I am comparing also have temperatures derived from the spectra or photometric surface brightness, which in combination with the radius allows me to calculate a luminosity. The natural plane for the interferometric data is the luminosity0-radius plane. The $L_{\rm SED}$ + $T_{\rm sp}$ dataset can again be converted into $L_{\rm SED}$–radius. The data presented in this paper are derived in the $T_{\rm SED}$–radius plane, and so can be converted into the $L_{\rm SED} - R$ plane. I emphasize that all of these comparisons can only be made assuming $T_{\rm SED} = T_{\rm sp} = T_{\rm eff} = T_{\rm br}$, where $T_{\rm br}$ is the brightness temperature measured for some eclipsing binaries. As Figure 4.11 shows, all datasets show a radius inflation with respect to the models.

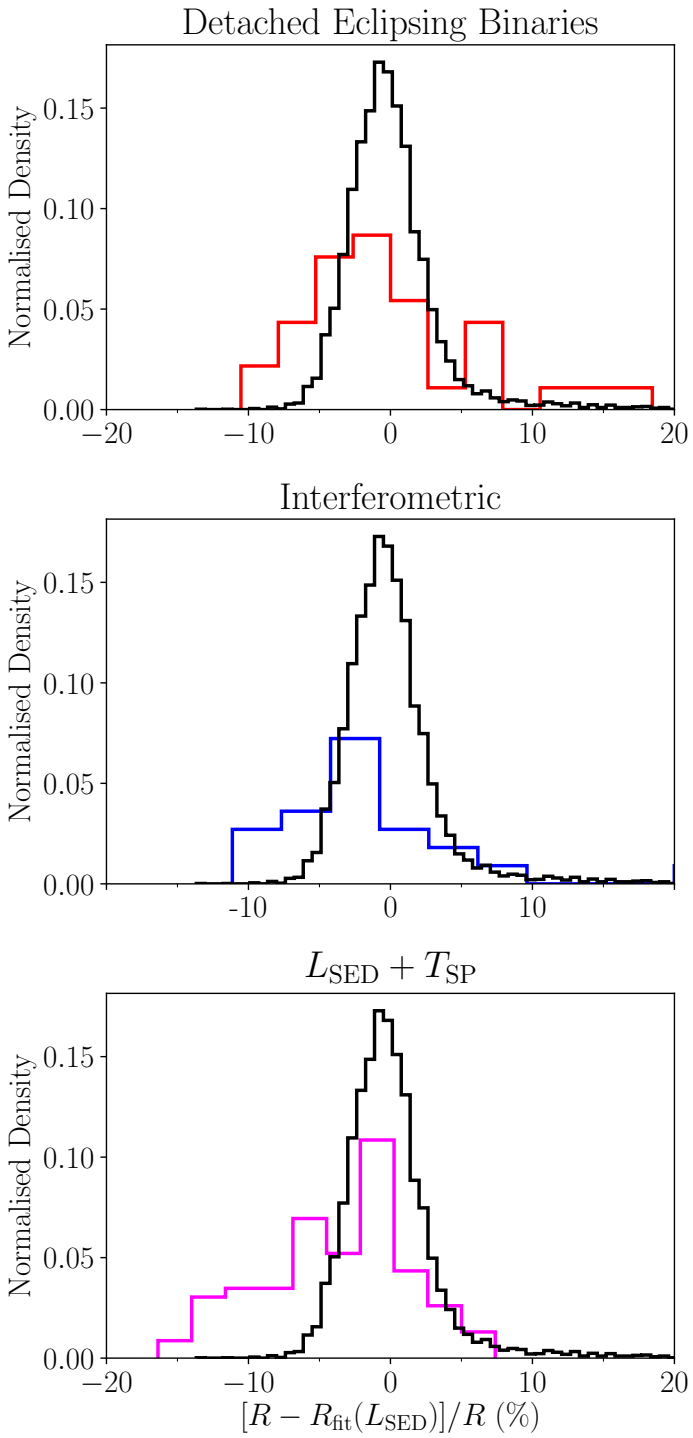

Figure 4.10: A comparison between the distributions of the relative residual of my measured radius R with respect to my $L_{\rm SED} - R$ relation $R_{\rm fit}(L_{\rm SED})$; defined in Equation 4.5. My sample is shown in black, with each of the others overplotted. Both the interferometric and DEB sample have median values about 3% below mine. The Mann et al. (2015) sample exhibits a bimodal structure, with the more pronounced peak occurring close to my median.

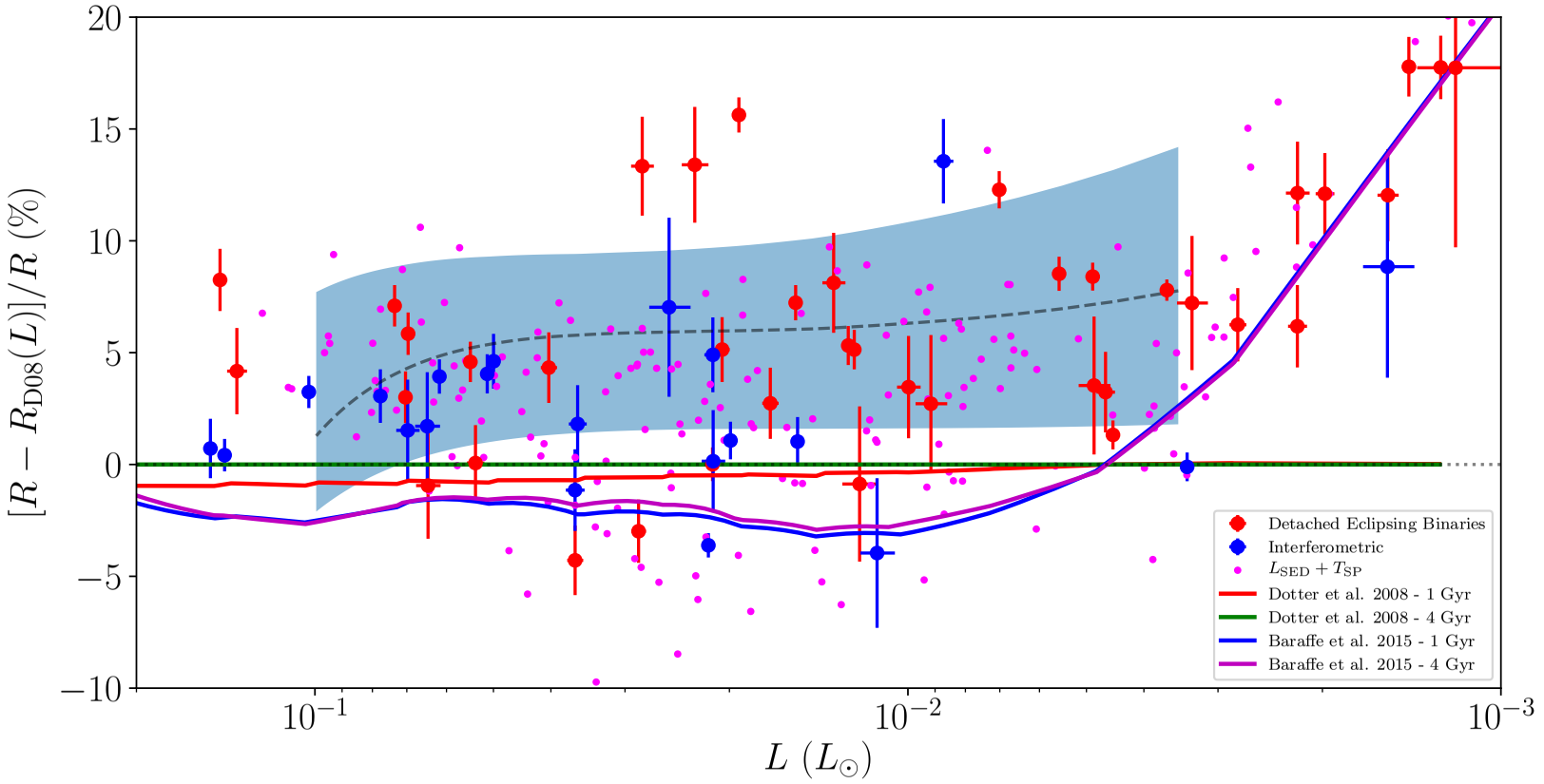

Figure 4.11: The radius inflation with respect to the Dotter et al. (2008) 4 Gyr isochrone ($[R - R_{\rm D08}(L)]/R$) obtained by the four different methods. Inflation is plotted as a function of luminosity. The red points show detached eclipsing binaries (Southworth 2015; Parsons et al. 2018). The blue points show interferometric stars (Boyajian et al. 2012). The pink points show stars from Mann et al. (2015). The error bars for this sample have been omitted for reasons of clarity. The luminosity–radius relation derived in this paper (grey dashed line) with its associated 68% density bounds is also shown. For comparison, model isochrones for 1Gyr and 4Gyr ages are shown for Dotter et al. (2008) at $z = 0.018$ and Baraffe et al. (2015). The original sources for Southworth (2015) are Welsh et al. (2015), Torres et al. (2014), Torres & Ribas (2002), Terrien et al. (2012), Stassun et al. (2004), Rozyczka et al. (2009), Rozyczka et al. (2007), Pietrzyński et al. (2013), Morales et al. (2009b), Morales et al. (2009a), Kraus et al. (2017), Kraus et al. (2011b), Hełminiak et al. (2015), and Hartman et al. (2018). The original sources for Parsons et al. (2018) are Pyrzas et al. (2012), Parsons et al. (2018), Parsons et al. (2016), Parsons et al. (2012c), Parsons et al. (2012a), Parsons et al. (2012b), and Parsons et al. (2010).

For the luminosity range for which my $L_{SED} - R$ relation is valid, there are a total of 29 DEBs, 16 interferometric stars and 154 $L_{SED} + T_{sp}$ stars. I determined which side of my median radius these samples fall. I found 62% of the DEBs, 88% of the interferometric stars and 79% of the $L_{SED} + T_{sp}$ sample to lie below my median; meaning that all 3 other methods yield a lower median radius than mine. This skew to lower radii across this range supports the distributions shown in Figure 4.10.

This difference between the methods might be due to starspots. First, any method which measures a spectroscopic temperature, especially in the optical, will not be sensitive to spots, because the immaculate photosphere spectrum will dominate the spot spectrum, leading to an over-prediction of the T_{eff} and under-prediction of radius. This affects both the eclipsing binary and $L_{SED} + T_{sp}$ sample and would result in radii smaller than those measured by my method. Although the $L_{SED} + T_{sp}$ and interferometric methods integrate under the SED of the star to find the luminosity, as SED fitting does, many of their objects saturate in WISE and so lack mid-IR coverage. Not sampling the region of the SED where the spotted photosphere has its strongest contribution relative to the immaculate photosphere, and may make a non-negligible contribution to the overall stellar flux, may cause the measured luminosity to be too low, again resulting in radii that are too small. In summary, I found the radii measured by all methods to be inflated above the theoretical sequence, albeit I measure radii that are larger than the other methods.

4.3.2 Contributions to the Radius Scatter

Figure 4.11 demonstrates that for a given luminosity there is a $3-7\%$ spread in measured radius. It is important to determine whether this radius spread is real, and if so what effects contribute to it.

4.3.2.1 Could observational uncertainties contribute to the scatter?

I first wished to establish whether the uncertainties in my radius determination could explain the spread before searching for a physical origin. Figure 4.3 shows 68% confidence contours for the uncertainty in R and T_{SED} for an unbiased sub-sample of my catalogue, which was discussed in Section 4.1.3. The mean uncertainty in this selection of stars is

1.6%; much less than the 3 – 7% spread that is observed. Furthermore I find a similar (but slightly larger) spread in the literature radii, with 62% of the DEBs, 56% of interferometric stars and 63% of the $L_{\rm SED} + T_{\rm sp}$ sample lying within my relation's 68% confidence bounds. Thus I conclude that the spread is not the result of observational uncertainties.

4.3.2.2 Does flux contamination from faint counterparts contribute to the scatter?

Wilson & Naylor (2017) show that the AllWISE bands can suffer contamination due to faint, hidden sources falling within the large PSFs of brighter stars. As well as making accurate catalogue matching problematic in crowded fields, this can also cause contamination to AllWISE photometry. Even a modest flux contamination from a stray faint source within the WISE PSF has the potential to cause a large discrepancy in both the retrieved $T_{\rm SED}$ and R. Fortunately, Wilson & Naylor (2018) provide a catalogue of Gaia DR2–WISE matches in the galactic plane, which allows me to assess the effect of contamination on my sample. According to their work, of the 2 334 sources that match between the catalogues, fewer than 4% were likely to be contaminated by 10% or more. The rest of the sky is less prone to crowding, so I suggest that 4% of sources suffering contamination is the upper limit for my entire sample. Were the AllWISE photometry affected by contamination due to the presence of an unseen counterpart, I would expect the contaminated sources to exhibit more inflated radii than clean sources. However, I found no correlation between radius inflation and the predicted flux contamination or probability found by Wilson & Naylor (2018); indicating that contamination in the WISE bands is unlikely to contribute towards the spread.

4.3.2.3 Do starspots contribute towards the radius spread?

Starspots introduce a second, cooler component to the SED; effectively diverting some of the luminosity of the star away from the immaculate photosphere. Jackson & Jeffries (2014) used a polytropic model including starspots to reproduce the radii of pre-main sequence (PMS) stars in the Pleiades and NGC 2516, which required spot coverages of between 35 and 51%. Using these models, they were able to find an 8% inflation in the stars when compared to the Baraffe et al. (2015) stellar models. Higl & Weiss (2017) were also able to explain observed radii with starspots by covering large percentages (up to

44%) of the surface of their models with spots.

My fitting assumed that the entire surface of the star is a single temperature. To examine the effect of starspots on my measured radii I wrote software which produced a catalogue of simulated magnitudes of stars with spots and ran this catalogue through the same fitting process used for the observed sample. I simulated the input catalogue by sampling from a grid with $\log(g) = 5.0$ and varying spot filling factor γ between $\gamma = 0.0 - 1.0$; whereas in all grids used for fitting data I have assumed $\gamma = 0.0$ (no spots). The composite photosphere consists of an immaculate and a spotted photosphere with temperatures $T_{\rm imac}$ and $T_{\rm spot}$ respectively. In determining the temperature of the spotted photosphere, I make the reasonable assumption (see Berdyugina 2005) that $T_{\rm spot} = 0.8\,T_{\rm imac}$ for 5000 K $< T_{\rm imac} <$ 3000 K. The synthetic magnitudes Z_i in this grid are given by

$$Z_{\lambda,\rm syn} = -2.5\log_{10}\left[\frac{\int_\lambda \left((1-\gamma)I_{\lambda\rm imac} + \gamma I_{\lambda\rm spot}\right) S_{\lambda,i} d\lambda}{\int_\lambda f^\circ_\lambda S_{\lambda,i} d\lambda}\right] + m^\circ_\lambda, \tag{4.8}$$

where $I_{\lambda\rm imac}$ and $I_{\lambda\rm spot}$ are the intensity of the immaculate and spotted photosphere respectively. The effective temperature $T_{\rm eff}$ of these spotted models becomes

$$T_{\rm eff,spotted} = \left((1-\gamma)\,T^4_{\rm imac} + \,\gamma\,T^4_{\rm spot}\right)^{\frac{1}{4}}. \tag{4.9}$$

To produce the simulated input catalogue I iterated through immaculate photosphere temperature, adopting the effective temperature of the combined photosphere as given in Equation 4.9. Each $T_{\rm eff,spotted}$ was mapped onto the corresponding stellar radius given by Equation 4.2. I utilised a Monte Carlo method to account for the uncertainties, which could potentially add to the spread. For each band I generated a CDF for the uncertainties in the observed catalogue and Monte Carlo sampled it for each simulated star. With this catalogue I then performed a fitting using the unspotted grid.

The fits resulting from this process are shown in Figure 4.12. What this makes clear is that spot coverage can contribute towards the perceived spread in radius. At $\gamma = 0.0$ and $\gamma = 1.0$, I recover the original $T_{\rm SED} - R$ relation as would be expected. For $0.0 < \gamma \leq 0.8$ the stars scatter to lower radii at increased $T_{\rm SED}$, conserving the overall luminosity. However,

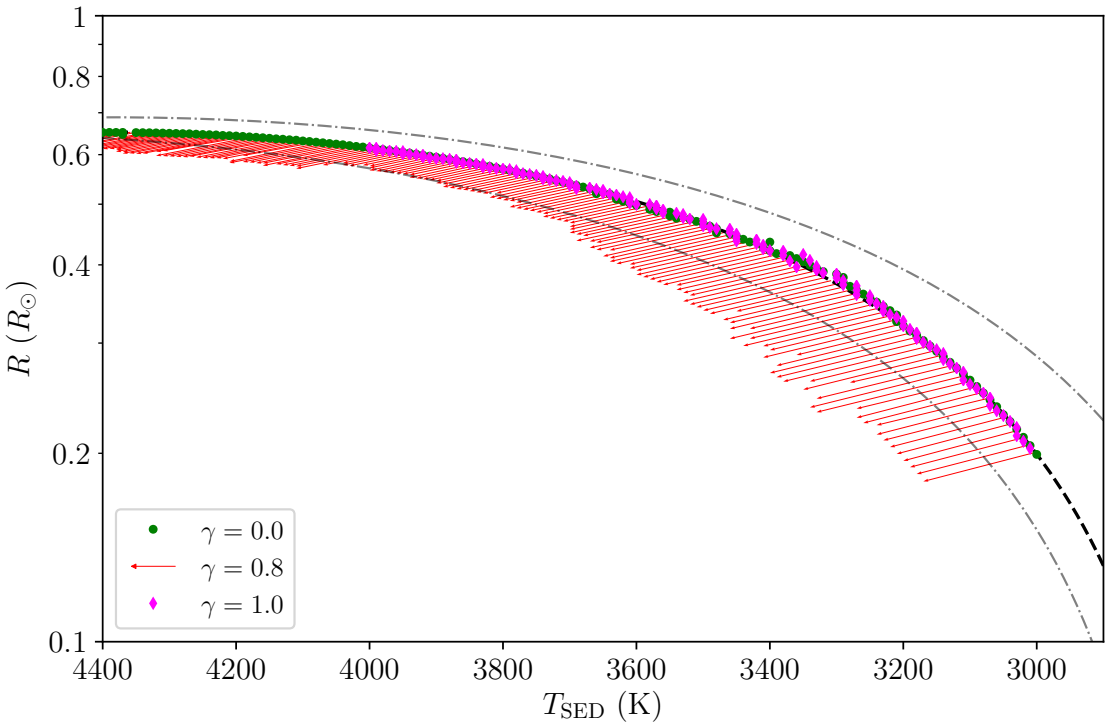

Figure 4.12: The points show the radius and temperature retrieved by fitting a catalogue of simulated synthetic photometry with varying spot filling factor γ. I show 0% (γ = 0.0) and 100% (γ = 1.0) spot coverage, which lie along the relation, along with γ = 0.8 which lies at the extremity of the spread. I show the 68% density bounds of my $T_{\rm SED} - R$ relation as grey dotted lines.

for $0.8 < \gamma < 1.0$ the fitting see the effects of the spotted photosphere in the SED and the begins retrieving temperatures closer to those of the spots, making measured radii become closer to the relation. This has the effect of producing a scatter in my relation which closely corresponds to the 68% confidence lines resulting from my $T_{\rm SED} - R$ relation presented in Section 4.2.2.

4.3.2.4 Correlations with activity

Although I have shown that the effect of starspots on my measurement technique is able to explain the observed scatter, this hypothesis would necessitate a correlation between measured radius and magnetic activity. To probe magnetic field strength I checked for correlations between radius inflation and markers of magnetic activity, the most reliable of which is rotation period $P_{\rm rot}$. I investigated a correlation with rotation period by assembling a sample of periods from McQuillan et al. (2013) and McQuillan et al. (2014) observed using Kepler. Unfortunately, there are only 21 targets in common with my sample, so I chose to supplement these catalogues with rotation periods determined from

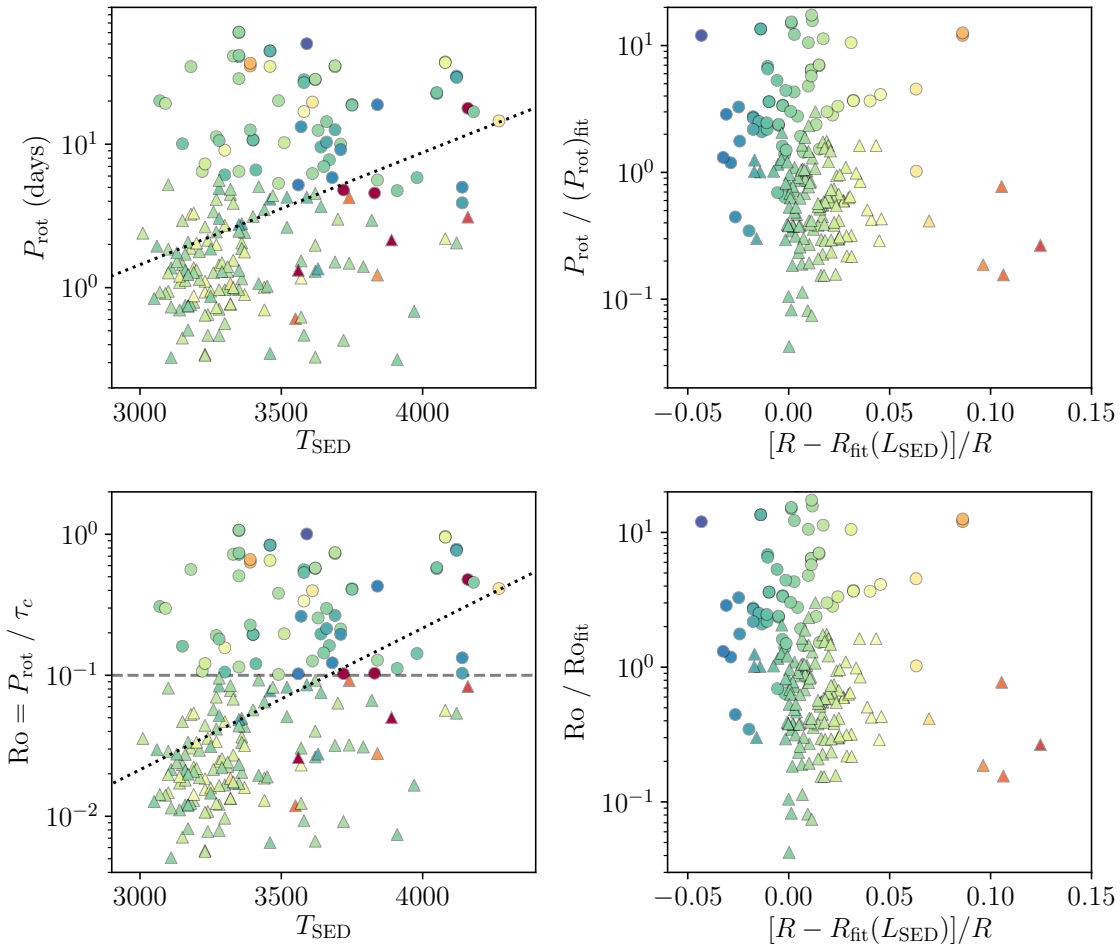

Figure 4.13: The correlation between my measured relative radius residual $[R - R(L)]/R$ and rotation period $P_{\rm rot}$ (left) and Rossby number Ro (right). The sample is divided between saturated (triangles) and unsaturated (circles) activity samples. The transition is marked by a grey dashed line and determined to be Ro = 0.1, both observationally (Newton et al. 2017) and theoretically (Reiners et al. 2009). I removed spurious correlations with spectral type from the right pane by performing a linear fit, shown as a black dotted line, in the accompanying left pane. Several stars at extreme inflations are not visible in the plot. The colour map denotes $[R - R_{\rm fit}(L_{\rm SED})]/R$.

Gaia DR2 lightcurves in Lanzafame et al. (2018) which are based on sparser lightcurves, but add an appreciable number of stars; resulting in a final sample of 189 stars which have rotation periods. I used a theoretical expression for convective turnover time τ_c, provided by Cranmer & Saar (2011), to determine the equivalent Rossby number Ro = $P_{\rm rot}/\tau_c$ for each star. To avoid spurious correlations with spectral type, I first performed a linear fit on both $P_{\rm rot}$ and Ro vs $T_{\rm SED}$ and corrected for it in my final correlations, which are shown alongside the fits in Figure 4.13. Rotation alone is adequate to show that my sample lacks appreciable correlations between magnetism and radius inflation, and is the most fundamental because more rapid rotation rates presumably promote a stronger dynamo action within the stellar interior. However, Wright et al. (2011) and

Newton et al. (2017) show that X-ray luminosity and H_α excess correlate well with rotation period in their unsaturated regimes. When unsaturated both can be used as additional markers of magnetic fields emergent at the stellar surface. It has been shown both observationally (Wright et al. 2011; Newton et al. 2017) and theoretically (Reiners et al. 2009) that activity saturates at around Ro $\simeq$ 0.1, meaning that 31% of my rotation sample would be in the unsaturated regime. Although rotation itself does not saturate, I have split the rotation periods into saturated and unsaturated sub-samples around this threshold to aid comparison with the following samples, which do.

I investigated the correlation with X-ray luminosity by crossmatching with DR6 of the XMM-Newton Serendipitous Source Catalog (3XMM DR6; Rosen et al. 2016), yielding 95 stars. This sample was divided into saturated and unsaturated sub-samples using the threshold $L_X/L_{\rm bol} \simeq 3 \times 10^{-4}$, defined from the lower limit of the spread around the saturated sample of Wright et al. (2018); meaning 53% of my stars are unsaturated. The X-ray luminosities are plotted as a function of relative radius residual in Figure 4.14. To avoid a spurious correlation with spectral type, and ensure that I only probe excess X-ray emission due to activity, as before I performed a linear fit to the data in the $T_{\rm SED} - L_X/L_{\rm bol}$ plane and used it to correct the values of $L_X/L_{\rm bol}$. Both the fit and final correlation with relative radius residual are shown in Figure 4.15. Both with and without the correlation with $T_{\rm SED}$ removed, the sample shows no strong correlation between X-ray luminosity and radius inflation. I note that there are a number of highly inflated stars that only appear in the saturated regime, suggesting these occurrences may be causally linked. However, as shown by Figure 4.10, these stars are sitting on the high inflation wing of the residual radius distribution, hence I conclude they are likely to be binaries.

Finally, I investigated the correlation with H_α by matching my catalogue with both DR2 of the INT Photometric Hα Survey of the Northern Galactic Plane (IPHAS2; Drew et al. 2005; Barentsen et al. 2014) and the VST Photometric Hα Survey of the Southern Galactic Plane and Bulge (VPHAS+; Drew et al. 2014). This results in a total of 573 stars which have H_α magnitudes. I have presented this sample in terms of $L_{H_\alpha}/L_{\rm bol}$ using

$$\frac{L_{H_\alpha}}{L_{\rm bol}} = W_{H_\alpha} \chi, \tag{4.10}$$

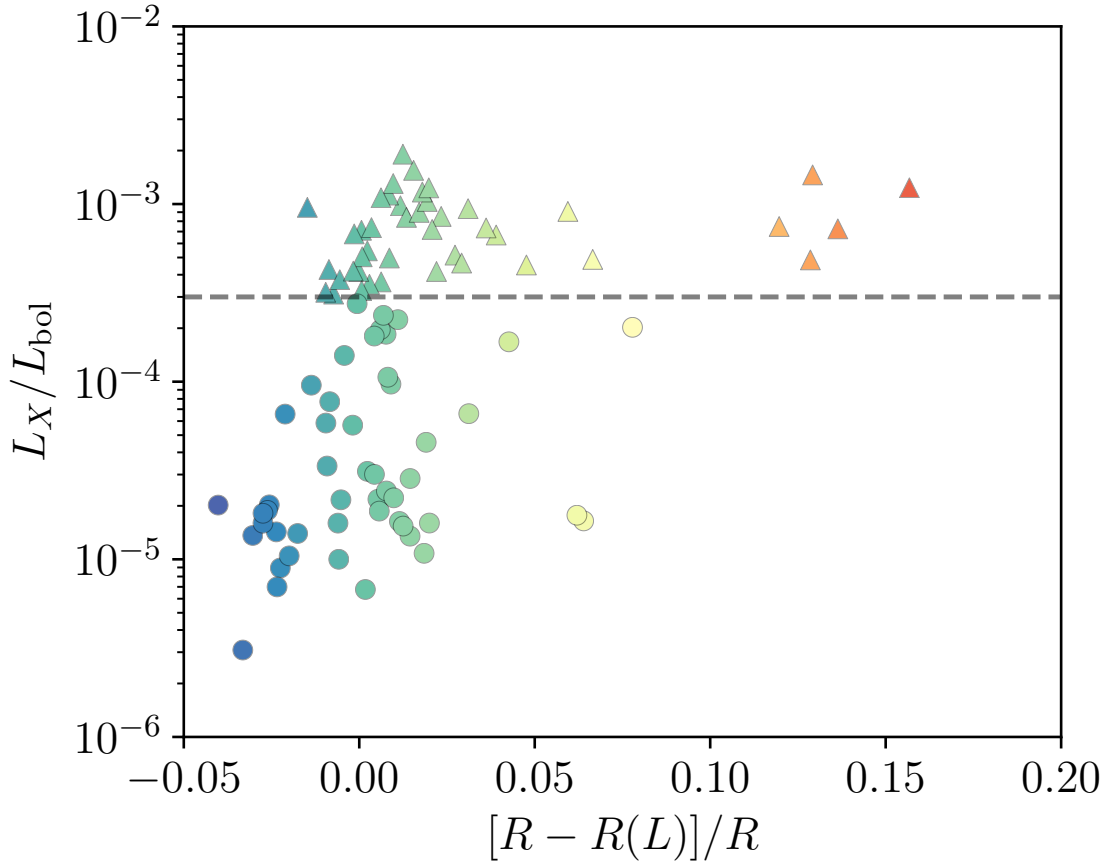

Figure 4.14: My sample of stars with X-ray luminosity $L_X/L_{\rm bol}$ against relative radius residual $[R - R_{\rm fit}(L_{\rm SED})]/R$. The sample is divided into stars that lie in the saturated (triangles) and unsaturated (circles) regimes. This transition is marked by a grey dashed line drawn at $L_X/L_{\rm bol} \simeq 3 \times 10^{-4}$, which corresponds to the lower limit from Wright et al. (2018). Several stars are omitted from the high inflation wing of this plot.

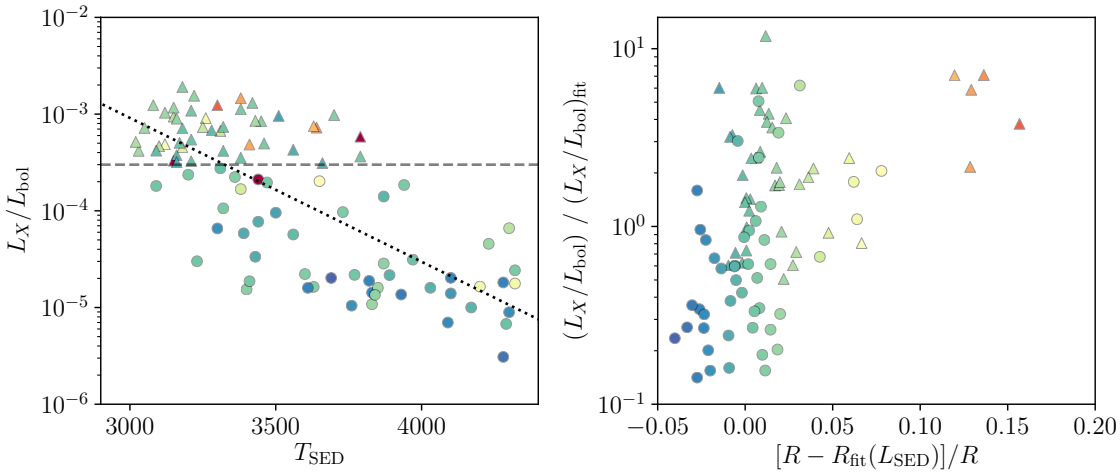

Figure 4.15: As Figure 4.14, but accounting for a potential spurious correlation in temperature. The left pane shows a correlation in my sample between $L_X/L_{\rm bol}$ and $T_{\rm SED}$, which is corrected for in the right plot using a linear fit (black dotted line).

where χ, introduced in Walkowicz et al. (2004), is the ratio of the continuum flux near H_α to the bolometric flux of the star; the values of which were interpolated from Table 8 of Douglas et al. (2014). The equivalent width of the H_α line W_{H_α} due to activity was determined by measuring the excess flux across the H_α band, of width $\Delta\lambda_{H_\alpha}$, using

$$W_{H_\alpha} = \Delta\lambda_{H_\alpha}\left[10^{0.4\,(m_r - m_{H_\alpha})\,-\,(BC_{H_\alpha} - BC_r)} - 1\right], \tag{4.11}$$

where m_r and m_{H_α} are the observed magnitudes, and BC_r and BC_{H_α}, the inactive model bolometric corrections. This sample is shown in Figure 4.16, along with the saturation threshold of $L_{H_\alpha}/L_{\rm bol} = 10^{-4}$ (Newton et al. 2017; Douglas et al. 2014). I note that some 53 of my W_{H_α} measurements are mildly negative, which indicates quiescence, thus I count these among the unsaturated sample. However due to resulting in negative $L_{H_\alpha}/L_{\rm bol}$ they do not appear on Figure 4.16. This demonstrates that my H_α sample spans both the saturated and unsaturated regimes, with around 25% of the sample being unsaturated.

To summarise, I have found that markers of both interior field strength ($P_{\rm rot}$) and surface field strength ($L_X/L_{\rm bol}$ and $L_{H_\alpha}/L_{\rm bol}$) show no appreciable correlation with radius inflation for M-dwarfs. All three markers are sampled in both the saturated and unsaturated activity regime, with between a quarter and a half of each being unsaturated.

4.3.2.5 How does metallicity affect the radius spread?

Differences in stellar metallicity could also cause a scatter in radii (Berger et al. 2006). A reduction in metallicity, and thus opacity, would allow the star to more efficiently radiatively dissipate internal energy, resulting in a smaller radius at the same luminosity (Berger et al. 2006). Stars within the solar neighbourhood show a metallicity spread with $\sigma = 0.2$ dex (Boone et al. 2006) with the lower extremity at $[M/H] \simeq -0.6$ (Neves et al. 2013). Comparing the Dotter et al. (2008) solar metallicity isochrones with those of [M/H] = ±0.25 in luminosity - radius space, gives a difference in radius of about ±4%. So, theory suggests the contribution to the spread is minimal. However, Mann et al. (2015) and Rabus et al. (2019) show a correspondence between metallicity and relative residual in radius for a number of M-dwarf stars.

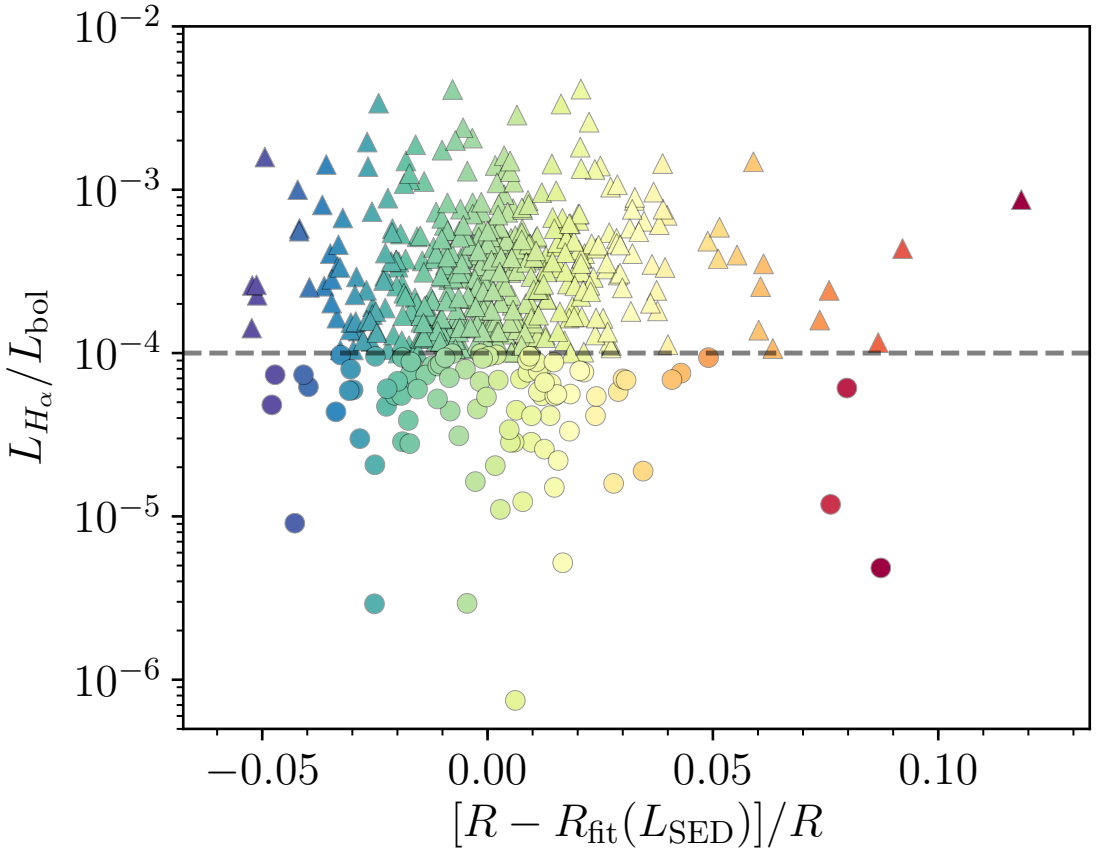

Figure 4.16: The sample of stars for which I have H_α luminosity $L_{H_\alpha}/L_{\rm bol}$ against relative radius residual $[R - R_{\rm fit}(L_{\rm SED})]/R$. The sample is divided into stars that lie in the saturated (triangles) and unsaturated (circles) regime, delimited by the dashed line drawn at $L_{H_\alpha}/L_{\rm bol} = 10^{-4}$, corresponding to the value from Douglas et al. (2014) and Newton et al. (2017)

.

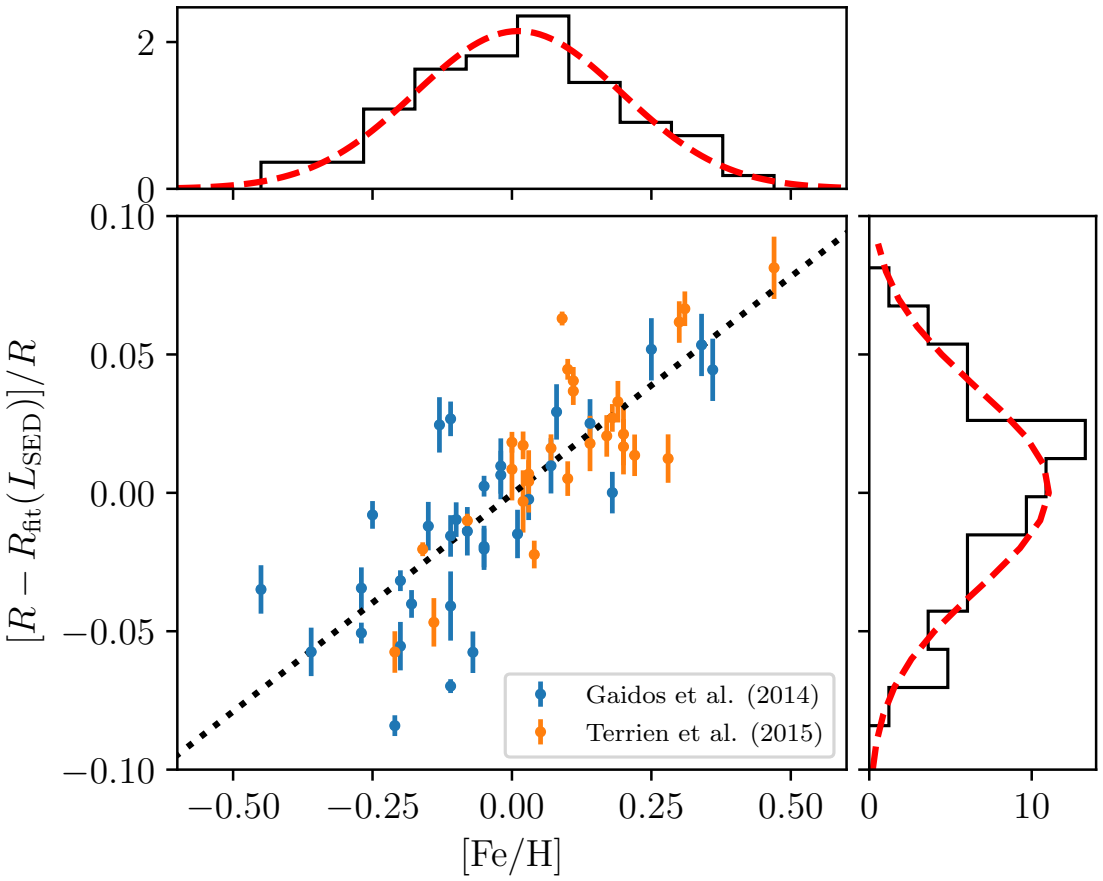

Figure 4.17: The correlation between radius residual and [Fe/H] for stars within the sample. The metallicities are from Terrien et al. (2015) (orange) and Gaidos et al. (2014) (blue). The radii and uncertainties are from my sample and fit using only solar metallicity atmospheres.

To investigate this in my data, I assembled a sample of stars from my catalogue with measurements of [Fe/H] from Terrien et al. (2015) and Gaidos et al. (2014). The sample which matched ranges between -0.5 < [Fe/H] < 0.5, indicating that my catalogue is relatively free of M-subdwarfs ([Fe/ H] < -0.5). I verified this using the Besançon population synthesis model (Robin et al. 2003), which yielded population sizes consistent with my sample and indicated ≃ 6% of my sample has [M/H] < −0.5 and ≃ 0.5% having [M/H] ≤ −1.0, as well as reproducing my distribution of metallicities well for [M/H] > -0.5. I ensured that these targets lie within the valid range of of the $L_{\rm SED} - R$ relation from Section 4.2.3 and I avoid the high inflation wing of the sample by choosing inflations $[R - R_{\rm D08}(L)]/R < 12\%$. I established in Section 4.3.1 that the radii from Mann et al. (2015) are inconsistent with my own, so I chose not to use them. The radius residuals resulting from the luminosity correction are shown as a function of [Fe/H] in Figure 4.17. The sample spans a residual of ±6%, which appears to correlate strongly with metallicity, and

corresponds well to the spread of metallicity in the solar neighbourhood.

This initially suggested that the spread was physical, and caused by metallicity, however the correlation is steeper than predicted by theory. Furthermore, I had measured all radii using only solar metallicity atmospheres. To determine the the error induced by this I produced grids for [M/H] = ±0.25 by interpolating synthetic photometry from [M/H] = ±0.5 and [M/H] = 0.0 grids [1, 2]. I fitted each star in the input catalogue with all three metallicities, allowing me to produce a $L_{\rm SED} - R$ relation for each metallicity following the procedure from Section 4.2.3. I found that SED fitting is able to determine luminosity consistently to within about 1%, regardless of which metallicity atmospheres are used. Thus, using the median radius from each luminosity bin, which I interpolated between bin midpoints, I calculated the difference between the radii measured at each metallicity and the radii measured at solar metallicity as a function of luminosity. Hence, I was able to measure the theoretical luminosity-dependent relationship between measured radius and [M/H] in the form of a linear relationship, with gradient $F(L_{\rm SED})$; values for which are tabulated in Table 4.2. This allowed me to determine the correct radius residual for each star, which are shown in Figure 4.18, using

$$\frac{\delta R}{R} = \frac{1}{R}\left(R - R_{\rm fit}(L_{\rm SED}) + F(L_{\rm SED})\,[{\rm Fe/H}]\right), \tag{4.12}$$

where $R_{\rm fit}(L_{\rm SED})$ is the $L_{\rm SED} - R$ relation given in Equation 4.5. The resulting corrected radii were fit with to yield another $L_{\rm SED} - R$ relation, which remains consistent to within 1% with the relation presented in Section 4.2.3 for $0.015\ L_\odot < L_{\rm SED} < 0.09\ L_\odot$. When corrected for metallicity, I found that the correlation between relative radius residual and metallicity was no longer significant (see Figure 4.18).

Therefore, the correlation of radius with metallicity in Figure 4.17 is the result of fitting stars with a spread of metallicities with only solar metallicity atmospheres, which determines $T_{\rm SED}$ hence R incorrectly. Thus the observed correlation between metallicity and radius spread in my sample is not physical and can be corrected for with accurate

1. To ensure solar abundance for all metallicities I used the BT-Settl AGSS2009 models, which adopts the Asplund et al. (2009) solar abundances, as opposed CIFIST which uses those of Caffau et al. (2011).
2. The BT-Settl AGSS2009 model atmospheres are available from https://phoenix.ens-lyon.fr/Grids/BT-Settl/AGSS2009/SPECTRA/

L_{SED} ($L_\odot$)	$F(L_{SED})$	L_{SED} ($L_\odot$)	$F(L_{SED})$	L_{SED} ($L_\odot$)	$F(L_{SED})$
0.0035	-0.0151	0.0365	-0.0668	0.0695	-0.0758
0.0045	-0.0188	0.0375	-0.0874	0.0705	-0.0436
0.0055	-0.0280	0.0385	-0.0857	0.0715	-0.0573
0.0065	-0.0342	0.0395	-0.0539	0.0725	-0.0480
0.0075	-0.0339	0.0405	-0.0811	0.0735	-0.0652
0.0085	-0.0411	0.0415	-0.0810	0.0745	-0.0584
0.0095	-0.0434	0.0425	-0.0641	0.0755	-0.0388
0.0105	-0.0436	0.0435	-0.0843	0.0765	-0.0432
0.0115	-0.0508	0.0445	-0.0675	0.0775	-0.0589
0.0125	-0.0553	0.0455	-0.0805	0.0785	-0.0278
0.0135	-0.0527	0.0465	-0.0602	0.0795	-0.0639
0.0145	-0.0563	0.0475	-0.0763	0.0805	-0.0604
0.0155	-0.0584	0.0485	-0.0742	0.0815	-0.0287
0.0165	-0.0630	0.0495	-0.0740	0.0825	-0.0409
0.0175	-0.0622	0.0505	-0.0643	0.0835	-0.0397
0.0185	-0.0676	0.0515	-0.0682	0.0845	-0.0606
0.0195	-0.0653	0.0525	-0.0601	0.0855	-0.0440
0.0205	-0.0695	0.0535	-0.0881	0.0865	-0.0219
0.0215	-0.0728	0.0545	-0.0593	0.0875	-0.0525
0.0225	-0.0751	0.0555	-0.0549	0.0885	-0.0344
0.0235	-0.0696	0.0565	-0.0607	0.0895	-0.0328
0.0245	-0.0756	0.0575	-0.0656	0.0905	-0.0501
0.0255	-0.0791	0.0585	-0.0598	0.0915	-0.0416
0.0265	-0.0769	0.0595	-0.0645	0.0925	-0.0185
0.0275	-0.0691	0.0605	-0.0702	0.0935	-0.0584
0.0285	-0.0767	0.0615	-0.0600	0.0945	-0.0371
0.0295	-0.0812	0.0625	-0.0543	0.0955	-0.0448
0.0305	-0.0665	0.0635	-0.0485	0.0965	-0.0211
0.0315	-0.0838	0.0645	-0.0396	0.0975	-0.0375
0.0325	-0.0881	0.0655	-0.0468	0.0985	-0.0257
0.0335	-0.0736	0.0665	-0.0671	0.0995	-0.0238
0.0345	-0.0812	0.0675	-0.0702		
0.0355	-0.0697	0.0685	-0.0175		

Table 4.2: The tabulated values for $F(L_{SED})$ in Equation 4.12. In between L_{SED} points we linearly interpolate neighbouring values.

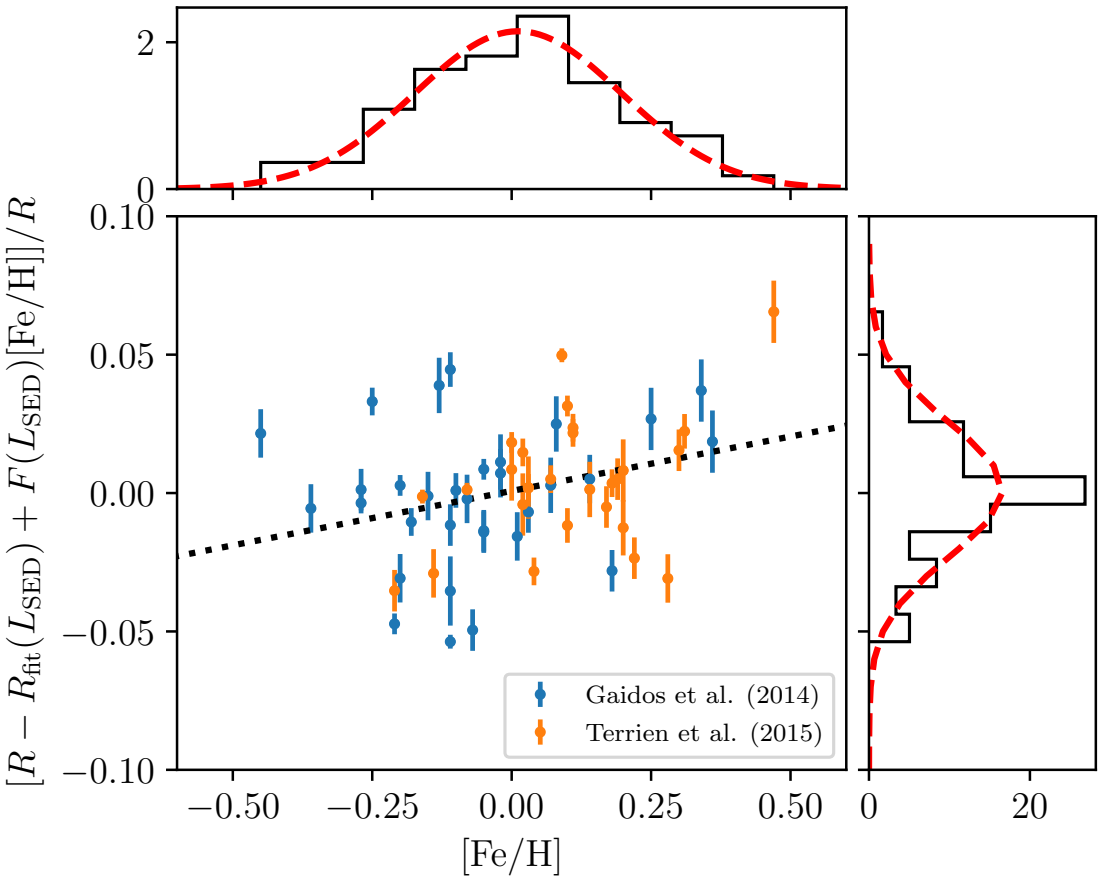

Figure 4.18: As Figure 4.17 but with the correction from Section 4.3.2.5 applied. This correction accounts for using only solar metallicity atmospheres to fit a range of metallicities.

measurements of the stellar luminosity and metallicity. Mann et al. (2015) also found a correlation between metallicity and radius within their sample, however it only appears as a function of $T_{\rm sp}$, not as a function of M_{K_s}—a proxy for luminosity. Interestingly, the interferometric and DEB sample show a very similar scatter to my uncorrected radii, however I attribute this to observational uncertainty. The mean uncertainty in metallicity from Gaidos et al. (2014) and Terrien et al. (2012) will result in a 1.7% spread in my measured radius in Figure 4.18. Given that my median radius uncertainty from the fitting process is 1.6% (see Section 4.2), this would be consistent with the 2.4% scatter seen in Figure 4.18. There could also be an intrinsic scatter of the stars in my sample, but to remain consistent with the spread it would have to be at most 1 to 2%. This leads me to conclude that our knowledge of M-dwarf radii is currently limited by the accuracy and precision of the metallicity measurement of the star.

4.3.2.6 The cause of the scatter - a summary

I have showed that faint contaminants in AllWISE photometry were not the cause of the scatter (see Section 4.3.2.2). I have also established that the uncertainties in my measurements were not able to explain the spread (see Section 4.3.2.1). I found that extremely high starspot coverage in most of the population could explain the scatter. But since stars with small spot coverages would have lower measured radii, and stars with larger coverages, larger radii, this would imply a measured radius–activity correlation, which I was unable to find (see Section 4.3.2.3 and Section 4.3.2.4). However, I found that there is a strong correlation between [Fe/H] and the radius measured by SED fitting. Although this could be misconstrued as a physical spread in radius caused by metallicity, I found that in fact this correlation resulted from using solar metallicity atmospheres to fit the SED of non-solar metallicity stars. When this is corrected for I found that the correlation disappeared, resulting in a scatter of about 2.4% in the subset for which I could find metallicities. This spread is consistent with the 2 to 3% found by Schweitzer et al. (2019). Uncertainty in [M/H] measurements accounts for about 1.7% of this spread, with my uncertainties in radius explaining the remainder. The accuracy of the measured metallicities also makes determinations of effective temperature problematic, imposing another limit on the accuracy of my radii. Therefore I suggest that the spread of this

corrected radius distribution is currently dominated by the accuracy and precision of current metallicity measurements (see Section 4.3.2.5) and the intrinsic spread in M-dwarf radii is less than 1 to 2%. This well characterised radius residual distribution also places an upper limit on the typical variability of spot filling factors of stars within the sample of $< 10\%$.

4.3.3 Explaining the Radius Inflation

I now address the question as to why the M-dwarf main sequence is inflated from theoretical predictions, and note in passing the problem also appears to apply to the pre-main sequence (Jackson et al. 2018). Section 1.8.1 summarises our current understanding of inflation—it is clear that the mechanism behind radius inflation in M-dwarfs remains a contentious point. So far the most compelling hypothesis has been dynamo driven magnetic fields, which would inhibit convection and probably modify the specific entropy in the convective region, and hence the internal structure of the star (see Section 1.4.1). Stars below a mass of approximately 0.35 $M_{\odot}$ are thought to have interiors that are fully convective (Limber 1958), making this a satisfying explanation. If this were to be the case, I might expect to see a spread in radius, from the theoretical non-magnetic models to some level of maximum inflation, provided I sampled a large range of rotation rates. However, I established in Section 4.3.2.5 that there is a tight (with perhaps a 1 to 2% intrinsic scatter) main sequence for M-dwarf stars, refuting this scenario. One could argue that I have not adequately considered the case that radius inflation has saturated, much like the activity does, for all of the stars in my sample. Figure 4.13 shows that I sample a large range of rotation periods, including at least a quarter of the sample for which activity is unsaturated. For saturation of radius inflation to be consistent with such tight a sequence, it would have to occur at rotation rates much slower than both saturation of photospheric activity indicators (at Ro = 0.1) and the slowest rotators in my sample Ro $\simeq$ 1.0.

A further argument against stellar magnetism being responsible for radius inflation comes from the fact that that all of the indicators of magnetic activity I studied show no appreciable correlation with measured radius residual (see Section 4.3.2.4). I would expect to see correlations between the activity and radius inflation were magnetism responsible.

Given these two arguments, I reluctantly conclude that stellar magnetism is currently unable to explain radius inflation in main sequence M-dwarf stars.

4.3.3.1 Alternate explanations for radius inflation

It is unlikely that magnetic fields are the cause of radius inflation in main sequence M-dwarf stars, so an alternate explanation must be sought. Metallicity is the main driving force behind the measured radius scatter, however in Section 4.3.2.5 it was shown to be caused by my measurement technique. This renders me unable to explain the inflated radii of main sequence M-dwarfs. However, one avenue of inquiry comes from the PARSEC 1.2S models (Chen et al. 2014; Marigo et al. 2017) which adopts an empirical $T - \tau$ relation as the boundary condition to their interiors. Given the temperature of the outer boundary of the stellar model interior, the $T - \tau$ relation determines the optical depth at the outer edge of this boundary, hence the efficiency of radiative dissipation through the stellar atmosphere. A higher opacity at the boundary would reduce the efficiency with which the star can dissipate energy, inherently reducing its measured effective temperature and effectively blanketing the star. As Figure 4.5 and Figure 4.6 show, this modification does a remarkably good job of characterising the degree of inflation and the intrinsic sequence for early to mid M-dwarf stars.

4.3.4 Determining Accurate M-dwarf Radii

I showed in Section 4.3.2.5 that metallicity can cause problems when determining M-dwarf radii. Using atmospheres of a different metallicity from the star being fitted causes the retrieved temperature, and thus the radius, to be incorrect. However, I have devised strategies for obtaining accurate M-dwarf radii in the face of these issues.

4.3.4.1 Without a metallicity measurement

If there is not a measured metallicity for a star, there are two strategies available. Firstly, disregarding the metallicity of the star and fitting indiscriminately with solar metallicity models yields radii accurate to better than 5%; in my case about 3.6%. For statistical samples and less precise applications, this may be adequate. However, my method can measure the luminosity of the star correctly to within a couple percent regardless of

metallicity (see Section 4.3.2.5). Thus, one can use the measured luminosity along with an empirical $L_{\rm SED} - R$ relation, such as that in Section 4.2.3, to obtain correct radii. The scatter about this relation ranges between 3.6% – 4.5%.

4.3.4.2 With a metallicity measurement

If the star has an accurate measurement of the metallicity, there are two more avenues open. The simplest option is to perform the fitting with an atmosphere of the appropriate metallicity. However for large samples it can be impractical to generate large grids of synthetic photometry at a number of differing metallicities. So my other suggestion is to follow the method presented in Section 4.3.2.5. This entails fitting the entire sample with solar metallicity models and correcting for the metallicity. Both strategies are highly dependent upon the accuracy and precision of the metallicity measurement. A metallicity constrained to about 10% induces a scatter of about 1.7% in measured radius. However, for cooler stars, with well constrained photometry and sufficiently accurate metallicities (better than about 3%), radius measurements of better than 1% can be achieved with this method.

4.4 Chapter Summary

I have measured the temperature, radius and luminosity of a sample of 15 279 late K and early M-dwarf stars using a modified spectral energy distribution fitting method. This method requires only accurate photometry and precision astrometry and thus adds a fourth method to those used to evaluate the veracity of stellar models. Importantly, this method works natively in the $T_{\rm eff} - R$ space which is crucial for the characterisation of exoplanets. I have derived empirical $T_{\rm SED} - R$ and $L_{\rm SED} - R$ relations, which can be used to characterise exoplanet host stars and validate stellar evolution models (Section 4.2.2 and Section 4.2.3).

The key conclusions of this chapter are as follows.

i. Currently, none of the purely theoretical stellar models can describe the mean radius inflation of the main sequence at temperatures lower than about 4000 K. The measured

radii are inflated by 3 – 7% compared to those predicted by models (Section 4.2.1).

ii. I have shown that M-dwarfs lie on a tight sequence (with a scatter smaller than 1 – 2%) (see Section 4.3.2.5). This is in conflict with magnetic models, which would suggest a spread in radius, from the theoretical sequence for non-magnetic models to a maximum inflation. I have also shown that there is no appreciable correlation between all observational markers of magnetic activity and radius inflation (see Section 4.3.2.4). This leads me to conclude that stellar magnetism is currently unable to explain radius inflation in main sequence M-dwarf stars (see Section 4.3.2). Furthermore, this would explain the unexpected result that detached eclipsing binaries are not inflated with respect to their single star counterparts (see Figure 4.10).

iii. I discovered that fitting a distribution of metallicities with only solar metallicity models introduces an apparent correlation between [Fe/H] and R (Section 4.3.2.5).

iv. However, I found that the SED fitting technique correctly measures the luminosity regardless of metallicity, meaning that I can correct the measured radii. Without a measured metallicity I achieved a precision of 3.6%. However, this was improved to 2.4% when corrected for metallicity. Given that the uncertainty in [M/H] accounts for 1.7% of this spread, it is clear that the precision of metallicity measurements is currently the limiting factor for this method (Section 4.3.4).

v. In the absence of metallicity measurements I present an empirical $L_{\rm SED} - R$ relation which can be used to measure correct radii to a precision of 3.6 – 4.5% (see Section 4.3.4).

Chapter 5

Revising Exoplanet Host Radii using Gaia DR2

"For me, it is far better to grasp the Universe as it really is than to persist in delusion, however satisfying and reassuring"

— *Carl Sagan*

The ability to make accurate determinations of stellar radii and temperatures is of vital concern for exoplanet characterisation, as measurements of an exoplanet's properties are inextricably tied to those of its host star. Throughout Chapter 3 and Chapter 4 I have demonstrated the effectiveness of the fitting method detailed in Section 2.1 when applied to long standing problems in stellar physics. Drawing upon the experience gleaned from this previous work, in this chapter I will apply this fitting methodology to characterising a small sample of exoplanet host stars. In doing so, constraints on the properties of the hosts and exoplanets will be revised and improved. The outcomes of this will be critically compared to the existing characterisation methods; which were reviewed in Section 1.9. In line with exoplanet literature, throughout this chapter I adopt $R_\star$ and R_p as the radius of the stellar host and exoplanet respectively.

5.1 Input Catalogue and Motivation

The input sample for the fitting consists of 20 stars from the *Panchromatic Exoplanet Treasury Programme* (PanCET, Sing 2016). This sample was chosen as they are stars for which there are characterisations in literature, allowing for comparison with previously used methods, and importantly their atmospheres have been well studied. Thus revising the host parameters for these stars will allow the community to rapidly assess how their climates will be impacted. Based on measurements from the literature, this sample spans $T_{\rm eff}$ values of 3000 - 7000 K; which samples the domain occupied by around 90% of the hosts of currently discovered exoplanets. This wide $T_{\rm eff}$ range necessitates the use of UV to mid IR photometry to thoroughly sample the SED for all targets. Due to the extremely limited sample size, I did not require that the star was observed in all bands. However, I did require that each star was sampled by at least 5 bands, causing GJ 436 to be omitted from the final catalogue; owing to only having acceptable photometric data in the $G_{\rm BP}$ and $G_{\rm RP}$ bands. The surveys from which I drew photometry, along with the selection criteria for the data, are detailed in Table 5.1. Thus the final sample contains 19 stars.

I detailed in Section 1.8.3 the process by which discovery and characterisation is currently performed on exoplanet systems. This involves determining properties for the combined stellar host–exoplanet system by fitting transit and radial velocity measurements to models, and then deriving absolute properties for the hosted exoplanet by setting the host star properties from stellar models and empirical relations. To validate the veracity of the existing literature values for the stellar host parameters in my input catalogue, I produced synthetic $G_{\rm G}$-band photometry—using the same method as in Section 2.1.4—at the distance prescribed by Gaia DR2 (Bailer-Jones et al. 2018) using the $T_{\rm sp}$ and $R_\star$ presented in the literature, and compared it directly to the observed $G_{\rm G}$-band photometry from Gaia DR2. The lower uncertainty bound in $G_{\rm G}$ was produced by adopting the lower uncertainty bound on $R_\star$ and $T_{\rm sp}$, and the upper uncertainty bound on distance $r_{\rm hi}$, and vice versa for the upper bound uncertainty. I note that the synthetic uncertainties here likely represent an over-estimate of the true luminosity uncertainty. This is due to the temperature and radius being correlated, and the joint distribution likely following lines of constant luminosity. Hence, the combined bounds imposed by the marginal dis-

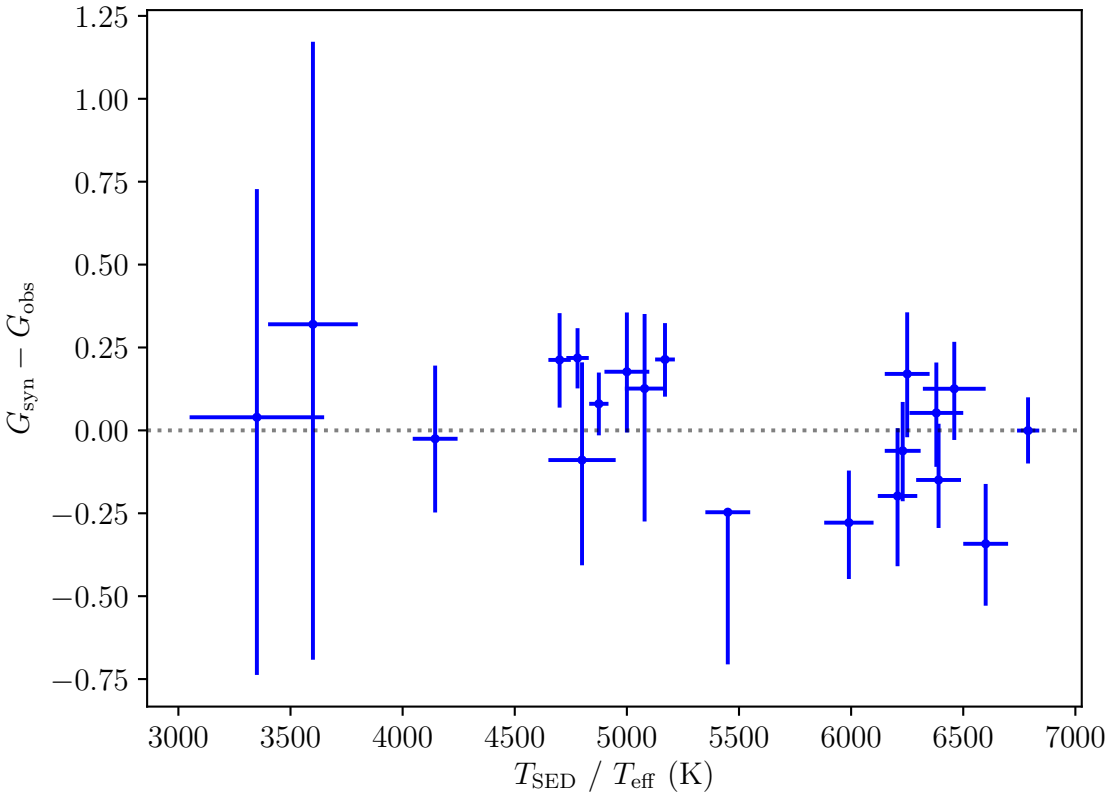

Figure 5.1: The residual between the synthetic and observed $G_{\rm G}$ photometry of exoplanet hosts as a function of temperature. The synthetic photometry were generated using stellar atmospheres from the $T_{\rm eff}$ and $T_\star$ presented in the literature and placed at the distance indicated by Gaia DR2 data. Note that the uncertainty bounds in this figure are likely over-estimates, as I did not have access to the underlying luminosity posterior distribution, and so were estimated from the uncertainty bounds in T_{rmeff} and $R_\star$.

tributions of both $T_{\rm sp}$ and $R_\star$ sample the extreme possible values of L. A more rigorous treatment of these uncertainties would necessitate access to the underlying estimation of the luminosity posterior distribution. The residual of the synthetic and observed $G_{\rm G}$-band magnitude is shown as a function of temperature in Figure 5.1. It is clear from this figure that there are some issues with this sample of stars. A third of the stars in the sample are further than 1σ away from their observed $G_{\rm G}$-band magnitude; which in itself should not come as surprising, given that the presented uncertainties should encompass two thirds of the probability in the luminosity posterior. However, the issue stems from the RMS residual, which is on the order of 20% in luminosity. In previous chapters, my technique provided luminosities to an uncertainty of $\sim 1-2\%$, showing the potential for an order of magnitude improvement over the literature. This is particularly evident in the M-dwarf regime, where my methodology was shown in Section 4.3.4 to be effective at achieving a mean uncertainty of 1% in $T_{\rm SED}$ and 2.6% in $R_\star$ when the metallicity of

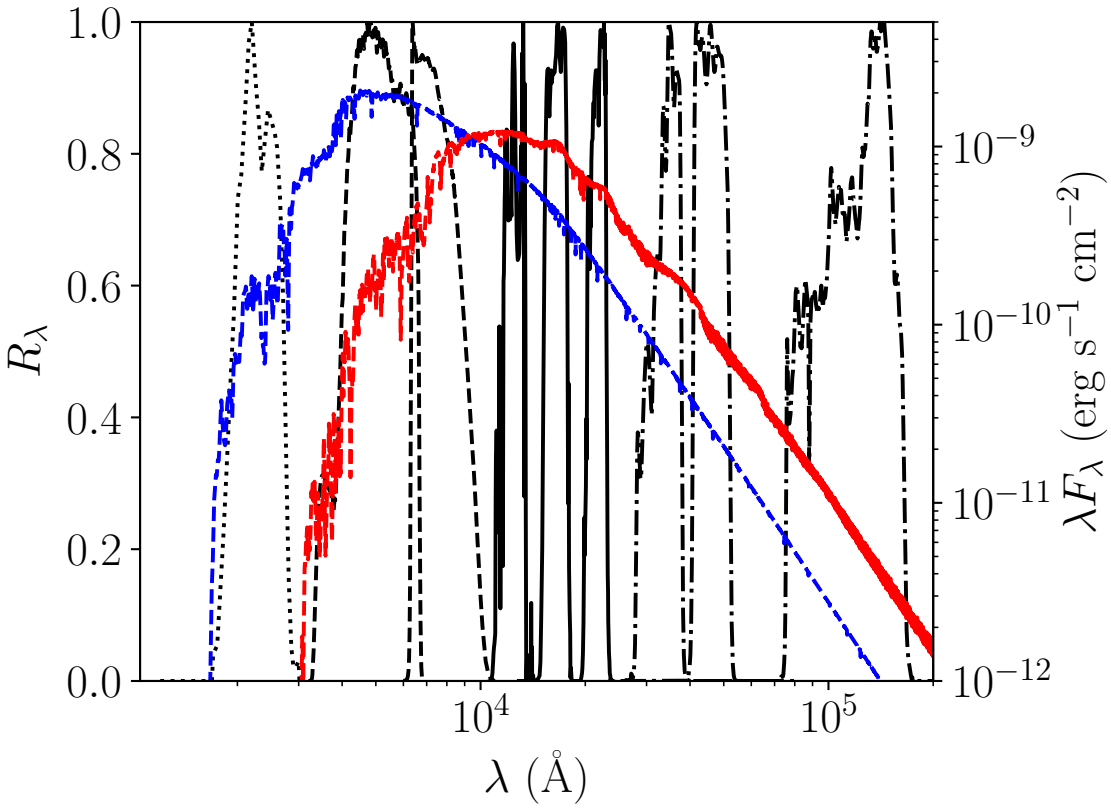

Figure 5.2: The coverage of all of the system responses used in the fitting process. The chosen systems sample the UV (GALEX, dotted), optical (Gaia DR2, dashed), near-IR (2MASS, solid) and mid-IR (WISE, dot-dashed). The model spectra correspond to the best fitting models for GJ 3470 (red) and WASP 79 (blue), which lie at the $T_{\rm SED}$ extremities of the sample. This illustrates that the bands used in the fit are more than adequate to sample the entire SED of all stars within the sample.

the target is known. Thanks to the advent of Gaia DR2, and the methodology presented in this thesis, we now have the potential to improve the accuracy and precision of the measured luminosities for exoplanet hosts, and the radius measurement of their hosted exoplanets, by an order of magnitude.

5.2 Method

The observed SEDs upon which the fitting procedure is performed are compiled from near-ultraviolet to mid-infrared archival survey data. The system responses of the bands used are shown in Figure 5.2 with stars at both $T_{\rm SED}$ extremities of the sample to justify their selection. I was careful to choose surveys whose characteristics and system responses were well understood, so the synthetic photometry in the grids closely replicate the observed photometry. Details of the input catalogue are presented in Section 5.1. Unreddened grids

were once again generated following the methodology in Section 2.1.4. As previously, the synthetic photometry for the grids was generated by folding the BT-Settl CIFIST stellar atmosphere grid (Allard et al. 2012b) through the system responses corresponding to the bands used for the fitting. As previously, I better constrained the 3D grid by applying a tophat prior to $\log(g)$. This was accomplished by matching the M_G magnitude to the best fitting point in the 4 Gyr Baraffe et al. (2015) isochrone and constraining the grid domain to ±0.5 dex either side of this central value; allowing for a change of up to nearly 60% in radius. A $T_{\rm eff}$ tophat prior was also determined by first performing an unconstrained fit and by-eye selecting the temperature bounds that encompass all probability above the constant background. As well as improving constraints upon $T_{\rm SED}$ and $R_\star$ bounds, this process aids in verifying models. If the fitting converged on a boundary of this grid subset, one could surmise that $\log(g)$ prescribed by the interiors is inconsistent with observations; of which none did.

5.2.1 Photometric Fitting

Owing to a much smaller sample size than in Chapter 3 and Chapter 4, for each of the stars in the sample I performed a full 3D grid search around the analytically determined radius. This produced a cube of χ^2 in $T_{\rm eff} - \log(g) - R_\star$, from which uncertainties for determined properties were drawn. As with Chapter 4, I adopted a floor on $\sigma_i = 0.01$ for the fitting, to remain clear of systematics.

I demonstrated in Section 4.3.2.5 that for M-dwarfs fitting only non-Solar metallicity targets with only solar metallicity atmosphere models induces an error in the measured radii. Fortunately, I proposed a strategy for obtaining corrected radii for non-Solar metallicity M-dwarfs in Section 4.3.4. These exploit the fact that the SED fitting technique is able to measure luminosity correctly regardless of disparity in metallicity between the target and grid. As Figure 5.9 shows, only M-dwarfs and late K-dwarfs are susceptible to this problem, meaning that only GJ 3470 and WASP-80 required correction; decreasing their final measured radii by 1.4% and 0.6% respectively.

Band	λ_{iso} (Å)	System	Selection Criteria	Source
NUV	2315	GALEX	δNUV < 0.1	Passbands: Morrissey et al. (2007) Bianchi et al. (2017)
G_{BP}	5320	Gaia DR2		Gaia Collaboration et al. (2016) Gaia Collaboration et al. (2018b) Passbands: Maı z Apellániz & Weiler (2018)
G_{RP}	7970			
J_{2MASS}	12410	2MASS	ph_qual = "AAA"	Skrutskie et al. (2006)
H_{2MASS}	16513			
$K_{s,2MASS}$	21656			
W_1	33792	WISE	ext_flg = 0 $\delta W_3/W_3 < 0.05$	Wright et al. (2010)
W_2	46293			
W_3	123338			

Table 5.1: The sources of the photometric data used for the SED fitting. To aid in comparison to plots, each filter is listed with its isophotal effective wavelength λ_{iso}, criteria used to select the photometry, and original source. The bands are grouped into photometric systems and in order of ascending λ_{iso}. The λ_{iso} is determined by integrating $f_\lambda = 1$ across the filter, unless directly quoted in the source paper. Due to the poor quality of the photometry, the W4 band has been omitted from the fitting.

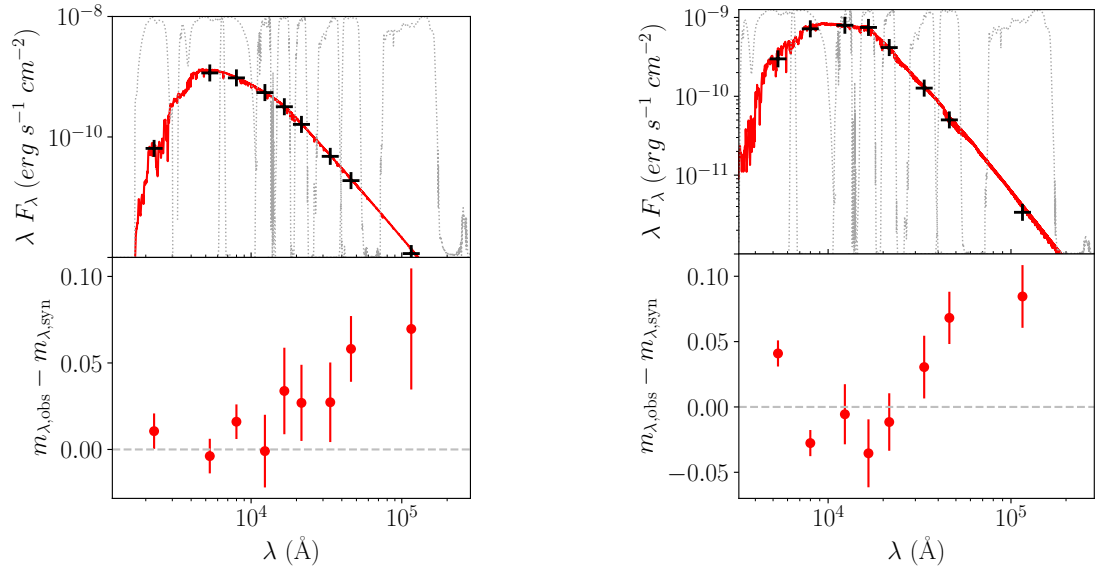

Figure 5.3: Fits of exoplanet hosts resulting from the use of the method presented in Section 4.1.3 and Section 2.1.6. They fits correspond to the WASP-121 (left) and WASP-80 (right); demonstrating fits to a bluer and redder host respectively. The best fitting model for each target is shown in the top panel (red) along with the photometry from which it was determined (black). The bottom panel shows the residuals of the observed photometry from the best fitting synthetic photometry.

5.3 Results

The exoplanet host properties resulting from the fitting, with the M-dwarf radius corrections applied, are shown with their associated uncertainties in Table 5.2. The entire sample is shown in the $T_{\mathrm{SED}} - R_\star$ plane in Figure 5.4, with the contours that denote the 68% confidence area in this space. With the revised stellar host properties comes revisions in the exoplanet properties. To derive the revised R_p, I adopted the fundamental measurement of $R_p/R_\star$, which can be found from the depth of the transit. Although this is measured by fitting the light curve to a transit model, the model itself—as well as good approximations to it—follow from simple geometric arguments; thus it remains effectively model independent. The revised planet masses were derived by combining my revised R_p and the ρ_p from the literature, determined via radial velocity. These revised exoplanet properties are tabulated in Table 5.3.

5.4 Discussion

The PanCET programme has until now been using literature data for exoplanet hosts, which are determined via the methods detailed in Section 1.9. Along with the newly

Name	$r_{\rm est}$ (pc)	$\log(g)$	$T_{\rm SED}$ (K)	R_* ($R_\odot$)
GJ 3470	$29.421^{+0.051}_{-0.051}$	$5.5^{+0.0}_{-0.5}$	3469^{+90}_{+50}	$0.553^{-0.012}_{-0.031}$
WASP-80	$49.788^{+0.116}_{-0.116}$	$4.8^{+0.2}_{-0.3}$	3971^{+90}_{+20}	$0.633^{-0.004}_{-0.029}$
HAT-P-11	$37.765^{+0.034}_{-0.034}$	$5.5^{+0.0}_{-0.4}$	4720^{+20}_{-40}	$0.772^{+0.016}_{-0.009}$
WASP-29	$87.595^{+0.312}_{-0.310}$	$5.5^{+0.0}_{-0.5}$	4750^{+10}_{-40}	$0.790^{+0.014}_{-0.007}$
WASP-69	$49.961^{+0.132}_{-0.131}$	$5.5^{+0.0}_{-0.6}$	4890^{-10}_{-50}	$0.804^{+0.020}_{+0.000}$
HD 189733	$19.764^{+0.013}_{-0.013}$	$5.5^{+0.0}_{-0.6}$	5040^{+10}_{-70}	$0.759^{+0.025}_{-0.005}$
WASP-52	$174.818^{+1.343}_{-1.323}$	$5.5^{+0.0}_{-0.6}$	5050^{+30}_{-60}	$0.829^{+0.020}_{-0.010}$
HAT-P-26	$141.837^{+1.152}_{-1.134}$	$5.5^{+0.0}_{-0.6}$	5060^{+10}_{-60}	$0.839^{+0.021}_{-0.003}$
HD 97658	$21.562^{+0.025}_{-0.025}$	$4.0^{+0.6}_{+0.0}$	5150^{+40}_{-30}	$0.750^{+0.010}_{-0.013}$
WASP-6	$197.119^{+1.632}_{-1.606}$	$4.5^{+0.1}_{-0.5}$	5440^{+30}_{-40}	$0.781^{+0.014}_{-0.010}$
WASP-74	$149.216^{+1.149}_{-1.132}$	$5.5^{+0.0}_{-0.6}$	5790^{+60}_{-50}	$1.541^{+0.028}_{-0.022}$
HAT-P-41	$348.185^{+4.530}_{-4.417}$	$4.0^{+0.6}_{+0.0}$	5900^{+60}_{-60}	$1.853^{+0.034}_{-0.035}$
HAT-P-32	$289.205^{+5.355}_{-5.167}$	$4.0^{+0.6}_{+0.0}$	6140^{+60}_{-70}	$1.294^{+0.024}_{-0.021}$
WASP-76	$194.459^{+6.206}_{-5.840}$	$4.3^{+0.7}_{+0.1}$	6170^{+40}_{-160}	$1.906^{+0.087}_{-0.032}$
WASP-62	$175.631^{+0.590}_{-0.586}$	$4.0^{+0.6}_{+0.0}$	6200^{+70}_{-60}	$1.248^{+0.018}_{-0.022}$
WASP-101	$201.224^{+1.152}_{-1.139}$	$5.0^{+0.0}_{-0.6}$	6370^{+40}_{-100}	$1.319^{+0.030}_{-0.015}$
WASP-121	$269.898^{+1.580}_{-1.562}$	$4.0^{+0.5}_{+0.0}$	6380^{+20}_{-20}	$1.557^{+0.016}_{-0.017}$
WASP-79	$246.690^{+1.820}_{-1.794}$	$4.3^{+0.6}_{-0.1}$	6680^{+60}_{-90}	$1.586^{+0.031}_{-0.023}$
KELT-7	$136.681^{+0.937}_{-0.925}$	$5.3^{+0.2}_{-0.4}$	6700^{+50}_{-100}	$1.763^{+0.038}_{-0.023}$

Table 5.2: The final revised properties for each star. The geometric distance $R_{\rm est}$ is from Bailer-Jones et al. (2018). The $\log(g)$, $T_{\rm SED}$ and R_* are inferred by the SED fitting. For the stars that require correction to the measured radius due to [Fe/H], both the R_* and $T_{\rm SED}$ have been corrected in this table. For information on how this is done, see Section 4.3.4.

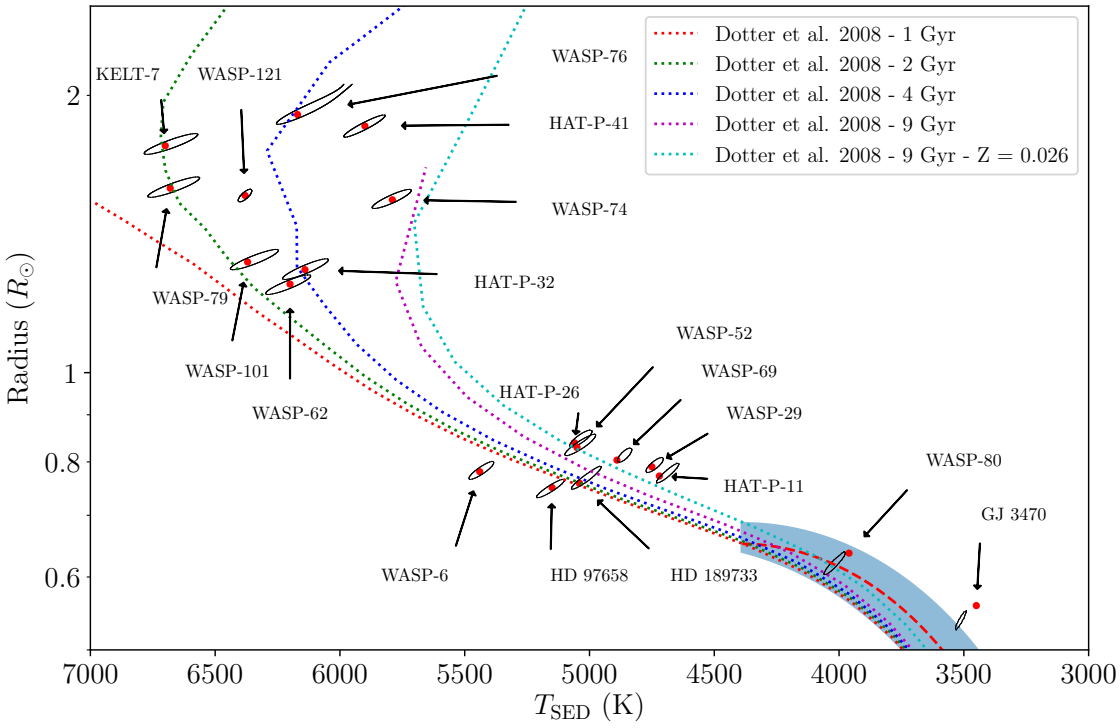

Figure 5.4: The host star properties are shown in $T_{\rm SED} - R_\star$ space, along with their associated 68% confidence contours. The M-dwarf temperature radius relationship derived in Section 4.2.2 and its bounds are plotted for comparison as a red dashed line and blue shaded region respectively.

measured stellar host parameters presented in this chapter comes a revision of the exoplanet parameters themselves; many of which differ considerably from those presented in literature. I show the revised radii in the $M_p - R_p$ plane in Figure 5.5, along with the residuals from the literature radii.

Name	R_p (R_J)	R_p/R_* Source	M_p (M_J)	ρ_p Source
GJ3470 b	$0.410^{+0.019}_{-0.028}$	Bonfils et al. (2012)	$0.060^{+0.024}_{-0.024}$	Bonfils et al. (2012)
WASP-80 b	$1.061^{+0.007}_{-0.048}$	Triaud et al. (2013)	$0.710^{+0.021}_{-0.068}$	Triaud et al. (2013)
HAT-P-11 b	$0.443^{+0.009}_{-0.006}$	Deming et al. (2011)	$0.093^{+0.014}_{-0.014}$	Bakos et al. (2010)
WASP-29 b	$0.777^{+0.021}_{-0.017}$	Hellier et al. (2010)	$0.246^{+0.038}_{-0.038}$	Hellier et al. (2010)
WASP-69 b	$1.022^{+0.063}_{-0.057}$	Anderson et al. (2014)	$0.250^{+0.035}_{-0.035}$	Anderson et al. (2014)
HD189733 b	$1.147^{+0.038}_{-0.008}$	Agol et al. (2010)	$0.316^{+0.052}_{-0.052}$	Boyajian et al. (2015)
WASP-52 b	$1.049^{+0.035}_{-0.028}$	Hébrard et al. (2013)	$0.272^{+0.025}_{-0.025}$	Hébrard et al. (2013)
HAT-P-26 b	$0.602^{+0.018}_{-0.010}$	Hartman et al. (2011a)	$0.070^{+0.018}_{-0.018}$	Hartman et al. (2011a)
HD97658 b	$0.203^{+0.006}_{-0.007}$	Van Grootel et al. (2014)	$0.026^{+0.005}_{-0.004}$	Van Grootel et al. (2014)
WASP-6 b	$1.099^{+0.020}_{-0.016}$	Gillon et al. (2009)	$0.384^{+0.071}_{-0.071}$	Gillon et al. (2009)
WASP-74 b	$1.470^{+0.029}_{-0.024}$	Hellier et al. (2015)	$0.851^{+0.068}_{-0.068}$	Hellier et al. (2015)
HAT-P-41 b	$1.853^{+0.045}_{-0.045}$	Hartman et al. (2012)	$1.026^{+0.154}_{-0.154}$	Hartman et al. (2012)
HAT-P-32 b	$1.898^{+0.036}_{-0.031}$	Hartman et al. (2011b)	$0.772^{+0.165}_{-0.110}$	Hartman et al. (2011b)
WASP-76 b	$2.023^{+0.093}_{-0.037}$	West et al. (2016)	$1.340^{+0.089}_{-0.089}$	West et al. (2016)
WASP-62 b	$1.347^{+0.021}_{-0.025}$	Hellier et al. (2012)	$0.551^{+0.079}_{-0.079}$	Hellier et al. (2012)
WASP-101 b	$1.440^{+0.035}_{-0.020}$	Hellier et al. (2014)	$0.577^{+0.064}_{-0.064}$	Hellier et al. (2014)
WASP-121 b	$1.887^{+0.021}_{-0.022}$	Delrez et al. (2016)	$1.448^{+0.072}_{-0.072}$	Delrez et al. (2016)
WASP-79 b	$1.738^{+0.055}_{-0.050}$	Smalley et al. (2012)	$1.013^{+0.225}_{-0.225}$	Smalley et al. (2012)
KELT-7 b	$1.561^{+0.035}_{-0.023}$	Bieryla et al. (2015)	$1.356^{+0.224}_{-0.209}$	Bieryla et al. (2015)

Table 5.3: The revised properties for each exoplanet in our sample. The radius was determined using my measured R_* and the value of R_p/R_* from the literature. The planet mass was then calculated using the revised value of R_p and the value of ρ_p from the literature.

The median residual for my measurements falls at 4%, with the mean residual occurring at 6%, indicating a small possible systematic; however this would need constraining with larger sample. The precision of the exoplanet measurements presented is drastically improved compared to the literature, showing a mean of a factor of two reduction in the size of the uncertainty of the exoplanet radii. Several of the sample are in good agreement with the previous literature determinations, with the measured radii for WASP-29 b, WASP-69 b and WASP-62 b agreeing within 1σ. However, only a third of exoplanet radii agree to within their uncertainty bounds. The disparity between this and the two thirds agreement in host star luminosities further supports my previous assertion in Section 5.1 that the synthetic G_G-band uncertainties for host stars are over-estimates. Given that the transit measurements provide a relatively direct route to the exoplanet radius given a measurement of the host radius, the natural conclusion to explain such a large departure from the literature would be that my measured host properties are incorrect.

An acid test of how well my newly derived host parameters reflect reality can be sought by generating synthetic G_G band photometry using the same method as in Section 2.1.4, with revised $R_\star$ and T_{SED} values presented in this chapter, and Gaia DR2 distance measurements (Bailer-Jones et al. 2018). I present a version of Figure 5.1 with the revised synthetic photometry overlaid for comparison in Figure 5.6. There are some crucial things to note about this comparison. My parameter measurements show a factor of 10 reduction in RMS residual in luminosity over those in the literature; a marked improvement in accuracy. Furthermore, compared to previous measurements, my dataset shows nearly a factor of 2 improvement to the mean luminosity uncertainty of the sample. Interestingly, comparing the literature values of T_{sp} with my values of T_{SED} shows that they are overall in good agreement, with 17 of the 19 T_{SED} measurements being within 2σ of literature T_{sp} values. Given all of these considerations, it seems that the work presented in this thesis chapter poses a considerable improvement to both the precision and accuracy of exoplanet host measurements over existing literature values. For this not to be the case, one of the following arguments I have made has to be shown as untenable. First, throughout this work I have assumed that the distances from Bailer-Jones et al. (2018) are a good representation of their true distance measurement. Owing to the large uncertainties

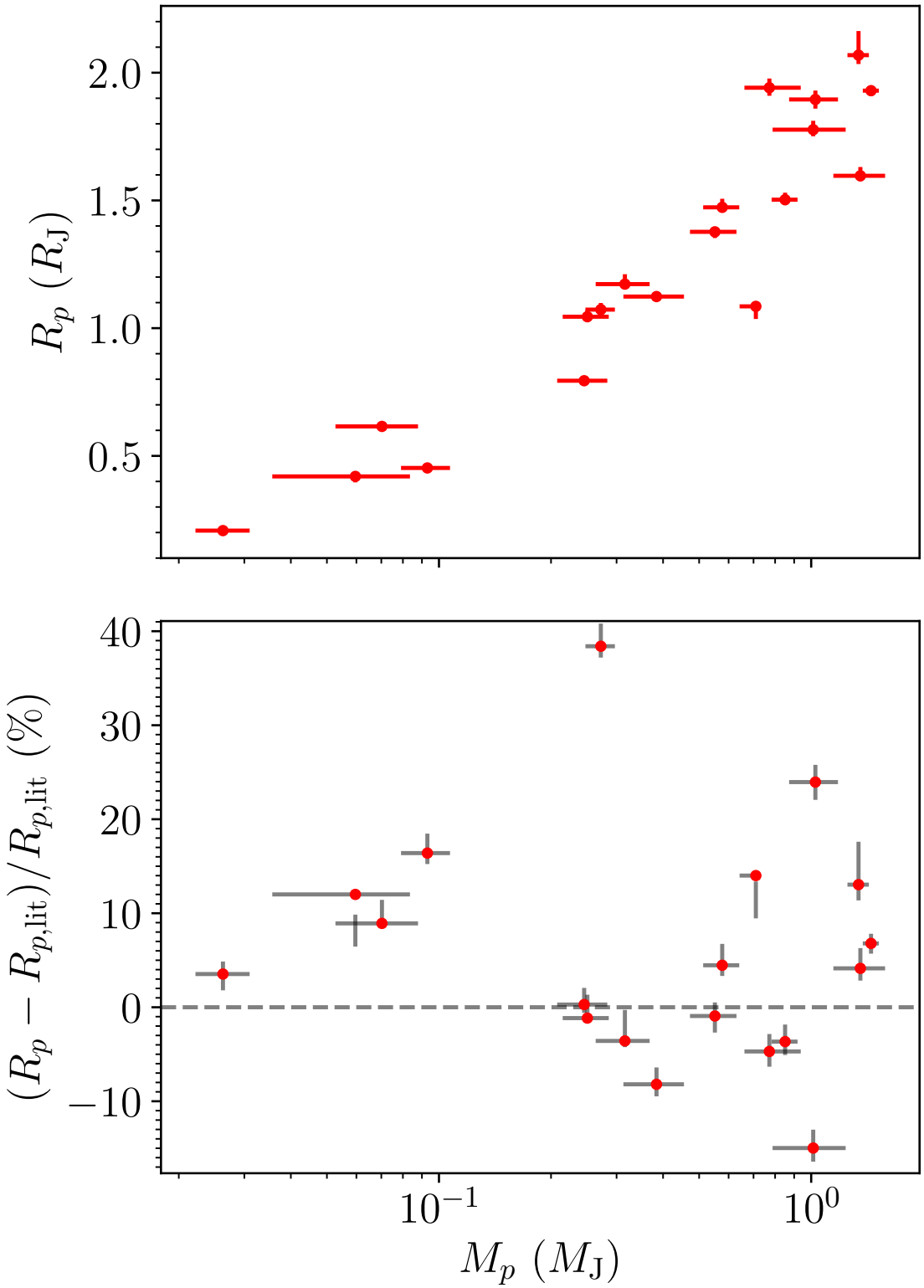

Figure 5.5: The revised exoplanet radii shown in the $M_p - R_p$ plane (top) and the residual in per cent between the literature radii and the revised radii in this thesis. Several revised radii agree well with the literature determinations. However, many are in disagreement, with the residual exhibiting an RMS difference of 13%.

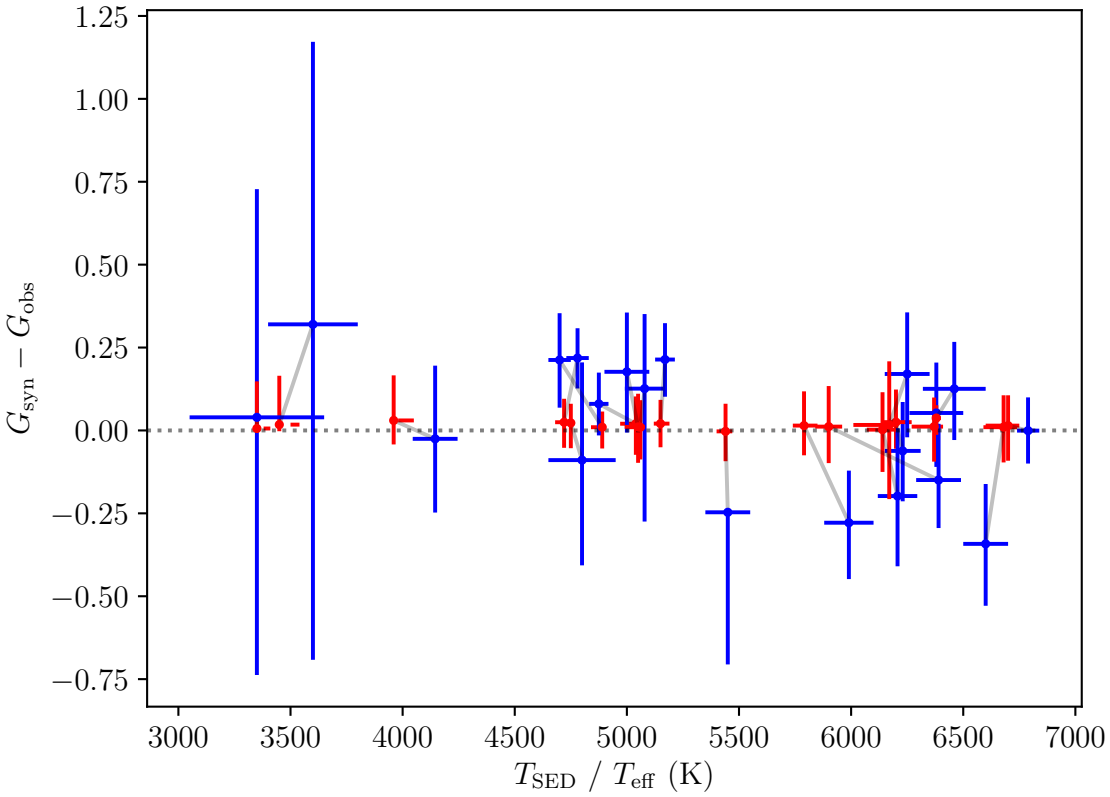

Figure 5.6: As Figure 5.6, but also containing the measured host parameters as found by the SED fitting performed in this chapter, shown in red. A line is drawn between my value and the literature value to indicate their correspondence. It is clear the parameters from my SED fitting better reflect the luminosity measured by Gaia than the existing parameters, and are also much better constrained.

on the existing literature values for distance, all but 4 are within 1σ of the much better constrained distance values I have adopted for this fitting. Furthermore, I have assumed that any systematic in distance is much smaller than the prescribed uncertainty. Due to the level of agreement shown with the radius residual of the DEB sample in Figure 4.10, large systematic or statistical errors of this nature seem unlikely. An argument could be levelled that the stellar atmosphere models that I have been using to produce the grids of synthetic photometry on which fitting is performed are in disagreement with reality. However, I showed in Section 3.5.1 that the fluxes provided by stellar atmospheres are in overall agreement with my observed, flux-calibrated spectra. Given this work was carried out in the M-dwarf regime, where there are noted problems with models, it seems unlikely that earlier types would succumb to serious problems. One could also argue that my fitting methodology is not sound, however the $T_{\rm SED}$ determined by my fitting are in overall agreement with the $T_{\rm sp}$ presented in the exoplanet literature and the luminosity is in firm agreement with that observed in Gaia DR2; once again supporting my radius measurements and making a counter-argument moot. I also note that at no point in this thesis has the Gaia $G_{\rm G}$ band magnitude been used for the purposes of fitting; which, if I had done so, may have forced agreement. Its wide response, with an effective width $\Delta\lambda_{\rm eff}$ in excess of 4000Å, make it an imprecise lens through which to constrain the colour of the stellar SED in the optical; however it does represent a robust measurement of visible luminosity. Hence, $G_{\rm G}$ provides one of the best indications we currently have of the true luminosity of the source, and the agreement seen between it and my synthetic photometry shows that I am able to reproduce both the overall flux and colour in the visible part of the SED.

I also performed a comparison between my values and the literature values in the $T_{\rm SED}/T_{\rm sp}-R_\star$ plane in Figure 5.7. This figure demonstrates that there is no clear systematic difference between the radii and temperatures presented in the literature and measured from SED fitting. Validation of the radius determinations for two systems can be found in the IRFM measurements found in the literature. By combining the $\theta_{\rm IRFM}$ measured for WASP-6 (Gillon et al. 2009) and WASP-80 (Triaud et al. 2013) with the distance estimates of Bailer-Jones et al. (2018), I find that $R_\star = 0.784 \pm 0.042\ R_\odot$ and $R_\star = 0.63^{+0.029}_{-0.03}\ R_\odot$ respectively. Both agree with my measured radii to within 1σ, and represent radii 10%

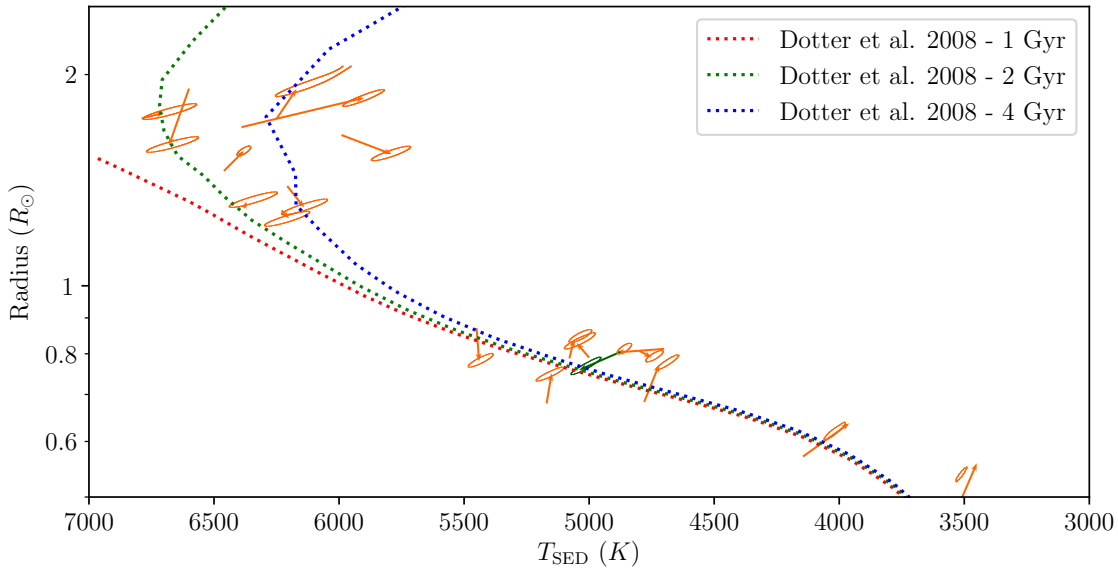

Figure 5.7: The arrows show the vector that maps the literature value from the PanCET primary target list onto the value measured in this thesis from the SED fitting process. The green denotes HD 189733, for which the literature radius was determined using interferometry. Those remaining, shown in orange, are derived from the light curves and stellar models.

smaller and 5% larger than their respective literature measurements.

Curiously, given that this sample of stars straddles the well understood solar regime, I am driven to critically question why the revisions are so sizeable. The stellar parameters adopted for the hosts are largely determined from models, however the models are in overall agreement with observations at earlier than late-K. As I addressed in Section 1.8.3, the key interface between observations and models comes from mapping the stellar density $\rho_\star$, which is measured from the transit, onto stellar interior models in the $R/M^{1/3}$–$T_{\rm eff}$ plane. I have already established that the $T_{\rm sp}$ observations are mostly consistent with my measured $T_{\rm SED}$, thus I am drawn to conclude that there may be some issues with the measurements of stellar density that are used to perform the mapping.

5.4.1 Sources of Systematic Error

I have shown that none of the fundamental assumptions about my underlying methodology could be responsible for explaining the large discrepancy between my stellar host parameters, and those described in the literature. However, there remain some important observational considerations that should be correctly treated in order to avoid large systematic errors in these measurements. In this section, I will enumerate several of them,

discuss their impact on measurements of exoplanet hosts, and where appropriate suggest strategies for their mitigation.

In each case I followed I similar methodology to Section 4.3.2.3, where I modified the input grid to emulate the physical effect being investigated, simulated a catalogue with this modified grid, and then fitted it using the same grid of CIFIST models used in the main fit. Where appropriate, I have also fitted the stars in the input catalogue with these modified grids to perform the inverse experiment, and compare model output with real data. For the $T_{\rm eff} - R$ relation used in making the simulated catalogues I adopted the 4 Gyr Baraffe et al. (2015) isochrone. Although I have previously corrected the Dotter et al. (2008) isochrone for M-dwarfs, the isochrone does not remain monotonic and well-defined for the $T_{\rm eff}$ between 3000 K and 6000 K; leading to problems with the interpolation.

5.4.1.1 Extinction

Interstellar dust poses a considerable hindrance for stellar characterisation. In Chapter 4 an upper limit of $d < 100$pc was placed on distance. At such close proximity interstellar extinction is negligible. However in this chapter the distance constraint is removed, necessitating a more rigorous approach towards the effects of extinction. The only star in the catalogue with a well measured extinction is HAT-P-41b with $E(B-V) = 0.11$ (Hartman et al. 2012), which is fortunately also the most distant. Given that all stars in the sample are on the MS or beyond, hence clear of the envelope from which they formed, I have made the reasonable assumption that extinction is a function only of distance. Thus I adopted an upper limit of $E(B-V) = 0.1$ for this sample. To assess the effect of dust on observations, extinction was introduced into the simulated catalogue using the method described in Section 2.1.7. I generated grids with $E(B-V) = 0.0, 0.01$ and 0.1. The difference between the reddened and unreddened fits is presented in Figure 5.8. It is clear that any extinction in the sightline to a planet host star will attenuate and redden the stellar SED, hence these fits moving to warmer $T_{\rm SED}$ at lower $R_\star$. However it is also clear that extinction affects low- and intermediate-mass star fits differently. Due to the prevalence of strong molecular bands in cooler stellar atmospheres, their SEDs are more distinctive than those above 4000 K. For sightlines through modest extinction, this allows the fitting technique to remain fairly fault tolerant for $T_{\rm SED}$ determinations. Whereas

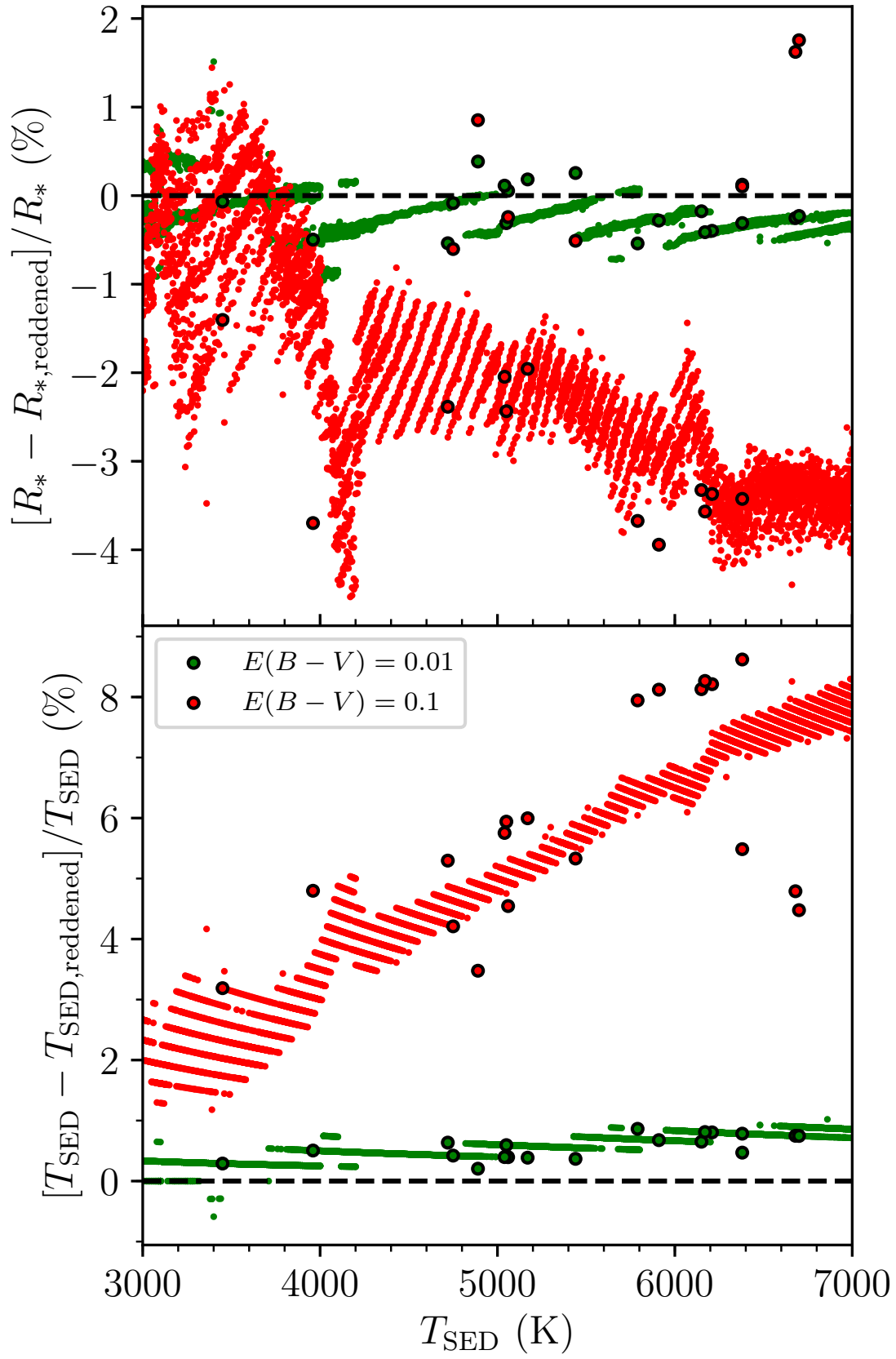

Figure 5.8: The radius (top) and temperature (bottom) residual resulting from fitting with grids of increasing extinction, compared to an unreddened grid. The residuals are with the $E(B-V) = 0$ grid compared to the $E(B-V) = 0.01$ grids (green) and $E(B-V) = 0.1$ grid (red).

hotter stars which are dominated by continuum emission have nearly double the residual in temperature. However, because the temperature is determined correctly for cool stars, the attenuation of brightness causes an underestimate of luminosity, hence radius. This fitting suggests that for nearby exoplanet hosts with $E(B-V) \lesssim 0.01$, neglecting extinction is a safe assumption, as the effect remains well below 1%. However, this investigation also suggests that grids should be reddened with an appropriate extinction before fitting if they are subject to an $E(B-V)$ much greater than 0.01, depending on $T_{\rm eff}$, to avoid errors of up to 4% in $R_\star$ and 8% in $T_{\rm SED}$ at $E(B-V) = 0.1$. Although, in principle, reddening could be introduced as a free-parameter in the SED fitting process itself, the constraints I have achieved so far are only weak due to degeneracies of extinction with both L and $T_{\rm SED}$; so alternate methods should currently be employed for measuring the extinction of targets.

5.4.1.2 Metallicity

In Section 4.3.2.5 I found that the scatter in the measured radius for M-dwarf stars exhibited a correlation with [Fe/H]. I showed that this was caused by fitting the distribution of metallicities in the solar neighbourhood using only solar metallicity models. Thus, I suggest that when performing SED fits of exoplanet host M-stars, one should be mindful of their metallicity and how treatments of metallicity will change the resulting temperature and radius. To test this for hotter stars, I have synthesised catalogues at [M/H] = -0.5, 0.0 and +0.5 at solar abundances. The atmospheres for this grid are provided by the AGSS2009 stellar atmospheres, which substitute the Caffau et al. (2011) solar abundances for those of Asplund et al. (2009). These grids are limited to a range of $\log(g) = 4.0 - 4.5$, due to this being the range of surface gravity covered by the AGSS2009 atmosphere grids at the required temperatures for all metallicities. The result of this fitting is shown in Figure 5.9. As one would intuitively expect, the metallicity-induced discrepancy has a much stronger effect in stars whose $T_{\rm SED} < 4000$ K, where the temperature in the photosphere is cool enough that strong molecular features in the atmosphere become commonplace. However, the discrepancy for stars with $T_{\rm SED} > 4000$ K remains systematically below the 1% level, presumably due to the lack of these molecular features. This means that metallicity should not pose a problem for measurements of solar-type exoplanet hosts.

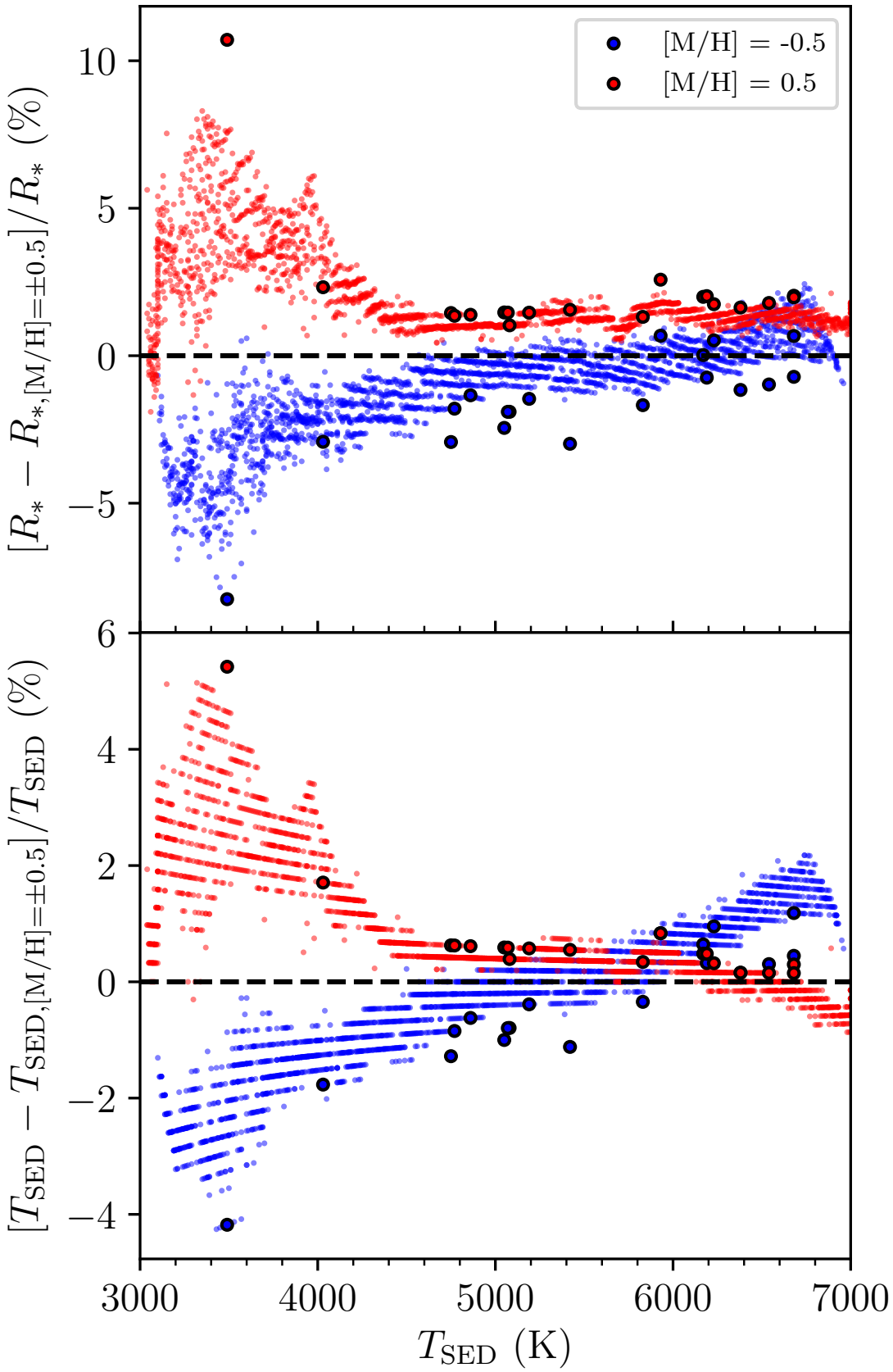

Figure 5.9: I fitted each of the targets with [Fe/H] = 0.0, -0.5 and +0.5 atmospheres. The residual of the retrieved radii and temperatures are shown in the top and bottom pane respectively. To assess the effect of metallicity on the technique, we have also taken those atmospheres and simulated catalogues with these grids, which are then fit with the CIFIST grids. Both the observed retrievals and the forward models are consistent, show that stars cooler than 4500 K suffer up to a 10% perturbation in radius if uncorrected. However, stars hotter than 4000 K retrieve the correct radii to within about 1%.

However, discrepancies of 10% in $R_\star$ and 5% in $T_{\rm SED}$ can be incurred by not properly accounting for metallicity for low-mass hosts.

5.4.1.3 Activity

It is particularly difficult to mitigate against the dynamic and unpredictable behaviour of starspots and plages on stellar surfaces. I demonstrated in Section 4.3.2.4 that starspots are able to perturb the temperature and radius measured by SED fitting techniques. However, I also established in Section 4.3.2.6 that to be consistent with the tight M-dwarf MS, filling factors for main sequence M-dwarfs should typically remain $< 10\%$.

Both starspots and plages can be modelled by adding a second temperature component into the model stellar photosphere (see Section 4.3.2.3). The temperature of the spotted component is reasonably assumed to be $T_{\rm spot} = 0.8\ T_{\rm imac}$ for 3000 K $< T_{\rm imac} <$ 7000 K (see Berdyugina 2005). However, determinations of $T_{\rm plage}$ have thus far only been constrained by observations of the solar surface to have a temperature contrast of $100 - 300$ K (Oshagh et al. 2014; Worden et al. 1998; Unruh et al. 1999; Meunier et al. 2010). Given this I adopt the upper end of this limit and reasonable estimate that $T_{\rm plage} = 1.05\ T_{\rm imac}$ for 3000 K $< T_{\rm imac} <$ 7000 K. The result of fits to the grids with activity included are shown in Figure 5.10. The scatter of points within this plot suggests that not correctly treating plages within the grids when characterising any star should not affect the measured parameters. However, I do note that the constraints on the temperature contrast and filling factors on stars other than the Sun make this an initial estimate. This investigation does however indicate that for sufficiently precise measurements of radius, one should take care to correctly treat starspots in the grids used for fitting. For stars with $T_{\rm SED} < 5000$ K, measured radii inflated by $1 - 3\%$ with $T_{\rm SED}$ up to 1.5% cooler should be expected; depending on error in $T_{\rm SED}$ and γ.

5.5 Chapter Summary

In this chapter I have shown that the SED fitting methodology that I applied to studies of stellar evolution can also be readily applied to measuring the parameters of arbitrary exoplanet host stars. In doing so, I have demonstrated that the method generalises well to

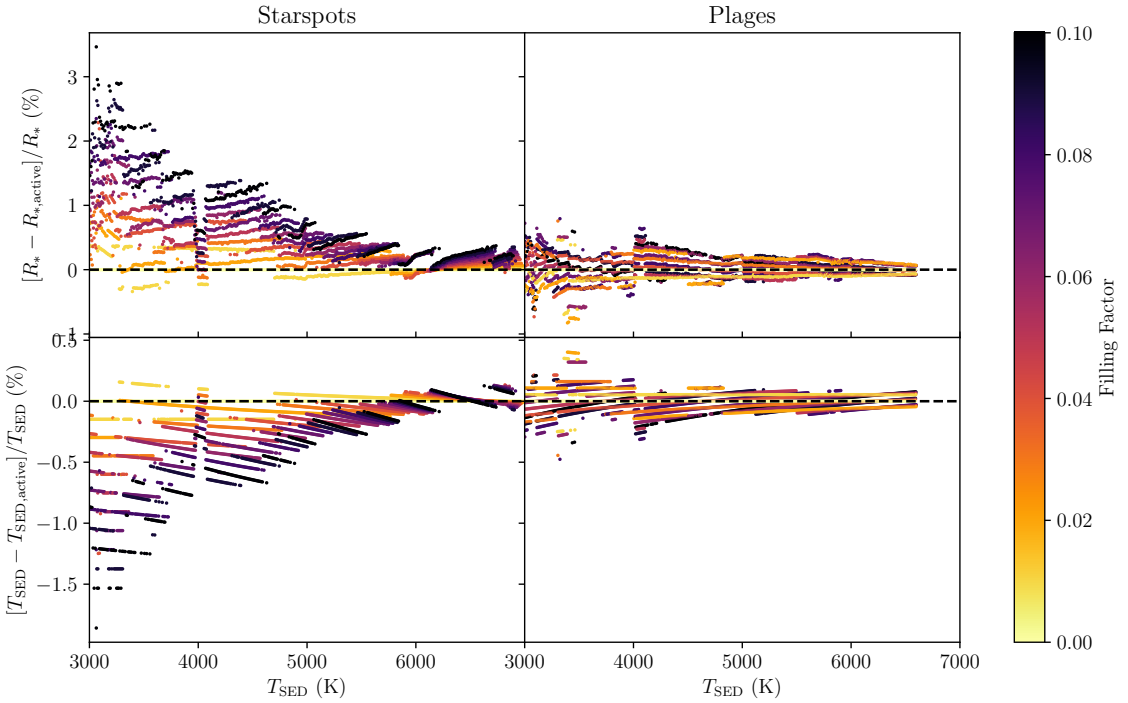

Figure 5.10: The scatter of the measured $R_\star$ (top) and T_{SED} (bottom) caused by starspots (left) and plage (right) as a function of input T_{eff}. This shows that for reasonable filling factors of up to ~ 10%, a scatter of 3% should be expected in $R_\star$ and about 2% in T_{SED}. This scatter reduces to < 1% for temperatures hotter than 5000 K. The plage models truncate at 6600 K due to the plage photosphere exceeding the upper T_{eff} limit of the CIFIST model grid.

stars earlier than M-dwarfs as long as the stellar atmospheres cover the required region of the $T_{\mathrm{eff}} - \log(g)$ plane and well characterised multi-waveband photometry exists for the target. I revised the radii of 19 exoplanet hosts, improving both the precision and accuracy of the measurement in the process. As a result, I have been able to revise the radii and masses of 19 well-studied studied exoplanets. The sample shows a mean of a factor of two reduction in the sizes of exoplanet radius uncertainties, presenting a considerable improvement over the literature. This chapter acts as a proof-of-concept that this method can serve as an independent, orthogonal means for determining exoplanet host parameters, separate from the methods usually employed by the exoplanet community. Given that the method relies only on readily available archival photometry and Gaia parallaxes, it serves as a promising means of characterising the abundant number of exoplanets currently being discovered by large surveys. With this application in mind, I performed a parameter space exploration to probe the effect of unconstrained observational uncertainties on measurements of $R_\star$ and T_{SED}, both of which are vital for the rapidly evolving field of exoclimatology (see Section 5.4.1).

Chapter 6

Conclusions and Future Work

"When you eliminate the impossible, whatever remains, however improbable, must be the truth. "

— Spock

6.1 Conclusions

This thesis has addressed the ubiquitous problem of measuring accurate stellar radii. Stellar spectral energy distributions encode properties of the stellar photosphere; with the integrated flux yielding the luminosity and the shape providing an indication of the temperature. I have introduced a method which measures these properties using only multi-waveband photometry and precise distances, in turn providing a new method for determining stellar radii.

This technique was first applied to understanding the well known discrepancy between the theoretical isochrones and observed stellar sequence for low-mass members of the Pleiades and Praesepe clusters. The measured inflation of $8-20\%$ for Pleiades members and $10-20\%$ for Praesepe members indicates that the stellar interior models are responsible for the disagreement. Not only does the isochrone at the measured age of either cluster not reproduce the stellar sequence at $T_{\rm eff} < 4000$K, but the observed sequence straddles a number of different ages. Were one to perform an isochrone fitting with only these low-mass members, one would measure both clusters to be $20-50$Myr old,

with both appearing older as the sample is extended toward lower masses. A powerful test of both the stellar atmospheres and the SED fitting methodology was performed by observing and robustly flux calibrating 20 low-mass stars from across both clusters. These spectra were directly compared to the synthetic spectra corresponding to the parameters determined from the stellar SED. Both show excellent agreement, however it is clear that a number of spectral features are still discrepant; especially towards the blue end of the spectra.

After establishing the nature of the discrepancy in pre-MS M-dwarfs, the same SED fitting methodology was applied to 15 279 main sequence M-dwarfs distributed across the sky. Lacking the well constrained distances of open clusters, this investigation harnessed the unprecedented number of distance measurements made available by Gaia DR2. This further built on the finding that, even for main sequence M-dwarfs, none of the purely theoretical stellar models can describe mean radius inflation on the main sequence at temperatures lower than about 4000K; with the measured stellar sequence being inflated by $3 - 7\%$ from the models. Magnetic models would suggest a spread in radius from the theoretical sequence for non-magnetic models up to a maximum inflation, and that this spread would be correlated with key observational indicators of magnetic activity. However, careful analysis showed that M-dwarfs follow a tight sequence (with a scatter smaller than 1 to 2%), and that none of the key indicators correlate with inflation - suggesting that stellar magnetism is currently unable to explain inflation in main-sequence M-dwarfs. It was shown that using only solar metallicity models for fitting a distribution of metallicities results in a spurious correlation with radius inflation. Given that SED fitting captures the luminosity accurately regardless of this disparity, accurate measurements of [Fe/H] permitted this perceived spread to be corrected.

Building on this work, the SED fitting methodology was extended to measuring the parameters of 19 near main-sequence exoplanet hosts. In doing so, the technique was demonstrated to generalise well to intermediate masses and longer distances. Using the measurement of the transit depth, the exoplanet radii were revised to be consistent with the measured stellar radii. The revised exoplanet radii range from about 14% smaller to 23% larger than their previously measured literature values. By generating synthetic

catalogues of observations, the effects of different uncertainties on measured parameters were assessed. At the extremity of measured extinction ($E(B-V) = 0.1$) the radii can appear deflated by up to 4%. Adopting the maximum reasonable starspot filling factor for M-dwarfs of 10%, it was shown that starspots could at most contribute an inflation of around 3% to the measured radius. It was also shown that when measuring via SED fitting, a poorly constrained uncertainty in [Fe/H] could cause the measured radius to be discrepant by ±10%, depending on the difference in metallicity.

More broadly, the work presented in this thesis proves the veracity of the SED fitting methodology that was introduced to address these long standing problems. Given its proven accuracy and ease of use, it shows promise as an orthogonal method that can be more widely applied to determining exoplanet host properties; independent of the transit fitting. In particular, for applications to large exoplanet surveys, such as TESS, the method could prove an indispensable tool with which to achieve a large number of exoplanet characterisations.

6.2 Future Work

There are a number of progressions from this work, either developing on ideas presented in this thesis, or addressing questions and deficiencies that this work has brought to light. First, the sample of studies could be expanded to constrain M-dwarf radius contraction over the pre-MS. Second, I have demonstrated that the SED fitting method already shows an improved precision over other methods for measuring stellar radii. However, despite this there are still a number of challenges posed by stellar activity and extinction that may prove problematic for widespread adoption for exoplanet host characterisation.

6.2.1 Constraining Radius Contraction in Pre-MS M-dwarfs

This thesis has established that the radii predicted by pre-MS models are discrepant from those measured for M-dwarfs at the ages of 132 and 665Myr. A natural progression of this work is to extend the SED fitting to encompass a larger number of open clusters which span a range of ages and metallicities. In doing so, the evolution of the discrepancy between theoretical models and observed radii can be examined in much more detail

throughout the pre-MS. By examining this effect more thoroughly over age, the exact timescale of pre-MS M-dwarf contraction can be determined, and the physics from which it results assessed. Another product of this investigation would be valuable empirical $T_{\rm SED} - R$ relationships with which to calibrate stellar interiors.

6.2.2 Large Scale Exoplanet Characterisation Campaigns

Another natural follow on from this work would be to extend the exoplanet characterisation methodology to a statistically significant sample of exoplanet hosts. The bountiful nature of the multi-waveband photometric data, afforded by archival data in all-sky surveys, combined with distances provided by Gaia DR2, means this technique is readily applicable where others may not be. Because no new observations are required, proactive campaigns can be performed speculatively with little risk of wasting valuable resources. For example, the technique could be performed on the TESS candidate target list (Stassun et al. 2018), which encompasses about 9.5 million stars; an insurmountable volume and complexity for other stellar characterisation techniques. Worthy of note is that the selection process for TESS targets favours bright, cool dwarfs, to maximise the transit signal of small planets; a population which this SED fitting technique was initially developed to study. The characterisation of these cool dwarfs is performed in Muirhead et al. (2018) using the colour–$T_{\rm eff}$ and $M_{K_s} - R_*$ relations of Mann et al. (2015); which have been shown to be less precise than this work and inconsistent with our observations.

A complication to address involves the relative scarcity of UV and MIR data, which pin the blue and red end of the SED respectively. An initial estimate shows that neglecting the WISE or Galex bands from fitting of the PanCET sample results in difference of $1-2\%$ in stellar radius. In principle meaning that using only Gaia DR2 and 2MASS photometry is sufficient to determine exoplanet host radii accurate to within current uncertainties. Additionally, reliable stellar characterisations for single stars at this precision necessitates improvements to methodology and the constraints to other stellar parameters.

6.2.3 Improving Measurements of [Fe/H]

It was established that one of the limiting factors currently facing attempts to measure M-dwarf radii are the imprecise measurements of metallicity for M-dwarfs. Uncertainty in metallicity contributes considerably to mean measured uncertainty of 2.4% in the M-dwarf sample; with the average uncertainty in [Fe/H] of around 10% contributing 1.7% to this figure. If methods for metallicity determination could constrain the measured values of [Fe/H] to $\sim$ 2% or better, radius uncertainties of around 1% could be achieved for M-dwarfs. Given the need of accurate radii in both stellar physics and exoplanet science, especially with the push towards observing super-Earth planets around low-mass stars, this added precision would prove an important development.

6.2.4 Deeper Understanding of Time-Varying Stellar Activity

It was demonstrated in this thesis that stellar activity has the potential of causing large errors in measurements of both $T_{\rm SED}$ and R. In particular Section 4.3.2.3 demonstrated that the SED fitting should measure an apparent spread due to small variations in spot filling factor. However, the tight measured sequence (see Section 4.3.2.5) implies that coverage of starspots in main-sequence M-dwarfs is remarkably consistent at $\gamma \leq 0.1$. This seems counter-intuitive considering the diverse levels of activity demonstrated in Section 4.3.2.4. Even at less than 10% surface coverage, starspots alone can cause up to 3% error in cool dwarfs, with the true effect of plages being poorly constrained for stars other than the Sun.

With this in mind, studying stellar activity, in particular the time-varying aspect, is important for future studies of both stars and exoplanets. The time varying aspect of activity is both an advantage and a disadvantage in applying archival data to radius measurement of stellar targets. It is probable that artefacts on the stellar surface will vary between the different epochs of observations employed in the fitting, which may average out to a smaller discrepancy in measured parameters, however it will make determining the true effect a more challenging process.

6.2.5 Disentangling Extinction

One further complicating factor in many measurements of stellar parameters is the previously mentioned problem of interstellar extinction. Problems due to metallicity were resolved by realising that the luminosity is conserved, allowing a fixed point around which to pivot other parameters. However, extinction attenuates stellar flux, removing this constraint. The reddening effect also means that measured $T_{\rm SED}$ for a star subject to even moderate extinction will be too cool.

Initial work on resolving this issue involved fixing $\log(g)$ and substituting $E(B-V)$ as a free parameter within the grids used for the fitting. Although some extinctions were preferred over others, the results obtained from the current methodology are not consistently conclusive; mainly due to the degeneracy in SED shape caused by the reddening. So, alternate methodologies must be adopted to yield solid constraints on extinction. This endeavour relies on accurate extinction laws, which can reproduce the observed extinction for all the required sightlines in the Galactic plane. The mean Galactic extinction has been well constrained, however the formation and re-processing of grains poses a number of problems in dense regions; including anomalous extinction laws caused by poorly understood grain size distributions.

To summarise, I have introduced a SED fitting technique that can be used to determine stellar radius and temperature, and has already been applied throughout this thesis to resolve a number of open questions in stellar physics and exoplanet science. Although I have suggested a number of improvements, the measurements resulting from this method are already more precise than are available from previous methods of determining stellar radii.

Bibliography

Abbett, William P., Michelle Beaver, Barry Davids, et al. 1997. 'Solar Convection: Comparison of Numerical Simulations and Mixing-Length Theory.' ApJ 480, no. 1 (May): 395–399.

Abramson, G. 2018. 'The Distance to the Pleiades According to Gaia DR2.' *Research Notes of the American Astronomical Society* 2, no. 3, 150 (August): 150.

Agol, Eric, Nicolas B. Cowan, Heather A. Knutson, et al. 2010. 'The Climate of HD 189733b from Fourteen Transits and Eclipses Measured by Spitzer.' ApJ 721, no. 2 (October): 1861–1877.

Allard, F., D. Homeier, & B. Freytag. 2012a. 'Models of very-low-mass stars, brown dwarfs and exoplanets.' *Philosophical Transactions of the Royal Society of London Series A* 370, no. 1968 (June): 2765–2777.

Allard, F., D. Homeier, B. Freytag, & C. M. Sharp. 2012b. 'Atmospheres From Very Low-Mass Stars to Extrasolar Planets.' In *EAS Publications Series*, 57:3–43. November.

Allard, France, Tristan Guillot, Hans-Günter Ludwig, et al. 2003. 'Model Atmospheres and Spectra: The Role of Dust.' In *Brown Dwarfs*, edited by Eduardo Martı n, 211:325. IAU Symposium. June.

An, D., D. M. Terndrup, M. H. Pinsonneault, et al. 2007. 'The Distances to Open Clusters from Main-Sequence Fitting. III. Improved Accuracy with Empirically Calibrated Isochrones.' ApJ 655 (January): 233–260.

Anderson, D. R., A. Collier Cameron, L. Delrez, et al. 2014. 'Three newly discovered sub-Jupiter-mass planets: WASP-69b and WASP-84b transit active K dwarfs and WASP-70Ab transits the evolved primary of a G4+K3 binary.' MNRAS 445 (December): 1114–1129.

Andrae, R., M. Fouesneau, O. Creevey, et al. 2018. 'Gaia Data Release 2: first stellar parameters from Apsis.' *ArXiv e-prints* (April).

Asplund, M., N. Grevesse, A. J. Sauval, & P. Scott. 2009. 'The Chemical Composition of the Sun.' ARA&A 47 (September): 481–522.

Astraatmadja, Tri L., & Coryn A. L. Bailer-Jones. 2016. 'Estimating Distances from Parallaxes. II. Performance of Bayesian Distance Estimators on a Gaia-like Catalogue.' ApJ 832, no. 2, 137 (December): 137.

Astropy Collaboration, Thomas P. Robitaille, Erik J. Tollerud, et al. 2013. 'Astropy: A community Python package for astronomy.' A&A 558, A33 (October): A33.

Bailer-Jones, C. A. L. 2015. 'Estimating Distances from Parallaxes.' PASP 127 (October): 994.

Bailer-Jones, C. A. L., J. Rybizki, M. Fouesneau, G. Mantelet, & R. Andrae. 2018. 'Estimating distances from parallaxes IV: Distances to 1.33 billion stars in Gaia Data Release 2.' *ArXiv e-prints* (April).

Bakos, G. Á., G. Torres, A. Pál, et al. 2010. 'HAT-P-11b: A Super-Neptune Planet Transiting a Bright K Star in the Kepler Field.' ApJ 710 (February): 1724–1745.

Baraffe, I., G. Chabrier, F. Allard, & P. H. Hauschildt. 1998. 'Evolutionary models for solar metallicity low-mass stars: mass-magnitude relationships and color-magnitude diagrams.' A&A 337 (September): 403–412.

Baraffe, I., D. Homeier, F. Allard, & G. Chabrier. 2015. 'New evolutionary models for pre-main sequence and main sequence low-mass stars down to the hydrogen-burning limit.' A&A 577, A42 (May): A42.

Baraffe, Isabelle, & Gilles Chabrier. 1996. 'Mass–Spectral Class Relationship for M Dwarfs.' ApJL 461 (April): L51.

Barber, R. J., J. Tennyson, G. J. Harris, & R. N. Tolchenov. 2006. 'A high-accuracy computed water line list.' MNRAS 368, no. 3 (May): 1087–1094.

Barentsen, G., H. J. Farnhill, J. E. Drew, et al. 2014. 'The second data release of the INT Photometric Hα Survey of the Northern Galactic Plane (IPHAS DR2).' MNRAS 444 (November): 3230–3257.

Barrado y Navascués, David, John R. Stauffer, & Ray Jayawardhana. 2004. 'Spectroscopy of Very Low Mass Stars and Brown Dwarfs in IC 2391: Lithium Depletion and Hα Emission.' ApJ 614, no. 1 (October): 386–397.

Bayo, A., C. Rodrigo, D. Barrado Y Navascués, et al. 2008. 'VOSA: virtual observatory SED analyzer. An application to the Collinder 69 open cluster.' A&A 492, no. 1 (December): 277–287.

Bekki, Kenji. 2009. 'Dark impact and galactic star formation: origin of the Gould belt.' MNRAS 398, no. 1 (September): L36–L40.

Bell, C. P. M., T. Naylor, N. J. Mayne, R. D. Jeffries, & S. P. Littlefair. 2012. 'Pre-main-sequence isochrones - I. The Pleiades benchmark.' MNRAS 424 (August): 3178–3191.

———. 2013. 'Pre-main-sequence isochrones - II. Revising star and planet formation time-scales.' MNRAS 434 (September): 806–831.

Bell, C. P. M., J. M. Rees, T. Naylor, et al. 2014. 'Pre-main-sequence isochrones - III. The Cluster Collaboration isochrone server.' MNRAS 445 (December): 3496–3511.

Benn, C., K. Dee, & T. Agócs. 2008. 'ACAM: a new imager/spectrograph for the William Herschel Telescope.' In *Ground-based and Airborne Instrumentation for Astronomy II*, 7014:70146X. Proc. SPIE. July.

Berdyugina, S. V. 2005. 'Starspots: A Key to the Stellar Dynamo.' *Living Reviews in Solar Physics* 2, 8 (December): 8.

Berger, D. H., D. R. Gies, H. A. McAlister, et al. 2006. 'First Results from the CHARA Array. IV. The Interferometric Radii of Low-Mass Stars.' ApJ 644 (June): 475–483.

Berger, T. E., A. M. Title, T. Tarbell, et al. 2007. 'What are 'Faculae'?' In *New Solar Physics with Solar-B Mission*, edited by K. Shibata, S. Nagata, & T. Sakurai, 369:103. Astronomical Society of the Pacific Conference Series.

Bernath, Peter. 2006. 'Metal Hydrides in Astronomy.' In *Astrochemistry - From Laboratory Studies to Astronomical Observations*, edited by Ralf I. Kaiser, Peter Bernath, Yoshihiro Osamura, Simon Petrie, & Alexander M. Mebel, 855:143–148. American Institute of Physics Conference Series. September.

Bianchi, Luciana, Bernie Shiao, & David Thilker. 2017. 'Revised Catalog of GALEX Ultraviolet Sources. I. The All-Sky Survey: GUVcat_AIS.' ApJS 230, no. 2, 24 (June): 24.

Bieryla, Allyson, Karen Collins, Thomas G. Beatty, et al. 2015. 'KELT-7b: A Hot Jupiter Transiting a Bright V = 8.54 Rapidly Rotating F-star.' AJ 150, no. 1, 12 (July): 12.

Binney, James, & Scott Tremaine. 1987. *Galactic dynamics.*

Blackwell, D. E., & M. J. Shallis. 1977. 'Stellar angular diameters from infrared photometry - Application to Arcturus and other stars; with effective temperatures.' MNRAS 180 (July): 177–191.

Blackwell, D. E., M. J. Shallis, & M. J. Selby. 1979. 'The infrared flux method for determining stellar angular diameters and effective temperatures.' MNRAS 188 (September): 847–862.

Blitz, L., & F. H. Shu. 1980. 'The origin and lifetime of giant molecular cloud complexes.' ApJ 238 (May): 148–157.

Bochanski, John J., Suzanne L. Hawley, Kevin R. Covey, et al. 2010. 'The Luminosity and Mass Functions of Low-mass Stars in the Galactic Disk. II. The Field.' AJ 139, no. 6 (June): 2679–2699.

Boesgaard, A. M., B. W. Roper, & M. G. Lum. 2013. 'The Chemical Composition of Praesepe (M44).' ApJ 775, 58 (September): 58.

Böhm-Vitense, E. 1958. 'Über die Wasserstoffkonvektionszone in Sternen verschiedener Effektivtemperaturen und Leuchtkräfte. Mit 5 Textabbildungen.' ZAp 46 (January): 108.

Bonaca, Ana, Joel D. Tanner, Sarbani Basu, et al. 2012. 'Calibrating Convective Properties of Solar-like Stars in the Kepler Field of View.' ApJL 755, no. 1, L12 (August): L12.

Bonfils, X., M. Gillon, S. Udry, et al. 2012. 'A hot Uranus transiting the nearby M dwarf GJ 3470. Detected with HARPS velocimetry. Captured in transit with TRAPPIST photometry.' A&A 546, A27 (October): A27.

Bonnell, Ian A., Rowan J. Smith, Paul C. Clark, & Matthew R. Bate. 2011. 'The efficiency of star formation in clustered and distributed regions.' MNRAS 410, no. 4 (February): 2339–2346.

Boone, R. H., J. R. King, & D. R. Soderblom. 2006. 'Metallicity in the solar neighborhood out to 60 pc.' *New Astronomy Review* 50 (October): 526–529.

Bourgés, L., S. Lafrasse, G. Mella, et al. 2014. 'The JMMC Stellar Diameters Catalog v2 (JSDC): A New Release Based on SearchCal Improvements.' In *Astronomical Data Analysis Software and Systems XXIII,* edited by N. Manset & P. Forshay, 485:223. Astronomical Society of the Pacific Conference Series. May.

Boutle, Ian A., Nathan J. Mayne, Benjamin Drummond, et al. 2017. 'Exploring the climate of Proxima B with the Met Office Unified Model.' A&A 601, A120 (May): A120.

Boyajian, T. S., K. von Braun, G. van Belle, et al. 2012. 'Stellar Diameters and Temperatures. II. Main-sequence K- and M-stars.' ApJ 757, 112 (October): 112.

Boyajian, T., K. von Braun, G. A. Feiden, et al. 2015. 'Stellar diameters and temperatures - VI. High angular resolution measurements of the transiting exoplanet host stars HD 189733 and HD 209458 and implications for models of cool dwarfs.' MNRAS 447 (February): 846–857.

Broeg, C., A. Fortier, D. Ehrenreich, et al. 2013. 'CHEOPS: A transit photometry mission for ESA's small mission programme.' In *Hot Planets and Cool Stars, Garching, Germany, Edited by Roberto Saglia; EPJ Web of Conferences, Volume 47, id.03005,* vol. 47. April.

Brun, Allan Sacha, & Matthew K. Browning. 2017. 'Magnetism, dynamo action and the solar-stellar connection.' *Living Reviews in Solar Physics* 14, no. 1, 4 (September): 4.

Caffau, E., H.-G. Ludwig, M. Steffen, B. Freytag, & P. Bonifacio. 2011. 'Solar Chemical Abundances Determined with a CO5BOLD 3D Model Atmosphere.' Sol. Phys. 268 (February): 255–269.

Canuto, V. M. 1990. 'The mixing length parameter alpha.' A&A 227, no. 1 (January): 282–284.

Casagrande, L. 2008. 'Infrared flux method and colour calibrations.' *Physica Scripta Volume T* 133, no. 1, 014020 (December): 014020.

Casali, M., A. Adamson, C. Alves de Oliveira, et al. 2007. 'The UKIRT wide-field camera.' A&A 467 (May): 777–784.

Chabrier, G. 2003. 'Galactic Stellar and Substellar Initial Mass Function.' PASP 115 (July): 763–795.

Chabrier, G., J. Gallardo, & I. Baraffe. 2007. 'Evolution of low-mass star and brown dwarf eclipsing binaries.' A&A 472, no. 2 (September): L17–L20.

Chabrier, G., & M. Küker. 2006. 'Large-scale α^2-dynamo in low-mass stars and brown dwarfs.' A&A 446 (February): 1027–1037.

Chabrier, Gilles. 2005. 'The Initial Mass Function: From Salpeter 1955 to 2005.' In *The Initial Mass Function 50 Years Later,* edited by E. Corbelli, F. Palla, & H. Zinnecker, 327:41. Astrophysics and Space Science Library. January.

Chabrier, Gilles, Isabelle Baraffe, & Bertrand Plez. 1996. 'Mass-Luminosity Relationship and Lithium Depletion for Very Low Mass Stars.' ApJL 459 (March): L91.

Charbonneau, David, Timothy M. Brown, David W. Latham, & Michel Mayor. 2000. 'Detection of Planetary Transits Across a Sun-like Star.' ApJ 529 (January): L45–L48.

Chaturvedi, P., R. Sharma, A. Chakraborty, B. G. Anandarao, & N. J. S. S. V. Prasad. 2018. 'Masses and Radii of Four Very Low-mass Stars in F+M Eclipsing Binary Systems.' AJ 156, 27 (July): 27.

Chen, Y., L. Girardi, A. Bressan, et al. 2014. 'Improving PARSEC models for very low mass stars.' MNRAS 444 (November): 2525–2543.

Claret, A. 2000. 'A new non-linear limb-darkening law for LTE stellar atmosphere models. Calculations for -5.0 <= log[M/H] <= +1, 2000 K <= T_{eff} <= 50000 K at several surface gravities.' A&A 363 (November): 1081–1190.

———. 2004. 'A new non-linear limb-darkening law for LTE stellar atmosphere models III. Sloan filters: Calculations for -5.0 ≤ log [M/H] ≤ +1, 2000 K ≤ T_{eff} ≤ 50 000 K at several surface gravities.' A&A 428 (December): 1001–1005.

Comeron, F., & J. Torra. 1994. 'The origin of the Gould Belt by the impact of a high velocity cloud on the galactic disk.' A&A 281 (January): 35–45.

Cortés-Contreras, M., V. J. S. Béjar, J. A. Caballero, et al. 2017. 'CARMENES input catalogue of M dwarfs. II. High-resolution imaging with FastCam.' A&A 597, A47 (January): A47.

Covey, K. R., Ž. Ivezić, D. Schlegel, et al. 2007. 'Stellar SEDs from 0.3 to 2.5 μm: Tracing the Stellar Locus and Searching for Color Outliers in the SDSS and 2MASS.' AJ 134, no. 6 (December): 2398–2417.

Cranmer, S. R., & S. H. Saar. 2011. 'Testing a Predictive Theoretical Model for the Mass Loss Rates of Cool Stars.' ApJ 741, 54 (November): 54.

Cropper, M., D. Katz, P. Sartoretti, et al. 2018. 'Gaia Data Release 2. Gaia Radial Velocity Spectrometer.' A&A 616, A5 (August): A5.

D'Antona, F., & I. Mazzitelli. 1997. 'Evolution of low mass stars.' Mem. Soc. Astron. Italiana 68:807.

Dalton, Gavin, Scott C. Trager, Don Carlos Abrams, et al. 2012. 'WEAVE: the next generation wide-field spectroscopy facility for the William Herschel Telescope.' In *Ground-based and Airborne Instrumentation for Astronomy IV*, vol. 8446, 84460P. Society of Photo-Optical Instrumentation Engineers (SPIE) Conference Series. September.

Delrez, L., A. Santerne, J.-M. Almenara, et al. 2016. 'WASP-121 b: a hot Jupiter close to tidal disruption transiting an active F star.' MNRAS 458 (June): 4025–4043.

Demarque, P., J.-H. Woo, Y.-C. Kim, & S. K. Yi. 2004. 'Y^2 Isochrones with an Improved Core Overshoot Treatment.' ApJS 155 (December): 667–674.

Deming, Drake, Pedro V. Sada, Brian Jackson, et al. 2011. 'Kepler and Ground-based Transits of the Exo-Neptune HAT-P-11b.' ApJ 740, no. 1, 33 (October): 33.

Demory, B. -O., D. Ségransan, T. Forveille, et al. 2009. 'Mass-radius relation of low and very low-mass stars revisited with the VLTI.' A&A 505, no. 1 (October): 205–215.

Deutsch, A. J. 1958. 'Harmonic Analysis of the Periodic Spectrum Variables.' In *Electromagnetic Phenomena in Cosmical Physics,* edited by B. Lehnert, 6:209. IAU Symposium. January.

Dieterich, S. B., T. J. Henry, D. A. Golimowski, J. E. Krist, & A. M. Tanner. 2012. 'The Solar Neighborhood. XXVIII. The Multiplicity Fraction of Nearby Stars from 5 to 70 AU and the Brown Dwarf Desert around M Dwarfs.' AJ 144, 64 (August): 64.

Dobbs, C. L., & I. A. Bonnell. 2007. 'Spiral shocks and the formation of molecular clouds in a two-phase medium.' MNRAS 376, no. 4 (April): 1747–1756.

Dobbs, C. L., I. A. Bonnell, & J. E. Pringle. 2006. 'The formation of molecular clouds in spiral galaxies.' MNRAS 371, no. 4 (October): 1663–1674.

Dobler, W., M. Stix, & A. Brandenburg. 2006. 'Magnetic Field Generation in Fully Convective Rotating Spheres.' ApJ 638 (February): 336–347.

Doi, M., M. Tanaka, M. Fukugita, et al. 2010. 'Photometric Response Functions of the Sloan Digital Sky Survey Imager.' AJ 139 (April): 1628–1648.

Dotter, A., B. Chaboyer, D. Jevremović, et al. 2008. 'The Dartmouth Stellar Evolution Database.' ApJS 178 (September): 89–101.

Douglas, S. T., M. A. Agüeros, K. R. Covey, et al. 2014. 'The Factory and the Beehive. II. Activity and Rotation in Praesepe and the Hyades.' ApJ 795, no. 2, 161 (November): 161.

Drew, J. E., E. Gonzalez-Solares, R. Greimel, et al. 2014. 'The VST Photometric Hα Survey of the Southern Galactic Plane and Bulge (VPHAS+).' MNRAS 440 (May): 2036–2058.

Drew, J. E., R. Greimel, M. J. Irwin, et al. 2005. 'The INT Photometric Hα Survey of the Northern Galactic Plane (IPHAS).' MNRAS 362 (September): 753–776.

Dubaj, D., & R. Monier. 2005. 'Effective temperature determinations using the Infrared Flux Method.' *Memorie della Societa Astronomica Italiana Supplementi* 8 (January): 142.

Durney, B. R., D. S. De Young, & I. W. Roxburgh. 1993. 'On the generation of the large-scale and turbulent magnetic fields in solar-type stars.' Sol. Phys. 145 (June): 207–225.

Eastman, Jason D., Joseph E. Rodriguez, Eric Agol, et al. 2019. 'EXOFASTv2: A public, generalized, publication-quality exoplanet modeling code.' *arXiv e-prints*, arXiv:1907.09480 (July): arXiv:1907.09480.

Eastman, Jason, B. Scott Gaudi, & Eric Agol. 2013. 'EXOFAST: A Fast Exoplanetary Fitting Suite in IDL.' PASP 125, no. 923 (January): 83.

Eddington, A. S. 1926. *The Internal Constitution of the Stars.*

Enoch, B., A. Collier Cameron, N. R. Parley, & L. Hebb. 2010. 'An improved method for estimating the masses of stars with transiting planets.' A&A 516, A33 (June): A33.

Evans, D. W., M. Riello, F. De Angeli, et al. 2018. 'Gaia Data Release 2. Photometric content and validation.' A&A 616, A4 (August): A4.

Falco, M., S. H. Hansen, R. Wojtak, & G. A. Mamon. 2013. 'Why does the jeans swindle work?' MNRAS 431 (April): L6–L9.

Feiden, G. A., & B. Chaboyer. 2013. 'Magnetic Inhibition of Convection and the Fundamental Properties of Low-mass Stars. I. Stars with a Radiative Core.' ApJ 779, 183 (December): 183.

Feiden, Gregory A., & Brian Chaboyer. 2014. 'Magnetic Inhibition of Convection and the Fundamental Properties of Low-mass Stars. II. Fully Convective Main-sequence Stars.' ApJ 789, no. 1, 53 (July): 53.

Ferraro, Francesco R., Elena Valenti, Oscar Straniero, & Livia Origlia. 2006. 'An Empirical Calibration of the Mixing-Length Parameter α.' ApJ 642, no. 1 (May): 225–229.

Fitzpatrick, E. L. 1999. 'Correcting for the Effects of Interstellar Extinction.' PASP 111 (January): 63–75.

Freytag, B., M. Steffen, H. -G. Ludwig, et al. 2012. 'Simulations of stellar convection with CO5BOLD.' *Journal of Computational Physics* 231, no. 3 (February): 919–959.

Gaia Collaboration, C. Babusiaux, F. van Leeuwen, et al. 2018a. 'Gaia Data Release 2. Observational Hertzsprung-Russell diagrams.' A&A 616, A10 (August): A10.

Gaia Collaboration, A. G. A. Brown, A. Vallenari, et al. 2018b. 'Gaia Data Release 2. Summary of the contents and survey properties.' *ArXiv e-prints* (April).

Gaia Collaboration, T. Prusti, J. H. J. de Bruijne, et al. 2016. 'The Gaia mission.' A&A 595 (November).

Gaidos, E., A. W. Mann, S. Lépine, et al. 2014. 'Trumpeting M dwarfs with CONCH-SHELL: a catalogue of nearby cool host-stars for habitable exoplanets and life.' MNRAS 443 (September): 2561–2578.

Gardner, Jonathan P., John C. Mather, Mark Clampin, et al. 2006. 'The James Webb Space Telescope.' Space Sci. Rev. 123 (April): 485–606.

Gatewood, George, Joost Kiewiet de Jonge, & Inwoo Han. 2000. 'The Pleiades, Map-based Trigonometric Parallaxes of Open Clusters. V.' ApJ 533, no. 2 (April): 938–943.

Geurts, Pierre, Damien Ernst, & Louis Wehenkel. 2006. 'Extremely randomized trees.' *Machine Learning* 63, no. 1 (April): 3–42.

Giannuzzi, M. A. 1995. 'The spectroscopic binary HD 23642 and the distance of the Pleiades.' A&A 293 (January): 360–362.

Gillen, Edward, Lynne A. Hillenbrand, Trevor J. David, et al. 2017. 'New Low-mass Eclipsing Binary Systems in Praesepe Discovered by K2.' ApJ 849, no. 1, 11 (November): 11.

Gillon, M., D. R. Anderson, A. H. M. J. Triaud, et al. 2009. 'Discovery and characterization of WASP-6b, an inflated sub-Jupiter mass planet transiting a solar-type star.' A&A 501 (July): 785–792.

Girardi, L., G. Bertelli, A. Bressan, et al. 2002. 'Theoretical isochrones in several photometric systems. I. Johnson-Cousins-Glass, HST/WFPC2, HST/NICMOS, Washington, and ESO Imaging Survey filter sets.' A&A 391 (August): 195–212.

Goncharskii, A. V., V. V. Stepanov, V. L. Kokhlova, & A. G. Yagola. 1977. 'Reconstruction of local line profiles from those observed in an Ap spectrum.' *Soviet Astronomy Letters* 3 (January): 147–149.

Goodricke, John. 1783. 'A Series of Observations on, and a Discovery of, the Period of the Variation of the Light of the Bright Star in the Head of Medusa, Called Algol. In a Letter from John Goodricke, Esq. to the Rev. Anthony Shepherd, D. D. F. R. S. and Plumian Professor at Cambridge.' *Philosophical Transactions of the Royal Society of London Series I* 73 (January): 474–482.

Gould, Benjamin Apthorp. 1879. 'Uranometria Argentina: Brightness and position of every fixed star, down to the seventh magnitude, within one hundred degrees of the South Pole; with atlas.' *Resultados del Observatorio Nacional Argentino* 1 (January): I–387.

Goyal, Jayesh M., Nathan Mayne, David K. Sing, et al. 2018. 'A library of ATMO forward model transmission spectra for hot Jupiter exoplanets.' MNRAS 474, no. 4 (March): 5158–5185.

Goyal, Jayesh M., Hannah R. Wakeford, Nathan J. Mayne, et al. 2019. 'Fully scalable forward model grid of exoplanet transmission spectra.' MNRAS 482, no. 4 (February): 4503–4513.

Groenewegen, M. A. T., L. Decin, M. Salaris, & P. De Cat. 2007. 'The Pleiades eclipsing binary HD 23642 revisited.' A&A 463, no. 2 (February): 579–587.

Großschedl, Josefa E., João Alves, Stefan Meingast, et al. 2018. '3D shape of Orion A from Gaia DR2.' A&A 619, A106 (November): A106.

Haisch, Jr., Karl E., Elizabeth A. Lada, & Charles J. Lada. 2001. 'Disk Frequencies and Lifetimes in Young Clusters.' ApJL 553, no. 2 (June): L153–L156.

Hambly, N. C., R. S. Collins, N. J. G. Cross, et al. 2008. 'The WFCAM Science Archive.' MNRAS 384, no. 2 (February): 637–662.

Han, Eunkyu, Philip S. Muirhead, Jonathan J. Swift, et al. 2017. 'Magnetic Inflation and Stellar Mass. I. Revised Parameters for the Component Stars of the Kepler Low-mass Eclipsing Binary T-Cyg1-12664.' AJ 154, no. 3, 100 (September): 100.

Hanbury Brown, R., J. Davis, R. J. W. Lake, & R. J. Thompson. 1974. 'The effects of limb darkening on measurements of angular size with an intensity interferometer.' MNRAS 167 (June): 475–484.

Hardy, L., H. Fathivavsari, J. Mendez, L. Dominguez-Palmero, & C. Benn. 2013. *Arc maps for the CuAr and CuNe lamps when used with ACAM/AUXCAM.* Technical report. ING.

Hartman, J. D., G. Á. Bakos, B. Béky, et al. 2012. 'HAT-P-39b-HAT-P-41b: Three Highly Inflated Transiting Hot Jupiters.' AJ 144, no. 5, 139 (November): 139.

Hartman, J. D., G. Á. Bakos, D. M. Kipping, et al. 2011a. 'HAT-P-26b: A Low-density Neptune-mass Planet Transiting a K Star.' ApJ 728, no. 2, 138 (February): 138.

Hartman, J. D., G. Á. Bakos, G. Torres, et al. 2011b. 'HAT-P-32b and HAT-P-33b: Two Highly Inflated Hot Jupiters Transiting High-jitter Stars.' ApJ 742, 59 (November): 59.

Hartman, J. D., S. N. Quinn, G. Á. Bakos, et al. 2018. 'HAT-TR-318-007: A Double-lined M Dwarf Binary with Total Secondary Eclipses Discovered by HATNet and Observed by K2.' AJ 155, 114 (March): 114.

Hauschildt, P. H. 1992. 'A fast operator perturbation method for the solution of the special relativistic equation of radiative transfer in spherical symmetry.' J. Quant. Spec. Radiat. Transf. 47, no. 6 (June): 433–453.

———. 1993. 'Multi-level non-LTE radiative transfer in expanding shells.' J. Quant. Spec. Radiat. Transf. 50, no. 3 (September): 301–318.

Hauschildt, Peter H., France Allard, & E. Baron. 1999. 'The NextGen Model Atmosphere Grid for 3000<=T_{eff}<=10,000 K.' ApJ 512, no. 1 (February): 377–385.

Hayashi, C. 1961. 'Stellar evolution in early phases of gravitational contraction.' PASJ 13 (January): 450–452.

Hayashi, Chushiro, & Reun Hoshi. 1961. 'The Outer Envelope of Giant Stars with Surface Convection Zone.' PASJ 13 (January): 442–449.

Hébrard, G., A. Collier Cameron, D. J. A. Brown, et al. 2013. 'WASP-52b, WASP-58b, WASP-59b, and WASP-60b: Four new transiting close-in giant planets.' A&A 549, A134 (January): A134.

Hellier, C., D. R. Anderson, A. C. Cameron, et al. 2014. 'Transiting hot Jupiters from WASP-South, Euler and TRAPPIST: WASP-95b to WASP-101b.' MNRAS 440 (May): 1982–1992.

Hellier, C., D. R. Anderson, A. Collier Cameron, et al. 2010. 'WASP-29b: A Saturn-sized Transiting Exoplanet.' ApJL 723 (November): L60–L63.

Hellier, C., D. R. Anderson, A. Collier Cameron, et al. 2012. 'Seven transiting hot Jupiters from WASP-South, Euler and TRAPPIST: WASP-47b, WASP-55b, WASP-61b, WASP-62b, WASP-63b, WASP-66b and WASP-67b.' MNRAS 426 (October): 739–750.

Hellier, C., D. R. Anderson, A. Collier Cameron, et al. 2015. 'Three WASP-South Transiting Exoplanets: WASP-74b, WASP-83b, and WASP-89b.' AJ 150, 18 (July): 18.

Hełminiak, K. G., D. Graczyk, M. Konacki, et al. 2015. 'Orbital and physical parameters of eclipsing binaries from the ASAS catalogue - VIII. The totally eclipsing double-giant system HD 187669.' MNRAS 448 (April): 1945–1955.

Henyey, L. G., Robert Lelevier, & R. D. Levée. 1955. 'The Early Phases of Stellar Evolution.' PASP 67, no. 396 (June): 154.

Herschel, William. 1802. 'Catalogue of 500 New Nebulae, Nebulous Stars, Planetary Nebulae, and Clusters of Stars; With Remarks on the Construction of the Heavens.' *Philosophical Transactions of the Royal Society of London Series I* 92 (January): 477–528.

Hertzsprung, E. 1923. 'On the relation between mass and absolute brightness of components of double stars.' Bull. Astron. Inst. Netherlands 2 (July): 15.

Hewett, P. C., S. J. Warren, S. K. Leggett, & S. T. Hodgkin. 2006. 'The UKIRT Infrared Deep Sky Survey ZY JHK photometric system: passbands and synthetic colours.' MNRAS 367 (April): 454–468.

Higl, J., & A. Weiss. 2017. 'Testing stellar evolution models with detached eclipsing binaries.' A&A 608, A62 (December): A62.

Hodgkin, S. T., M. J. Irwin, P. C. Hewett, & S. J. Warren. 2009. 'The UKIRT wide field camera ZYJHK photometric system: calibration from 2MASS.' MNRAS 394 (April): 675–692.

Høg, E., C. Fabricius, V. V. Makarov, et al. 2000. 'The Tycho-2 catalogue of the 2.5 million brightest stars.' A&A 355 (March): L27–L30.

Horne, K. 1986. 'An optimal extraction algorithm for CCD spectroscopy.' PASP 98 (June): 609–617.

Huenemoerder, David P., & Lawrence W. Ramsey. 1987. 'CCD Echelle Observations of the Active RS CVn System II Pegasi.' ApJ 319 (August): 392.

Hunter, John D. 2007. 'Matplotlib: A 2D Graphics Environment.' *Computing in Science and Engineering* 9 (May): 90–95.

Ilee, J. D., C. J. Cyganowski, C. L. Brogan, et al. 2018. 'G11.92-0.61 MM 1: A Fragmented Keplerian Disk Surrounding a Proto-O Star.' ApJL 869, no. 2, L24 (December): L24.

Ireland, L. G., & M. K. Browning. 2018. 'The Radius and Entropy of a Magnetized, Rotating, Fully Convective Star: Analysis with Depth-dependent Mixing Length Theories.' ApJ 856, 132 (April): 132.

Jackson, R. J., C. P. Deliyannis, & R. D. Jeffries. 2018. 'The inflated radii of M-dwarfs in the Pleiades.' MNRAS (February).

Jackson, R. J., & R. D. Jeffries. 2014. 'The effect of starspots on the radii of low-mass pre-main-sequence stars.' MNRAS 441 (July): 2111–2123.

Jeans, J. H. 1902. 'The Stability of a Spherical Nebula.' *Philosophical Transactions of the Royal Society of London Series A* 199:1–53.

Jones, Eric, Travis Oliphant, Pearu Peterson, et al. 2001. *SciPy: Open source scientific tools for Python.* [Online; accessed <today>].

Kausch, W., S. Noll, A. Smette, et al. 2015. 'Molecfit: A general tool for telluric absorption correction. II. Quantitative evaluation on ESO-VLT/X-Shooterspectra.' A&A 576, A78 (April): A78.

Kesseli, A. Y., P. S. Muirhead, A. W. Mann, & G. Mace. 2018. 'Magnetic Inflation and Stellar Mass. II. On the Radii of Single, Rapidly Rotating, Fully Convective M-Dwarf Stars.' AJ 155, 225 (June): 225.

Kiessling, Michael K.-H. 2003. 'The "Jeans swindle": A true story - mathematically speaking.' *Advances in Applied Mathematics* 31 (1): 132–149.

King, D. L. 1985. 'Atmospheric Extinction at the Roque de los Muchachos Observatory, La Palma.' *RGO/La Palma Technical Note* 31, no. 1 (September): 5.

Kippenhahn, Rudolf, & Alfred Weigert. 1990. *Stellar Structure and Evolution.*

Kochukhov, Oleg, & Denis Shulyak. 2019. 'Magnetic Field of the Eclipsing M-dwarf Binary YY Gem.' ApJ 873, no. 1, 69 (March): 69.

Kraus, A. L., S. T. Douglas, A. W. Mann, et al. 2017. 'The Factory and the Beehive. III. PTFEB132.707+19.810, A Low-mass Eclipsing Binary in Praesepe Observed by PTF and K2.' ApJ 845, 72 (August): 72.

Kraus, A. L., & L. A. Hillenbrand. 2007. 'The Stellar Populations of Praesepe and Coma Berenices.' AJ 134 (December): 2340–2352.

Kraus, A. L., R. A. Tucker, M. I. Thompson, E. R. Craine, & L. A. Hillenbrand. 2011a. 'The Mass-Radius(-Rotation?) Relation for Low-mass Stars.' ApJ 728, 48 (February): 48.

———. 2011b. 'The Mass-Radius(-Rotation?) Relation for Low-mass Stars.' ApJ 728, 48 (February): 48.

Kron, Gerald E. 1947. 'The Probable Detecting of Surface Spots on AR Lacertae B.' PASP 59, no. 350 (October): 261.

Kroupa, P. 2002. 'The Initial Mass Function of Stars: Evidence for Uniformity in Variable Systems.' *Science* 295 (January): 82–91.

Kroupa, Pavel. 2001. 'On the variation of the initial mass function.' MNRAS 322, no. 2 (April): 231–246.

Kroupa, Pavel, Carsten Weidner, Jan Pflamm-Altenburg, et al. 2013. 'The Stellar and Sub-Stellar Initial Mass Function of Simple and Composite Populations.' In *Planets, Stars and Stellar Systems Vol. 5, by Oswalt, Terry D.; Gilmore, Gerard, ISBN 978-94-007-5611-3. Springer Science+Business Media Dordrecht, 2013, p. 115,* edited by Terry D. Oswalt & Gerard Gilmore, 5:115.

Lada, Charles J. 2006. 'Stellar Multiplicity and the Initial Mass Function: Most Stars Are Single.' ApJL 640, no. 1 (March): L63–L66.

Lada, Charles J., August A. Muench, Jr. Haisch Karl E., et al. 2000. 'Infrared L-Band Observations of the Trapezium Cluster: A Census of Circumstellar Disks and Candidate Protostars.' AJ 120, no. 6 (December): 3162–3176.

Lamers, Henny J. G. L. M., & Emily M. Levesque. 2017. *Understanding Stellar Evolution.*

Lanzafame, A. C., E. Distefano, S. Messina, et al. 2018. 'Gaia Data Release 2. Rotational modulation in late-type dwarfs.' A&A 616, A16 (August): A16.

Lanzafame, A. C., & F. Spada. 2015. 'Rotational evolution of slow-rotator sequence stars.' A&A 584, A30 (December): A30.

Lanzafame, A. C., F. Spada, & E. Distefano. 2017. 'Evidence of radius inflation in stars approaching the slow-rotator sequence.' A&A 597, A63 (January): A63.

Larson, R. B. 1985. 'Cloud fragmentation and stellar masses.' MNRAS 214 (June): 379–398.

Lawrence, A., S. J. Warren, O. Almaini, et al. 2007. 'The UKIRT Infrared Deep Sky Survey (UKIDSS).' MNRAS 379 (August): 1599–1617.

Lecavelier Des Etangs, A., F. Pont, A. Vidal-Madjar, & D. Sing. 2008. 'Rayleigh scattering in the transit spectrum of HD 189733b.' A&A 481 (April): L83–L86.

Ligi, R., C. Dorn, A. Crida, et al. 2019. 'From the stellar properties of HD 219134 to the internal compositions of its transiting exoplanets.' A&A 631, A92 (November): A92.

Limber, D. N. 1958. 'The Structure of the M Dwarf Stars. I.' ApJ 127 (March): 363.

Lindegren, L., J. Hernández, A. Bombrun, et al. 2018. 'Gaia Data Release 2. The astrometric solution.' A&A 616, A2 (August): A2.

Lockwood, G. W., B. A. Skiff, G. W. Henry, et al. 2007. 'Patterns of Photometric and Chromospheric Variation among Sun-like Stars: A 20 Year Perspective.' ApJS 171 (July): 260–303.

Lodieu, N., N. R. Deacon, & N. C. Hambly. 2012. 'Astrometric and photometric initial mass functions from the UKIDSS Galactic Clusters Survey - I. The Pleiades.' MNRAS 422, no. 2 (May): 1495–1511.

López-Morales, M. 2007. 'On the Correlation between the Magnetic Activity Levels, Metallicities, and Radii of Low-Mass Stars.' ApJ 660 (May): 732–739.

Luri, X., & Gaia DPAC. 2019. 'Gaia DR2: contents and properties of the second Gaia data release.' In *Highlights on Spanish Astrophysics X*, 16–24. March.

Lutz, T. E., & D. H. Kelker. 1973. 'On the Use of Trigonometric Parallaxes for the Calibration of Luminosity Systems: Theory.' PASP 85 (October): 573.

MacDonald, J., & D. J. Mullan. 2014. 'Surface Magnetic Field Strengths: New Tests of Magnetoconvective Models of M Dwarfs.' ApJ 787, 70 (May): 70.

———. 2017. 'Magnetic Modeling of Inflated Low-mass Stars Using Interior Fields No Larger than ~ 10 kG.' ApJ 850, 58 (November): 58.

Maı z Apellániz, J., & M. Weiler. 2018. 'Reanalysis of the Gaia Data Release 2 photometric sensitivity curves using HST/STIS spectrophotometry.' A&A 619, A180 (November): A180.

Mandel, Kaisey, & Eric Agol. 2002. 'Analytic Light Curves for Planetary Transit Searches.' ApJ 580, no. 2 (December): L171–L175.

Mann, A. W., T. Dupuy, A. L. Kraus, et al. 2019. 'How to Constrain Your M Dwarf. II. The Mass–Luminosity–Metallicity Relation from 0.075 to 0.70 Solar Masses.' ApJ 871, 63 (January): 63.

Mann, A. W., E. Gaidos, & M. Ansdell. 2013. 'Spectro-thermometry of M Dwarfs and Their Candidate Planets: Too Hot, Too Cool, or Just Right?' ApJ 779, 188 (December): 188.

Mann, Andrew W., Gregory A. Feiden, Eric Gaidos, Tabetha Boyajian, & Kaspar von Braun. 2015. 'How to Constrain Your M Dwarf: Measuring Effective Temperature, Bolometric Luminosity, Mass, and Radius.' ApJ 804 (May).

Marigo, P., L. Girardi, A. Bressan, et al. 2017. 'A New Generation of PARSEC-COLIBRI Stellar Isochrones Including the TP-AGB Phase.' ApJ 835, 77 (January): 77.

Masana, E., C. Jordi, & I. Ribas. 2006. 'Effective temperature scale and bolometric corrections from 2MASS photometry.' A&A 450 (May): 735–746.

Mayne, N. J., & Tim Naylor. 2008. 'Fitting the young main-sequence: distances, ages and age spreads.' MNRAS 386, no. 1 (May): 261–277.

Mayor, Michel, & Didier Queloz. 1995. 'A Jupiter-mass companion to a solar-type star.' Nature 378 (November): 355–359.

McQuillan, A., S. Aigrain, & T. Mazeh. 2013. 'Measuring the rotation period distribution of field M dwarfs with Kepler.' MNRAS 432 (June): 1203–1216.

McQuillan, A., T. Mazeh, & S. Aigrain. 2014. 'Rotation Periods of 34,030 Kepler Main-sequence Stars: The Full Autocorrelation Sample.' ApJS 211, 24 (April): 24.

Melis, Carl, Mark J. Reid, Amy J. Mioduszewski, John R. Stauffer, & Geoffrey C. Bower. 2014. 'A VLBI resolution of the Pleiades distance controversy.' *Science* 345, no. 6200 (August): 1029–1032.

Menten, K. M., M. J. Reid, J. Forbrich, & A. Brunthaler. 2007. 'The distance to the Orion Nebula.' A&A 474, no. 2 (November): 515–520.

Meunier, N., M. Desort, & A.-M. Lagrange. 2010. 'Using the Sun to estimate Earth-like planets detection capabilities . II. Impact of plages.' A&A 512, A39 (March): A39.

Michelson, A. A., & F. G. Pease. 1921. 'Measurement of the Diameter of α Orionis with the Interferometer.' ApJ 53 (May): 249–259.

Miller, G. E., & J. M. Scalo. 1979. 'The initial mass function and stellar birthrate in the solar neighborhood.' ApJS 41 (November): 513–547.

Moehler, S., A. Modigliani, W. Freudling, et al. 2014. 'Flux calibration of medium-resolution spectra from 300 nm to 2500 nm: Model reference spectra and telluric correction.' A&A 568, A9 (August): A9.

Monnier, J. D. 2003. 'Optical interferometry in astronomy.' *Reports on Progress in Physics* 66 (May): 789–857.

Morales, J. C., I. Ribas, C. Jordi, et al. 2009a. 'Absolute Properties of the Low-Mass Eclipsing Binary CM Draconis.' ApJ 691 (February): 1400–1411.

Morales, J. C., G. Torres, L. A. Marschall, & W. Brehm. 2009b. 'Absolute Dimensions of the G7+K7 Eclipsing Binary Star IM Virginis: Discrepancies with Stellar Evolution Models.' ApJ 707 (December): 671–685.

Morris, Brett M., Leslie Hebb, James R. A. Davenport, Graeme Rohn, & Suzanne L. Hawley. 2017. 'The Starspots of HAT-P-11: Evidence for a Solar-like Dynamo.' ApJ 846, no. 2, 99 (September): 99.

Morrissey, Patrick, Tim Conrow, Tom A. Barlow, et al. 2007. 'The Calibration and Data Products of GALEX.' ApJS 173, no. 2 (December): 682–697.

Muirhead, Philip S., Courtney D. Dressing, Andrew W. Mann, et al. 2018. 'A Catalog of Cool Dwarf Targets for the Transiting Exoplanet Survey Satellite.' AJ 155, no. 4, 180 (April): 180.

Mullan, D. J., & J. MacDonald. 2001. 'Are Magnetically Active Low-Mass M Dwarfs Completely Convective?' ApJ 559 (September): 353–371.

Munari, U., S. Dallaporta, A. Siviero, et al. 2004. 'The distance to the Pleiades from orbital solution of the double-lined eclipsing binary HD 23642.' A&A 418 (April): L31–L34.

Murray, C. D., & A. C. M. Correia. 2010. 'Keplerian Orbits and Dynamics of Exoplanets.' In *Exoplanets*, edited by S. Seager, 15–23.

Narayanan, Vijay K., & Andrew Gould. 1999. 'Correlated Errors in HIPPARCOS Parallaxes toward the Pleiades and the Hyades.' ApJ 523, no. 1 (September): 328–339.

Naylor, Tim. 2009. 'Are pre-main-sequence stars older than we thought?' MNRAS 399, no. 1 (October): 432–442.

Neff, James E., Douglas O'Neal, & Steven H. Saar. 1995. 'Absolute Measurements of Starspot Area and Temperature: II Pegasi in 1989 October.' ApJ 452 (October): 879.

Neves, V., X. Bonfils, N. C. Santos, et al. 2013. 'Metallicity of M dwarfs. III. Planet-metallicity and planet-stellar mass correlations of the HARPS GTO M dwarf sample.' A&A 551, A36 (March): A36.

Newton, E. R., D. Charbonneau, J. Irwin, et al. 2014. 'Near-infrared Metallicities, Radial Velocities, and Spectral Types for 447 Nearby M Dwarfs.' AJ 147, 20 (January): 20.

Newton, E. R., J. Irwin, D. Charbonneau, et al. 2017. 'The Hα Emission of Nearby M Dwarfs and its Relation to Stellar Rotation.' ApJ 834, 85 (January): 85.

Nicolet, B. 1981. 'Geneva photometric boxes. III. Distances and reddenings for 43 open clusters.' A&A 104 (December): 185–197.

Nielsen, L. D., F. Bouchy, O. Turner, et al. 2019. 'A Jovian planet in an eccentric 11.5 day orbit around HD 1397 discovered by TESS.' A&A 623, A100 (March): A100.

Nutzman, Philip, & David Charbonneau. 2008. 'Design Considerations for a Ground-Based Transit Search for Habitable Planets Orbiting M Dwarfs.' *Publications of the Astronomical Society of the Pacific* 120 (March): 317.

O'Neal, Douglas, Steven H. Saar, & James E. Neff. 1996. 'Measurements of Starspot Area and Temperature on Five Active, Evolved Stars.' ApJ 463 (June): 766.

Offner, S. S. R., P. C. Clark, P. Hennebelle, et al. 2014. 'The Origin and Universality of the Stellar Initial Mass Function.' *Protostars and Planets VI:* 53–75.

Oke, J. B. 1990. 'Faint spectrophotometric standard stars.' AJ 99 (May): 1621–1631.

Oliphant, Travis E. 2015. *Guide to NumPy.* 2nd. USA: CreateSpace Independent Publishing Platform.

Oshagh, M., N. C. Santos, D. Ehrenreich, et al. 2014. 'Impact of occultations of stellar active regions on transmission spectra. Can occultation of a plage mimic the signature of a blue sky?' A&A 568, A99 (August): A99.

Osterbrock, Donald E. 1953. 'The Internal Structure of Red Dwarf Stars.' ApJ 118 (November): 529.

Pál, A. 2009. 'Tools for discovering and characterizing extrasolar planets.' PhD diss., Department of Astronomy, Eötvös Loránd University.

Pan, Xiaopei, M. Shao, & S. R. Kulkarni. 2004. 'A distance of 133-137 parsecs to the Pleiades star cluster.' Nature 427, no. 6972 (January): 326–328.

Parker, E. N. 1955. 'Hydromagnetic Dynamo Models.' ApJ 122 (September): 293.

———. 1979. *Cosmical magnetic fields: Their origin and their activity.*

Parsons, S. G., B. T. Gänsicke, T. R. Marsh, et al. 2012a. 'An accurate mass and radius measurement for an ultracool white dwarf.' MNRAS 426 (November): 1950–1958.

Parsons, S. G., B. T. Gänsicke, T. R. Marsh, et al. 2018. 'The scatter of the M dwarf mass-radius relationship.' MNRAS 481, no. 1 (August): 1083–1096.

Parsons, S. G., C. A. Hill, T. R. Marsh, et al. 2016. 'The crowded magnetosphere of the post-common-envelope binary QS Virginis.' MNRAS 458 (May): 2793–2812.

Parsons, S. G., T. R. Marsh, C. M. Copperwheat, et al. 2010. 'Precise mass and radius values for the white dwarf and low mass M dwarf in the pre-cataclysmic binary NN Serpentis.' MNRAS 402 (March): 2591–2608.

Parsons, S. G., T. R. Marsh, B. T. Gänsicke, et al. 2012b. 'A precision study of two eclipsing white dwarf plus M dwarf binaries.' MNRAS 420 (March): 3281–3297.

Parsons, S. G., T. R. Marsh, B. T. Gänsicke, et al. 2012c. 'The shortest period detached white dwarf + main-sequence binary.' MNRAS 419 (January): 304–313.

Pecaut, M. J., & E. E. Mamajek. 2013. 'Intrinsic Colors, Temperatures, and Bolometric Corrections of Pre-main-sequence Stars.' ApJS 208, 9 (September): 9.

Pepe, Francesco A., Stefano Cristiani, Rafael Rebolo Lopez, et al. 2010. 'ESPRESSO: the Echelle spectrograph for rocky exoplanets and stable spectroscopic observations.' In *Proceedings of the SPIE, Volume 7735, id. 77350F (2010).* Vol. 7735. July.

Percival, S. M., M. Salaris, & M. A. T. Groenewegen. 2005. 'The distance to the Pleiades. Main sequence fitting in the near infrared.' A&A 429 (January): 887–894.

Perryman, M. 2009. *Astronomical Applications of Astrometry: Ten Years of Exploitation of the Hipparcos Satellite Data.* Cambridge University Press.

Perryman, M. A. C., L. Lindegren, J. Kovalevsky, et al. 1997. 'The Hipparcos Catalogue.' A&A 500 (July): 501–504.

Pietrzyński, G., D. Graczyk, W. Gieren, et al. 2013. 'An eclipsing-binary distance to the Large Magellanic Cloud accurate to two per cent.' Nature 495 (March): 76–79.

Pinsonneault, M. H., J. Stauffer, D. R. Soderblom, J. R. King, & R. B. Hanson. 1998. 'The Problem of HIPPARCOS Distances to Open Clusters. I. Constraints from Multicolor Main-Sequence Fitting.' ApJ 504 (September): 170–191.

Plez, B. 1998. 'A new TiO line list.' A&A 337 (September): 495–500.

Prialnik, Dina. 2009. *An Introduction to the Theory of Stellar Structure and Evolution.*

Pudritz, Ralph, Paul Higgs, & Jonathan Stone. 2007. *Planetary Systems and the Origins of Life.*

Pyrzas, S., B. T. Gänsicke, S. Brady, et al. 2012. 'Post-common envelope binaries from SDSS - XV. Accurate stellar parameters for a cool 0.4 $M_{\&sun;}$ white dwarf and a 0.16 $M_{\&sun;}$ M dwarf in a 3 h eclipsing binary.' MNRAS 419 (January): 817–826.

Quirrenbach, A., P. J. Amado, J. A. Caballero, et al. 2014. 'CARMENES instrument overview.' In *Proceedings of the SPIE, Volume 9147, id. 91471F 12 pp. (2014).* Vol. 9147. July.

Rabus, Markus, Régis Lachaume, Andrés Jordán, et al. 2019. 'A discontinuity in the T_{eff}-radius relation of M-dwarfs.' MNRAS 484 (April): 2674–2683.

Rajpurohit, A. S., F. Allard, S. Rajpurohit, et al. 2019. 'Exploring the stellar properties of M dwarfs with high-resolution spectroscopy from the optical to the near-infrared (Corrigendum).' A&A 622, C1 (February): C1.

Rajpurohit, A. S., F. Allard, G. D. C. Teixeira, et al. 2018. 'Photospheric properties and fundamental parameters of M dwarfs.' A&A 610, A19 (February): A19.

Rajpurohit, A. S., C. Reylé, F. Allard, et al. 2013. 'The effective temperature scale of M dwarfs.' A&A 556, A15 (August): A15.

Rees, J. M. 2017. In prep.

Reiners, A., G. Basri, & M. Browning. 2009. 'Evidence for Magnetic Flux Saturation in Rapidly Rotating M Stars.' ApJ 692 (February): 538–545.

Renzini, A. 1987. 'Some embarrassments in current treatments of convective overshooting.' A&A 188, no. 1 (December): 49–54.

Rhode, Katherine L., William Herbst, & Robert D. Mathieu. 2001. 'Rotational Velocities and Radii of Pre-Main-Sequence Stars in the Orion Nebula Cluster.' AJ 122, no. 6 (December): 3258–3279.

Ricker, George R., Joshua N. Winn, Roland Vanderspek, et al. 2014. 'Transiting Exoplanet Survey Satellite (TESS).' In *Proceedings of the SPIE, Volume 9143, id. 914320 15 pp. (2014).* Vol. 9143. August.

Rizzuto, Aaron C., Andrew Vanderburg, Andrew W. Mann, et al. 2018. 'Zodiacal Exoplanets in Time (ZEIT). VIII. A Two-planet System in Praesepe from K2 Campaign 16.' AJ 156, no. 5, 195 (November): 195.

Robin, A. C., C. Reylé, S. Derrière, & S. Picaud. 2003. 'A synthetic view on structure and evolution of the Milky Way.' A&A 409 (October): 523–540.

Rodrigo, C., E. Solano, A. Bayo, M. Cortés-Contreras, & F. Jiménez-Esteban. 2019. 'VOSA: SED building and analysis of thousands of stars in the framework of Gaia.' In *Highlights on Spanish Astrophysics X*, edited by B. Montesinos, A. Asensio Ramos, F. Buitrago, et al., 430–430. March.

Rodriguez, Joseph E., Juliette C. Becker, Jason D. Eastman, et al. 2018. 'A Compact Multiplanet System with a Significantly Misaligned Ultra Short Period Planet.' AJ 156, no. 5, 245 (November): 245.

Rodriguez, Joseph E., Samuel N. Quinn, Chelsea X. Huang, et al. 2019. 'An Eccentric Massive Jupiter Orbiting a Subgiant on a 9.5-day Period Discovered in the Transiting Exoplanet Survey Satellite Full Frame Images.' AJ 157, no. 5, 191 (May): 191.

Rosen, S. R., N. A. Webb, M. G. Watson, et al. 2016. 'VizieR Online Data Catalog: XMM-Newton Serendipitous Source Catalogue 3XMM-DR6 (XMM-SSC, 2016).' *VizieR Online Data Catalog* 9050 (September).

Röser, S., & E. Schilbach. 2013. 'A new assessment of the kinematic distance to the Pleiades: based on radial velocities and proper motions only.' In *Advancing the Physics of Cosmic Distances,* edited by Richard de Grijs, 289:66–69. IAU Symposium. February.

Rozyczka, M., J. Kaluzny, W. Krzeminski, & B. Mazur. 2007. 'Variable Stars in the Field of the Open Cluster NGC2204.' *Acta Astronomica* 57 (December): 323–329.

Rozyczka, M., J. Kaluzny, P. Pietrukowicz, et al. 2009. 'A New Lower Main Sequence Eclipsing Binary with Detached Components.' *Acta Astronomica* 59 (December): 385–401.

Russell, H. N., W. S. Adams, & A. H. Joy. 1923. 'A Comparison of Spectroscopic and Dynamical Parallaxes.' PASP 35, no. 206 (August): 189.

Russell, Henry Norris. 1912a. 'On the Determination of the Orbital Elements of Eclipsing Variable Stars. I.' ApJ 35 (June): 315.

———. 1912b. 'On the Determination of the Orbital Elements of Eclipsing Variable Stars. II.' ApJ 36 (July): 54.

Russell, Henry Norris, & Harlow Shapley. 1912a. 'On Darkening at the Limb in Eclipsing Variables. II.' ApJ 36 (December): 385.

Russell, I. Henry Norris, & Harlow Shapley. 1912b. 'On Darkening at the Limb in Eclipsing Variables.' ApJ 36 (October): 239.

Rybizki, Jan, Markus Demleitner, Morgan Fouesneau, et al. 2018. 'A Gaia DR2 Mock Stellar Catalog.' PASP 130, no. 989 (July): 074101.

Salpeter, E. E. 1955. 'The Luminosity Function and Stellar Evolution.' ApJ 121 (January): 161.

Schwarzschild, K. 1906. 'On the equilibrium of the Sun's atmosphere.' *Nachrichten von der Königlichen Gesellschaft der Wissenschaften zu Göttingen. Math.-phys. Klasse* 195 (January): 41–53.

Schweitzer, A., V. M. Passegger, C. Cifuentes, et al. 2019. 'The CARMENES search for exoplanets around M dwarfs: Different roads to radii and masses of the target stars.' *arXiv e-prints* (April).

Seager, S., & G. Mallén-Ornelas. 2003. 'A Unique Solution of Planet and Star Parameters from an Extrasolar Planet Transit Light Curve.' ApJ 585, no. 2 (March): 1038–1055.

Ségransan, D., P. Kervella, T. Forveille, & D. Queloz. 2003. 'First radius measurements of very low mass stars with the VLTI.' A&A 397 (January): L5–L8.

Siess, L., E. Dufour, & M. Forestini. 2000. 'An internet server for pre-main sequence tracks of low- and intermediate-mass stars.' A&A 358 (June): 593–599.

Sing, D. 2016. *The Panchromatic Comparative Exoplanetary Treasury Program.* HST Proposal, October.

Skrutskie, M. F., R. M. Cutri, R. Stiening, et al. 2006. 'The Two Micron All Sky Survey (2MASS).' AJ 131 (February): 1163–1183.

Smalley, B., D. R. Anderson, A. Collier-Cameron, et al. 2012. 'WASP-78b and WASP-79b: two highly-bloated hot Jupiter-mass exoplanets orbiting F-type stars in Eridanus.' A&A 547, A61 (November): A61.

Smette, A., H. Sana, S. Noll, et al. 2015. 'Molecfit: A general tool for telluric absorption correction. I. Method and application to ESO instruments.' A&A 576, A77 (April): A77.

Soderblom, D. R., L. A. Hillenbrand, R. D. Jeffries, E. E. Mamajek, & T. Naylor. 2014. 'Ages of Young Stars.' *Protostars and Planets VI:* 219–241.

Soderblom, David R., Ed Nelan, G. Fritz Benedict, et al. 2005. 'Confirmation of Errors in Hipparcos Parallaxes from Hubble Space Telescope Fine Guidance Sensor Astrometry of the Pleiades.' AJ 129, no. 3 (March): 1616–1624.

Solanki, S. K. 1999. 'Spots and Plages: the Solar Perspective.' In *Solar and Stellar Activity: Similarities and Differences, ASP Conference Series 158, ed. C. J. Butler & J. G. Doyle. ISBN 1-886733-78-3 (1999), p.109,* edited by C. J. Butler & J. G. Doyle, 158:109. Astronomical Society of the Pacific Conference Series.

Somers, G., & M. H. Pinsonneault. 2016. 'The Impact of Starspots on Mass and Age Estimates for Pre-main Sequence Stars.' In *Young Stars & Planets Near the Sun*, edited by J. H. Kastner, B. Stelzer, & S. A. Metchev, 314:91–94. IAU Symposium. January.

Southworth, J. 2015. 'DEBCat: A Catalog of Detached Eclipsing Binary Stars.' In *Living Together: Planets, Host Stars and Binaries,* edited by S. M. Rucinski, G. Torres, & M. Zejda, 496:164. Astronomical Society of the Pacific Conference Series. July.

Southworth, J., P. F. L. Maxted, & B. Smalley. 2005. 'Eclipsing binaries as standard candles. HD 23642 and the distance to the Pleiades.' A&A 429 (January): 645–655.

Sozzetti, A., G. Torres, D. Charbonneau, et al. 2007. 'Improving Stellar and Planetary Parameters of Transiting Planet Systems: The Case of TrES-2.' ApJ 664 (August): 1190–1198.

Spitzer, Jr., Lyman. 1942. 'The Dynamics of the Interstellar Medium. III. Galactic Distribution.' ApJ 95 (May): 329.

Spitzer, Lyman. 1978. *Physical processes in the interstellar medium.*

Spruit, H. C. 1976. 'Pressure equilibrium and energy balance of small photospheric fluxtubes.' Sol. Phys. 50, no. 2 (December): 269–295.

Stahler, S. W. 1988. 'Understanding young stars - A history.' PASP 100 (December): 1474–1485.

Stassun, K. G., R. D. Mathieu, L. P. R. Vaz, N. Stroud, & F. J. Vrba. 2004. 'Dynamical Mass Constraints on Low-Mass Pre-Main-Sequence Stellar Evolutionary Tracks: An Eclipsing Binary in Orion with a 1.0 M_{solar} Primary and a 0.7 M_{solar} Secondary.' ApJS 151 (April): 357–385.

Stassun, K. G., R. J. Oelkers, J. Pepper, et al. 2018. 'The TESS Input Catalog and Candidate Target List.' AJ 156, 102 (September): 102.

Stassun, Keivan G., Karen A. Collins, & B. Scott Gaudi. 2017. 'Accurate Empirical Radii and Masses of Planets and Their Host Stars with Gaia Parallaxes.' AJ 153, no. 3, 136 (March): 136.

Stauffer, J. R., L. W. Hartmann, G. G. Fazio, et al. 2007. 'Near- and Mid-Infrared Photometry of the Pleiades and a New List of Substellar Candidate Members.' ApJS 172 (October): 663–685.

Stauffer, J. R., R. Schild, D. Barrado y Navascués, et al. 1998. 'Results of a Deep Imaging Survey of One Square Degree of the Pleiades for Low-Luminosity Cluster Members.' ApJ 504 (September): 805–820.

Stebbins, J. 1911. 'A New Bright Variable Star, β Aurigae.' ApJ 34 (September): 112–130.

Stello, D., & P. E. Nissen. 2001. 'The problem of the Pleiades distance. Constraints from Strömgren photometry of nearby field stars.' A&A 374 (July): 105–115.

Strassmeier, Klaus G. 2009. 'Starspots.' A&A Rev. 17, no. 3 (September): 251–308.

Tashkun, Sergey A., Valery I. Perevalov, Jean-Luc Teffo, et al. 2004. 'CDSD-1000: the high-temperature carbon dioxide spectroscopic databank and information system.' In Proc. SPIE, edited by Leonid N. Sinitsa & Semen N. Mikhailenko, 5311:102–113. Society of Photo-Optical Instrumentation Engineers (SPIE) Conference Series. January.

Taylor, B. J. 2006a. 'The Benchmark Cluster Reddening Project. I. Reddening Values for the Hyades, Coma, and Praesepe.' AJ 132 (December): 2453–2468.

Taylor, M. B. 2006b. 'STILTS - A Package for Command-Line Processing of Tabular Data.' In *Astronomical Data Analysis Software and Systems XV*, edited by C. Gabriel, C. Arviset, D. Ponz, & S. Enrique, 351:666. Astronomical Society of the Pacific Conference Series. July.

Terrien, R. C., S. W. Fleming, S. Mahadevan, et al. 2012. 'The Metallicity of the CM Draconis System.' ApJL 760, L9 (November): L9.

Terrien, Ryan C., Suvrath Mahadevan, Rohit Deshpande, & Chad F. Bender. 2015. 'A Near-Infrared Spectroscopic Survey of 886 Nearby M Dwarfs.' *The Astrophysical Journal Supplement Series* 220, 16 (September): 16.

Thies, Ingo, & Pavel Kroupa. 2007. 'A Discontinuity in the Low-Mass Initial Mass Function.' ApJ 671, no. 1 (December): 767–780.

Tognelli, E., P. G. Prada Moroni, & S. Degl'Innocenti. 2011. 'The Pisa pre-main sequence tracks and isochrones. A database covering a wide range of Z, Y, mass, and age values.' A&A 533, A109 (September): A109.

Topka, K. P., T. D. Tarbell, & A. M. Title. 1997. 'Properties of the Smallest Solar Magnetic Elements. II. Observations versus Hot Wall Models of Faculae.' ApJ 484, no. 1 (July): 479–486.

Torra, J., C. Turon, & A. Blaauw. 1988. *The European astrometry satellite HIPPARCOS. Scientific aspects of the Input Catalogue preparation II. Proceedings of a colloquium held at Sitges, Catalonia, Spain, 25 - 29 January 1988.* Technical report. January.

Torres, G. 2013. 'Fundamental properties of lower main-sequence stars.' *Astronomische Nachrichten* 334 (February): 4.

Torres, G., J. Andersen, & A. Giménez. 2010. 'Accurate masses and radii of normal stars: modern results and applications.' A&A Rev. 18, nos. 1-2 (February): 67–126.

Torres, G., & I. Ribas. 2002. 'Absolute Dimensions of the M-Type Eclipsing Binary YY Geminorum (Castor C): A Challenge to Evolutionary Models in the Lower Main Sequence.' ApJ 567 (March): 1140–1165.

Torres, G., C. H. Sandberg Lacy, K. Pavlovski, et al. 2014. 'The G+M Eclipsing Binary V530 Orionis: A Stringent Test of Magnetic Stellar Evolution Models for Low-mass Stars.' ApJ 797, 31 (December): 31.

Trampedach, Regner, Robert F. Stein, Jørgen Christensen-Dalsgaard, Åke Nordlund, & Martin Asplund. 2014. 'Improvements to stellar structure models, based on a grid of 3D convection simulations - II. Calibrating the mixing-length formulation.' MNRAS 445, no. 4 (December): 4366–4384.

Triaud, A. H. M. J., D. R. Anderson, A. Collier Cameron, et al. 2013. 'WASP-80b: a gas giant transiting a cool dwarf.' A&A 551, A80 (March): A80.

Tsuji, T., K. Ohnaka, & W. Aoki. 1996. 'Dust formation in stellar photospheres: a case of very low mass stars and a possible resolution on the effective temperature scale of M dwarfs.' A&A 305 (January): L1.

Unruh, Y. C., S. K. Solanki, & M. Fligge. 1999. 'The spectral dependence of facular contrast and solar irradiance variations.' A&A 345 (May): 635–642.

Valenti, J. A., & N. Piskunov. 1996. 'Spectroscopy made easy: A new tool for fitting observations with synthetic spectra.' A&AS 118 (September): 595–603.

Valenti, Jeff A., & Debra A. Fischer. 2005. 'Spectroscopic Properties of Cool Stars (SPOCS). I. 1040 F, G, and K Dwarfs from Keck, Lick, and AAT Planet Search Programs.' ApJS 159, no. 1 (July): 141–166.

Vallenari, Antonella. 2018. 'The future of Astrometry in Space.' *Frontiers in Astronomy and Space Sciences* 5, 11 (April): 11.

Van Grootel, V., M. Gillon, D. Valencia, et al. 2014. 'Transit Confirmation and Improved Stellar and Planet Parameters for the Super-Earth HD 97658 b and its Host Star.' ApJ 786, no. 1, 2 (May): 2.

van Leeuwen, F. 2007. 'Validation of the new Hipparcos reduction.' A&A 474, no. 2 (November): 653–664.

van Leeuwen, Floor. 1983. 'The Pleiades, an astrometric and photometric study of an open cluster.' PhD diss., Leiden Observatory, Leiden University, P.O. Box 9513, 2300 RA Leiden, The Netherlands.

Vogt, S. S. 1979. 'A spectroscopic and photometric study of the star spot on HD 224085.' PASP 91 (October): 616.

von Braun, Kaspar, Tabetha S. Boyajian, Gerard T. van Belle, et al. 2014. 'Stellar diameters and temperatures - V. 11 newly characterized exoplanet host stars.' MNRAS 438, no. 3 (March): 2413–2425.

Walkowicz, Lucianne M., Suzanne L. Hawley, & Andrew A. West. 2004. 'The χ Factor: Determining the Strength of Activity in Low-Mass Dwarfs.' PASP 116, no. 826 (November): 1105–1110.

Walter, F. M. 1996. 'Stellar plages (review).' In *Stellar Surface Structure,* edited by Klaus G. Strassmeier & Jeffrey L. Linsky, 176:355. IAU Symposium. January.

Ward-Thompson, D., J. Di Francesco, J. Hatchell, et al. 2007. 'The James Clerk Maxwell Telescope Legacy Survey of Nearby Star-forming Regions in the Gould Belt.' PASP 119, no. 858 (August): 855–870.

Welsh, W. F., J. A. Orosz, D. R. Short, et al. 2015. 'Kepler 453 b - The 10th Kepler Transiting Circumbinary Planet.' ApJ 809, 26 (August): 26.

West, R. G., C. Hellier, J.-M. Almenara, et al. 2016. 'Three irradiated and bloated hot Jupiters:. WASP-76b, WASP-82b, and WASP-90b.' A&A 585, A126 (January): A126.

Wilson, O. C. 1978. 'Chromospheric variations in main-sequence stars.' ApJ 226 (December): 379–396.

Wilson, T. J., & T. Naylor. 2017. 'The effect of unresolved contaminant stars on the cross-matching of photometric catalogues.' MNRAS 468 (July): 2517–2525.

———. 2018. 'A contaminant-free catalogue of Gaia DR2-WISE Galactic plane matches: including the effects of crowding in the cross-matching of photometric catalogues.' MNRAS 481 (December): 2148–2167.

Winn, J. N. 2010. 'Exoplanet Transits and Occultations.' In *Exoplanets, edited by S. Seager. Published by University of Arizona Press, Tucson, AZ, 2010, 526 pp. ISBN 978-0-8165-2945-2., p.55-77,* edited by S. Seager, 55–77.

Winn, J. N., & D. C. Fabrycky. 2015. 'The Occurrence and Architecture of Exoplanetary Systems.' ARA&A 53 (August): 409–447.

Worden, J. R., O. R. White, & T. N. Woods. 1998. 'Evolution of Chromospheric Structures Derived from Ca II K Spectroheliograms: Implications for Solar Ultraviolet Irradiance Variability.' ApJ 496 (March): 998–1014.

Wright, E. L., P. R. M. Eisenhardt, A. K. Mainzer, et al. 2010. 'The Wide-field Infrared Survey Explorer (WISE): Mission Description and Initial On-orbit Performance.' AJ 140, 1868-1881 (December): 1868–1881.

Wright, Nicholas J., Jeremy J. Drake, Eric E. Mamajek, & Gregory W. Henry. 2011. 'The Stellar-activity-Rotation Relationship and the Evolution of Stellar Dynamos.' ApJ 743, 48 (December): 48.

Wright, Nicholas J., Elisabeth R. Newton, Peter K. G. Williams, Jeremy J. Drake, & Rakesh K. Yadav. 2018. 'The stellar rotation-activity relationship in fully convective M dwarfs.' MNRAS 479, no. 2 (September): 2351–2360.

Yi, S. K., Y.-C. Kim, & P. Demarque. 2003. 'The Y^2 Stellar Evolutionary Tracks.' ApJS 144 (February): 259–261.

Yi, S., P. Demarque, Y.-C. Kim, et al. 2001. 'Toward Better Age Estimates for Stellar Populations: The Y^2 Isochrones for Solar Mixture.' ApJS 136 (October): 417–437.

Zwahlen, N., P. North, Y. Debernardi, et al. 2004. 'A purely geometric distance to the binary star Atlas, a member of the Pleiades.' A&A 425 (October): L45–L48.